Magnetism and transport in nanostructured domain wall systems

Roberts, Hywel

Award date:
2008

Awarding institution:
University of Bath

MAGNETISM AND TRANSPORT IN NANOSTRUCTURED DOMAIN WALL SYSTEMS

Submitted by Hywel Gwynedd Roberts
for the degree of
Doctor of Philosophy
of the University of Bath
May 2008

Contents

Abstract

The precise control of ferromagnetic domain wall formation opens up exciting avenues of research and potential application in spintronics — the manipulation of charge carriers via their spin properties. Recent experiments on Cobalt-Platinum multilayers containing artificially created domains provide the motivation for this work.

In this thesis the electronic structure of CoPt multilayers are calculated by an *ab initio* multiple scattering method, and attempts are made at replicating the systems used in experiments, including lattice relaxations and the effects of substitutional alloying.

The magnetic reversal process in Pt/Co/Pt trilayer systems is studied in the framework of micromagnetics, in which effects such as exchange, magnetocrystalline anisotropy and the demagnetising field are treated phenomenologically. The results are compared to recent experiments and the switching mechanism can be understood in terms of domain growth and domain wall nucleation.

A ballistic transport framework is outlined in terms of a tight binding Green function method. The domain wall is modelled as a change in the local spin reference frame. The method is applied to Cobalt Platinum trilayers, and it is found that the resulting domain wall resistances are sensitive to the details of the Fermi energy bands.

Subsequently, the angular dependence of domain wall resistivity in Pt/Co/Pt systems is studied by a model based on the anisotropic resistivity tensor that is expected in a domain wall. The results are used to extract resistivity parameters from experimental data, and a positive domain wall resistivity is identified, whilst resulting arguments provide supporting evidence for the Levy-Zhang theory of domain wall resistance.

Finally, recent experiments on the dilute magnetic semiconductor (Ga,Mn)As have provided evidence for a negative intrinsic domain wall resistance in this material. By applying a similar model to that used on the CoPt systems, it is shown that the anomalous magnetoresistance effect can also provide a significant negative contribution to the measured resistance via induced eddy current at the domain wall boundary.

Acknowledgements

Firstly I would like to thank my supervisor Dr. Simon Crampin for his support and guidance during my time at the University of Bath. A substantial contribution to this thesis is from the experimental work of Prof. Simon Bending and Dr. Atif Aziz to whom I am also indebted.

Thanks also go to the members of the administrative and IT staff at the department of physics who have been of great assistance over the past few years.

Included in this list of acknowledgements are my fellow students who have made my time here an enjoyable experience. An additional mention goes to John Neal with whom I worked on an additional project during my studies in Bath.

Yn olaf, hoffwn ddiolch i fy nheulu am eu cefnogaeth. Hebddynt hwy ni fyddai hyn wedi bod yn bosib.

Publications

During this project the following paper were published:

1. A. Aziz, S.J. Bending, H. Roberts, S. Crampin, P.J. Heard, and C.H. Marrows; *Artificial domain structures realized by local gallium focused Ion-beam modification of Pt/Co/Pt trilayer transport structure*, Journal of Applied Physics **98**, 124102 (2005).

2. A. Aziz, S.J. Bending, H. Roberts, S. Crampin, P.J. Heard, and C.H. Marrows; *Investigation of artificial domains realized by local gallium focused ion-beam modification of Pt/Co/Pt trilayer structures*, Journal of Applied Physics **99**, 08C504 (2006).

3. J.S. Neal, H.G. Roberts, M.R. Connolly, S. Crampin, S.J. Bending, G. Wastlbauer, and J.A.C. Bland; *Magnetisation reversal in epitaxial Fe(100) disks studied by high resolution scanning Hall probe microscopy*, Ultramicroscopy **106**, 614 (2006).

4. A. Aziz, S.J. Bending, H.G. Roberts, S. Crampin, P.J. Heard, and C.H. Marrows; *Angular Dependence of Domain Wall Resistivity in Artificial Magnetic Domain Structures*, Physical Review Letters **97**, 206602 (2006).

5. H.G. Roberts, S. Crampin, and S. J. Bending; *Extrinsic anisotropic magnetoresistance contribution to measured domain wall resistances of in-plane magnetized (Ga,Mn)As*, Physical Review B **76**, 035323 (2007).

Abbreviations

AMR	Anomalous MagnetoResistance
APW	Augmented PlaneWave
ASA	Atomic Sphere Approximation
CIW	Current In Wire
CPA	Coherent Potential Approximation
CPW	Current Perpendicular to Wire
DFT	Density Functional Theory
EHE	Extraordinary Hall Effect
FCC	Face Centred Cubic
GMR	Giant MagnetoResistance
HCP	Hexagonal Close Packed
IBZ	Irreducible Brillouin Zone
LDA	Local Density Approximation
MFM	Magnetic Force Microscopy
TB	Tight Binding

Chapter 1

Introduction

This thesis concerns the investigation of spintronic devices by theoretical methods, with the aim of illuminating the magnetic and electrical properties in systems fabricated experimentally. The term spintronics encompasses work in which electrical currents are manipulated via the charge carrier spin as opposed to conventional electronics that do not take advantage of this additional degree of freedom. Such devices are not solely of academic interest: contemporary data storage methods, such as those found in computer disk drives, rely on spintronic technology for data manipulation. Recent years have seen rapid progress in this field, owing, in part, to advancements made in device fabrication techniques, in particular the ability to pattern nanoscale features in multilayer devices. Continuing on from this research, regions of non-colinear magnetism termed ferromagnetic domain walls have been the subject of renewed interest in recent times owing to their potential applications to non-volatile data storage and novel logic devices. The characterisation of devices based on domain wall physics is therefore important for future progress in this rapidly developing field.

1.1 The basics of magnetism

To answer the question 'What is a domain wall?' it is first necessary to understand the origins of magnetism. The type of magnetism studied in this thesis is ferromagnetism and as such the bulk of this introduction will outline the basic

concepts with which the reader must be acquainted. Subsequent chapters deal with the specifics in greater detail.

When it is said a material is magnetised or is magnetic what do we mean? The magnetic property of a material originates in the motion of its constituent charge carriers. This can be split up into two contributions: the first, known as the orbital moment arises due to the motion of electrons around the nuclear core, and the second, usually a larger effect due to the spin of the electron, is known simply as the spin moment. In a non-magnetic atom these contributions are cancelled internally — for instance, in the case of spin moments there are equal numbers of clockwise and anticlockwise spin rotations giving a vector sum of zero. However a number of effects can break this symmetry, leading to the formation of a magnetic state the magnitude of which can be expressed in terms of the magnetic moment per unit volume, usually called the magnetisation strength or intensity, traditionally denoted by the vector $\mathbf{M}$. Since the common types of magnetism are dependent on an external applied field a magnetic susceptibility is defined as being induced $\mathbf{M}$ per unit applied field or

$$\chi = \frac{\partial \mathbf{M}}{\partial \mathbf{H}}. \tag{1.1}$$

A summary of the common types of magnetism is now presented. A very weak magnetism can be exhibited in all materials, the direction of which is opposite to that of an applied magnetic field. This *diamagnetism* arises due to symmetry breaking in the orbital moments under the external field but has negative susceptibilities that are orders of magnitude smaller than other types of magnetism. Another magnetic state that is induced by an external field is *paramagnetism*. In contrast to diamagnetism this effect is due to the spin moment — atoms have differing spin occupancies. In pure paramagnetism, the absence of an applied field results in moments that are randomly distributed due to thermal agitation resulting in a cancelling of the internal magnetic field. Application of an external field results in the average magnetisation shifting from zero to having a positive component in the direction of the field as moments in the sample align with it. In contrast to diamagnetism, paramagnetic susceptibilities are always positive.

The type of magnetism commonly exploited in magnetic devices and permanent magnets is *ferromagnetism*, and is by far the field that has received the greatest attention in recent years both theoretically and experimentally. The mechanism

underlying ferromagnetism is similar to that observed in paramagnetism, namely individual atoms having an intrinsic moment associated with a spin asymmetry. Crucially in this case atoms of the solid are not independent but are subject to interactions of sufficient strength that overcome the thermal disordering. The net result is that individual moments tend to align with their neighbours in macroscopic regions of homogenous magnetisation known as *domains*. The nature of the interaction (*exchange*) that leads to this spontaneous ordering is quantum mechanical and will be discussed in greater detail in subsequent sections. Despite this localised ordering the global ground state of a bulk ferromagnetic material is often demagnetised due to domains within a crystal aligning in opposite directions to ensure the minimisation of energetically unfavourable stray fields (*magnetostatic energy*). The exchange energy is isotropic with respect to the crystal, only depending on the relative orientation of the atomic moments; however, certain directions are favoured due to effective interactions with the crystal lattice (*magnetocrystalline anisotropy*), and as a result the inter-domain angles are usually 90° or 180° in cubic materials. Stray fields are also minimised by domains that run parallel to the surface of a sample. This effect is less important in bulk crystals, but can be significant in mesoscopic systems, thus the magnetostatic energy is also referred to as a shape anisotropy. An applied magnetic field provides another source of anisotropy and, depending on the system energetics, can induce the rotation of atomic moments until they are colinear with the field vector. As a result, domains aligned with the field grow and others contract resulting in an increase of the sample magnetisation in the field direction. As the magnitude of the external field is increased moments continue to rotate until the sample consists of one large domain. This condition is known as the saturisation state; the application of a greater field cannot increase the ferromagnetic magnetisation any more. This is a common experimental tool to measure the properties of a system as the reversal process can allow the study of domain wall motion, and the exact reversal mechanism is dependent on several material parameters. A schematic of a typical magnetisation process is shown in figure 1.1. In ultra-thin films the stray fields giving rise to the shape anisotropy effect are significantly smaller owing to the reduced domain volume. If the crystalline anisotropy favours a single crystal direction perpendicular to the film, the magnetisation can point out of the sample plane even with no coercing applied field — the sample is said to be perpendicularly magnetised. In this thesis Cobalt-Platinum layers are studied which exhibit this type of behaviour.

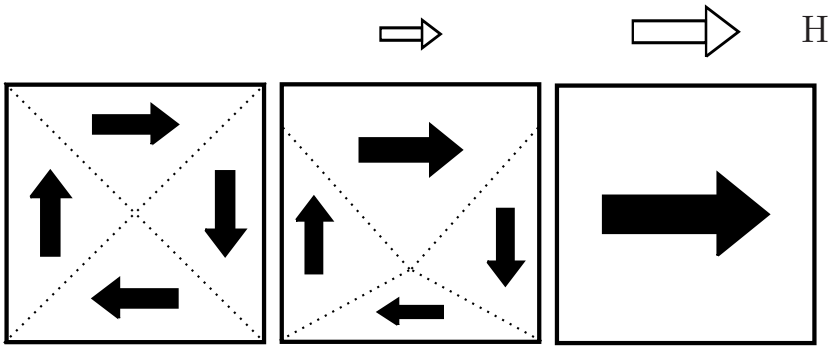

Figure 1.1: Demonstration of sample magnetisation by an external field. Image (a) shows a ferromagnetic sample in the ground state, the direction of the aligned moments in each domain is indicated by the black arrows and correspond to interdomain angles of 90°. The domains in the demagnetised sample form a closed circuit enabling the stray magnetic field to be minimised. (b) As an external field, H, is applied the domain in the direction of the field starts to grow by rotating atomic moments at its interfaces. (c) Finally when the field is sufficiently large the sample is fully magnetised along the field direction.

One of the defining features of ferromagnetism is *hysteresis*, or the irreversibility of magnetisation. If one plots the net ferromagnetic magnetisation versus the applied field intensity in a reversal process it becomes apparent that the path taken going from negative to positive saturisation is different to that taken in reverse. In some ferromagnets the sample remains significantly magnetised even under no applied field, a situation known as remanence, and the opposing field needed to switch the magnetisation is known as the coercive field. A typical hysteresis curve is demonstrated in figure 1.2a. Another characteristic feature of a ferromagnetic material is the *Curie temperature*. When a ferromagnet is spontaneously magnetised the interatomic interactions dominate the thermal noise, however as the temperature is increased the directions of the atomic moments are subject to larger random fluctuations. The transition point between ferromagnetic ordering and a randomly magnetised paramagnetic state is called the Curie point, above which $\mathbf{M}$ is zero under no applied field. Cobalt has the highest known elemental Curie temperature and retains around 97% of its saturisation magnetisation at room temperature [1].

The anisotropic magnetoresistance or AMR effect is a directional dependence of the resistivity of a ferromagnet, such that the resistance parallel to the magnetic moment vector differs from the resistance perpendicular to it. AMR was first explained by Kondo [2] as the scattering of s-type electrons by orbital moments

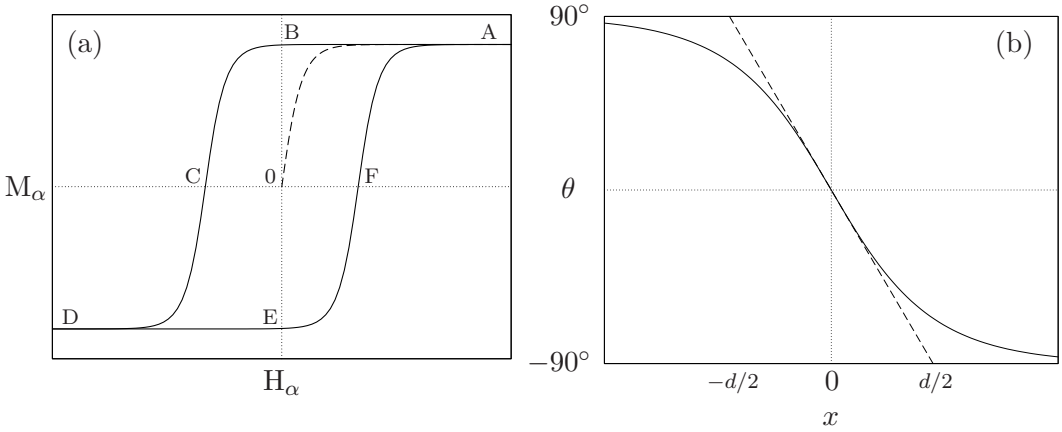

Figure 1.2: (a) Hysteresis loop of a typical ferromagnet along axis α. The curve starts at the position 0 where the sample is under no applied field and has zero net magnetisation owing to domain closure. A positive field is applied and the sample becomes magnetised up to some saturisation value (0→A). When the field is reduced the original path is not taken in reverse, instead at zero field the sample can retain as significant fraction of its magnetisation (point B). As the field is reversed the magnetisation is reduced, passing through the zero point at C. The value of H at this point is called the coercive field. Finally when the negative field is large enough the sample becomes fully magnetised in the opposite direction (point D). Reversing this process takes us through points E and F and finally back to A. (b) Variation in the moment rotation angle θ in crossing a domain wall separating two domains with magnetisation angles $\pm 90°$, representing magnetisation in the $\pm z$ directions. The dashed line represents the gradient of the steepest point of the curve, defining the conventional domain wall width, d.

induced by the $3d$ spin moment. Since the atomic moments differ in orientation in a multi-domain state, a significant resistance change can be observed when the domains are eradicated, attributable directly to the AMR effect. This is one of many *extrinsic* effects that have caused problems for researchers investigating the electrical properties of spintronic devices experimentally.

The interface between two domains is not an abrupt change in the magnetisation but rather a gradual rotation from one state to another, and the region in which the magnetisation rotates is called a *domain wall*. A domain wall becomes necessary due to the exchange energy cost associated with an abrupt change in the magnetisation. In competition is the anisotropy energy lost by aligning along the preferred crystal axis of the sample, and it is the balance between these two interactions that determine the characteristic scale on which the magnetisation rotates, known as the domain wall width. It is possible to classify common do-

main walls into types based on the angle between the domains, either 90° or 180° (or near these values) and the plane of rotation in the transition region producing either Bloch or Néel walls. Figure 1.2b shows the profile of a 180° domain wall separating two domains magnetised in the $\pm z$ direction, that is, perpendicular to the profile direction, x. The rate of rotation is greatest in the middle of the domain wall ($x = 0$) and this slope is indicated by the dashed line. Several definitions of the domain wall width, d, exists in the literature. The most common is after Lilley [3] in which a linear continuation of the steepest gradient is used, as demonstrated by the dashed line. In the case of a Bloch wall the rotation occurs perpendicularly to the profile axis x, effectively rotating about this axis. In contrast, Néel type walls rotate in the direction of the domain wall cross-section, lying along the x axis at $x = 0$. The type of wall present in any given sample is dependent on the energetics of the competing magnetic interactions.

A contemporary area of research is that of current induced domain wall motion. The subject was first studied by Berger [4, 5, 6] in the early 80s, and it was found that a force sufficient to mobilise a domain wall could indeed be exerted by an electric current. For an account of recent advancements in this field the reader is referred to the review article by C.H. Marrows [7].

We conclude this brief introduction to magnetism by mentioning two other magnetic groundstates that are common in materials: Ferri- and Antiferro- magnetism. These types contrast with ferromagnetism as an *antiparallel* alignment of spin is favoured. In antiferromagnetism neighbouring moments are identical in magnitude but oppositely aligned, and no spontaneous magnetisation is present due to exact cancellation. An external magnetic field can coerce the moment to align and similar to the paramagnetic state susceptibilities range from 10^{-5} to 10^{-2}. The susceptibilities are highly temperature dependent as at low temperature the ordered spin arrangement is maintained reducing χ significantly. Above a specific temperature named after Nèel the material becomes paramagnetic. Examples of antiferromagnetic materials are Cr, MnO and FeS. In Ferrimagnetism more than one magnetic atom is present, the lattice consists of two sublattices occupied by the different atoms. The moments are aligned as in antiferromagnetism but the magnitude of the moments are not the same, the result being that the magnetic flux is not exactly compensated for and a net spontaneous magnetisation can exist below the Curie temperature. Common ferrimagnets include Yttrium Iron garnet (YIG) and magnetite.

1.2 GMR and Domain wall based devices

Devices based on the giant magnetoresistance (GMR) effect are commonly used as magnetic sensors in devices such as computer hard drives, and share many similar features to domain wall based resistance systems. Figure 1.3 shows a ferromagnetic/non-magnetic multilayer GMR spin-valve system containing two different types of ferromagnet. The first, a 'hard' ferromagnet has a high coercive field, and is denoted by the two layers marked with green arrows, while in the middle of the sample a 'soft' ferromagnet with a lower coercive field is denoted by the cyan arrow. The non-magnetic spacer, denoted by the light grey regions, decouple the short range exchange interactions between neighbouring ferromagnetic regions. The structure is engineered to have the anti-ferromagnetic (opposing moments) configuration in the ground state (no external field) through magnetostatic interactions. In this state an additional resistance is measured due to the spin dependent scattering at the layer boundaries; an electron travelling in the material can be scattered by the abrupt change in the spin channel band structures. Application of an external field coerces the soft material's atomic moments to align with it, and the resulting decrease in the current perpendicular to plane (CPP) resistance, which can therefore be used to identify the presence of the external field, is attributed to the removal of the scattering from the spin dependent band structure. A review of GMR technology can be found in reference [8].

Domain wall based systems operate on a similar principle to the GMR materials, but the current is in the plane (CIP) of the material and, in the case of naturally forming domain walls, the material can be chemically homogenous. Figure 1.4 shows a schematic of such a thin layered system, where two perpendicularly magnetised domains (cyan arrows) are separated by a single domain wall, denoted by the dark grey region. In contrast to the abrupt change in magnetisation found in the GMR system the magnetisation rotates gradually between domains in these systems. The presence of the domain wall alters the resistivity of the region it occupies, although the exact nature of this contribution is still a matter of contention in the literature. Application of an external field, perpendicularly to the sample in this case, eradicates the domain wall by coercing domain alignment in the sample. The measurable change in resistance can be attributed to the removal of the intrinsic domain wall contribution and any extrinsic factors such as AMR, or the Lorentz magnetoresistance that results from the deflection of

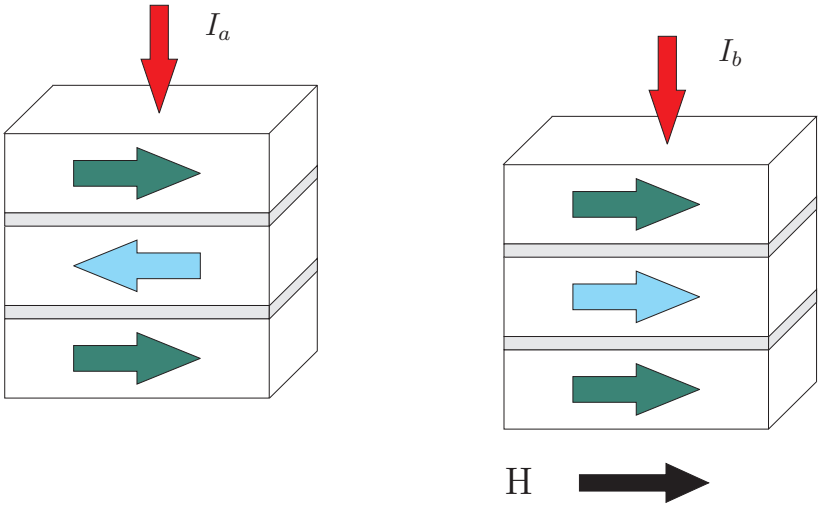

Figure 1.3: Diagram illustrating the basic mechanism of the GMR principle. Three ferromagnetic layers representing a 'hard' (green arrows) and 'soft' (blue arrow) magnetic material are exchange decoupled by non-magnetic spacers denoted by the grey region. In the ground state the layers are antiferromagnetically aligned due to the magnetostatic energy, whilst under an applied field, H, the central soft layer is coerced to align with the harder ferromagnets. The net effect is a decrease of the resistance so that $I_a < I_b$ for a fixed driving voltage, a measurable difference that indicates the magnetic state of the device.

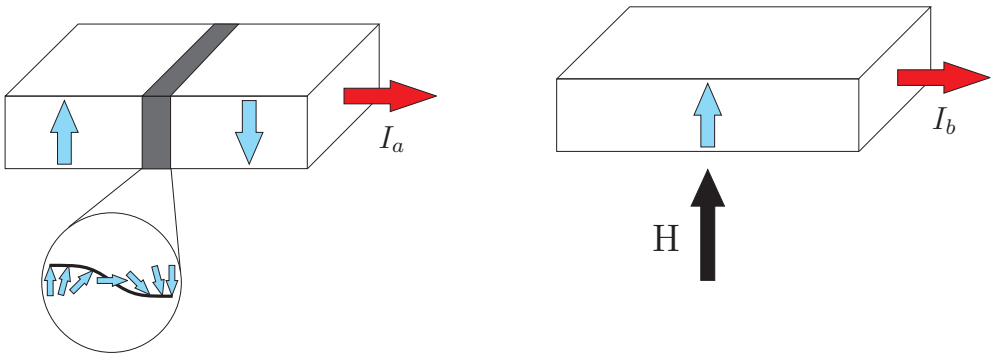

Figure 1.4: Setup of a domain wall resistance based layer device with similarities to the GMR based system. Here only a single domain wall is shown, whilst in principle many of these domain walls can be used in series. In the left panel two domains are separated by a single domain wall. Application of a perpendicular external field aligns both domains, erasing the domain wall and a change in the electrical properties is measurable so that $I_a \neq I_b$.

current lines by the magnetic domains. This property, coupled with domain wall motion opens up the possibility of not only magnetic sensors but logic devices and data storage using domains as information quanta.

Ferromagnetic domain magnetoresistance has been a subject of speculation from as early as the 1930s, with the first experiments reporting no resistance change as a function of the domain configuration [9, 10]. However, owing to an improvement in measurement resolutions, Heaps [11] was able to measure a small resistance change in a strained Ni wire as the magnetisation was saturated. The interpretation of these results were in term of the AMR effect, rather than a contribution from a scattering due to the domain walls. It was some time later, in the late 1960s and early 1970s, that the topic was revisited using bulk crystals of high purity. The most prominent experiments were performed on Iron whiskers by Coleman *et al.* [12, 13, 14] in which resistance increases of up to an order of magnitude were found for multidomain states at low temperatures, but subsequent analysis showed that this effect was due to Kohler magnetoresistance (see below). Following on from such studies, thin films were employed for magnetoresistance measurements as a precursor to modern experiments that use such layered structures. Okamoto *et al.* [15, 16] and Masuda *et al.* [17] performed experiments on films of GdCo and MnBi to measure changes in the resistance that were associated with the domain configuration.

Although these experiments demonstrate that a multidomain configuration can affect the resistance of a sample, the changes cannot straightforwardly be attributed to an intrinsic domain wall resistance. So called extrinsic effects dominate the measured resistance change, including the Kohler effect in which the Lorentz force alters the trajectory of electrons in the sample, and the magnetisation-dependent ordinary and anisotropic magnetoresistances. Owing to its small size, the scattering from a domain wall is difficult to measure and consequently very little progress was made in this field until the mid 1990s.

A brief discussion of the main theories of domain wall resistance will now be presented before the modern experimental works are described.

1.3 Theories of domain wall resistance

The earliest paper that attempted a theoretical treatment of domain wall resistance was by Cabrera and Falicov [18] in 1974. In this work they calculated the reflection coefficient of spin up and spin down electrons, with the domain wall acting as a spin-dependent potential. Spherical Fermi surfaces were used with a rigid shift of the parabolic bands to account for the exchange splitting in two regimes: where the exchange splitting is small relative to the Fermi energy; and where the exchange is much larger than the Fermi energy. In the first case the resistance was found to decay exponentially with respect to the wall width and consequently the positive domain wall resistances obtained were small ($\approx 10^{-4}$ of background) for realistic domain wall sizes. Considerations of large spin polarisations were restricted to domain walls of atomic abruptness, setting up a straightforward tunnelling problem in which the conductance goes to zero for half-metallic systems. In a second paper by the same authors [19] diamagnetic Lorentz force effects were considered that also gave rise to a positive magnetoresistance.

Despite the authors' claim that the results can be used to interpret experimental results on Fe whiskers, they concluded that electrons can traverse the wall adiabatically if the wall is wide enough — resulting in a contribution that is vanishingly small for real systems. Following this, Berger [4] presented arguments in favour of the adiabatic model of spin rotation and proposed a different mechanism in which eddy currents formed around a domain wall due to the Hall effect contribute to the resistance. These eddy currents lose energy by the usual Joule heating mechanism and an additional resistance will therefore be measured. Berger suggested this mechanism could account for the experimental results of Okamoto *et al.* [15, 16] and Masuda *et al.* [17].

Many years later the topic was revisited by Viret *et al.* [20] who presented a semi-classical model of domain wall resistance based on the Larmor precession of the electron around the rotating local moment as it traverses a domain wall. They proposed that as an electron enters the domain wall region the change in the local exchange field direction causes the electron to rotate about this field at a pseudo-Larmor frequency as shown in figure 1.5a. However, this rotation is not rapid enough to make the process totally adiabatic and the spin of the electron and local magnetisation are not aligned. Assuming that the resistivities of both

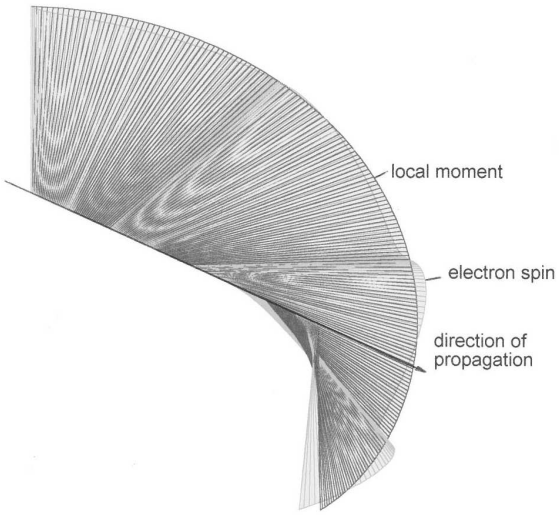

Figure 1.5: Numerical simulation of the canting of the conduction electron spin as it attempts to follow the local magnetisation during traversal of the domain wall in the laboratory frame of reference. *Image and caption from* [20].

spin channels differ and are independent in the domains, then the mixing of the channels will result in an increase of the resistance that can by understood by a two resistor model as the channels become coupled. A comparison of this model with the experimental data presented in the same paper shows good agreement. This model also predicts that narrower domain walls offer a greater impedance to current flow as this adiabatic perturbation will be greater.

Two preeminent papers on domain wall resistance exist in the literature, both published shortly after the Viret paper in 1997: that of Levy and Zhang [21], often used to interpret experimental findings of a positive domain wall resistance; and that of Tatara and Fukuyama [22], the most cited reference in studies where a negative intrinsic domain wall resistance was found.

Levy and Zhang used the spin dependent Hamiltonian that has been applied to model GMR in multilayer systems:

$$H_0 = -\frac{\hbar^2\nabla^2}{2m} + V(\mathbf{r}) + J\sigma \cdot \mathbf{M}(\mathbf{r}), \tag{1.2}$$

where $V(\mathbf{r})$ is the non magnetic potential, J is the exchange splitting and σ is the electron spin vector. This Hamiltonian can be spin diagonalised by rotating the spin operator to be parallel with the local magnetisation vector, $\mathbf{M}(\mathbf{r})$. In

the case of colinearly magnetised samples, this process is trivial, such that

$$H_\theta = R_\theta^{-1} H_0 R_\theta = -\frac{\hbar^2 \nabla^2}{2m} + V(\mathbf{r}) + J\sigma_z, \tag{1.3}$$

where R_θ is the operator that rotates between the two representations. In a system containing a domain wall the rotation angle θ is now a function of the position and the rotated Hamiltonian is not so simple. As position and momentum do not commute the kinetic energy term becomes

$$R_\theta^{-1}\left(-\frac{\hbar^2 \nabla^2}{2m} R_\theta\right) = -\frac{\hbar^2 \nabla^2}{2m} + V_{\text{pert}}. \tag{1.4}$$

This additional term, V_{pert}, represents corrections to the wavefunction that arise from the rotating background magnetisation, and is the quantum equivalent of the misstracking referred to in the Viret paper. Levy and Zhang then use a Boltzmann transport method with a spin dependent impurity scattering potential to produce several useful equations that can be tested experimentally, one of which relates the domain wall resistivity anisotropy to the resistivities of the spin channels:

$$\frac{R_{\text{CPW}}}{R_{\text{CIW}}} = 3 + \frac{10\sqrt{\rho_0^\uparrow \rho_0^\downarrow}}{\rho_0^\uparrow + \rho_0^\downarrow}. \tag{1.5}$$

Here R_{CPW} and R_{CIW} are the currents both perpendicular and parallel to the plane of the domain wall and $\rho_0^\uparrow$ and $\rho_0^\downarrow$ are the spin up(down) channel resistivities.

In contrast to Levy and Zhang, the work of Tatara and Fukuyama [22] outlines a mechanism that can lower the resistance of a sample in the presence of a domain wall. In metallic samples containing impurities the interference of complementary electron waves around a closed scattering loop can result in a greater probability of locating an electron at an impurity, an effect known a weak localisation. As a result, the conductivity of a metal is decreased by this backscattering effect, particularly in low dimensional systems where the probability of a self-crossing scattering series is increased. The authors show that the domain wall can contribute to the decoherence of electrons, hence reducing the constructive interference of the weak localisation. In this case, these electrons are no longer weakly bound to the impurity and the resistivity of the material is reduced; however, this effect becomes less significant as the temperature of the system is increased. Recent studies to measure weak localisation effects in Co and CoPt layered wires

have failed to detect WL effects in these materials within the limits of their high-resolution measurements [23, 24, 25].

Many other theoretical works exist on the subject of domain wall resistivity, a brief summary of these is now presented.

The dephasing model of domain wall resistance was investigated again by Jonkers *et al.* [26] using a time dependent approach to the spin dependent impurity scattering. They found that the domain wall reduces the resistivity of the sample and obtained good agreement with results based on the formalism of Tatara and Fukuyama [22] .

All the models presented so far are based upon a simplified two band model of the electron states. Van Hoof *et al.* [27] presented a ballistic calculation of domain wall resistivity for various transition metals employing realistic band structures. It was found that the ballistic conductivity is enhanced significantly over the predictions of a two band model due to the near degeneracy of bands near the Fermi energy, e.g. in Cobalt the magnetoresistance is 0.33% for realistic domain widths as opposed to 0.008% for a two band model.

Braatas *et al.* [28] performed ballistic calculations in a two band model, and found, as did van Hoof *et al.*, that the domain wall resistivities are vanishingly small. They also conducted diffusive transport calculations using the Kubo formula and found that the domain wall resistance can be strongly enhanced when the scattering lifetimes of the two spin channels differ. It turns out that generalising this diffusive method to realistic band structures is cumbersome [29]. Around the same time the group also published a paper that claimed to offer another explanation for the observed negative resistance in some experiments [30]. The domain wall is expected to have a small effect on the exchange splitting, slightly altering the magnetisation and therefore the charge distribution in each spin channel, hence the resistance in the classical Drude conduction model is changed. In fact it was shown that the resistance due to the domain wall could be either positive or negative depending on the spin dependent relaxation rates.

Work by Dugaev *et al.* [31] considered electron-electron interactions in the vicinity of the domain wall, with the ferromagnetic bandstructure treated in a two-band model with appropriate spin transformations made in the domain wall re-

gion. Within a semi-classical model they then calculated spin and charge densities, and the transport characteristics that are modified by spin-accumulation effects. The role of spin accumulation in the resistance properties of a domain wall was studied further by the authors in references [32, 33]. Around the same time Dzero *et al.* [34] looked at the spin accumulation at domain boundaries in the ballistic limit, and found that this effect can produce significant magnetoresistances. They found that this couldn't account for the positive domain wall resistance found in Ebels *et al.* [35], but propose a new type of domain wall that produces a larger spin accumulation effect, without giving details. It was also shown by Šimánek [36] using calculations based on the kinetic energy of the Wigner function, that spin accumulation effects cannot account for the observed resistance in the experiment.

Gallego *et al.* [37] performed density functional theory calculations on NiFe systems. By using the Kubo-Greenwood formula and a linear domain wall model they found an increase of the CIW and CPW resistivities relative to the single domain state. They also found that the AMR effect is greatly reduced inside a domain wall.

In the diffusive limit Bergeret *et al.* [38] calculated the domain wall resistance in mesoscopic magnetic wires with spin dependent impurity scattering. The kinetic properties were derived from the matrix distribution function, and the model applied to two cases: a narrow domain wall with small exchange splitting and a longer domain wall in the adiabatic limit. In both cases the domain wall resistance is found to be positive.

Yavorsky *et al.* [39] modelled GMR caused by a Bloch wall in pure Fe by *ab initio* electronic structure calculations. The conductance was calculated using a linearised Boltzmann equation in the relaxation time approximation. Thin domain walls were required to produce appreciable magnetoresistances, with a relationship that is inversely proportional to the domain wall width. This is in agreement with the findings of van Hoof *et al.* [27].

Kudrnovský *et al.* [40] have used realistic potentials in calculations of domain wall resistance in common ferromagnets. Ballistic calculations were also carried out on substitutional alloys based on Co with impurities of Cu, Ni and Cr by using the coherent potential approximation. It was found that a positive domain

wall resistance is present in all cases studied.

Theoretical studies have also been performed on systems with unusual or low dimensional geometries. For example, Pereira and Miranda [41] have considered the extreme case of Luttinger liquid behaviour in a nanowire and showed that in this system a domain wall can switch the material to a spin-charge insulator. Magnetoresistance studies of spring ferromagnets were performed by Inoue *et al.* [42] in the ballistic limit. They show that the domain wall resistance does not have a monotonic dependence on the domain wall width, and that a negative domain wall resistance may be possible under certain conditions. Zhang and Xiong [43] have performed micromagnetic and conductance calculations on ferromagnetic zig-zag wires. A transfer matrix method was used, and it was found that the domain wall resistance could be positive or negative depending on the wall width.

More recently, the transport properties of domain walls in ferromagnetic nanowires have been studied by Gopar *et al.* [44]. A two band model was employed and the conduction obtained from the Landauer formula. Studying the transmission of electrons through a domain wall in different regimes, they find that the positive domain wall resistance is largely unaffected by the precise profile of the wall.

Falloon *et al.* [45] used a classical two-resistor model coupled with a two-band Hamiltonian to calculate the resistances of a domain wall in a nanowire with simple, confined transverse modes. The ballistic regime is used to obtain the conductance parameter for the resistor model. It is found that the resistance is small compared to interface GMR, but is within an order of magnitude of experiments by Ebels *et al.* [35]. The torque exerted on a domain wall by the spin polarised current is also calculated to estimate the speed of the resulting domain wall motion.

Koma and Yamanaka [46] take the approach that the resistance changes can be explained in terms of heat generation in a sample. In their model the domain wall is predicted to occupy a region near an impurity that minimises the total heat generation, and this principle of impurity scattering is used to explain the domain wall resistance found in experiments.

Nakamura and Nonoyama [47] studied the effect of domain wall pinning on the electron conduction in the random phase approximation. They find that the

domain wall enhances the resistance due to the presence of spin fluctuations around it. It is also found that domain wall pinning reduces these fluctuations and consequently suppresses this effect.

Dilute ferromagnetic semiconductors are promising candidates for spin injection into semiconductors [48] and a wide range of applications in spintronics. A common material used in such studies is (Ga,Mn)As, of which a brief account is now given. Fabrication of this material is usually done via molecular-beam epitaxy (MBE) and introducing Mn impurities into the growth process, where direct lattice substitution occurs with a Ga atom. Ferromagnetism is achieved at relatively low Mn impurity concentrations, typically values of 1–6% are used. The main limiting factor in development of practical (Ga,As)Mn based devices is the relatively low Curie temperature of around 70 K [49, 50] although with selective p-type doping values of 170 K have be achieved [51]. In terms of theoretical modelling of semiconductor devices Vignale and Flatté [52] claim that a domain wall can give rise to non-linear transport, with obvious comparisons to the effects observed in a p-n junction. Nguyen and coworkers [53] studied a resistance contribution from a domain wall in the semiconductor zinc blende. They conclude that the domain wall resistance remains non-zero in the absence of disorder in the adiabatic case, in contrast to the result of Cabrera and Falicov [18] in metal systems. Later, Oszwaldowski *et al.* [54] used a disorder free Landauer-Büttiker method to calculate the domain wall resistance in (Ga,Mn)As and found that the value of the resistance given by Nguyen in the adiabatic limit was overestimated, and found the exact value to be highly sensitive to the precise shape of the wall. Their results were found to be an order of magnitude too small to explain the experimental findings of Chiba *et al.* [55].

Recent theoretical efforts have also focused on superconductor-ferromagnetic hybrid devices, for example references [56, 57]. The Cooper pair phenomenon of superconductivity prefers antiparallel spin alignments, in competition with the parallel orientation found in ferromagnetism leading to new phenomena such as coupling between vortex structures of superconductivity and ferromagnetic domains.

1.3.1 Recent experiments

The intrinsic domain wall resistance has been a subject of much debate in recent years with a range of experiments and theories that disagree not only on the magnitude of the contribution but also its sign. A problem that has plagued the field is that of extrinsic contributions to the resistance, such as the AMR effect, that can either mask the intrinsic domain wall signature or be misinterpreted as an intrinsic contribution. Early experiments were performed on samples with naturally forming domain walls in homogeneous materials that have dimensions larger than the typical domain size. As a result, domains are often randomly oriented and the isolation of a resistance attributable to a single wall is difficult. Advances in experimental methods have enabled the study of so-called mesoscopic systems in which the device geometry is carefully prepared to gain some degree of control over the domain wall formation. Examples include the engineering of the magnetocrystalline anisotropy to control the domain magnetisation vector and minimise extrinsic effects. In other systems a constriction has been placed in the domain wall to localise it inside the constriction as well as to control the domain wall width.

In this section a brief overview of the most important experiments is given, starting with those that provide evidence of a positive contribution and subsequently those that suggest a negative value of the domain wall resistance.

1.3.2 Positive domain wall resistance

One of the earliest modern experiments to tackle the issue of the domain wall resistance is that of Viret and colleagues [20]. To accommodate their semi-classical model of domain wall resistance they presented experimental data on polycrystalline, in-plane magnetised Cobalt ($t = 28$ nm) and Nickel ($t = 30$ nm) films at room temperature. The resistivity contribution from the domain walls is found to be dominated by the large AMR effect, owing, in part, to the large size of the domains in the samples. The authors overcome this by outlining a protocol to remove the known AMR behaviour by transverse and longitudinal measurements and subsequently report a small positive contribution ($\approx 10^{-5}$) to the background resistance from the domain wall.

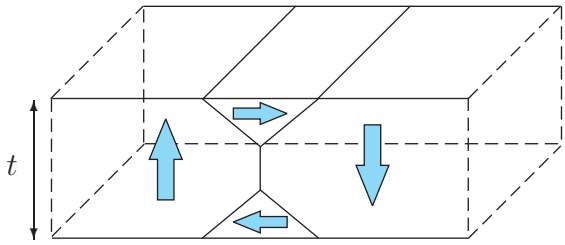

Figure 1.6: Example of magnetic closure domains, otherwise known as Néel caps, found in some thin films that can contribute to the measured magnetoresistance. The thickness of the film is t.

In a subsequent paper the same group published results on out-of-plane magnetised HCP Cobalt thin films [58]. Under no applied field the stripe domains found in the sample have random orientation, however, upon application of an in-plane magnetic field the domains align into a parallel stripe configuration. The advantage of this system is that the high density of domains results in a decrease of the dilution effect, a term used to describe the situation where domain walls are separated by large domains reducing the relative signal from the additional magnetoresistance. In this configuration a domain wall resistance $\approx 1\%$ was measured. It was pointed out by other authors [59, 60, 7] that several problems are present in this experimental setup. Firstly, the observed magnetoresistance is independent of whether the domain aligning procedure is performed or not, implying that this may be an effect of the AMR when the current flows through the labyrinth pattern of the randomly distributed domains. In addition, the perpendicular anisotropy in these films is not enough to prevent the formation of Néel caps (see figure 1.6) that occupy a substantial height of the film [60]. Again, these will provide a contribution to the resistivity through the AMR effect, and as a result the measured value cannot be attributed to an intrinsic domain wall resistance with any degree of certainty.

These problems were overcome by Klein *et al.* [61] who performed magnetoresistance measurements on samples of the perovskite and $4d$ itinerant ferromagnet $SrRu0_3$. This material exhibits a very large uniaxial anisotropy and as a result the sample is guaranteed to be free of Néel caps that largely invalidated the findings of the previous experiment. The same property also eliminates the contributions of AMR and Lorentz magnetoresistance in the experiments. Perpendicular stripe domains were formed and well characterised by Lorentz mode transmission electron microscopy [62]. At low temperatures, they determined a domain wall resistivity of around 700% of the background value, which they attribute to the narrow ($\approx$ 3 nm) domain walls in the material. In this case, they question the

validity of models based on the spin misstracking effect for these narrow domain walls and obtain good agreement with models based on the GMR effect, where the interface is abrupt.

Li *et al.* [63] have performed magnetoresistance measurements on thin (4–20 nm) $Pr_{2/3}Sr_{1/3}Mn0_3$ films. They obtain samples with both in-plane and out-of-plane magnetisations by changing the substrate material to control the orientation of the strain induced anisotropy. Studies on the in-plane magnetised samples yielded no significant magnetoresistance effects. However, in out-of-plane maze domain systems significant changes were found between the single domain and multi-domain states. The magnetoresistance was found to be $\approx 400\%$ in a 6 nm film at 50 K, although, surprisingly, this effect is diminished rapidly as the film thickness is increased and peaks at a temperature of 50K. It is clear that these system would benefit from further experimental studies to clarify the origin of these dependencies.

More recently, Rahman *et al.* [64] have performed experiments on $Tb_{21}Fe_{67}Co_{12}$ amorphous films (t=50–300 nm) with perpendicular magnetocrystalline anisotropy. The domain walls form a maze like configuration, and it was found that the domain density increased with respect to the layer thickness. Owing to this effect, the positive magnetoresistance is found to increase linearly with the film thickness, exhibiting a maximum of 3.7% for films with $t = 300$ nm. They also find that the domain wall resistance is increased as the wall width is reduced. The authors assert that AMR effects are generally weak in amorphous films and that this effect is further diluted by the strong perpendicular anisotropy, that also minimises the Lorentz magnetoresistance, and attribute the change to domain wall spin scattering phenomena.

The mixed transition metal equiatomic alloy FePd has been used by several authors for transport measurements. This material has a strong uniaxial anisotropy, and can be grown on MgO with this axis out of the layer plane, therefore resulting in dense stripe patterns without the presence of Néel caps. After measuring bulk AMR and Lorentz contributions and finding them negligible, Ravelosona *et al.* [65] found a magnetoresistance of 6% at liquid Helium temperatures and 2% at 200 K in 100 nm thick films. They also compare their results to the theory of Levy and Zhang by using estimates of the various parameters that enter the model, and find a reasonable agreement between experimental results and pre-

dictions of the resistivity anisotropy, although the isotropic domain distribution prevented the extraction of individual CIW and CPW contributions.

A more precise measurement of the CIW and CPW resistivities was made by Viret *et al.* [66] on 50 nm FePd films using an 'union jack' patterned system. The growth process leads to domains that are aligned in parallel down one of the 100 μm channels, and therefore perpendicularly to the other, ideal for measuring the resistivity anisotropy of a domain wall. By appropriate probe placement the two resistivity elements were extracted from the data and after great effort to exclude AMR effects it is found that the domain wall magnetoresistance is 8.2% for CPW and 1.3% of CIW, in quantitative agreement with the models of Levy and Zhang.

Danneau *et al.* [67] have measured domain wall resistance in 40 nm thick FePd layers containing parallel domain walls that have been imaged by MFM. These 8 nm wide walls are moved by an applied field between sets of probes, allowing the inter-probe resistances to be measured. The results show discrete changes in the resistance, consistent with the moving domain wall interpretation. The authors take great care to measure extrinsic effects and in these well characterised devices the positive magnetoresistance was measured at 10%, a value that can be interpreted in terms of a spin misstracking model. Recently Tanigawa *et al.* [68] have performed measurements on domain walls in 18 nm thick FePd films with perpendicular magnetisation containing notches to induce domain wall trapping. It was found that the interface resistance measured was positive and $\approx 0.016\ \Omega$ per domain wall, around 3 times larger than found by Danneau *et al.* .

In 1998 Mibu [69] and coworkers used a NiFe/CoSm exchange-spring bilayer system to study the magnetoresistance of Bloch like walls. The domain wall forms between the layers of magnetically hard CoSm, in the soft NiFe layers. A current is applied in the plane of the material, and the resistance measured is that parallel to the domain wall. After evaluating the AMR contribution by an averaging procedure, a small $> 0.1\%$ parallel-to-the-domain wall resistance effect was measured.

Mathur *et al.* [70] studied domain wall resistance in 200 nm thick $La_{0.7}Ca_{0.3}MnO_3$ layers in a Wheatstone bridge configuration with carefully placed notch constrictions to trap 100 nm long 180° domain walls at known locations. In these samples

the domain wall area resistance was found to be 8×10^{-14} Ωm^2 — four orders of magnitude greater than expected. Wolfman and coworkers [71] have formed devices with nanoconstriction via high resolution *e*-beam lithography to trap and alter the widths of domain walls. In these devices they measure very large contributions of $\approx 16\%$ to the magnetoresistance by 38 nm wide domain walls, and they imply that the geometric constriction of the domain wall may play a large factor in this.

Narrow Cobalt nanowires were formed by Ebels *et al.* [35], with a wire diameter of 35 nm. They obtain surprisingly large positive domain wall resistance of 100–600% of the background resistance — clearly more than can be justified by the model of Levy and Zhang. The authors attribute this large value to spin accumulation effects, although this was disputed by Šimánek [36] who claimed that this contribution is suppressed due to the spin misstracking.

Xu *et al.* [72] have used a cross shaped $Ni_{80}Fe_{20}$ (t=30 nm) sample to study domain walls trapped at the junction. Micromagnetic calculations were performed to study the magnetic configuration in the sample and, after excluding AMR and Lorentz contributions, they deduce a positive intrinsic domain wall resistance of $\approx 10^{-4}$ of the background value.

Prieto *et al.* [73] have studied domain wall resistance in a thin (2–20 nm) Gd layer sandwiched between two layers of 100 nm thick permalloy. Unlike other experiments where the domains and current flow are in the plane of the sample, the current flows perpendicularly to the layers and the domains are in the permalloy layers, whilst a domain wall is formed and confined in the Gd layer if the two permalloy layers are oppositely magnetised. The results of transport measurements show a domain wall resistance of $\approx 23\%$ in a sample with a 4 nm Gd layer and $\approx 31\%$ for a 2 nm thick Gd layer. This is a large effect, but in reasonable agreement with Levy-Zhang theory for the narrow domain walls.

Lepadatu and Xu [74] formed domain walls with constrictions in a 30 nm thick Permalloy layer gown on a Si(100) substrate. A similar system was made but with the ferromagnetic layer changed to Ni. The 1 μm wide channels are constricted at their centre with constriction widths of 50 nm to 350 nm in 50 nm increments, and they find that domain walls form in samples width constriction width ≤ 250 nm. Magnetoresistance measurements were made at room temperature and a

positive change in the resistance was found as a domain wall is formed in the constriction. In the analysis the authors find that ballistic magnetoresistance is present in the narrower constrictions. However, in the samples fabricated with wider constrictions the larger contribution is claimed to be from spin-dependent impurity scattering as put forward by Levy and Zhang. In the 250 nm sample the domain wall magnetoresistance was determined to be 1.7% in NiFe and 1.82% in the pure Ni layer system.

Leven and colleagues [75] have studied domain wall resistance in multilayers of $(\mathrm{Co}(0.3\ \mathrm{nm})/\mathrm{Pt}(1\ \mathrm{nm}))_{10}$. Micromagnetic calculations are also performed to confirm the magnetisation distribution in the layers. They evaluate the AMR contributions to the measured resistance by using longitudinal and transverse measurements. It was found that an additional positive resistance exists in the presence of a domain wall, and the domain wall resistivity is $\approx 0.23\ \mu\Omega$ cm.

In 2005 Buntinx [76] measured a positive domain wall resistance in Cobalt thin films with 180° Néel walls. Domains are artificially created in a controllable and reversible way by exchange biasing the cobalt layer by growth on a patterned CoO base. The AMR effect is identified and removed, leaving a measurable interface resistance of $6.4\times10^{-17}\ \Omega\mathrm{m}^2$ for a single domain wall. The authors find this is fully consistent with the theory of Levy and Zhang.

Lee *et al.* [77] have performed measurements on 5 μm wide, 30 nm thick Cobalt strips with thickness a modulation of 8 nm to artificially form domains with a length of 700 nm. After extracting the AMR contribution from the domain wall, they determine a contribution of 0.14% that they attribute to domain wall scattering.

1.3.3 Negative domain wall resistance

One of the first experiments to measure the domain wall resistance in a Ni wire was done by Giordano *et al.* [78], who found a negative contribution from the domain walls. In a sample with a diameter of 30 nm they measured a resistance of $-3\ \Omega$ at 4.2 K that was attributable to the domain walls. The theory of Tatara and Fukuyama predicts a value of $-11\ \Omega$ for an equivalent system, although Giordano and colleagues suggest that uncertainties in the parameters used could

account for this difference. In subsequent experiments on Ni wires Giordano *et al.* [79] attempted to improve their isolation of a single domain wall's contribution to the resistance, and conclude that a resistance of $-0.085\ \Omega$ is attributable to the domain wall. They extended their work to narrow Co wires [80], but the results were somewhat unclear displaying both positive and negative contributions in different samples, although they identified an overall negative domain wall contribution by discounting certain samples as having large AMR contributions. Extending their study to permalloy, they deduced a domain wall resistance of $\approx -0.14\ \Omega$, again consistent with a negative domain wall resistance picture.

Otani *et al.* [81] studied Cobalt wires with widths ranging between 0.2–2 μm and found a negative domain wall contribution to the resistivity that decreased linearly with the sample width. In the same work, paired Cobalt disks were fabricated with diameters 0.4–5.0 μm and at the interface a 180° domain wall was formed that lowered the resistance by $\approx 1\%$. In a later experiment the same group studied domain wall resistance in 40 nm thick epitaxial Co wires with two distinct magnetic orientations. In the first the magnetisation was aligned in the plane of the wire, and after accounting for AMR and Lorentz magnetoresistance a negative domain wall resistance was found, but only in the narrow temperature range 200–220 K, which it is suggested could be due to the suppression of surface scattering. In the perpendicularly magnetised sample a small positive domain wall resistance was observed ranging from 3×10^{-4} $\mu\Omega$ cm at 5 K to 6.9×10^{-4} $\mu\Omega$ cm at 300 K. These experiments were extended to 50 and 100 nm thick Fe grown on MgO. The periodic domain structure was imaged by MFM, and it was found that Néel caps are present in the sample. Despite this, the authors claimed that a negative resistance is present below 66 K (8.7×10^{-9} Ω cm at 8 K in the 50 nm sample), whilst above this a positive domain wall resistance exists. Clearly more work is required to clarify the exact nature of the mechanism leading to the observed behaviour in these samples.

Taniyama and coworkers [82] measured a negative domain wall resistance in devices based on Cobalt zigzag wires. In this setup a domain wall is formed at a 90° bend in the wire, in which two different types of domain wall can form. They attempted to remove the AMR contribution by comparing these two structures and record a domain wall resistivity of -1.8×10^{-6} $\mu\Omega$ cm at 5 K. They discuss the negative value obtained in terms of the model of Tatara and Fukuyama, but conclude that their signal persists up to 200 K, where the weak localisation effects

suggested by the theory should be minimal.

Rüdiger *et al.* have performed a series of well characterised experiments on epitaxially grown Fe, Co and FePt thin-layer microstructures. A summary of these experiments is given in reference [83]. Great care was taken to account for AMR in Fe samples by balancing the competing contributions from the Lorentz magnetoresistance. It was found that a negative resistance contribution was made to the resistance, although the temperature at which the experiments were performed (65.5 K) discounted the weak-localisation theory of Tatara and Fukuyama. Owing to the fact that the negative value is relatively insensitive to the domain wall profile, the authors suggest that this reduction may not be due to an intrinsic domain wall resistance. They propose that effect may be due to the reduction of surface scattering as electron trajectories are altered at the surface. This is supported by the fact that thicker films show a reduced resistance contribution, as the surface effect become less significant. MFM and micromagnetic simulations on HCP Cobalt layers show that Néel caps form in the samples studied in experiments (thickness=55–185 nm). In these materials they find a small positive domain wall resistivity of roughly 0.5% of the background resistivity, although they suggest that half of this contribution may be a Hall effect phenomena. In FePt layers with very high anisotropy there are no Néel caps present and a definite positive domain wall resistance is measured of $\approx 0.3\%$ that cannot be explained by extrinsic contributions. Of these three sets of experiments, this positive contribution is considered by the authors to be the most likely measure of a true intrinsic domain wall resistance.

20 nm thick NiFe wires were studied by Nagahama and coworkers [84] with CoSm pads to control domain formation. A negative domain wall resistance of -0.17 Ω per wall was found, but the authors indicated that this could be attributed directly to an AMR contribution.

In the work of Hausmanns *et al.* [85] the reversal process of Co wires is studied experimentally and by micromagnetic calculations, and the negative resistance observed experimentally can largely be accounted for by the AMR effect that they deduce from the configurations found from the calculations.

Buntinx *et al.* [86] performed experiments on Cobalt zigzag wire and using a combination of MFM images and micromagnetic simulations showed that the

resistance changes they measured could be fully explained in terms of the AMR effect.

1.3.4 Dilute magnetic semiconductors

The first experiment to study the domain walls in a dilute ferromagnetic semiconductor was that of Rüset *et al.* [49]. They fabricated a device based on a 19 nm thick layer of $Ga_{0.976}Mn_{0.024}As$ with two 10 nm wide (or less) constrictions in a 400 nm wide wire, separated by a 100 nm wide, 500 nm long island. Under the influence of a parallel magnetic field the bulk wire regions switch their in-plane magnetisation at lower field values than the smaller island, resulting in controllable domain wall nucleation. The process was done progressively, with the first sample having no constriction and exhibiting only AMR effects. Subsequently, the sample was etched to produce a system with constrictions and a narrower island region, and in this case a magnetoresistance of 8% was attributed to the domain wall spin accumulation effect. Further etching led to resistances of up to 2000%, implying that the constrictions now act as a tunnel barrier to electron transport.

Tang *et al.* [87] have performed experiments on 90° domain walls in in-plane magnetised $(Ga_{0.948},Mn_{0.052})As$. The domain walls are created at the edge of their device and driven through by an in-plane magnetic field. As the domain wall passes a set of probes, measurements are taken of the potentials and are averaged along the top and bottom of the sample to eliminate the Hall effect contribution. Eddy currents that arise at the domain interface are evaluated by a simple model that accounts for the altering resistivity tensor in each domain due to the effect of the AMR. This is subtracted from their experimental results to yield an intrinsic domain wall resistance, which they measure to be $-0.33\ \Omega$ in 60 μm wide devices and $-1.0\ \Omega$m in 30 μm wide devices. In the latter case, this value implies that, when scaled for the 15 nm wide walls, the charge carries experience resistance free transport in the domain wall region. The authors suggest that these results could be interpreted in terms of the weak localisation model of Tatara *et al.* [22].

In experiments on in-plane magnetised $Ga_{0.99}Mn_{0.01}As$ layers by Wosiński *et al.* [88] domain wall resistances were measured in both unconstrained systems and samples with a constriction to trap domain walls. In the former devices the au-

thors attribute a positive resistance to the domain walls, whilst in the constricted devices they measure a negative domain wall and suggest that the weak localisation model may be responsible. However, in their experiments no discussion is given of the exact micromagnetic state in the devices, or any possible extrinsic contributions to the measured potentials.

Chiba and colleagues have performed studies on domain wall resistance in layers of (Ga,Mn)As [55] with magnetisations perpendicular to the film. Samples are fabricated with alternating etches to form artificial domain walls, and unetched structures are also created. Because of the 180° domain walls the changing sign of the Hall effect will produce eddy currents at the domain interface. These are evaluated by the authors by both theoretical methods and geometric considerations and removed from the final results as an extrinsic contribution. They also evaluate the AMR contribution to the resistance and find it cannot be responsible for the measured signal. It is found that the resistance can best be described by the model of Levy and Zhang [21].

1.3.5 Magnetic point contacts

Nanocontacts provide a testing ground for measuring ballistic conductance effects in ferromagnets. Initial experiments were performed by García *et al.* [89] who found that a magnetoresistance of 280% was present at room temperature in point contacts made from Ni wires. This effect was attributed to the trapping of domain walls in the point contacts, and it was shown later by Bruno [90] that domain wall confinement can occur in the samples. In his paper Bruno studies the effect of a geometric constriction on the domain wall profile, and shows that if the constriction is smaller that the natural domain wall width, then confinement occurs in which the domain wall size shrinks to the characteristic size of the constriction, independent of the material parameters. It seems reasonable to suggest that the large resistances observed by García may be related to the narrowness of a domain wall formed in the centre of the point contacts.

Subsequently the García group reinvestigated the resistance properties of nanocontacts in electrodeposited Ni systems [91] and report both a positive and negative contribution of up to 25% were measured, depending on the exact sequence of magnetic fields and current pulses used to manipulate the domain wall. A similar

electrochemical deposition method has been used by Hua and Chopra [92] to fabricate Ni nanocontacts, who claim negative magnetoresistances of up to 3000%, and later the same authors, using a different electrodeposition technique, obtain a massive negative magnetoresistance of 100000% [93].

Owing to the nanoscale constriction, transverse electron modes can become confined, leading to discrete jumps in the resistance. A natural method for performing calculations on these systems is in the Landauer picture, where a transmission matrix is used to calculate the conductance of the system:

$$G = \frac{G_0}{2} \sum_{i,\sigma} T_{i,\sigma}, \tag{1.6}$$

where G_0 is a quanta of conduction given by $2e^2/h$ and $T_{i,\sigma}$ is the transmission coefficient of the i^{th} quantum channel. Such calculations have been performed by several authors, including references [94, 95]. In general it is found that the abrupt domain walls increase the backscattering of conduction electrons resulting in an increase of the resistance.

Many other theoretical and experimental works have appeared in the literature regarding the magnetoresistance of ferromagnetic nanocontacts. Since the bulk of this thesis concerns systems in which the domains are not located in such atomic constrictions, the reader wishing to learn more about recent discoveries is urged to read the review given by C.H. Marrows in [7].

After reviewing the current body of literature in the field of domain wall magnetoresistance it is clear that the only consensus possible is that further clarifying work is required (see table 1.1). An aim of the work described in this thesis has been to study the domain wall resistance in Cobalt Platinum trilayer systems, and unambiguously identify the contribution from the domain wall by excluding extrinsic effects. The bulk of this thesis contains the details of theoretical work conducted on these trilayers, but before this is presented a quick description of the fabricated devices is given.

System	Domain wall resistance
$SrRuO_3$ [61]	700%
Co [35]	100–600%
Co [77]	0.14%
Co [81]	−1%
(Ga,Mn)As [87]	−100%

Table 1.1: A selection of results from the literature demonstrating the large range of values obtained for the domain wall resistance.

1.4 Cobalt Platinum trilayer systems

Thin films of Cobalt Platinum trilayers are ideal candidates for the study of domain wall physics owing to the large perpendicular anisotropy found in these materials [96]. Out-of-plane magnetised domains form naturally in the ferromagnetic Cobalt layer of the Pt/Co/Pt system; however, for accurate and reproducible measurements of the domain wall resistance an additional level of control over the exact micromagnetic configuration is desirable. This thesis concerns the modelling of devices fabricated with this purpose in mind, where careful manipulation of the material properties using high-spatial-resolution ion beams induces tailored domain formation. In addition to this, other attractive features of the system include that the large perpendicular anisotropy and thin Cobalt layers exclude the possibility of Néel cap formation that has plagued some of the experiments reported earlier. Another benefit is that the relatively high background resistivity ($\approx 21\ \mu\Omega$ cm) allows Lorentz magnetoresistance effects to be neglected entirely. This combination of factors enables the intrinsic domain wall contribution to be measured directly without having to remove extrinsic contributions post-measurement as was necessary in some of the experiments found in the literature.

Experimentally, the sandwich structure was fabricated upon a Si/SiO_2 substrate at room temperature using dc magnetron sputtering. Initially a base consisting of a 3.5 nm thick Platinum layer was deposited as a substrate for the ferromagnetic Cobalt layer of mean thickness 0.5–0.6 nm. Finally, a capping layer of 1.6 nm thick Platinum was deposited to complete the trilayer structure. Following the sputtering procedure the Cobalt layer is just a few atoms thick and it is likely that pin-hole defects are present in the otherwise continuous Cobalt sheet, but, as will be shown in Chapter 2, the material is magnetically continuous due to induced moments on the Platinum atoms. The thin Platinum substrate and capping layer

were fabricated as such to reduce the effects of current shunting, where much of the current flows through the magnetically neutral Platinum layers.

Devices were patterned from the trilayer sheet using optical lithography and reactive ion etching with a 1:1 mixture of SF_6 and Ar. Early devices were fabricated into 2 μm wide Hall bar structures to study the magnetic reversal properties, whilst later devices used a Wheatstone bridge geometry to study magnetoresistance in 1 μm wide channels.

One of the key features of the experimental study modelled in this work is the ability to artificially control the formation of the domains by use of focused beam ion irradiation. The use of ion irradiation to alter the magnetic properties in Co/Pt has been documented by other authors, e.g. Bonder *et al.* [97] used Ar ions to alter the magnetisation from in plane to out of plane in Co/Pt multilayers. Similar studies of Gallium and Helium irradiation can be found in the literature, for instance [98, 99, 100]. The Ga ions reduce the perpendicular anisotropy of the CoPt layer by introducing surface roughness and forming a CoPt alloy at the interface. Under the coercion of an applied field an uniformally magnetised sample will reverse its magnetisation. This reversal will occur at lower field values in the region of lowered magnetic anisotropy, leading to the formation of an oppositely magnetised domain in the irradiated region. In the experiments presented here the Ga ions can be focused with a spacial resolution of $\approx$ 10 nm, allowing precise domain patterns of arbritrary size and shape to be formed. Initial experiments showed that this thin capping layer rendered the structures extremely sensitive to the 30 KeV incident Ga ions, to an extent were the Cobalt layer was damaged to an unsatisfactory level. To control the dose of ions reaching the active material, layers of SiO_2 of varying thicknesses (0–24 nm) were used and the result of this study, along with expanded experimental detail, are given in reference [101]. It was found that the irradiation increased the sample resistivity due to the additional alloying, for instance in the transport systems studied in Chapter 5 the resistance is increased by $\approx$2.5% in the irradiated region; although no specific information is known about the degree of alloying in these systems.

After perfecting this irradiation technique, as found in reference [101], systems were formed to observe the magnetic switching properties and directly measure the domain wall resistance. An array of stripes was formed using the above method, consisting of alternating irradiated/unirradiated regions. Figure 1.7

show the precision with which such structures can be formed, including creating domains with arbitrary angle with respect to the sample channel. The magnetisation change in samples based on 2 μm wide Hall crosses were measured by the extraordinary Hall effect (EHE) and the reversal process of these systems with respect to the applied field are documented in [102].

Transport studies were performed using a Wheatstone bridge geometry as seen in figure 1.7. The wire width in these magnetotransport systems was 1 μm and a 8 nm SiO_2 layer was used as a shielding layer for the Ga irradiation.

Magnetoresistance measurements on a stripe-domain 'superlattice' structure are shown in figure 1.8a as a function of the applied field. The structure seen in these curves can be attributed to the formation of domains in the sample, and hence the resistance change is due to the intrinsic domain wall resistance. In the plot the domain width is 0.5 μm and they make an angle of 90° with the channel length. Several experiments were performed on the 1 μm samples, and figure 1.8b shows the change in the magnetoresistance as a function of the number of domains for samples with different domain lengths. The measured values scales linearly with the number of domains and is independent of the domain widths, an observation consistent with the measurement of an intrinsic domain wall resistance. Similar measurements were made on systems where the domain wall angle with respect to the channel is varied. Further details of these experiments are given in Chapter 5.

1.5 Summary

Domain walls have opened a whole branch of study in the field of spintronics. Properties such as domain wall motion and in-plane resistance variations make these systems unique, and in exploiting these properties novel devices can be created that may have applications in fields such as data storage and magnetic sensing.

A number of theories and experiments were discussed in the literature review, but a coherent picture of the domain wall electrical properties is difficult to obtain. In this work the aim is to study domain walls in nanostructured devices through

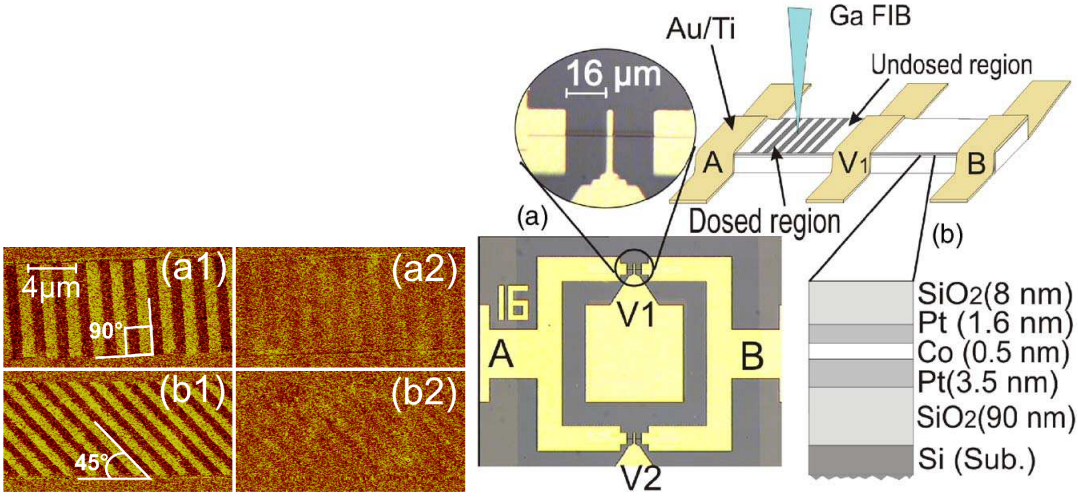

Figure 1.7: (a) Optical micrograph of the Wheatstone bridge structure used to investigate domain wall resistance. A 10 μm ac current flows between A and B, and the voltage is measured between the loads V_1 and V_2. The expanded region shows the top two Pt(1.6 nm)/Co(0.5 nm)/Pt(3.5 nm) leads of dimension 1×16 μm^2. Thick 150 nm Ti/Au fingers are deposited to create low-resistance voltage contacts to the Pt/Co/Pt wires. Six doped regions of width 1 μm separated by 1 μm undosed regions are patterned in the top left and bottom right Pt/Co/Pt leads. (b) Schematic of the top leads of the bridge structure. *Caption and image taken from* [101].

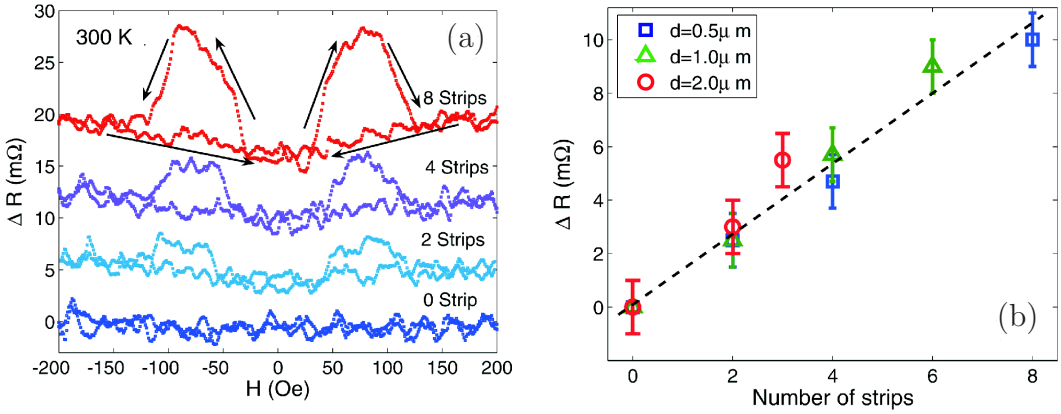

Figure 1.8: Magnetoresistance (offset vertically for clarity) of bridge structures containing 0, 2, 4 and 8 irradiated strips at 300 K. (b) Maximum resistance change as a function of number of irradiated strips of various widths, d.

a variety of theoretical techniques, and apply the results to analyse data taken from experiments on Cobalt-Platinum trilayers.

Chapter 2

Electronic structure and magnetism of Cobalt Platinum

In this chapter we aim to obtain an understanding of the magnetism in layered systems containing Cobalt and Platinum. To accomplish this electronic structure calculations are employed in the framework of density functional theory on multilayers, surfaces and systems with substitutional alloying that replicate the effects of the interfacial mixing expected in fabricated trilayers. The objective is to calculate the layer resolved magnetic moment distribution in these systems, elucidating the properties of samples used in the experiment. These results are also used in Chapter 5 to provide supporting evidence and aid in the interpretation of experimental measurements of domain wall resistivity.

2.1 Introduction

The existence of the magnetic ground state present in certain atomic systems is intrinsically an electron-electron effect. For isolated atoms it is possible to deduce the magnetic moments by using Hund's rules to determine the occupancy of spin up and spin down states and the spin-orbit coupling effect.

In condensed matter, magnetism is split up into two broad classes. The first, known as *localised magnetism*, involves electron states that are similar to those

in atomic theory and hence reasonably described by Hund's law. Good examples of this type of behaviour are seen in rare earth metals where highly localised $4f$ states are responsible for magnetism. However this theory is unable to explain the magnetisation found in transition metals such as Fe, Co and Ni, with predicted values of the moment being much larger than those measured experimentally. Weiss [103] attempted to model these metals by his 'molecular field theory', in which nominally non-interacting atoms are subject to an internal magnetic field that is proportional to the observed magnetisation. The theory achieved limited success in predicting the behaviour of the transition metals, but no insight was given into the origin of this field which we know today as being due to exchange. In transition metals the electronic states are significantly altered by the crystal lattice and we must look to energy band theory to predict the occupancies of hybridised electron states. This type of itinerant magnetism is termed *band magnetism*. The theory was first proposed by Stoner in which a molecular field term was incorporated into simplified energy band calculations, the result being that the energy bands break their spin degeneracy and are displaced in opposite directions relative to the Fermi energy, thus altering spin occupancies. Subsequently Heisenberg explained the molecular field in terms of the exchange interaction and more recently the development of density functional theory has enabled precise calculations of the energy bands in magnetic systems through the inclusion of many body effects. In real systems the distinction between localised and band magnetism becomes blurred and we observe a spectrum of states between the two. In transition metals the d bands are responsible for the spontaneous magnetism, the strong exchange coupling and flat band dispersion at the Fermi energy (see figure 2.1) providing the ideal conditions for ferromagnetism. A density of states plot is given for FCC Cobalt in figure 2.2 showing the band resolved contributions. The fact that the d bands dominate the available states at the Fermi energy is clear.

A convenient unit of magnetic moment is the Bohr magneton equivalent to the spin moment of one electron

$$1\mu_b = \frac{e\hbar}{2m_e}, \tag{2.1}$$

and is used throughout this thesis.

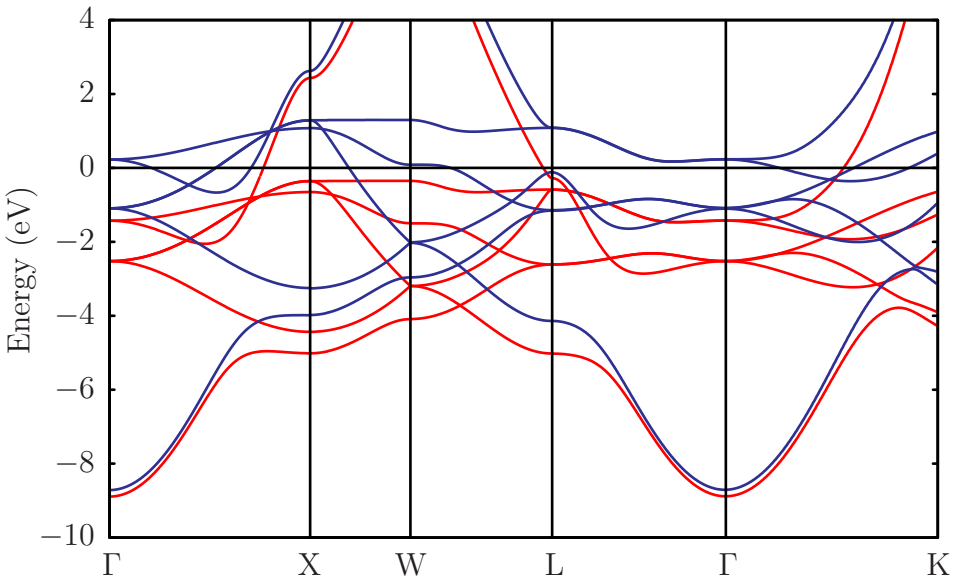

Figure 2.1: Band structure of FCC Cobalt between points of high symmetry in the Brillouin zone. The majority (red) and minority (blue) bands exhibit low dispersion and strong exchange splitting near the Fermi energy (grey line).

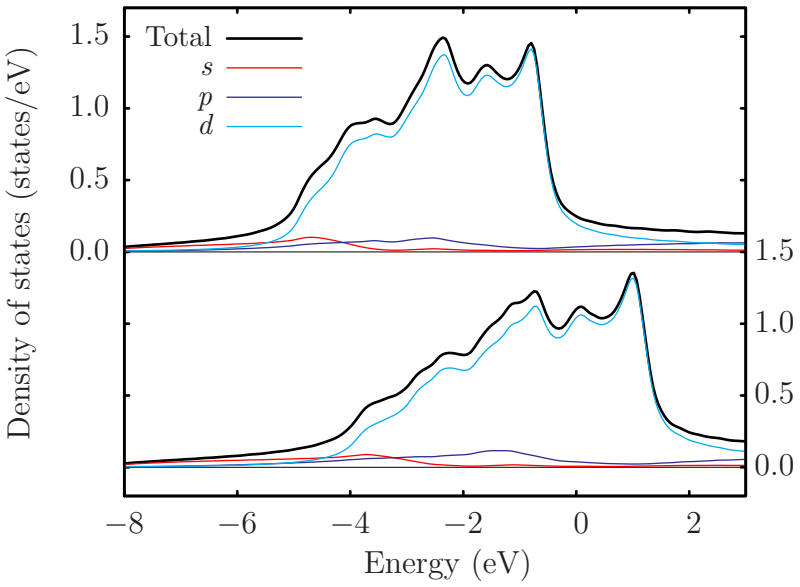

Figure 2.2: Band resolved density of states of FCC Cobalt, showing majority (top pane) and minority (bottom pane) states. The small contribution from states with f character are not shown.

2.2 Electronic structure techniques

To determine the total electronic wave function of a material, Ψ, we must solve the time independent Schrödinger equation for an interacting many body system:

$$(T + V)\,\Psi = E\Psi. \tag{2.2}$$

The operators on the left hand side contain the complex interactions present in condensed matter. T is the kinetic energy operator and the potential V accounts for all electron-electron, electron-core interactions as well as describing the influence of external applied fields. It should not surprise the reader that in all but the simplest cases the equation becomes impractical to solve owing to the sheer number of particles in a macroscopic system. A well established approximation is to consider a single particle Hamiltonian that reproduces the properties of equation (2.2) but does not explicitly contain all the troublesome interactions, such that

$$H\psi_n = (T + V_{\text{ext}} + V_{\text{coul}} + V_{\text{xc}})\,\psi_n, \tag{2.3}$$

where V_{ext} is the potential due to the positive atomic cores, V_{coul} is the electron-electron coulomb interactions, and V_{xc} is the correction for exchange and correlation effects. One of the earliest attempts at solving equation (2.3) was made by Hartree, who approximated the wavefunction by a product of non-interacting single particle wavefunctions, with no allowance made for the effects of exchange or correlation. Subsequently great improvements were made in the Hartree-Fock approximation [104], in which exchange interactions are included by the use of Slater determinants. However these calculations are time consuming due to the non-locality of the included exchange term. Further extensions have been made to include correlation effects, but the complex nature of these calculations, especially in the solid state, render all but the simplest calculations impractical. The need for a viable method of accurately solving (2.3) including the effects of exchange and correlation led to the development of density functional theory. As the following calculations and some work in Chapter 4 use this method a brief overview will now be given. Readers already familiar with DFT may wish to continue to the following section.

2.2.1 Density Functional Theory

Density functional theory (DFT) is based on the works of Hohenberg and Kohn in 1964 [105] followed by Kohn and Sham in 1965 [106]. It replaces the 3N variables of an N electron system with only the 3 coordinates of the system charge density, $\rho(\mathbf{r})$, which is calculated as

$$\rho(\mathbf{r}) = \sum_{n=1}^{\mathrm{N}} \psi_n^*(\mathbf{r})\psi_n(\mathbf{r}), \tag{2.4}$$

where n labels single particle states. It was Hohenberg and Kohn who first pointed out the role of the charge density in the search for the electronic ground state. They concluded that

- The groundstate energies are unique functionals of the charge density with

$$E[\rho(\mathbf{r})] = \int \Big(V_{\mathrm{ext}}(\mathbf{r})\rho(\mathbf{r}) + F[\rho(\mathbf{r})] \Big) d\mathbf{r}. \tag{2.5}$$

- The minimum of energy obtained by the variational principle is exactly equivalent to the groundstate energy.

The last statement asserts that electron-electron interactions need not be approximated, therefore a functional must exist describing the exchange and correlation effects exactly. The work of Kohn and Sham a year later was to put these statements into a calculable form. Applying the variational principle to equation 2.5 with the charge density given by equation 2.4 results in the following expression for $F[\rho(\mathbf{r})]$:

$$F[\rho(\mathbf{r})] = E_{\mathrm{coul}} + T_{\mathrm{s}}[\rho(\mathbf{r})] + E_{\mathrm{xc}}[\rho(\mathbf{r})], \tag{2.6}$$

where E_{coul} is the classical Coulomb contribution, and $T_{\mathrm{s}}[\rho(\mathbf{r})]$ is the kinetic energy of a system of non-interacting electrons of density $\rho(\mathbf{r})$ moving in some potential $V_{\mathrm{s}}(\mathbf{r})$, and $E_{\mathrm{xc}}[\rho(\mathbf{r})]$ is a term describing the contributions from exchange and correlations and modifications to the kinetic energy not accounted for in $T_{\mathrm{s}}[\rho(\mathbf{r})]$. Although the Kohn-Sham theory is exact, it is not possible to know the precise form of the E_{xc} functional except in a few simple cases. Various approximate schemes have been proposed, the earliest by Kohn and Sham in their original paper known as the local density approximation or LDA. In the

LDA, the exchange-correlation energy functional is given by

$$E_{\mathrm{xc}}[\rho(\mathbf{r})] = \int \rho(\mathbf{r})\varepsilon_{\mathrm{xc}}[\rho(\mathbf{r})]d\mathbf{r}, \tag{2.7}$$

where $\varepsilon_{\mathrm{xc}}[\rho(\mathbf{r})]$ is the exchange-correlation energy per particle of a homogeneous electron gas. An extension to the LDA is the local spin density approximation (LSDA) where a spin-polarised electron gas is considered instead. This is the scheme applied in the following LKKR calculations. Although the L(S)DA is a gross simplification of the problem it has been shown that in practice the approximations work well enough for quantitative predictions. Further developments in the representation of the exchange-correlation functional led to the generalised-gradient approximation (GGA) [107, 108, 109], in which improvements are made to the LDA by non-local corrections to the charge density gradient in $\varepsilon_{\mathrm{xc}}[\rho(\mathbf{r})]$.

2.2.2 LKKR: A layered multiple scattering method

A brief summary is now given of the Layered Korringa-Kohn-Rostoker (LKKR) method, a computational technique for solving the Kohn-Sham equations in systems with certain geometries, which has been used to study the electronic and magnetic structure of Pt/Co/Pt systems. The detailed technical nature of the implementation [110, 111, 112] is such that only the key concepts and those that impact the discussion in subsequent calculations are discussed in any detail. The above references are provided for the reader wishing to gain a deeper understanding of the method.

The LKKR method centres on the determination of the electronic Green function for the system. In condensed matter theory Green functions lend themselves naturally to electronic structure calculations due to their applicability to multiple scattering theory. If the single particle Schrödinger equation is written as

$$H\psi(\mathbf{r}) = E\psi(\mathbf{r}), \tag{2.8}$$

then the corresponding Green function satisfies the inhomogeneous problem

$$(H - E)G(\mathbf{r}, \mathbf{r}'; E) = \delta(\mathbf{r} - \mathbf{r}'). \tag{2.9}$$

$G(\mathbf{r}, \mathbf{r}'; \mathrm{E})$ is the system Green function, which if known, yields almost all information of experimental relevance. For instance, the local density of states can be obtained from the imaginary part of G via

$$\rho(\mathbf{r}; E) = -\frac{1}{\pi}\mathrm{Im}G(\mathbf{r}, \mathbf{r}; E) \equiv \sum_n |\psi_n(\mathbf{r})|^2 \delta(E - E_n), \tag{2.10}$$

where n indexes single particle states. Owing to these properties it turns out that knowledge of the Green function is usually sufficient for investigations on condensed matter systems without requiring explicit calculation of the wavefunctions. The obvious question then is 'How does one obtain the system Green function in practice?'

The LKKR method is an extension of the KKR method pioneered in the works of Korringa [113] and later Kohn and Rostoker [114]. The foundations of both methods are based in multiple scattering theory where the task of obtaining the Green function is broken down into determining the single site scattering properties of an atomic potential, characterised by a scattering operator known as the t-matrix. Subsequently the individual scatterers are coupled together to form an ensemble from which the Green function is determined.

Calculating the scattering of an incoming wave by an arbitrary potential to determine the t-matrix can be a complex task. Introducing an atom to a crystal deforms the spherically symmetric potential at the atomic boundaries and the corresponding loss of spherical symmetry results in a difficult coupled channel problem. However, it has been demonstrated that using just the spherically averaged potential, such as in the atomic sphere approximation (ASA) [115], give satisfactory results without the complexities of a full potential problem. This approximation has been used in the work reported here. The LKKR method has not been used to study energetics, for which the full potential is required [116].

The standard KKR method is primarily used in calculations on close-packed bulk systems. Historically, the fact that individual scattering elements and the structural part of the Green function could be separated was exploited to reduce computation effort, although modern computers have made this benefit obsolete. For treating systems such as multilayers the technique suffers from unfavourable scaling with respect to the number of layers in an unit cell. The LKKR is a method designed specifically to overcome these limitations. Unlike the KKR

where all 3 dimensions are treated equally, the LKKR constructs a solid on a layer by layer basis. In the xy plane the 2D equivalent [117] of the KKR method is used to obtain the scattering properties of a single layer, using an atomic basis for Green function expansion. Subsequently layers (stacked along z) are coupled in a planewave basis set that aquire an increasingly large imaginary component with respect to the layer separation. From the resultant attenuation it follows that only a modest number of basis elements are required to converge scattering properties. Owing to this efficiency the scaling of calculations is linear (or better) with respect to the number of layers in the unit cell.

An equation that embodies the LKKR technique is the 2D Brillouin zone integral for the energy dependent scattering matrix of a layer — the scattering path operator — given by

$$\underline{\underline{\tau}} = \int_{\Omega} \frac{\mathrm{d}\mathbf{K}_{\parallel}}{\Omega} \left[\underline{\underline{t}}^{-1} - \underline{\underline{g}}(\mathbf{K}_{\parallel}) - \underline{\underline{\Delta}}(\mathbf{K}_{\parallel}) \right]^{-1}, \tag{2.11}$$

where Ω is the Brillouin zone area, and the matrix elements $t^{i}_{LL'}$ are those of the atomic t-matrix representing the single site problem, $g^{ij}_{LL'}(\mathbf{K}_{\parallel})$ are the *intralayer* structural part of the Green function and $\Delta^{ij}_{LL'}(\mathbf{K}_{\parallel})$ sum up the *interlayer* scattering terms. The indices i and j label individual atomic sites. The ASA used here employs spherically symmetric potentials and a natural choice of basis to expand the scattering matrices are angular momentum states of character $L = (\ell, m)$, denoted by the subscript in these terms. The explicit energy dependence has been dropped from the notation. Once this scattering path operator is known determining the total Green function when $\mathbf{r}$ and $\mathbf{r}'$ are within a given site is trivial via

$$G(\mathbf{r}, \mathbf{r}') = \sum_{LL'} Y_L(\mathbf{r}) Z_{\ell}(r) \tau_{LL'} Z_{\ell'}(r') Y^{*}_{L'}(\mathbf{r}') - \sum_{L} Y_L(\mathbf{r}_{>}) Z_{\ell}(r_{>}) J_{\ell}(r_{<}') Y^{*}_{L}(\mathbf{r}'_{<}), \tag{2.12}$$

where $Z_{\ell}(r)$ and $J_{\ell}(r)$ are suitably normalised regular and irregular radial solutions to the single site scattering problem for determining t, and Y_L are spherical harmonics. $r_{>}$ ($r_{<}$) is the greater (lesser) of r, r'. By integrating equation (2.10) the charge density can be extracted and a new Coulomb potential is constructed by the solving the Poisson equation

$$-\nabla^2 V_{\mathrm{c}} = 4\pi\rho. \tag{2.13}$$

The new potential is used as the next input into the problem (with newly calculated V_{ext}), and the iteration procedure repeated until the change in quantities of interest between subsequent iterations is below a certain threshold. Since the strong Coulomb forces tend to over-correct for charge imbalances, a weighting method is used, for example linear mixing:

$$V = \alpha V_{\text{new}} + (1 - \alpha) V_{\text{old}}, \tag{2.14}$$

where α is a mixing parameter and V_{old} and V_{new} are the old and new potentials. Values of α used are dependent on the type of system under study. In bulk calculations values of around 0.05 or even higher are used, ensuring rapid convergence. Conversely surface systems with substitutional alloying require values of around 0.0005 to converge and as such can be time consuming calculations. To accelerate the convergence process the mixing scheme of Broyden [118] can be used, where the storage of previous iterations allows the solution to be extrapolated. However the scheme is not guaranteed to converge, particularly in surface systems where often linear mixing has to be applied until the calculation is reasonably converged before finishing off with the Broyden method.

2.2.3 CASTEP: A planewave pseudopotential method

Owing to the lattice mismatch between the bulk phases of Cobalt and Platinum one can expect compound structures to undergo structural relaxations — resulting in the breaking of lattice symmetries. To gain an insight into these changes requires a scheme capable of evaluating the total energy to a reasonable degree of accuracy. The use of the atomic sphere approximation in the LKKR method prevents it from treating the energetics of a system with sufficient accuracy. Instead, the CASTEP code has been used. The planewave DFT code CASTEP allows the calculation of electronic states based on pseudopotential methods and has been used extensively in the literature for surface adsorption (e.g. [119, 120]) and structural (e.g. [121]) studies. The specific details of the implementation are not given in this thesis and readers wishing to learn more are encouraged to follow references [122, 123], although a brief summary of the planewave pseudopotential scheme is now presented.

CASTEP uses a planewave basis set to expand the electronic wavefunctions, this

provides many advantages such as the use of fast Fourier transform methods and the flexibility of a non-localised basis set. However, to keep the potentially infinite Fourier series tractable the planewaves are truncated, omitting those with kinetic energy above a certain value. Problematically, the valence wavefunctions in a solid can oscillate rapidly near the atomic cores in order to maintain orthogonality with the core electrons, and as such the energy cutoff could be un-feasibly high. If one makes the assumption that the chemical properties of a solid rely only on the electrons located away from the core and that core electrons are screened, playing no significant role in interatomic interaction, the problem can be simplified. This is the justification behind the pseudopotential approximation where a potential is generated that produces the original valence electron wavefunction beyond some cutoff distance, r_c from the core but which is much weaker than the true potential, to the extent of not binding any core electrons. The non-uniqueness of the generating potential can be exploited to produce weak pseudopotentials that greatly reduce the number of planewaves needed for accurate representation of the resulting wavefunctions. In practice, generating good pseudopotentials involves a balance between basis set size and accuracy by altering the cutoff and smoothness of the wavefunctions near the core.

2.3 Calculations

Now that an outline of the two DFT codes used in the investigations presented here has been given, we detail results of calculations on crystalline systems containing Cobalt and Platinum. Initially, LKKR calculation on bulk systems are presented, moving on to multilayers and surfaces, where a discussion of interface relaxation is given. Finally calculations to simulate the effect of interdiffusion at layer boundaries are described.

2.3.1 Bulk Cobalt and Platinum

The LKKR is a technique optimised for calculations on multilayers and surfaces. Regardless, it can still be used for studies of bulk systems by assembling the bulk crystal in a layered fashion. This may be in contrast to the method to which the reader may be accustomed, where a 3D unit cell is specified in standard bulk

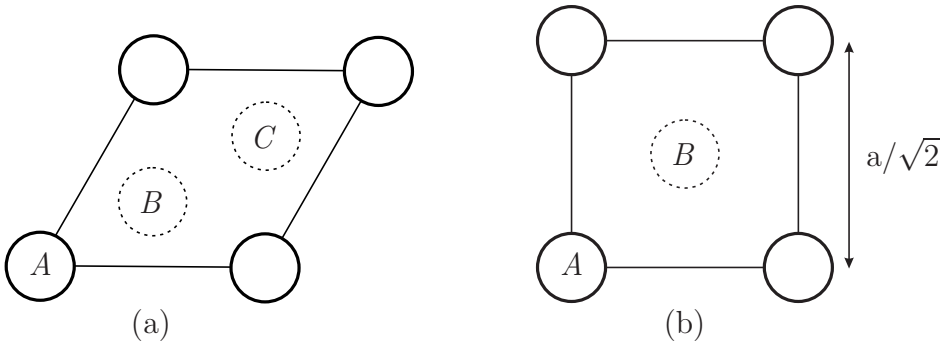

Figure 2.3: Schematic demonstration of FCC stacking in (a) the (111) plane, exhibiting *ABC...* stacking. A unit cell is shown by the solid lines, with the origin at atom A. Moving to the next layer displaces the in-plane coordinates of the equivalent atom to point B, similarly location B translates to C when moving to the neighbouring layer. The lattice constant, a, is also defined in terms of the atomic separation. The layers are separated by $a/\sqrt{3}$ in the z direction. (b) the (100) plane exhibiting *AB...* stacking, with interlayer separation a/2.

methods. To initialise a LKKR calculation a 2D unit cell is defined along with a translation vector describing the offset between the neighbouring layers. A layer or group of layers are repeated periodically *ad infinitum* in the z direction according to these translation vectors to build up a crystal. The obvious practicalities mean that in computation the layers are not actually summed indefinitely, but instead treated with a layer doubling algorithm until the slab scatters electrons in a manner identical to that of a semi-infinite slab to within a prescribed tolerance as described in the given references.

A bulk crystal has planes along which it is convenient to define a unit cell, in a face centred cubic (FCC) lattice two such planes are given by the indices (111) and (100). Although from a computational perspective the technical details of constructing the crystal from these stackings are different, fully converged results should produce identical potentials. This situation is contrasted in multilayer and surface systems where the broken symmetry makes the systems dependent on the layer geometry. Figure 2.3 demonstrates the unit cells and translation vectors in both the (111) and (100) stackings.

Bulk Cobalt (Z=27) has two stable crystographical configurations: FCC and hexagonal close packed (HCP) with an HCP→FCC phase transition observed [124] near 670 K. In the FCC configuration the experimentally measured lattice constant, a, is 3.544 Å [125] — implying a Cobalt metallic radius of 2.506 Å.

The HCP lattice has a broken symmetry along the c axis resulting in crystal parameters, a= 2.507 Å and c= 4.076 Å [125].

Bulk Platinum has a FCC structure with lattice constant 3.924 Å [125] occupying a larger volume than Cobalt with a nuclear charge 78 and a partially filled $4d$ band, and is often termed a 'near ferromagnet' because of its proximity to the quantum critical point.

2.3.2 Convergence

Preliminary calculations were performed on bulk Platinum. As expected, spin-polarised calculations show that Platinum is spin degenerate exhibiting no intrinsic spin magnetic moment. Initial non-relativistic band structure calculations demonstrated an insufficient description of the electronic states, a study of the band structure shows that the energy difference between certain states are over-estimated when compared to those found in the literature (e.g. [126]) and provide a poor description of the *sp*-hybridised band. It was found that scalar-relativistic corrections [127] are therefore required to correctly describe the heavy Platinum atom.

Before performing investigations on systems of interest we must ensure that the calculations are properly converged with respect to the parameter set used. In the LKKR calculations, a balance must be found between accuracy and computational convenience by converging the results with respect to

- $\ell_{\max}$ — The maximum number of angular momentum states used to describe single site scattering.
- N_E — The number of energy points in the valence contour integration.
- N_{g} — The interlayer planewave basis.
- $N_{\mathbf{K}_\parallel}$ — The number of $\mathbf{K}_\parallel$ points in the irreducible 2D Brillouin zone.

$\ell_{\max}$	Magnetic moment (μ_b)	
	(111)	(100)
2	1.58	1.59
3	1.64	1.65
4	1.66	1.67

(a)

N_E	Magnetic moment (μ_b)	
	(111)	(100)
8	1.67	1.67
16	1.64	1.65
32	1.64	1.65

(b)

N_{g} (111)	Magnetic moment (μ_b)	N_{g} (100)	Magnetic moment (μ_b)
13	1.65	13	1.64
19	1.64	25	1.65
31	1.64	37	1.65

(c)

N_K (111)	Magnetic moment (μ_b)	N_K (100)	Magnetic moment (μ_b)
18	1.67	10	1.61
45	1.64	36	1.65
135	1.64	136	1.64

(d)

Table 2.1: Convergence of atomic moment in bulk Cobalt system with (111) stacking with respect to (a) the maximum angular momentum term. (b) the number of E points, $\ell_{\max}$. (c) the number of interlayer planewaves. (d) the number of $\mathbf{K}_{\|}$-points in the IBZ. Default parameters are $\ell_{\max} = 3$, $N_E = 16$, $N_{\mathrm{g}} = (111) - 19, (100) - 25$, $N_{\mathrm{k}} = (111) - 45, (100) - 36$.

$\ell_{\max}$ — Atomic basis

Whilst solving the single site problem an atomic basis is convenient for describing the angular part of the solution. The radial Schrödinger equation of this problem is

$$\left[-\frac{1}{2r^2}\frac{d}{dr}\left(r^2\frac{d}{dr}\right)+\frac{\ell\left(\ell+1\right)}{2r^2}+V(r)\right]R_\ell(r)=ER_\ell(r), \tag{2.15}$$

where $R_\ell(r)$ represents the regular and irregular radial solutions. The angular momentum states become less significant to quantities such as the charge density, and magnetic moments at higher values of ℓ due to the increasingly repulsive contribution of the $\ell(\ell+1)/2r^2$ term to this equation. Table (2.1a) shows the variation in the calculated moment per atom in FCC Cobalt in both the (111) and (100) stacking with respect to the maximum value of ℓ included in the basis set. In both cases a difference exists in the 3rd significant figure when increasing $\ell_{\max}$ from 3 to 4. However consideration must be given to the computational practicalities of the additional basis elements. Previous studies [128] on transition metal surfaces have shown that basis sets with $\ell_{\max}=3$ are sufficient to obtain reliable results whilst balancing the significant increase in computing power required as ℓ is increased. With these considerations all subsequent work is done with a value of $\ell_{\max}=3$ unless otherwise stated.

N_E — Energy points

When evaluating the total charge density an integral is performed over the local density of states for occupied states

$$\rho(\mathbf{r})=\int_{E_{\min}}^{E_f}\rho(\mathbf{r};E)\,\mathrm{d}E, \tag{2.16}$$

where $\rho(\mathbf{r};E)$ is given by equation (2.10) and the Fermi energy E_f is defined by charge neutrality. In practice the core states are treated separately and this integral is explicitly performed for the valence states only, hence $E_{\min}$ is placed between core and valence state energies. For practical integration the energy contour is deformed into the upper half of the complex energy plane where the the energy $E=\xi+i\delta$ follows a semicircular contour in the complex plane. This

method has the added advantage of providing Gaussian smoothing of the Green function, reducing the number of points required for accurate integration. Table (2.1b) shows convergence data for the Cobalt test systems with respect to N_E. Throughout the work 16 energy points are used which also gives a reasonable convergence of the Fermi energy position, consistent with findings reported in reference [128].

N_g — Planewave basis

The allowed planewave basis set used in interlayer coupling is determined by the structure of the crystal. Figure 2.1c demonstrates the system convergence with respect to the number of planewaves for both layer geometries. In this work 19 planewaves are used in calculations on (111) systems, in the (100) case 25 planewaves are used.

$N_{\mathbf{K}_\parallel}$ — Brillouin zone sampling set

When calculating the τ matrices via equation (2.11) and quantities like the density of states an integral is performed over the Brillouin zone. In terms of computation this is achieved by sampling the reciprocal space at regular intervals with a predefined k-point set. As the LKKR method effectively solves for a slab of material the Brillouin zone is flat in the direction perpendicular to the layer; having a surface Brillouin zone (SBZ) characterised by a 2D wavevector $\mathbf{K}_\parallel$. States located at $(\mathbf{K}_\parallel, \mathrm{K}_\perp)$ in an equivalent 3D Brillouin zone are projected onto the point $\mathbf{K}_\parallel$. The 2D Brillouin zone has symmetries that can be exploited to reduce the number of $\mathbf{K}_\parallel$ points required, necessitating only the sampling of a reduced area — the irreducible Brillouin zone (IBZ). In a hexagonal lattice the IBZ is a wedge with area 1/12th of the full Brillouin zone, similarly in a square lattice only 1/8th of the full Brillouin zone is sampled. The algorithm of Cunningham [129] provides an efficient way of sampling the IBZ for square and hexagonal lattices, yielding successively refined sets of $\mathbf{K}_\parallel$ points. A table showing calculated values of the magnetic moment of a bulk Cobalt system constructed from both (111) and (100) layers is shown for different sets of $N_{\mathbf{K}_\parallel}$ k-points in table (2.1d). Although some small improvements can be made by using a 135 $\mathbf{K}_\parallel$-point set, we take the system as being sufficiently converged with 45 $\mathbf{K}_\parallel$-points for (111)

systems, consistent with the work of Pustogowa *et al.* [130]. Similarly for the (100) system 36 $\mathbf{K}_{\|}$-points are deemed to be sufficient. Increasing $N_{\mathbf{K}_{\|}}$ to the next allowed number — 136 — does not have a significant impact on the values obtained.

2.3.3 Bulk and multilayer systems

In the previous section parameters suitable for ensuring converged results were identified. We now study the electronic properties of systems of interest with the LKKR code. Firstly bulk systems are examined, allowing comparison with the results on mixed systems in later sections.

Motivated by the resulting structural changes expected when materials are alloyed, initial studies were conducted on the influence of the atomic volume on the magnetism of crystalline Cobalt. Figure 2.4 shows the predicted variation of the atomic moment of bulk FCC Cobalt with respect to the change in lattice constant. Linear behaviour is found in the region between the bulk constant of Cobalt and Platinum, but a sharp drop is seen below 2.35Å where the moments are rapidly suppressed. This is in reasonable agreement with the work of Steinle-Neumann *et al.* [131] who perform full potential linearised muffin tin calculations on FCC Cobalt in a study of the elastic constants of transition metals. From the Stoner model it can be shown that the criterion for ferromagnetism [132, 133] is

$$I(E_f)n(E_f) > 1, \tag{2.17}$$

where $n(E_f)$ is the paramagnetic density of states at the Fermi energy, and $I(E_f)$ is the so called Stoner parameter. This condition implies that ferromagnetism is stronger in materials with a large density of states at the Fermi energy, therefore any factor that alters the density of states bandwidth will influence the magnitude of the magnetic moments. Figure 2.5 illustrates this point by displaying the density of states for paramagnetic FCC Cobalt at three different lattice constants. Band narrowing and associated increase in $n(E_f)$ is clearly observed as the spacing becomes larger, consistent with the trend in magnetic moments predicted by the Stoner model.

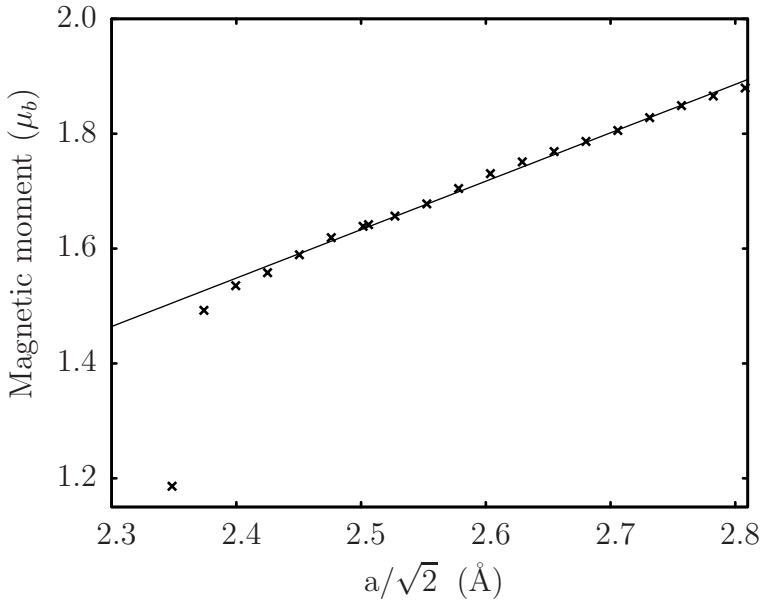

Figure 2.4: Magnetic moment per atom of FCC Cobalt plotted against atomic separation. Calculated values are denoted by points while a fit of the linear region (first two points are ignored) is also plotted.

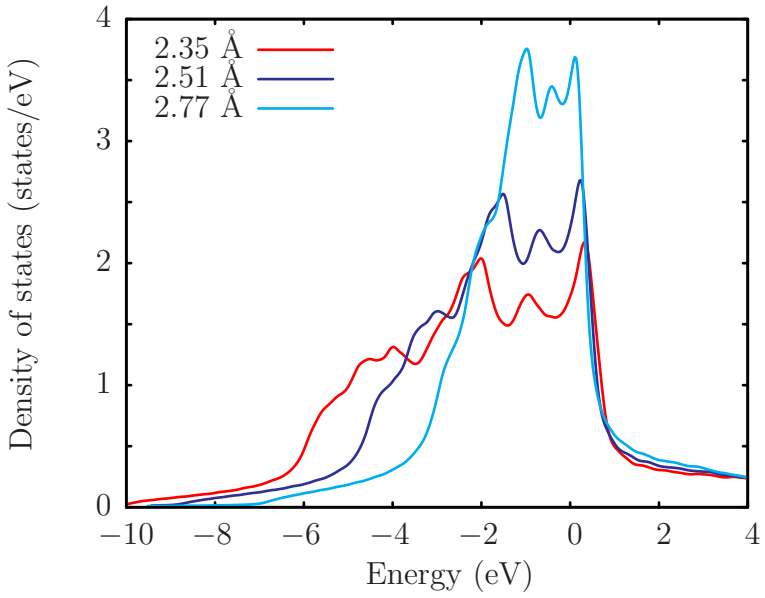

Figure 2.5: Density of states plots for FCC bulk Cobalt at different atomic separations, the values of a/$\sqrt{2}$ are displayed in the key. An imaginary energy of 0.005 Ha is included in the calculations to provide Gaussian smoothing.

2.3.4 Cobalt-Platinum multilayers

Previous calculations on Cobalt Platinum multilayers include the work of Pustogowa *et al.* [130] who used a relativistic LKKR method to study the magnetic anisotropy energy and magnetic structure of both alloy and multilayer systems built on FCC Platinum (100) and (111) surfaces. Layer resolved moment distributions are given for $(Co_1Pt_1)\times 5$ multilayers placed on both substrates; up to 10 layers of 50% alloy on the (100) surface; and 10 layers of pure Cobalt on the (100) surface. Unlike the experiments studied in this thesis, where a sandwich structure is considered, all these calculations were done on systems without a Platinum capping layer. Using their relativistic framework Pustogowa *et al.* extract data for the orbital contribution to the magnetic moment of these systems and find values of the order 0.1 μ_b for systems stacked on the (100) surface and 0.08 μ_b for systems with a (111) stacking. In their calculation the lattice constants were fixed at that of bulk Platinum, allowing for no structural relaxation.

Before proceeding there are issues regarding the precise crystal structure of the systems to resolve. No detailed information is known about the structure of the sputtered samples, including the degree of intermixing at the surfaces. To proceed assumptions were made about the lattice that are also convenient from a computational perspective. It is known that bulk Platinum adopts a FCC structure, and provides the dominant contribution to the chemical composition of the Pt(3.5 nm)/Co(0.5 nm)/Pt(1.6 nm) trilayers used in the experiment. We therefore assume that the Platinum layers in these systems adopts this bulk FCC lattice. Bulk Cobalt has both HCP and FCC phases, but here we assume the FCC case, with the Cobalt expanding in the plane of the layer to match the lattice spacing of Platinum. The surface x-ray diffraction studies of Ferrer *et al.* [134] on ultrathin (2–12 layer) Cobalt films grown on the Pt(111) surface supports this assertion. They find that although some disorder exists the Cobalt films predominantly exhibit a strained FCC lattice, particularly in the case of the thinner films. However annealing to ≈450 K and ≈550 K introduces HCP and alloying phases respectively.

For calculations in this section it is assumed that the Cobalt layers occupy a continuation of the Platinum FCC structure, adopting its in-plane spacing. Calculations are presented for two scenarios: (1) where the layer-layer spacing of Cobalt is set to that of bulk Platinum, so the Cobalt atoms are directly sub-

stituted into the Platinum lattice sites, (2) a more realistic scenario where the Cobalt atoms are allowed to relax out of plane thus altering the Co-Co and Co-Pt interlayer spacings forming a tetragonal structure. We will now present results for the first case.

Species	Magnetic moment μ_b							(a)
Co	1.86	1.93	2.05	2.03	2.03	2.03	2.03	2.03
Pt	-	0.25	0.28	0.24	0.24	0.25	0.23	0.23
Pt	-	-	0.28	0.16	0.10	0.11	0.09	0.08
Pt	-	-	-	0.24	0.10	0.07	0.03	0.02
Pt	-	-	-	-	0.24	0.11	0.03	−0.01
Pt	-	-	-	-	-	0.25	0.09	0.02
Pt	-	-	-	-	-	-	0.23	0.08
Pt	-	-	-	-	-	-	-	0.23

Species	Magnetic moment μ_b							(b)
Co	1.86	1.84	1.89	1.89	1.89	1.89	1.89	1.89
Co	1.86	1.83	1.82	1.82	1.82	1.82	1.82	1.82
Co	1.86	1.84	1.89	1.89	1.89	1.89	1.89	1.89
Pt	-	0.21	0.24	0.20	0.20	0.20	0.20	0.20
Pt	-	-	0.24	0.14	0.09	0.10	0.08	0.08
Pt	-	-	-	0.20	0.09	0.06	0.04	0.03
Pt	-	-	-	-	0.20	0.10	0.04	0.02
Pt	-	-	-	-	-	0.20	0.08	0.03
Pt	-	-	-	-	-	-	0.20	0.08
Pt	-	-	-	-	-	-	-	0.20

Table 2.2: Atomic moments of (a) .../$CoPt_n$/$CoPt_n$/... and (b) .../Co_3Pt_n/Co_3Pt_n/... multilayer structures, with n=0–7. The units shown represent layers that are repeated periodically. Layers are built up from the (111) stacking, and no lattice relaxations are present.

Tables (2.2) and (2.3) show the calculated magnetic moment distribution in periodically repeating $CoPt_n$ multilayers in the (111) and (100) stacked systems. Because of their greater relevance to the experiment, calculations on Co_3Pt_n systems are also presented in the same tables. For comparison, the moment of FCC Cobalt at the same atomic volume is shown in the first column. As demonstrated previously, this moment is enhanced by 0.22 μ_b over that of equilibrium Cobalt due to band narrowing. The addition of Platinum to form a 1:1 ordered alloy leads to a further increase in the Cobalt moment and notably a spin polarisation of the Platinum atom occurs as the $5d$ valence band hybridise with the $3d$ bands of the Cobalt. It is notable that the induced moments are dependent on the layer stacking; in the (100) configuration the Cobalt atom shows a larger increase in

Species	Magnetic moment μ_b							(a)
Co	1.86	2.01	2.10	2.12	2.11	2.10	2.10	2.10
Pt	-	0.37	0.29	0.30	0.27	0.26	0.26	0.27
Pt	-	-	0.29	0.18	0.12	0.08	0.07	0.08
Pt	-	-	-	0.30	0.12	0.05	0.01	0.01
Pt	-	-	-	-	0.27	0.08	0.01	0.00
Pt	-	-	-	-	-	0.24	0.07	0.01
Pt	-	-	-	-	-	-	0.26	0.08
Pt	-	-	-	-	-	-	-	0.27

Species	Magnetic moment μ_b							(b)
Co	1.86	1.86	1.91	1.92	1.90	1.90	1.90	1.91
Co	1.86	1.88	1.86	1.86	1.86	1.86	1.86	1.86
Co	1.86	1.86	1.91	1.92	1.90	1.90	1.90	1.91
Pt	-	0.28	0.26	0.26	0.20	0.20	0.21	0.22
Pt	-	-	0.26	0.19	0.07	0.04	0.06	0.08
Pt	-	-	-	0.26	0.07	−0.01	−0.01	0.01
Pt	-	-	-	-	0.20	0.04	−0.01	−0.01
Pt	-	-	-	-	-	0.20	0.06	0.01
Pt	-	-	-	-	-	-	0.21	0.08
Pt	-	-	-	-	-	-	-	0.22

Table 2.3: Atomic moments of (a) .../$CoPt_n$/$CoPt_n$/... and (b) .../Co_3Pt_n/Co_3Pt_n/... multilayer structures, with n=0–7. The units shown represent layers that are repeated periodically. Layers are built up from the (100) stacking, and no lattice relaxations are present.

the polarisation when compared to the (111) system. The Platinum atom shows a greater difference still of 0.12 μ_b between the two configurations. Band analysis shows that this difference in both atoms are due to a greater spin splitting of the d bands in the (100) case. These values are in excellent agreement with the findings of Pustogowa *et al.* [130] discussed earlier in this work.

Increasing the Platinum concentration further through the addition of another layer results in a further increase in the moment of the Cobalt layer in both cases, although the striking difference in the Platinum polarisation between the (111) and (100) is reduced significantly. Subsequent increases in the number of Platinum layers show that the magnetic properties of the Cobalt and Platinum interface saturate rapidly. The Platinum atoms return to a bulk non-ferromagnetic state with a buffer layer of 3 atoms in both cases, again consistent with the findings of reference [130]. The moment differences at the interfaces persist between the (111) and (100) systems for all the systems calculated.

Changing the Cobalt layer thickness to 3 atoms gives a system closer to that studied in experiments. Comparing these directly to the single Cobalt layer systems one can say that the moments do not exhibit the same degree of variation as the Platinum concentration is increased. The larger number of Cobalt nearest neighbours dampens the increases of polarisation seen in the Cobalt layers, and subsequently the interfacial Platinum atom exhibits lower polarisation. It is also notable that the contrast between the moments of the (111) and (100) systems is reduced.

2.3.5 Lattice relaxations

The size mismatch between Cobalt and Platinum means the structures found in the previous section are unlikely to be those found in practice. To improve on this situation total energy calculations were performed using CASTEP.

Initial converged calculations on bulk Cobalt were performed using 4 Cobalt atoms per unit cell. Planewaves with kinetic energy above 360 eV were truncated, with finite basis set corrections [135] employed to accommodate the change in basis with respect to the unit cell dimensions when performing geometry optimisations. The k-space sampling scheme of Monkhorst and Pack [136] was used with 20 k-points in the IBZ after a total of 48 symmetry operations performed on the full Brillouin zone. The GGA exchange correlation functional as parametrised by Perdew, Burke, and Ernzerhof [108] was used along with the core corrected library pseudopotential generated with the same functional. Calculations on bulk FCC Cobalt produced good agreement with known experimental observables (atomic separation = 2.51 Å, moment =1.68 μ_b). Calculation without the additional core density produce an overestimate of the exchange splitting (2.13 μ_b) that results in a larger atomic separation than expected at 2.58 Å, confirming the importance of this additional core density in producing accurate calculations.

Three common ordered bulk alloys of Cobalt and Platinum are known: CoPt, $CoPt_3$ and Co_3Pt. The equiatomic alloy CoPt has a tetragonally distorted FCC lattice, with alternating monolayers of Cobalt and Platinum stacked in the (100) configuration (a=2.682 Å, c=3.675 Å [137]). $CoPt_3$ has a FCC lattice with alternating layers of Platinum and ordered Cobalt-Platinum arranged in the (100) stacking (a=3.854 Å [138]). Finally, the Co_3Pt studied here exhibits the same

structure as $CoPt_3$ but with lattice sites inverted with respect to occupation, consisting of single layers of Cobalt separated by single layer of ordered Cobalt Platinum (a=3.664 Å [139]). These have been studied experimentally and theoretically by several authors. In terms of theory Kootte *et al.* [139] have performed self-consistent band structure calculations using the localised spherical wave (LSW) method on the above alloys at experimental lattice spacings. Uba *et al.* [140] present results on CoPt and $CoPt_3$ using a relativistic Linearised muffin tin orbital (LMTO) method to obtain self-consistent potentials to supplement experiments on the magneto-optical properties of the alloys. Kashyap *et al.* use an LMTO method in calculations on the ordered alloys. Ellipsometric and Kerr-effect studies were made by Lange *et al.* [141] on the $CoPt_3$ system, who also present relativistic tight-binding LMTO calculations. Similarly Kulatov *et al.* [142] gives results for $CoPt_3$ using a scalar-relativistic LMTO method. Galankis *et al.* [143] present full-potential LMTO results on $CoPt_3$ [143]. Finally Paudyal *et al.* [144] studied the alloy systems in a scalar-relativistic TB-LMTO framework. These calculations are in fair agreement concerning the predicted moments and provide reasonable agreement with experiment where present. No experimental values for Co_3Pt could be found in the literature.

It was found that the results of CASTEP calculations on these systems were significantly different from the above results. Table (2.4) shows data on the moments of these ordered alloys for experiment, selected calculations from the above and those obtained from the CASTEP code.

System	Moment per unit cell (μ_b)			
	Experiment	Theory		Castep
$CoPt_3$	2.43 [145]	2.50 [139]	2.46 [140]	3.67
CoPt	1.90 [146]	2.06 [139]	1.90 [140]	2.46
Co_3Pt	-	5.28 [139]	5.54 [147]	5.91

Table 2.4: Comparison of moments in ordered CoPt alloys between experiment, local orbital methods found in the literature and the CASTEP planewave code.

It appears that the electronic structure of these Cobalt Platinum compounds is not well described by the CASTEP calculations. Changing the exchange-correlation functional was found to make only minor changes to the moments, insufficient to explain the large differences found. Attempts at improving the accuracy of calculation by generating pseudopotentials with smaller cut off radii and more accurate representations of the core charge density also proved unsuccessful. It is concluded that crucial information is lost in the pseudisation of the

potential when describing Cobalt in the presence of Platinum.

This situation is not unique to Cobalt Platinum alloys. Studies [148] on the (001) surface of Vanadium using pseudopotentials and the GGA exchange-correlation functional by Bryk *et al.* predicted that the surface layer poseses a large moment of 1.7 μ_b, a remarkable result given the paramagnetic nature of bulk Vanadium. This finding was in contrast to previous calculations [149] that used a tight binding linear muffin tin orbital method in the ASA, which predicted a non-magnetic ground state. Experiments [150] were in agreement with the LMTO calculations, failing to detect an enhanced moment at the surface. Further study [151] compared the results of a FLAPW calculation with a pseudopotential method and found similar discrepancies in the results. These studies call into question the pseudopotential approximation when dealing with magnetic transition metal system. Kresse *et al.* [152] studied the effect of the pseudopotential generation scheme on the results in the V(001) system. It was found that altering the cutoff radii reproduce results consistent with all-electron calculations. However similarly small cutoff radii were used in [148] producing the erroneous result. Although Cocula *et al.* [153] produce better agreement with spin-dependent pseudopotentials methods, it is clear that more work, outside the scope of this thesis, is required on the transferability of pseudopotentials for transition metal systems before results for the Cobalt Platinum system of interest here can be obtained with confidence.

See section 2.6 *for additional comments on this problem.*

In light of this an empirical evaluation of the relaxation at the Co-Pt interface is made. The data presented on the experimentally measured lattice parameters of 50:50 ordered tetragonal Cobalt Platinum alloy shows a change of +6.9% (−3.2%) from the in-plane spacing of bulk Co (Pt). The interlayer spacing is altered by +3.6% (−6.2%) from the bulk phases. The relative changes in the spacings show that the larger Platinum atom has a large influence in determining the in-plane spacing, whilst the layer-layer spacing contracts to conserve the total volume of both bulk atoms to within 0.6%. With this argument we supplement results at rigid Platinum spacings by presenting results for relaxed lattices, in which the in-plane spacing of bulk Platinum is used but allowing contraction along the z-axis, to preserve atomic volume.

We now repeat the previous LKKR calculations but with this volume conserving relaxed structure. Since the attenuation of the planewave basis is affected by the interlayer spacing which is reduced in these systems, the convergence of the calculations was re-evaluated initially. As the lattice relaxations are most severe between neighbouring layers of Cobalt we present convergence calculations of the magnetic moments in a distorted Cobalt lattice with respect to the number of planewaves in table 2.5. It is clear that when comparing the convergence data with those obtained for the unrelaxed lattice that the moments are slightly less well converged. However, the error in using 19 planewaves for interlayer coupling is comparable to that from the $\ell_{\max}$ truncation. The minor improvements in increasing the basis set are outweighed by the increase in computational time required, particularly as the Pt-Pt and Pt-Co interlayer spacings will be affected to a lesser degree by the relaxation. Therefore the planewave basis is kept at (111) - 19 and (100) - 25 for the following calculations on relaxed structures. Results are presented in tables 2.6 and 2.7 for relaxed (111) and (100) stacked multilayers respectively.

Although the relaxation has little effect on the moment of the homogeneous Cobalt system, multilayers containing the larger Platinum atoms show a marked difference to the previous results. In this case the moment distribution is similar in both the (111) and (100) systems, with the moment of the Cobalt atom saturating at around 1.83 μ_b in both. A total difference is found of 0.20 μ_b and 0.27 μ_b respectively when compared to the unrelaxed lattices, consistent with the relationship between atomic volume and magnetic moment found in the previous section. Integrating the charge density within an atomic sphere gives an indication of charge transfer between species. For CoPt the charge transfer is found to be 0.18 electrons from the Cobalt atom to the Platinum, as is expected from their electronegativities. In the non-equiatomic systems the transfer of electrons from the Cobalt is found to be roughly constant at 0.09, a fact that can be understood in terms of the difference in the Co-Pt coordination number, being double

N_g (111)	Magnetic moment (μ_b)	N_g (100)	Magnetic moment (μ_b)
13	1.88	13	1.71
19	1.84	25	1.72
31	1.85	37	1.73

Table 2.5: Convergence of atomic moments with respect to the planewave basis set for tetragonally distorted Cobalt (a=2.775 Å, c= 2.901 Å).

Species	Magnetic moment μ_b							(a)
Co	1.84	1.90	1.86	1.81	1.82	1.81	1.81	1.83
Pt	-	0.31	0.29	0.24	0.25	0.24	0.24	0.24
Pt	-	-	0.29	0.08	0.04	0.04	0.03	0.04
Pt	-	-	-	0.24	0.04	0.00	−0.02	−0.01
Pt	-	-	-	-	0.25	0.04	−0.02	−0.02
Pt	-	-	-	-	-	0.24	0.03	−0.01
Pt	-	-	-	-	-	-	0.24	0.04
Pt	-	-	-	-	-	-	-	0.24

Species	Magnetic moment μ_b							(b)
Co	1.84	1.86	1.87	1.84	1.84	1.84	1.84	1.84
Co	1.84	1.81	1.84	1.83	1.83	1.83	1.83	1.83
Co	1.84	1.85	1.87	1.84	1.84	1.84	1.84	1.84
Pt	-	0.28	0.27	0.22	0.22	0.22	0.22	0.23
Pt	-	-	0.27	0.11	0.06	0.06	0.06	0.07
Pt	-	-	-	0.22	0.06	0.00	0.00	0.01
Pt	-	-	-	-	0.22	0.06	0.00	0.00
Pt	-	-	-	-	-	0.22	0.06	0.01
Pt	-	-	-	-	-	-	0.22	0.07
Pt	-	-	-	-	-	-	-	0.23

Table 2.6: Atomic moments of (a) .../$CoPt_n$/$CoPt_n$/... and (b) .../Co_3Pt_n/Co_3Pt_n/... multilayer structures, with n=0–7. The units shown represent layers that are repeated periodically in the z direction. Layers are built up from the (111) stacking, systems have the in-plane spacing of Platinum and volume conserving relaxations along z.

in the first case. Similarly for the (100) stacked multilayers the charge transfer is found to be 0.12 for CoPt and approximately 0.06 for the Platinum rich systems. Band resolved occupancies show that the magnetism in both Cobalt and Platinum atoms are due to the spin polarisation of their d bands, while a small negative splitting [−0.03 (111), −0.04 (100)] is found in the p bands of Platinum in CoPt, being halved for systems with two or more Platinum layer in a unit cell.

Multilayers with a Cobalt thickness of 3 layers show a slight increase in the interfacial moments in comparison to the monolayer structures. This is in contrast with calculations on unrelaxed structures, although the magnitude of the moments do not change significantly between the relaxed and unrelaxed structures for the tri-Cobalt systems. As expected the central Cobalt layer exhibits a drop in moment due to its separation from the Platinum, an effect more pronounced in the (100) case, where a difference of $\approx 0.20\ \mu_b$ is found. The small negative

Species	Magnetic moment μ_b							(a)
Co	1.72	1.90	1.90	1.83	1.81	1.82	1.83	1.84
Pt	-	0.44	0.33	0.28	0.25	0.26	0.27	0.28
Pt	-	-	0.33	0.10	0.03	0.02	0.04	0.06
Pt	-	-	-	0.28	0.03	−0.03	−0.03	0.00
Pt	-	-	-	-	0.25	0.02	−0.03	−0.02
Pt	-	-	-	-	-	0.26	0.04	0.00
Pt	-	-	-	-	-	-	0.27	0.06
Pt	-	-	-	-	-	-	-	0.28

Species	Magnetic moment μ_b							(b)
Co	1.72	1.81	1.91	1.90	1.89	1.89	1.89	1.88
Co	1.72	1.73	1.69	1.69	1.68	1.68	1.68	1.68
Co	1.72	1.81	1.91	1.90	1.89	1.89	1.89	1.88
Pt	-	0.36	0.30	0.26	0.27	0.25	0.25	0.26
Pt	-	-	0.30	0.10	0.06	0.04	0.04	0.04
Pt	-	-	-	0.26	0.06	−0.01	−0.01	−0.01
Pt	-	-	-	-	0.27	0.04	−0.01	0.00
Pt	-	-	-	-	-	0.25	0.04	−0.01
Pt	-	-	-	-	-	-	0.25	0.04
Pt	-	-	-	-	-	-	-	0.26

Table 2.7: Atomic moments of (a) .../$CoPt_n$/$CoPt_n$/... and (b) .../Co_3Pt_n/Co_3Pt_n/... multilayer structures, with n=0–7. The units shown represent layers that are repeated periodically in the z direction. Layers are built up from the (100) stacking, systems have the in-plane spacing of Platinum and volume conserving relaxations along z.

contribution to the interfacial Platinum moments from the p states persists in these systems, while an addition negative contribution to the Cobalt polarisation [−0.04 (interface), −0.02 (centre)] exists in both stacking geometries.

2.3.6 Surface systems

The multilayer calculations of the previous section are now extended to surface geometries. Surface systems present an interesting problem for electronic structure calculations. The broken symmetry means that methods exploiting the periodicity of the system become a hindrance in the direction normal to the surface. One common technique to overcome this problem is the supercell method where a vacuum gap is placed at the surface to decouple a slab with its periodically repeating neighbours. The problems with this method are that a sufficient vac-

uum gap must be included to isolate slabs, and a thick enough slab must be used to replicate bulk properties at its centre. The LKKR method allows considerable improvement over the supercell approach by replicating the properties of a converged bulk system as a semi-infinite substrate upon which the finite layered surface is placed. In this case the system Fermi energy is no longer allowed to vary, but is fixed at that of the bulk Platinum substrate. As a result charge neutrality is not guaranteed with charge flowing in or out of the system as required. The transition of the substrate from bulk potentials to the surface is not discontinuous, therefore buffer layers are required between the substrate and Cobalt layers to account for this change. Three layers of Platinum are placed on top of fixed potential Platinum substrate and allowed to relax self-consistently, this has been found sufficient in our calculations on multilayers and previous electronic structure calculations [130, 154] due to the rapid decay of perturbations to the Platinum potential from the interface. Two layers containing no nuclei are placed on top of the completed surface, to allow for charge spill-out [155].

The experimental trilayers of interest in this thesis have a Platinum capping layer around 3.5 nm in thickness, corresponding to approximately 7 atomic layers. The average thickness of the sandwiched Cobalt is 0.5 nm equivalent to 3 atomic layers. The Platinum substrate used in the experiments is sufficiently thick to have reverted to bulk properties, thus validating the use of the [bulk]/surface method implemented in the LKKR. A diagram of a typical surface system used in the calculations is shown in figure 2.6.

Results are presented for [Pt]/Pt_3/Co_n/Pt_7 sandwich systems with n=1–5, shown in figures 2.7 and 2.8 for (111) and (100) structures respectively in both unrelaxed and relaxed configurations. The first notable feature is the near symmetric moments found in the Cobalt layers, implying that any surface effects on the Cobalt are largely negated by the Platinum capping layers. In the (111) systems a pronounced interface effect is found for the unrelaxed lattice, with the interfacial Cobalt showing a greater spin splitting, although the effect is almost fully quenched by the second layer. In contrast, the fully relaxed structures exhibit a more homogeneous distribution, with a slight lowering of the moment at the interface, although this is compensated for by the increase in the induced interfacial Platinum moment in the case of systems with n>1. These findings are in good agreement with the results of the multilayer studies in sections 2.3.4 and 2.3.5, where a slight reduction at the interface was found for the relaxed struc-

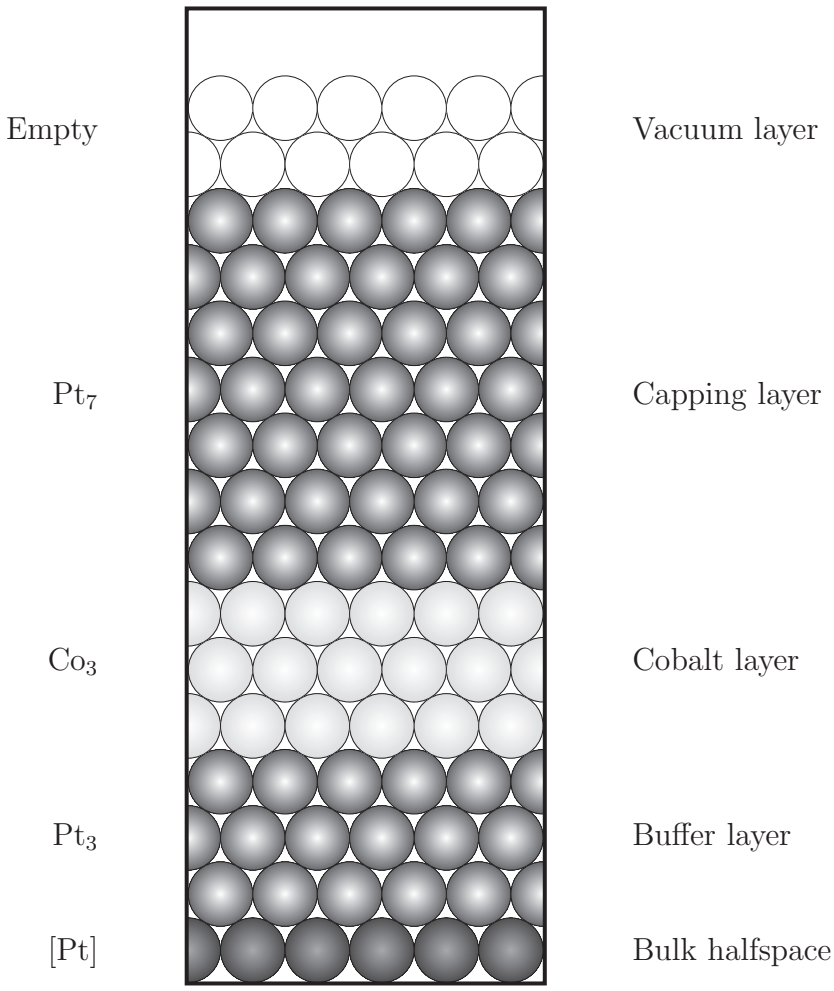

Figure 2.6: 2D analogue of a crystal used to model a [Pt]/Pt_3/Co_3/Pt_7 surface system in the LKKR calculations. The darker spheres in the bottom layer represent the terminating layer of the frozen potential bulk Platinum halfspace in which the potential is stacked *ad infinitum*. Upon the halfspace 3 layers of Platinum are placed for self-consistent relaxation. The lighter spheres represent the 3 atomic layers of Cobalt, capped by 7 layer of Platinum. Self-consistent potentials are calculated for both Cobalt layers and Platinum capping layers. Finally the white spheres represent the two layers containing no nuclei to allow for charge spill-out.

tures. Again, for the single Cobalt layer systems the increase in coordination number with respect to Platinum increases the moment on both species. Similar conclusions can be drawn for systems stacked in the (100) plane. However, the reduction in the polarisation of the relaxed systems in this case is not as pronounced as seen for the (111) stacking, and still exhibits a small increase at the interface. One can draw the conclusion regarding the experimental systems that, despite showing small variations between the stacking geometries and layer thickness, the systems are fairly robust with regards to the magnetism with a consistent Platinum polarisation of 0.2–0.3 μ_b at interfaces. Similarly for the Cobalt layers the moments remain in the range 1.7–1.9 μ_b for all systems studied, however spin-orbit interactions would provide a modest additional contribution to both species.

2.4 The CPA: Treating substitutional alloying

So far results have been presented for pure CoPt systems with no attempt made to account for the expected alloying present at the interfaces. Since the systems are fabricated by sputtering there is likely to be mixing of Cobalt and Platinum during the growth process. We now turn our attention to such concerns, using the coherent potential approximation (CPA) [156] to deal with substitutional disorder. This technique has been applied successfully to many bulk alloys [157, 158], as well as to study interdiffusion effects at interfaces [159, 160].

Prior to the development of the CPA many different schemes were employed for calculations on random alloy systems. Early attempts at modelling substitutional disorder that move beyond rigid bands models were made in the virtual crystal approximation (VCA) where an averaged potential is repeated periodically [161, 162]. Although showing some success in calculations on semiconductor alloys such as (Ga,Al)As it generally provides a poor description of real alloy bands, especially in transition metal systems. An improvement is made in the averaged t-matrix approximation (ATA), in which as the name suggests the t-matrix representing single site scattering from an alloy is constructed using the concentration weighted average of constituent elements. Although showing some of the scattering properties of the alloy, comparisons with experiments are generally not in good agreement (e.g. [163]).

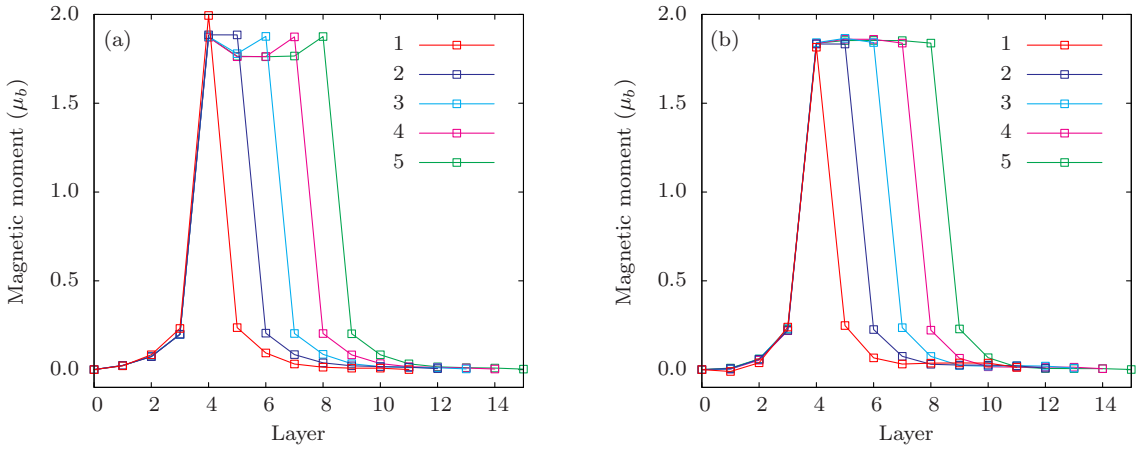

Figure 2.7: Layer resolved atomic moments in a [Pt]/Pt_3/Co_n/Pt_7 surface system with (111) layer stacking, where [Pt] denotes the bulk halfspace. (a) displays data on *unrelaxed* structures, while (b) shows the results for volume conserving *relaxed* lattices. The terminating layer in the bulk halfspace is located at 0. The tabulated data is also given in Appendix A.

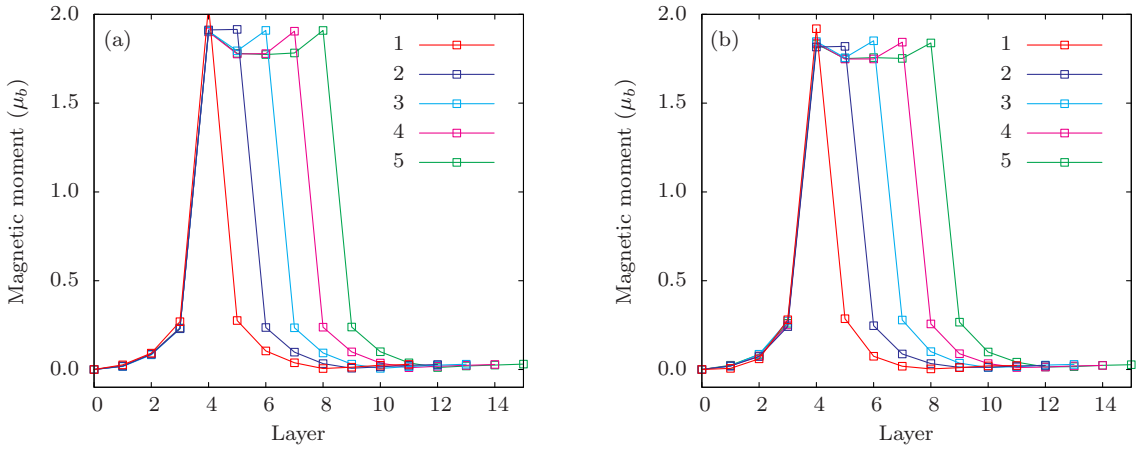

Figure 2.8: Layer resolved atomic moments in a [Pt]/Pt_3/Co_n/Pt_7 surface system with (100) layer stacking, where [Pt] denotes the bulk halfspace. (a) displays data on *unrelaxed* structures, while (b) shows the results for volume conserving *relaxed* lattices. The terminating layer in the bulk halfspace is located at 0. The tabulated data is also given in Appendix A.

The coherent potential approximation, like the ATA, uses a scattering matrix method to predict the properties of an alloy. The basic premise is the definition of an effective medium to replace the disordered alloy, which has the property that its scattering remains, on average, unchanged by the substitution of a constituent atom in to a lattice site. The formalism was first outlined for the semi-relativistic KKR method by Stocks *et al.* [164], with the extension to the LKKR method first made by Kaiser *et al.* [165]. Let us consider a binary alloy A_xB_{1-x} in which the atoms are arranged in a periodic lattice with random occupancy conforming to the fractional concentration x and 1−x for A and B respectively. Dropping the basis set indices, the scattering path operator for an isolated impurity of type A(B) embedded in an effective medium representing the alloy is $\tau_A(\tau_B)$, whilst the effective medium alone is characterised by τ_{eff}. The scattering properties of a particular lattice site must equal that of the surrounding medium and the weighted average of τ_A and τ_B:

$$x\tau_A + (1-x)\tau_B = \tau_{\text{eff}}. \tag{2.18}$$

A single site scattering matrix t_{eff} is defined which describes the scattering from the random field of the disordered medium within the single site approximation. The expression for the effective medium scattering path operator is given by:

$$\tau_{\text{eff}} = \int \frac{d\mathbf{K}}{\Omega}(t_{\text{eff}}^{-1} - g(\mathbf{K}))^{-1}, \tag{2.19}$$

where $g(\mathbf{K})$ is the structural Green function depending on the alloy lattice. As this underlying structure is the same for atoms A, B and the effective medium the structural Green functions will be identical. By using this fact and manipulating equations (2.18) and (2.19) the following expression can be derived:

$$\tau_A = \left[\tau_{\text{eff}}^{-1} + t_A^{-1} - t_{\text{eff}}^{-1}\right]^{-1}, \tag{2.20}$$

where the integral over the reciprocal lattice has been dropped in the notation. The expression for τ_B is similarly obtained. It is clear that equations (2.18)–(2.20) define a self-consistency problem that must be solved to calculate τ_{eff}. Ginatempo and Staunton [166] detail an iterative method for this purpose, that has been implemented in the LKKR code. This takes as a starting guess the ATA value of the single site scattering matrix of the alloy:

$$t_{\text{eff}} = x\, t_A + (1-x)\, t_B. \tag{2.21}$$

In the calculation of τ_{eff} reported here full use of the crystal symmetry is made via hardwired routines.

2.4.1 Bulk alloy

Initially the magnetic properties of a bulk FCC random CoPt alloy were studied. Previous work on this system include relativistic and scalar-relativistic KKR calculations of Ebert *et al.* [167] who found that orbital contributions to the magnetic moments are enhanced in the Platinum rich systems, but good agreement is found with experiment with both sets of calculations. They do not however state the lattice spacings used in their work, for example whether concentration-dependent values were used. Later Koepernik *et al.* [168] performed scalar-relativistic LCAO-CPA calculations for the bulk alloy, using a fixed lattice spacing throughout, and they claim good agreement with the experimental curve taken from Ebert *et al.*.

In the calculations it was found that, when using atomic basis sets including $\ell = 3$, the iterative scheme sometimes failed to converge for certain systems. Results are therefore presented for systems with $\ell_{\max} = 2$ as well as those values that were obtained with $\ell_{\max} = 3$. The accumulated data for existing experimental studies on the lattice spacing in CoPt disordered alloy as a function of concentration is given in Appendix A (figure A.1). In these calculations we use both experimental and fixed lattice parameters and results are shown on separate plots in figures 2.9 and 2.10. Our calculations show good agreement with the those mentioned previously, showing non-linear behaviour in the concentration averaged moment at higher Platinum concentrations. It is found that the polarisation of the Platinum atom is insensitive to the lattice parameter, showing nearly identical polarisation values at all alloy compositions in both cases. Consistent with calculation in previous section, the Cobalt atom shows a dependence on its local volume, the expanded atom exhibiting a greater moment.

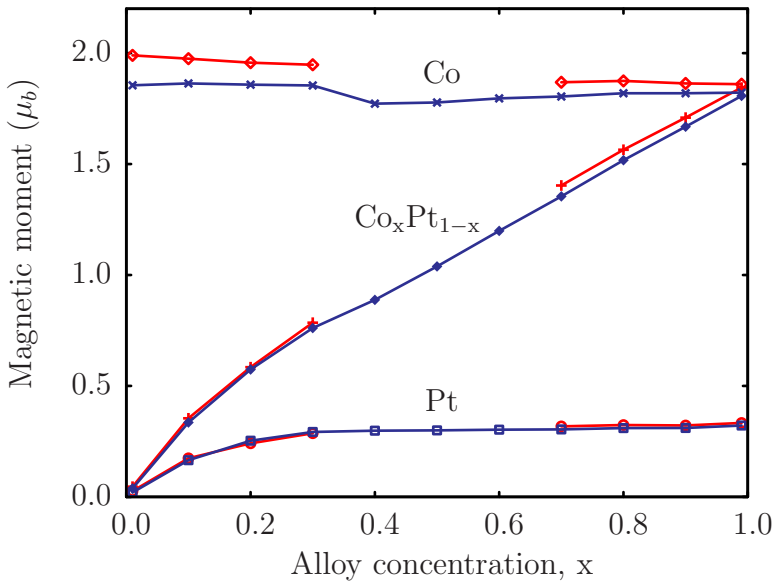

Figure 2.9: Magnetic moments of disordered Co_xPt_{1-x} alloy. Data is shown for the alloy at bulk Platinum spacing with $\ell_{max} = 2$ (blue lines) and $\ell_{max} = 3$ (Red lines) where available.

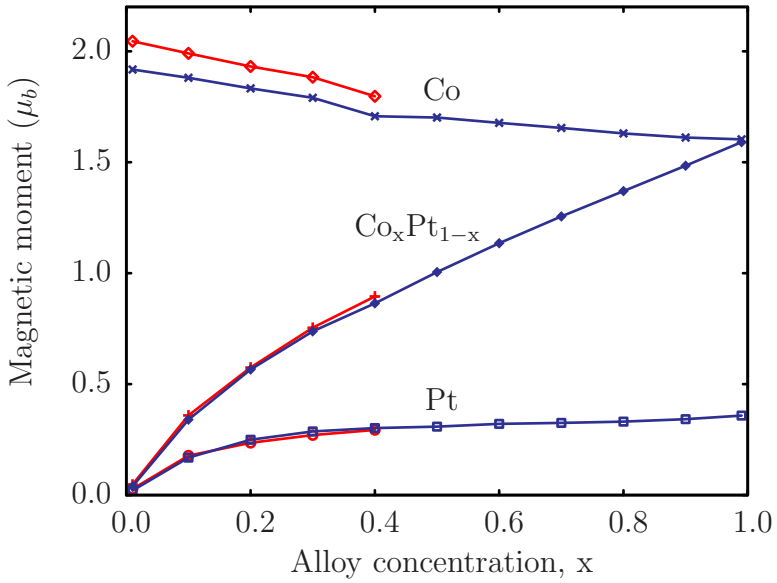

Figure 2.10: Magnetic moments of disordered Co_xPt_{1-x} alloy. Data is shown for the alloy at experimentally measured spacings with $\ell_{max} = 2$ (blue lines) and $\ell_{max} = 3$ (Red lines) where available.

2.4.2 Boundary interdiffusion in surface systems

We now use the CPA with the LKKR method to investigate the effect of interdiffusion, allowing for layer dependent mixing of the Cobalt and Platinum atoms. Because of the layer resolved scattering treatment in the LKKR method, it is able to deal with systems with a layer dependent alloy concentration. Figure 2.11 illustrates calculations performed on systems consisting of a Co_3 layer sandwich in the surface system, where interdiffusion (x=0.1, 0.3, 0.5) is present in the interface layer between the upper Cobalt layer and Platinum capping layer. It is found that the average moment in the alloyed layer are well described by the bulk alloy calculations.

2.5 Summary

In this chapter the results of LKKR calculations on Cobalt-Platinum systems in several geometries have been reported. Results have been presented for (100) and (111) FCC stackings in multilayer and surface systems with rigid Platinum spacings and more realistic relaxed structures. Finally the effect of alloying was considered in the coherent potential approximation in bulk alloys and calculations were demonstrated where interdiffusion is present at the interface of a surface system.

Perhaps the most important conclusion to come out of this Chapter is that the systems are well behaved magnetically under a different array of conditions. No 'dead layers' have been found with regards to the magnetism in multilayer or surface systems. Indeed alloy properties vary systematically with respect to the concentration of constituent elements, showing only slight non-linear behaviour at low Cobalt concentrations. This is an important conclusion for experimental samples in which disorder and alloying is expected to dominate. Under these conditions the magnetisation is still expected to be continuous due to the induced Platinum moment, an important consideration for the applicability of the micromagnetic simulations presented in the following Chapter. These calculations are also used in Chapter 5 to give a semi-quantitative explanation of the observed anisotropy in the domain wall resistivity tensor.

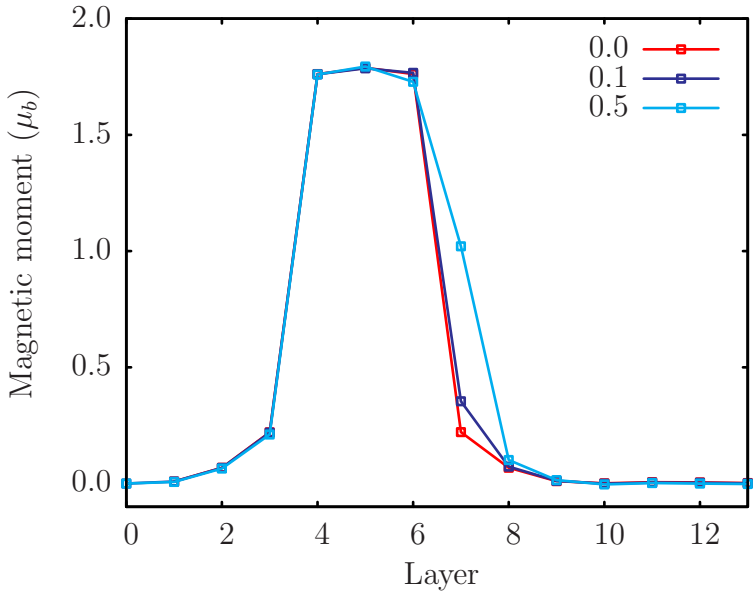

Figure 2.11: Layer resolved atomic moments in a fully relaxed [Pt]/Pt_3/Co_3/Co_xPt_{1-x}/Pt_6 (111) system. The alloy is located in the 7^{th} layer, values of x are shown in the key.

2.6 Addendum

Subsequent to the completion of this work, and motivated by our findings, the problems encountered with the CASTEP code in relation to Cobalt-Platinum systems have been studied by the CASTEP group. The conclusions of a preliminary study are reproduced here from a private communication with K. Refson [169], which may be of assistance to others studying these materials.

It was shown that a newer pseudopotential generator built in to the latest versions of the CASTEP code but unavailable during our study improves on the moment and pressure errors found with the library files, confirming our initial conclusion that a pseudopotential error was at least partly at fault. Calculations were performed on the bulk alloy $CoPt_3$ with a = 3.857 Å and using a 16×16×16 k-point set and the PBE exchange-correlation functional. For comparison, the full-potential LMTO results of Galanakis *et al.* [143] were used, who obtained a unit cell moment of 2.54 μ_b. The results of calculations using the library and generated pseudopotentials are shown in table 2.6, rows 1 and 2. Clearly a large proportion of the moment and pressure error is corrected by this new pseudisation method. The Cobalt semi-core 3*s* and 3*p* states were added to the pseudopotential description and resulted in another modest improvement (row 3 in table 2.6).

Further attempts at improving the accuracy by reducing the pseudisation radius (rows 4 and 5) and the core and charge augmentation radius (rows 6 and 7) made little difference to the obtained results.

A possible explanation for the remaining discrepancy is the range of different exchange-corelation functionals used in the literature, to which the moments and pressures can be sensitive. Clearly these systems still warrant further study.

I am in gratitude to Dr Keith Refson for his expert assistance in this matter.

	System	Magnetic moment (μ_b)			Pressure (GPa)
		Total	Co	Pt	
1	Library	3.56	2.62	0.16	−21.87
2	Generated	3.20	2.18	0.17	−7.53
3	Semicore Co	3.04	2.08	0.16	−5.88
4	Co (r_c=2.25)	3.05	2.12	0.16	−5.88
5	Co (r_c=2.0)	3.05	2.14	0.15	−5.98
6	Co (r_{inner}=1.0)	3.07	2.14	0.15	−6.14
7	Pt (r_{inner}=1.24)	2.99	2.14	0.14	−5.89

Chapter 3

Micromagnetics

In this Chapter the magnetic switching behaviour of irradiated Pt/Co/Pt trilayer devices are studied by a micromagnetic model that is implemented in the object-orientated micromagnetics framework (OOMMF) code [170]. Often in experiment detailed information about the sample magnetisation is unavailable, and the tools used to probe the system are hysteresis curves, where only the averaged magnetisation is measured. Thus the ability to predict the detailed magnetic structure makes micromagnetics an important theoretical contribution to the understanding of the physics in such systems. So that the reader is familiar with the concepts used in the results section, a brief review of micromagnetics is presented at first, including some specifics of the OOMMF implementation. Subsequently, energy parameters that are relevant to the systems studied in the experiment are discussed. Finally results are presented illustrating the switching properties of the irradiated region, and it is deduced that differences between theory and experiment can be explained by the presence of sample defects in the fabricated systems.

3.1 EHE measurements on Pt/Co/Pt trilayers

In the remainder of this chapter the unit of applied field is the Oersted (Oe) which is equal to 1x10^{-4} Tesla, and is a unit traditionally used in experimental work in this field. In addition, the unit of magnetisation is the e.m.u/cm^3 which

is equivalent to 1000 Am^{-1} as a measure of dipole moment per unit volume.

The purpose of this stage of the experimental work was to demonstrate that domains and walls can be formed reproducibly in devices based on trilayers of Pt(3.5 nm)/Co(0.5 nm)/Pt(1.6 nm) by the Ga ion irradiation method described in the chapter 1. The Hall cross bars used in this study are based on the intersection of a 2 μm wide channel with 3 perpendicular wires as shown schematically in figure 3.1. A 3 μm wide region was defined at the crossing points of the channels by applying heavy ion beam irradiation to damage the sample outside the active region, indicated by the dark areas in the figure. The total length of the undamaged region was 10 μm. Subsequently, a lightly irradiated rectangular region was formed in the central cross, of dimensions $X \times 3$ μm, with X= 0.25 μm, 0.5 μm, 1.0 μm, 2.0 μm, 4.0 μm.

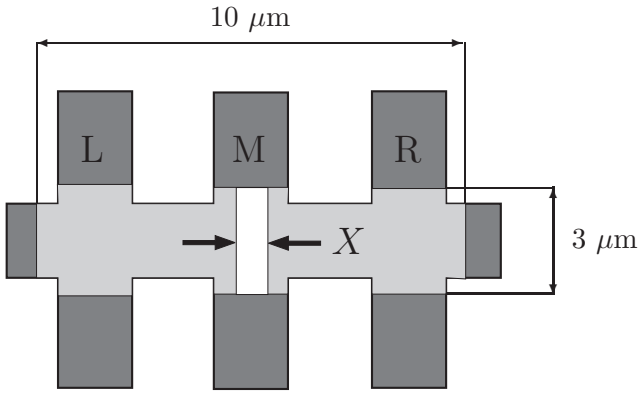

Figure 3.1: Sketch of the device used in the experiments discussed here. The darkened region represents 'magnetically dead' material that has been severely damaged by irradiation. The light grey region is the unirradiated material, forming two leads either side of the lightly irradiated central region, which is shown in white. This rectangle has an area $X \times 3$ μm.

The out-of-plane magnetisation is probed experimentally via the extraordinary Hall effect (EHE). Current flows along the horizontal channel, with voltage measurements made perpendicular to the current by probe pairs L, M and R. In this case the total Hall resistivity is given by [171]

$$\rho_{\mathrm{H}} = R_0 \mathrm{H}_z + R_e 4\pi \mathrm{M}_z, \tag{3.1}$$

where the first term represents the ordinary Hall voltage contribution with R_0 the ordinary Hall coefficient, and H_z the out-of-plane component of an applied field. The second term is the extraordinary Hall term, where M_z is the sought after out-of-plane component of the magnetisation and R_e the EHE coefficient. Thus,

after removing the ordinary Hall effect, changes in the out-of-plane component of the averaged magnetisation can be measured by this technique.

Figure 3.2 shows EHE voltage measurements by the M probes in a system containing a 1 μm wide irradiated region. If the entire system is saturated by a large ($H_z > +100$ Oe) out-of-plane field then the magnetisation of the whole sample (both irradiated and unirradiated regions) is in alignment with the field as indicated by the stationary, positive EHE voltage at point a. The field is reversed to point c where a rapid change of the magnetisation occurs that is attributed to the central region switching to a negative magnetisation, with the system ending up in an antiferromagnetic configuration at point d on the curve. Upon reversing the field sweep direction the system exhibits hysteresis, following a new path along e to saturation at point b. This minor hysteresis loop is associated with the physics in which we are interested — the reversal dynamics of the irradiated region. These loops will be studied in greater detail in the following sections. If, on the other hand, the negative field is increased from point d onwards then at point f one of the unirradiated sides flips to a negative magnetisation state, followed shortly by the other at position g. At point h the system is fully saturated in the negative z direction. Following the lower path from h onwards indicates that the samples shows near identical behaviour in reverse, with minor differences arising due to non-homogeneities in the sample.

The measured hysteresis behaviour of the central irradiated regions is shown in figure 3.3. These correspond to the upper minor loop seen in the previous figure, and data are shown for regions with X=0.5 μm, 1.0 μm, 2.0 μm and 4.0 μm. Thus, in these plots the two unirradiated regions either side of the central region have a fixed out-of-plane magnetisation in the positive z direction, corresponding to a positive EHE voltage. The data has been displaced vertically to centre the curves at zero for illustration purposes. It can be seen that the loops are asymmetric, particularly in the case of the narrower irradiated regions, where the negative reversal field becomes increasingly large. Owing to this behaviour, the reversal curve for the 0.25 μm wide region is not shown as the switching point corresponds to that of the unirradiated regions, masking the signal. These transitions from positive to negative saturisation are abrupt, whilst a more gradual change is observed on the reverse sweep, with discrete jumps of the magnetisation clearly visible.

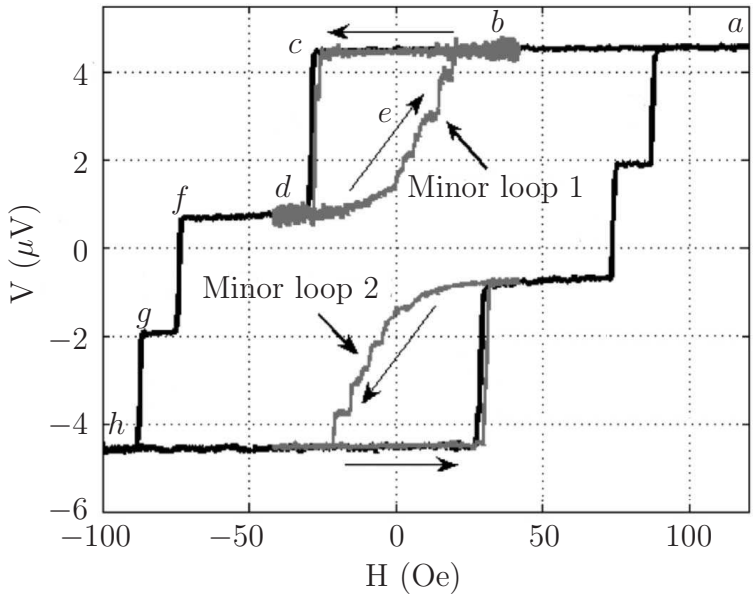

Figure 3.2: EHE voltage measurements as a function of perpendicular magnetic field at 300K at a Hall cross which has a 1×3 μm^2, dosed region at its centre. [*adapted from Ref.* [102]]

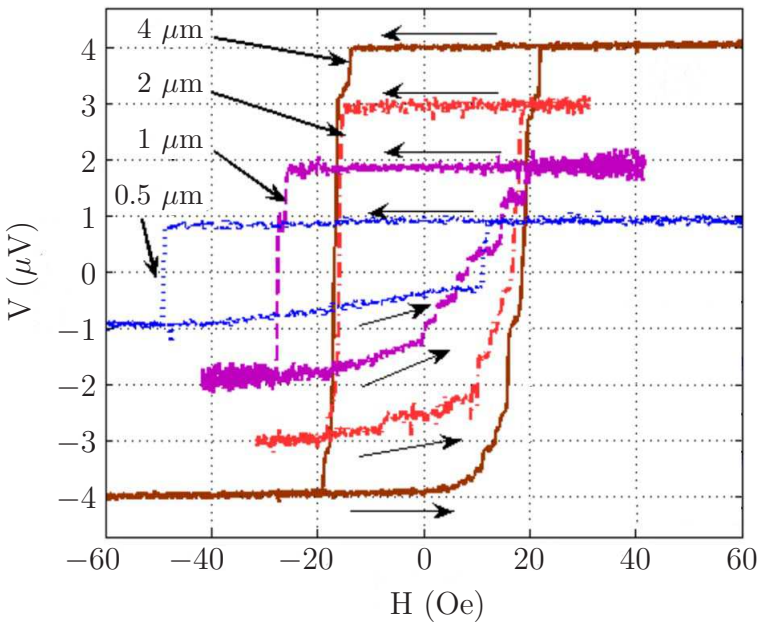

Figure 3.3: EHE voltage measurements at 300 K of minor loops of irradiated regions with widths varying from 500 nm up to 4 μm. Samples were first saturated in positive fields, and the external field then swept down until the dosed region reversed, at which point it was swept back up again. [*adapted from Ref.* [102]]

3.2 Basic theory and implementation of micromagnetics

The goal of micromagnetics* is to calculate the system-wide magnetic configuration of a ferromagnetic system. In this context, such simulations enable the calculation of hysteresis curves analogous to those measured experimentally, and the magnetisation that gives rise to such hysteresis behaviour can be studied in detail. Unlike traditional electronic structure calculations based on identical, translationally invariant unit cells, the magnetisation can vary on the length-scale of the entire sample; it is clear that significant approximations are required to make the problem tractable. The keystone of the micromagnetic method is the continuum approximation in which the individual atomic moments are replaced by a continuous magnetic vector field, $\mathbf{M}(\mathbf{r})$. Furthermore, the complex interactions of the full system Hamiltonian are reduced to a set of phenomenologically determined parameters used in simplified energy terms.

The total Gibbs free energy in the Heisenberg model for a sample of volume Ω is given by

$$E = \int_{\Omega} \left(E_{exch} + E_{anis} + E_z + E_{demag}\right) \mathrm{d}V, \tag{3.2}$$

where the energy density terms on the right hand side represent the exchange interaction, crystalline anisotropy, external field (Zeeman) term and magnetostatic interactions respectively. To determine stable global ferromagnetic configurations this free energy term must be minimised with respect to the magnetic structure, but the complicated energy landscape usually gives many local minima, and the path taken is often highly dependent on the initial state of the system. Before details of this minimisation are given, a brief discussion of these energy terms is now presented.

3.2.1 Exchange interaction

The long range order observed in ferromagnetism derives principally from the direct exchange interaction that was first studied in detail by Heisenberg [173]. Its origins cannot be readily interpreted in terms of a classical picture, hence we

*a term coined by Brown in his treatise on the subject [172]

turn to a quantum description of particles. Let us consider a pair of electrons with general coordinates λ_1 and λ_2. Given that these particles are fermions, the Pauli exclusion principle leads to the exchange condition

$$\psi(\lambda_2, \lambda_1) = -\psi(\lambda_1, \lambda_2). \tag{3.3}$$

It can therefore be said that the wavefunction of the electron system must be antisymmetric under the exchange of two particles. It is possible to break the wavefunction up in terms of a spatial (ϕ) and a spin (χ) element such that

$$\psi(\lambda_1, \lambda_2) = \phi(\mathbf{r}_1, \mathbf{r}_2)\chi(\sigma_1, \sigma_2). \tag{3.4}$$

It is clear that to preserve the antisymmetry required in this equation that if ϕ is symmetric under exchange then χ must be antisymmetric and vice-versa. The exchange interaction arises owing to this coupling of the spatial and spin part of the wavefunction. In systems where the interatomic distances are small the massive nuclear charge is screened by electrons localising between them according to work outlined by Bethe and Slater in the 1930s. The proximity of the electrons necessitates that exchanging two electrons will produce a spatial wavefunction with the same symmetry, hence leading to an antisymmetric spin configuration. The opposite is true when the atoms are located further apart, the electrons localise nearer to the individual nuclei and swap spatial symmetry when exchanged. Bethe and Slater produced a plot (see reference [174]) showing the relationship between the atomic separation and the strength of this interaction. Cobalt is found near the peak of this curve indicating strong ferromagnetic exchange interactions.

In his paper Heisenberg deduced the energy difference between the possible states. They can be written as:

$$E = -\mathrm{J}\mathbf{S}_1 \cdot \mathbf{S}_2, \tag{3.5}$$

where $\mathbf{S}_1$ and $\mathbf{S}_2$ are unit vectors in the direction of the electron spin moment. Here J is the exchange integral that denotes the strength of the exchange interaction, which practically is often determined by experiment. It is clear that if $\mathrm{J} < 0$ then an antiparallel alignment will lower the energy of the system, resulting in anti-ferromagnetic coupling between electrons on neighbouring atoms. Conversely $\mathrm{J} > 0$ results in ferromagnetic behaviour as the energy is minimised when

$\mathbf{S}_1 \cdot \mathbf{S}_2 = 1$. Because of the local nature of the d-bands the direct exchange interaction is short range, thus nearest neighbour models of exchange are employed in theoretical treatments. A more convenient quantity of exchange strength is the exchange parameter, A, given by $A = Na^2 J\bar{M}^2$ in cubic materials [175], where N is the number of atoms per unit volume, a is the lattice constant and $\bar{M}$ is the effective spin per atom in μ_b. This is used in the remainder of this chapter in units of J/m.

Other types of exchange phenomena exist such as the RKKY interaction. These are important in rare-earth metals but are dominated in most ferromagnets by the direct exchange, and are not considered in this work.

3.2.2 Crystalline anisotropy

In a ferromagnetic material there are often specific directions of magnetic alignment that are preferred. These are usually related to the crystal structure of the material and this type is commonly referred to as the magnetocrystalline anisotropy. There are two common types of crystalline anisotropy: uniaxial and cubic.

Materials that exhibit uniaxial anisotropy have a single preferred axis of magnetic alignment, with examples such as HCP Cobalt in which the anisotropy axis points perpendicularly to the (111) plane. Other systems that typically exhibit this type of behaviour are thin films, where the broken symmetry perpendicular to the surface picks out this direction for uniaxial magnetocrystalline anisotropy. If θ denotes the angle between the magnetisation and the axis of easy magnetisation then the energy will be a minimum for $\theta = 0°, 180°$ and a maximum for $\theta = 90°$, 270°. Expanding the energy in terms of powers of $\sin^2\theta$ gives

$$E = K_1 \sin^2\theta + K_2 \sin^4\theta + K_3 \sin^6\theta + \dots \ . \tag{3.6}$$

The coefficient K_n are the anisotropy constants, and have magnitudes that decay rapidly with increasing n. Terms higher that $n = 2$ are normally too small to obtain a reliable value. In the work presented here only the K_1 term is used, referred to as K in the remainder of this chapter.

For completeness cubic anisotropy is now discussed briefly. For bulk crystals without the broken symmetry seen in HCP Cobalt or thin films the anisotropy is often cubic. In this case there are 3 perpendicular axis of easy magnetisation, and the energy can be expressed in terms of the directional cosines $(\alpha_1, \alpha_2, \alpha_3)$ of the magnetisation with respect to the cubic axis:

$$E = K_1(\alpha_1^2\alpha_2^2 + \alpha_2^2\alpha_3^2 + \alpha_3^2\alpha_1^2) + K_2\alpha_1^2\alpha_2^2\alpha_3^2 + K_3(\alpha_1^2\alpha_2^2 + \alpha_2^2\alpha_3^2 + \alpha_3^2\alpha_1^2)^2 + \ldots, \tag{3.7}$$

where again the coefficents K_n decay rapidly with increasing n.

3.2.3 Zeeman energy

The Zeeman energy term represents the additional anisotropy provided by an externally applied magnetic field. The individual moments minimise their Zeeman energy by aligning with the field.

The expression is simply

$$E_z = -\mathbf{M} \cdot \mathbf{H}_{ext}, \tag{3.8}$$

where $\mathbf{H}_{ext}$ is the applied field vector.

3.2.4 Demagnetising field

The demagnetising energy is the energy cost of generating a compensating magnetic field owing to abrupt changes in the magnetisation profile, and as such a closed magnetic circuit is preferred in a material rather that a single homogenous magnetisation that has poles at the surface. Maxwell's equations state that

$$\nabla \cdot \mathbf{B} = 0, \tag{3.9}$$

$$\nabla \times \mathbf{H} = 0. \tag{3.10}$$

Relating these field is the expression

$$\mathbf{B} = \mu_0(\mathbf{H} + \mathbf{M}). \tag{3.11}$$

Thus to satisfy equation (3.9) any divergence in $\mathbf{M}$ must be counterbalanced by a H-field, which is now labelled $\mathbf{H}_d$. In a single domain system this field opposes the magnetisation, resulting in energetics that favour a multi-domain state. Usually to solve this problem a general solution of the form

$$\mathbf{H}_d = -\nabla\phi_m \tag{3.12}$$

is employed which automatically satisfies (3.10), where ϕ_m is a newly defined scalar magnetic potential. Combining equations (3.9) and (3.11) then gives:

$$\nabla^2\phi_m^{in} = \nabla \cdot \mathbf{M} \tag{3.13}$$

inside the sample, and

$$\nabla^2\phi_m^{out} = 0 \tag{3.14}$$

in the absence of a magnetic moment outside the sample boundaries. Usually these equations are solved subject to the boundary conditions on the surface of the magnet

$$\phi_m^{in} = \phi_m^{out} \qquad \text{and} \qquad \frac{\partial\phi_m^{in}}{\partial\mathbf{n}} - \frac{\partial\phi_m^{out}}{\partial\mathbf{n}} = \mathbf{M}\cdot\mathbf{n}. \tag{3.15}$$

Where $\mathbf{n}$ is a unit vector perpendicular to the surface of the magnet and is positive in the outwards direction. Combining these with equation (3.13) we can calculate the scalar potential, and finally the effective demagnetising field is obtained from (3.12). The energy [density] is then given by:

$$E = -\mu_0\mathbf{M}\cdot\mathbf{H}_d \tag{3.16}$$

In terms of computation this is the most troublesome contribution as the problem is non-local in nature. Many strategies have been developed for efficient calculation of the demagnetising field including hybrid finite element/ boundary element methods [176] which remove the need to calculate the field outside the sample, and methods based on Fourier transforms techniques [177].

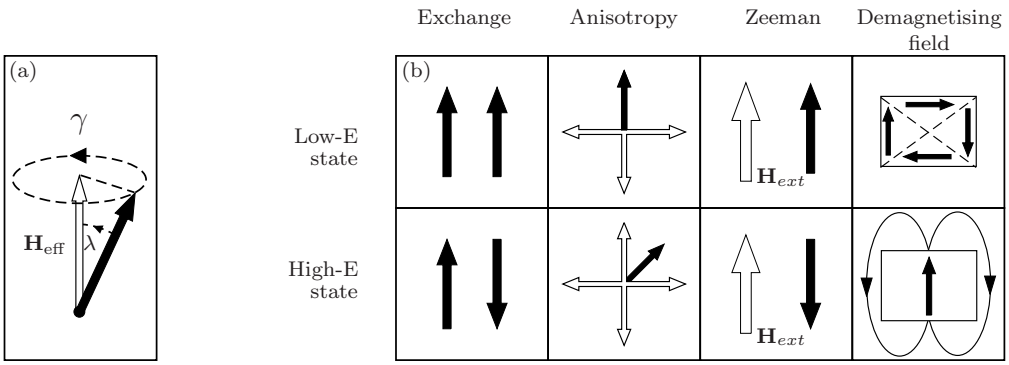

Figure 3.4: (a) Illustration of the gyroscopic effect of a magnetic moment about an effective field. The quantity γ represents the gyroscopic ratio, whilst λ accounts for damping in the system. (b) Illustration of the four energy terms considered in the micromagnetic model used in this work. Both low and high energy states are shown. Moment vectors are represented by black arrows. The demagnetising field diagram shows the magnetisation of an entire sample, whilst the anisotropy type shown is cubic as represented by the transparent arrows.

3.2.5 Magnetisation evolvers — finding stable solutions

In micromagnetic simulations the goal is to replicate the magnetic configurations found in experiment by evolving an initial magnetic state until a stable solution is reached. Typically the starting solution is either a previously calculated state if simulating the switching behaviour under an external field, or a random configuration to simulate quenching the system from above to below the Curie temperature. It is important to realise that these systems can have many stable configurations (some related by symmetry) corresponding to local minima in the energy landscape, and this is also true in the experimental situation. Effects such as remanence are proof of this, so one is not necessarily seeking the global energy minima. Two common methods that have been employed to determine stable configurations are direct energy minimisation and the dynamic Landau-Lifshitz-Gilbert approach [178, 179].

In the former case, local minima of energy is found by techniques such as the conjugate gradient method, with the advantage of being easy to implement and computationally efficient in finding a stable configuration. However, no connection is made with the physical motions of the moment vectors during the transition between states, so if one wishes to study a system where the dynamics are important, for instance domain wall motion, then an alternative method must be

used.

An equation of motion for the magnetic polarisation was derived by Landau and Lifshitz (LL) in 1935 [178] of the form,

$$\frac{d\mathbf{M}}{dt} = -\gamma\left(\mathbf{M}\times\mathbf{H}_{\text{eff}}\right) - \frac{\lambda}{M}\mathbf{M}\times\left(\mathbf{M}\times\mathbf{H}_{\text{eff}}\right), \tag{3.17}$$

which is equivalent to the formulation given by Gilbert years later [179]. The first term on the right hand side describes the precession of a moment around an effective field, $\mathbf{H}_{\text{eff}}$, at the Larmor precession frequency as demonstrated in figure 3.4. γ is the electronic gyromagnetic ratio. The second term describes damping in the system in a phenomenological fashion, such as that arising from coupling with collective excitation phenomena such as phonons and magnons, or simple thermal excitations. Without this mechanism of energy loss the system would never converge, but simply precess around $\mathbf{H}_{\text{eff}}$ indefinitely. The dimensionless damping parameter λ is a complicated function of the magnetisation state, which is often set to a value between 0.5 and 1 for computational convenience — allowing for realistic values would make convergence time consuming. The effective field is related to the functional derivative of the Gibbs free energy:

$$\mathbf{H}_{\text{eff}} = -\mu^{-1}\frac{\partial E_{Gibbs}}{\partial \mathbf{M}}. \tag{3.18}$$

Equation (3.17) can be integrated in time to evolve the magnetic configuration in a physically meaningful way. As $\mathbf{H}_{\text{eff}}$ itself is a function of the magnetisation only a small time step can be taken before it needs updating. As the integration proceeds the system converges on an energy minimum and $d\mathbf{M}/dt \to 0$, at which point a stable magnetic configuration has been determined.

3.2.6 OOMMF code

The OOMMF code [170] is a public domain micromagnetics package and is the standard code used in micromagnetic simulations. The 3D solver Oxsii offers greater flexibility than the older mmsolve2D unit, and is the code used in the work presented in the following sections. A finite difference method is employed

to discretise the magnetisation function to points on a cuboid mesh that covers the entire sample volume. The discretised form of the LL equation evolves the system magnetisation from some specified initial configuration, until the driving torques are below a chosen tolerance. Once a stable configuration is found the simulation is terminated and the micromagnetic state recorded. When performing a calculation of hysteresis behaviour the previously stored configuration is used as the initial solution. Further documentation of the method and technicalities of the implementation can be found in reference [170].

In the micromagnetic calculations presented here the material is characterised by only three parameters: the saturisation magnetisation, M_s; the exchange parameter, A; and the anisotropy strength, K. The exact value of these parameters for the Co/Pt material used in this study cannot be reliably extracted from experiment, and only estimates can be tested by simulation.

The saturisation magnetisation is a function of the individual atomic moments that constitute the material, and as such will be influenced by the alloying present in these systems. The effect of the Platinum alloying is two-fold: firstly the atom has only a small induced polarisation as seen in Chapter 2, reducing the averaged value significantly. In addition Platinum has a greater atomic volume, further reducing the saturisation magnetisation. The value of the saturisation magnetisation quoted for bulk Cobalt is 1400 e.m.u./cm^3, however we expect this to be significantly reduced by the factors mentioned above. In these calculations we start with a value of 800 e.m.u./cm^3, but also demonstrate results found employing a higher value.

The value used for the exchange constant was 1×10^{-11} J/m, which is consistent with other systems found in the literature [180].

The anisotropy constant of the unirradiated region has been measured in the literature as 9.8×10^5 J/m^3 [181]. Given that the irradiation process is known to reduce the anisotropy locally, this puts an upper limit on the anisotropy constant in the irradiated region.

The central layer in the experimental systems being simulated is 0.5 nm thick, and in these calculations the Platinum substrate and cap are considered to be non-magnetic, and are hence not accounted for in these simulations. In the

experiment the hysteresis measurements are performed for system with the unirradiated regions in both the positive and negative saturisation states, although they are found to exhibit nearly identical behaviour. In the simulation these two states are identical by symmetry.

In this work we are interested in the switching behaviour of the central irradiated region when subject to an external, perpendicularly applied magnetic field. It is assumed that in the experiment the two unirradiated regions are pinned in a saturated state when making minor loop measurements owing to their larger perpendicular crystalline anisotropy. Implicit in this assumption is that any domain walls are fully contained within the irradiated region. Full advantage is taken of this in the calculations presented here: the magnetisation of the unirradiated region is fixed out-of-plane with no relaxation of spins allowed, providing an opportunity for significant improvements in terms of memory and processor usage. The total system length is 10 μm, which proved impractical to compute using realistic mesh sizes with the computational resources available. The demagnetising field strength decays rapidly as a function of the distance from the atomic moment and as a result including the whole of the sample in the calculation is unnecessary. For simplicity the approximation that the unirradiated regions are rectangular is made in this work. Calculations of the effective demagnetising field in a 0.25 μm wide irradiated region as a function of the unirradiated region's length, L_s, is given in figure 3.5. It can be seen that the system converges rapidly with increasing L_s, and the length of the sides used in the calculations presented here was 3 μm, which gives a $> 99\%$ accuracy of the fixed demagnetising field representation, whilst satisfying practical considerations.

Finally, as this demagnetising field is unchanging the obvious strategy is to calculate the contribution once and applying it as a fixed H-field in the calculations, which is given the label $\mathbf{H}_d^{\text{fix}}$. In this situation the static unirradiated region need only be in memory for a single calculation of the demagnetising field, thus saving significantly on computation resources. A schematic illustration of this method, with region labels, is shown in the inset of figure 3.5. In a simulation the exchange governed boundary conditions on region B are accounted for by two 1 cell wide strips of material in contact with the sides of region B. The magnetisation in these strips is fixed out-of-plane to emulate the boundary with region A and C, and are sufficient to account for full exchange coupling between the regions in the nearest neighbour model used in the code.

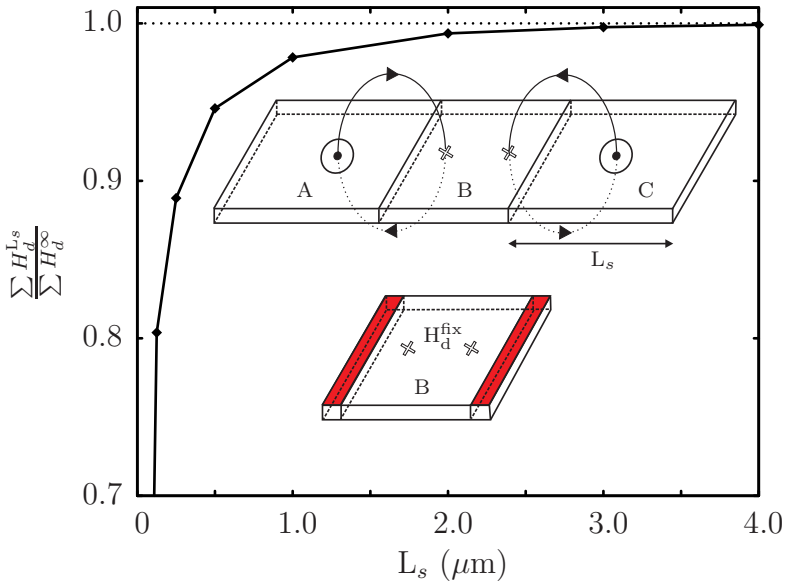

Figure 3.5: [*main plot*] Convergence of demagnetising field strength produced by the saturated side regions in the volume occupied by the central region with respect to the length of the sides. The mesh size used in this calculation was 2.5 nm×2.5 nm×0.5 nm, and M_s = 800 e.m.u/cm^3. [*inset top*] Three region system such as that in the experiment. Regions A and C are the unirradiated domains of equal length L_s with fixed out-of-plane magnetisation giving rise to a demagnetising field contribution in the central irradiated domain denoted B. [*inset bottom*] Equivalent system used in computation. The fixed demagnetising field, $\mathbf{H}_d^{\text{fix}}$, is evaluated prior to calculation and added as an external field. The red regions denote a single layer of material from regions A and B to account for the exchange interactions present at the boundaries.

3.2.7 Convergence

The subject of convergence with respect to grid size in micromagnetic simulations has been extensively covered in the literature (for an in-depth study see reference [182]), and it has been shown that an artificial pinning potential can exists for domain walls unless the grid size is equal to, or less than $\sqrt{A/K}$, known as the exchange length. Simulations presented here are performed on grids conforming to this requirement, for instance in the calculation detailed in the following section the parameters A=1×10^{-11} J/m and K=4×10^5 J/m^3 were used, thus a mesh of 5 nm×5 nm×0.5 nm was employed, with the third dimension equal to the film thickness. An additional constraint on the grid size is provided by the cubic mesh: the system dimensions must be an integer multiple of the grid size. Thus the meshes employed in these calculations were of in-plane spacings 5 nm, 4 nm or 3.125 nm as determined by the exchange length.

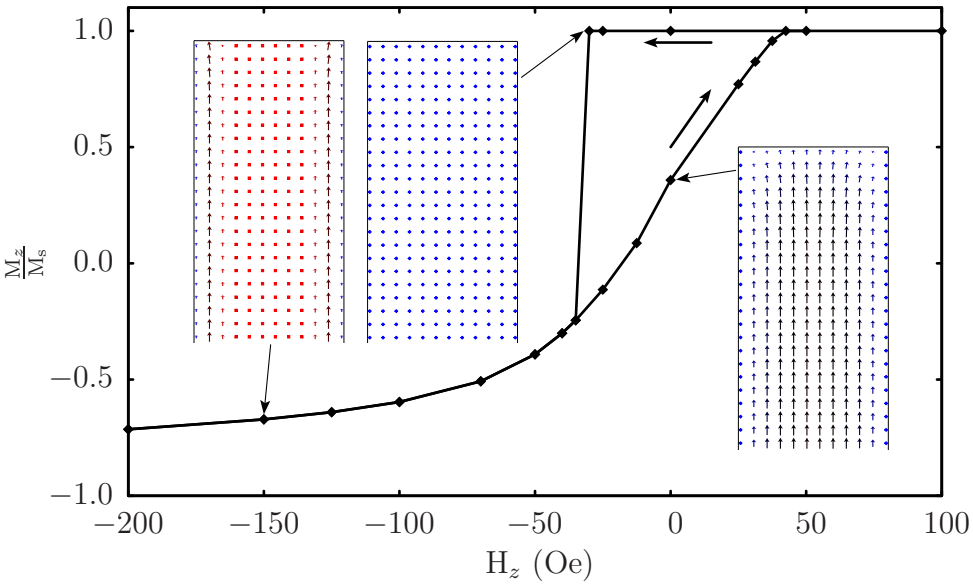

Figure 3.6: Hysteresis curve of a 0.5 μm wide irradiated region. The magnetisation is initially random (not shown on plot) and saturated to +100 Oe before cycling down to −200 Oe and back. [*inset*] Micromagnetic configuration of a representative area of the central region at various point of the curve. The blue (red) colour represents the +z (−z) component of the magnetisation vectors, which are averaged over many cells. [M_s=800 e.m.u/cm^3, A=1×10^{-11} J/m, K=4×10^5 J/m^3]

The convergence parameter that specifies the tolerance on d$\mathbf{M}$/dt was set to 1×10^{-4} deg/ns. In these calculations the value of γ is 1.769×10^5 m A^{-1} [180] and λ=0.5, a value larger than the expected experimental number but which allows the systems to converge in a reasonable amount of time, at the expense of accurate predictions of domain wall velocities.

3.3 OOMMF calculations

In figure 3.6 a hysteresis plot of the averaged z component of the magnetisation, M_z, as a fraction of the saturisation magnetisation is shown for an irradiated region with X=0.5 μm. The parameters used in this set of calculations were M_s=800 e.m.u/cm^3, A=1×10^{-11} J/m, K=4×10^5 J/m^3.

A random number generator was used to initialise the magnetisation to a paramagnetic state before the simulation is run. As in the experiment, the magnetisation was saturated first in the positive z direction by a magnetic field of

+100 Oe applied out-of-plane. As expected, the whole system is magnetically homogenous at this field value, as can be seen in figure 3.6. Following this saturation process the field strength is reduced in stages, whilst the moments remain stationary, passing through the zero field point, and exhibiting a fully saturated remanent state. At $H_z = -30$ Oe a breakdown of the magnetic ordering occurs, and a discontinuous jump of the magnetisation was observed in the hysteresis curve, resulting in a net negative magnetisation. Observing the magnetic configuration in detail shows that at this transition point the saturated state breaks down to form temporary domains, but these are only an intermediate stage of the breakdown dynamics, and are destroyed by domain wall motion to form a single domain with a mixture of in-plane and out-of-plane components. Increasing the negative field further results in a smooth increase in the magnitude of the negative magnetisation, this is due to the rotation of the single domain as it gains an increasingly large out-of-plane component. The magnetisation state is shown at H_z=−150 Oe in the inset of figure 3.6, and it can be seen that the central domain has rotated fully out-of-plane, and a clear domain wall structure can be observed at both boundaries. The magnetic profile shown is truncated for display purposes, showing only the top edge, where edge effects are manifested as small deviation in the magnetic alignment.

Following this negative saturisation procedure, the direction of the field was reversed, and the magnetisation follows the same path of domain rotation back to the break-down point at −30 Oe. Hysteresis behaviour is then observed as decreasing the negative field further takes the system along a new path, in which the magnetisation change is far less rapid than the critical breakdown found in the opposite direction. For these parameters the domain magnetisation continues its rotation as a single unit in proportion to the applied field, and the magnetisation at H_z=0 Oe is shown in the inset of figure 3.6. Apart from edge effects the moments of the central domain are fully in-plane and parallel to the long edge of the central region to reduce the demagnetising field energy. At $\approx$ +42 Oe the magnetisation has rotated fully and returns to the positive saturated state.

The two domain walls that form at the edges of the device during negative saturisation have moment rotations that occur along an axis running parallel to the device channel. The domain wall can rotate either clockwise or anticlockwise between the domains, and the exact direction depends on the initial conditions. In the example here both domain walls are rotating in the same direction. Owing

to the size of the mesh used the domain wall width is typically around 4-6 cells, although it is not possible to extract the exact size and profile of the domain wall owing to this low resolution of mesh points.

3.4 Parameter space calculations

The illustrative example used in the previous section exhibits qualitative as well as quantitative differences to the curve measured in experiments. Pinning potentials set-up by the impurities and defects in the sample will impact the reversal process of the samples in ways that cannot be reliably simulated in these calculations. However, the values of A, K and M_s in the experiment are also unclear and we are free to change these in the calculation to observe their effects on the switching dynamics. Because of the computationally demanding nature of these calculations only a small set of parameters could be tested. The results of these calculations are now demonstrated.

3.4.1 Exchange parameter

The hysteresis curve calculations presented in the previous section were repeated, but with the exchange parameters changed from 1.0×10^{-11} J/m to 0.5×10^{-11} J/m and 2.0 $\times10^{-11}$ J/m, and the results are compared to the previous simulation in figure 3.7.

A small difference in the switching field is found between the three systems, with the stronger exchange coupled systems exhibiting a slightly larger coercive field. This can be understood simply by recalling that the exchange energy prefers an uniformally magnetised state. Another clear trend is the offset in the paths taken on the reverse sweep, with the systems of lower exchange parameter exhibiting a greater level of negative saturation at any given field value. As the central domain rotates the increased exchange energy favours alignment with the unirradiated regions at the boundaries, thus reducing the negative out-of-plane component of the total magnetisation. When the domain has fully rotated out-of-plane the domain wall widths vary in the sample, being dependent on the relative strengths of A and K. As A is increased the domain wall grows as the abruptness

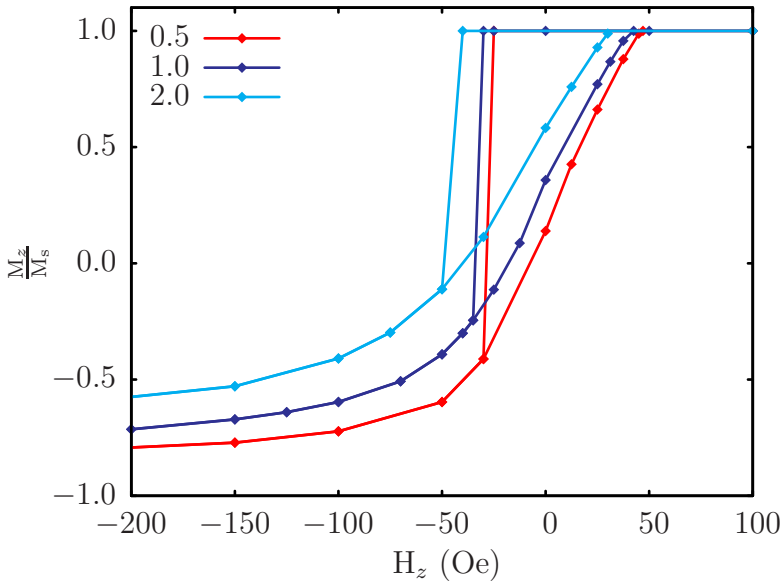

Figure 3.7: Hysteresis curve of a sample with a 0.5 μm wide irradiated region. The values shown in the key are the exchange strength parameter A in $\times 10^{-11}$ J/m. [M_s=800 e.m.u/cm^3, K=4$\times$10^5 J/m^3]

of the magnetisation change becomes more costly, with the domain wall becoming diffuse in the systems with larger A. Although the changes in the exchange energy results in quantitative changes to the hysteresis curve the reversal mechanism remains the same.

Whilst the simulation results exhibit hysteresis behaviour, the details are not so satisfactory when compared directly to experiment. At field values of -50 Oe all the experimental samples show full negative saturisation with $dM_z/dt \approx 0$, clearly this is not the case in these simulations where the magnetisation shows significant variation up to -150 Oe for the three cases studied. Thus attention is turned to the value of the anisotropy parameter, K.

3.4.2 Anisotropy parameter

The anisotropy energy plays a crucial role in establishing the desired out-of-plane magnetic profile in thin films structures, and in this section we seek to understand the influence of K on the system dynamics. The value of the anisotropy strength parameter used in the previous calculations was 4×10^5 J/m^3, chosen in the knowledge that the unirradiated region has a K value of 9.8×10^5 J/m^3, giving an upper limit. As the anisotropy becomes weaker a transition must occur where

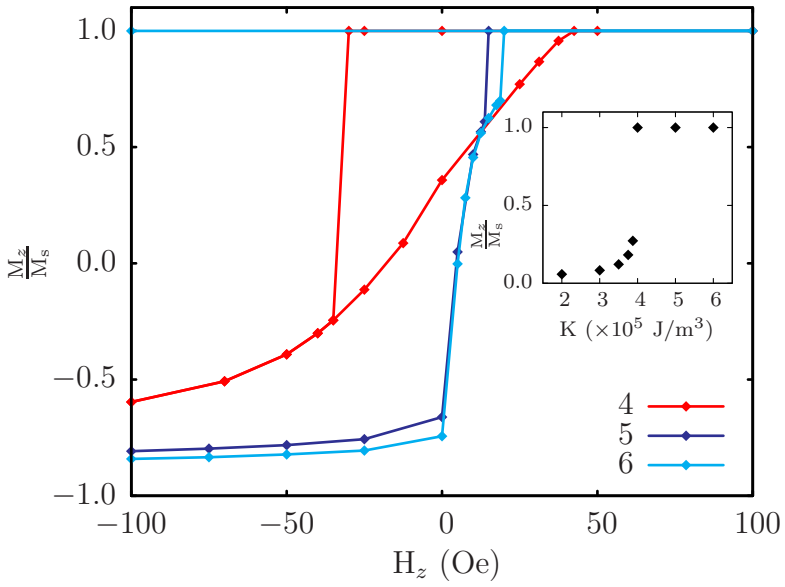

Figure 3.8: Hysteresis curve of a 0.5 μm wide irradiated region as a function of the anisotropy strength parameter, K. The value of K is shown in the key in $\times 10^5$ J/m^3. [*inset*] Value of the out-of-plane magnetisation as a function of the uniaxial anisotropy strength, K. The value of the external field is fixed at +50 Oe perpendicular to the film. [M$_s$=800 e.m.u/cm^3, A=1$\times 10^{-11}$ J/m]

the system magnetisation switches from out-of-plane to in-plane. To explore this feature in the systems studied here the averaged out-of-plane magnetisation was recorded as a function of K for a sample with a 0.5 μm wide irradiated region. In these calculations a +50 Oe biasing field was applied out-of-plane, and the results are shown in the inset of figure 3.8. As expected, a clear transition point from in-plane to out-of-plane magnetisation is found as K is varied. Furthermore, this transition point is found near the K=4$\times 10^5$ J/m^3 value used for the previous calculations. As K is lowered below this point, the magnetic configuration is dominated by the demagnetising field of the irradiated region, with this in-plane configuration reducing the energy associated with open surface poles to an extent that overcomes the weakened anisotropy. For the purposes of this work we are not interested in this lower range of K values as parameters that produce the out-of-plane configuration found in experiment are sought. At greater values of K the uniaxial anisotropy is dominant, resulting in the abrupt transition to a fully saturated state. As the previous calculation were performed near the observed transition point the obvious question is whether the switching dynamics of the system are affected if K lies away from this point.

Similar sets of calculations to those in the previous section were performed with

K=5×10^5 J/m^3 and 6×10^5 J/m^3. As before, the systems were saturated in the $+z$ direction from a random configuration, and a negative applied field used to determine the break down fields. It was found that the break down fields in the simulations are at unphysically large values. As an example, for the K=5×10^5 J/m^3 system the switching field is ≈ -5200 Oe — way in excess of the field range used in the experiments. This large discrepancy between theory and experiment can be understood in terms a few simple arguments. In the computation the material is continuous, with homogenous material parameters through the sample. If the magnetisation is fully saturated in the $+z$ direction, then the force exerted by a field applied in the opposite direction ($-z$) will pass through the pivot point, and as a result the cross-terms in equation (3.17) vanish and the system is locked in this state. In practice the moments are not exactly aligned along the z axis owing to the tolerance parameter in the convergence of the previous calculation, and a large external field can provide enough torque to overcome the convergence tolerance and the restoring effects of exchange and anisotropy, so that the system is able to break down to the negatively saturated state. This situation is a feature of the simulation alone, and in the experimental system the situation is expected to be quite different. The presence of pinhole defects, the randomness of alloying, grain boundaries, fluctuations in film thickness and random thermal fluctuations break the symmetry mentioned above, and enables the magnetisation to break down at lower field values.

To provide some insight into the possible effect of random disorder — such as those due to thermal effects — the magnetic moments of the converged saturated sample were given a small Gaussian displacement from the saturated state. The data was read in from the Cartesian OOMMF output, then converted to spherical polar coordinates and the moments were rotated in a random direction with angle governed by a Gaussian distribution centred at 0°, with a full-width-half-maximum of 1°. As a result the magnetisation of the saturated state is reduced to 799.880 e.m.u/cm^3. The breakdown field of this altered system is reduced to -2500 Oe, significantly lower than the -5200 Oe of the unperturbed system. Although this additional disorder does not replicate the complex situation found in the experimental system, it serves to illustrate how a break in the homogeneity can dramatically alter the required breakdown fields. Although a full study of disorder effects is desirable, the micromagnetic framework used places limits on what can be achieved. As an example, the study of grain boundaries becomes difficult owing to the regular cubic grid used; properties such as K, A and M_s can

only be varied on a cell by cell basis, thus making the study of realistic crystal deformities troublesome.

A reliable quantitative analysis of the break down fields is not possible with the tools and information available, however we can say with some certainty that the mechanism in the experiment is a sudden break down due to domain formation followed immediately by domain wall motion. The nucleation sites are likely to be at impurities or structural defects, thus it is unsurprising that the break down field magnitude is dependent on the area of the region. A saturisation of the breakdown sites is reached for the larger samples, explaining the trends seen in experiment.

The remainder of the work in this chapter concerns the negative-to-positive reversal dynamics.

Comparing the reversal curves in figure 3.8 it is clear that on the reverse sweep the switchover is far more abrupt for the newly calculated systems. Looking closer at the specific details of the reversal processes in these systems provides the explanation for these stark differences. For the system with K=4×10^5 J/m^3 the irradiated region rotates as a block, as described in the previous section, producing the smooth curve in proportion to the changing field. It is clear that this reversal mechanism arises due to the relatively weak anisotropy allowing rotations in the plane of the material to dominate. In contrast, the newly calculated systems exhibit a domain wall motion mechanism owing to the constraint of perpendicular magnetisation enforced by the strong anisotropy. Prior to domain wall motion the magnetisation near the walls relaxes, rotating gradually as the field is swept upwards from large negative values. This is reflected in the small magnetisation change from large negative fields down to zero. As the field becomes positive, the domain walls on either side of the irradiated region are driven towards the centre of the sample as the central domain is reversed, as shown in figure 3.9. As the field is increased the two sides meet in the middle of the sample and the domain walls are destroyed, completing the reversal process.

The obvious question is why does the domain wall motion not, once started, continue until the central domain is destroyed? This phenomenon can be explained in terms of the demagnetising field overlap between the two newly created positively magnetised regions. The demagnetising field favours an antiferromagnetic

alignment of the three domains, thus, energetically a negative magnetisation of the irradiated region is preferred by this term that resists the change resulting from domain wall motion. As the domain wall converges at the centre of the sample the field generated by the left and right regions overlap, thus strengthening the effective field retarding the domain wall motion. When the external field is increased the central domain shrinks as a larger demagnetising field overlap is required to balance the energies, as seen by the curved region in the hysteresis plots. Owing to edges effects the demagnetising field is weakest at the top and bottom of the central domain, and at a certain field value a rapid and sudden total reversal occurs, originating from these edges, as manifested by the sudden jump in the hysteresis curve.

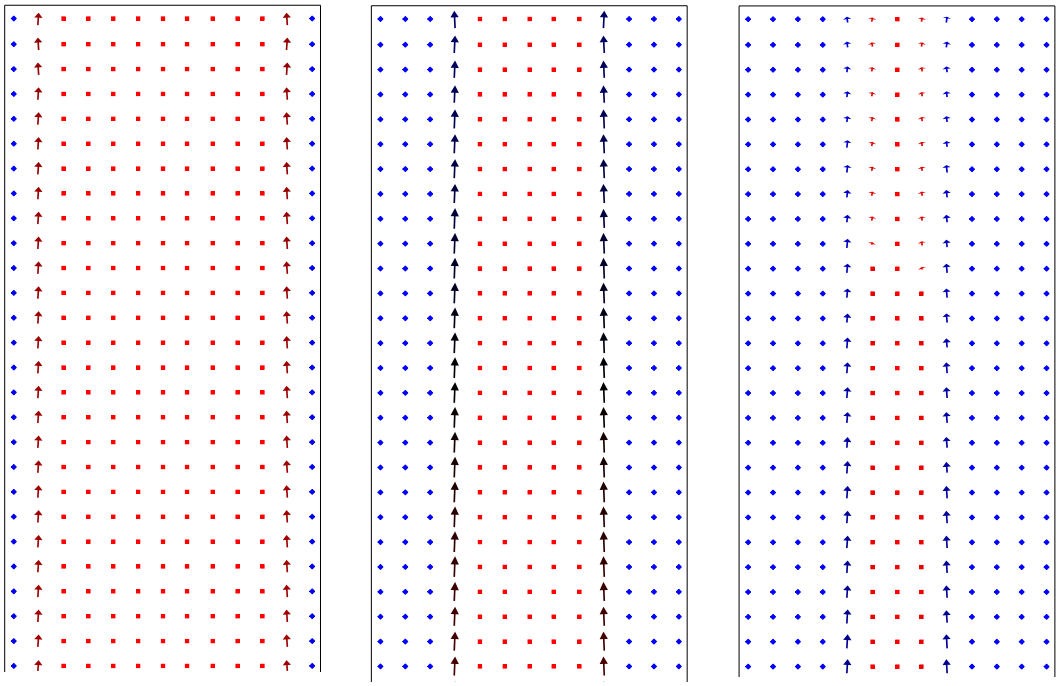

Figure 3.9: Magnetisation profile of a 0.5 μm wide sample subject to increasing applied fields. The sample is first saturated by a -100 Oe field (not shown) and then reduced in stages to 0 Oe, subsequently the field is increased in the positive direction to 5 Oe and 10 Oe as indicated by the key below the images. Blue (red) components of the arrows represent the $+z(-z)$ component of the magnetisation vectors. The two domain walls can clearly be seen separating the three domain in the samples, and domain mobility is observed as the field is increased. [M_s=800 e.m.u/cm^3, A=1×10^{-11} J/m, K=5×10^5 J/m^3]

3.4.3 Saturisation magnetisation

Subsequent to the bulk of these calculations the value of M_s was measured in the experimental system by vibrating sample magnetometry, and found to be 1010$\pm$20% e.m.u/cm^3. The estimates used in the previous section are therefore reasonable within the bounds of error, but similar calculations are now performed with the new value of M_s= 1000 e.m.u/cm^3 to study the effect such an increase has on the system dynamics. The dimensions of the system remains identical to those in the previous section. Initial calculations using the parameters K=6×10^5 J/m^3 and A=1×10^{-11}J/m demonstrated that the increased demagnetising field strength in the system resulted in an in-plane magnetisation. To explore this behaviour further, the z-component of the magnetisation was measured against

the anisotropy strength, with an applied field of +50 Oe in the same fashion as performed in the previous section. The results shown in the inset of figure 3.10 demonstrate that a larger value of K is required to obtain the desired characteristic out-of-plane magnetisation. The transition occurs near K=6.25×10^5 J/m^3, so for the calculations presented in figure 3.10 the value K=8×10^5 J/m^3 was used for the M_s=1000 e.m.u/cm^3 case, whilst K=6×10^5 J/m^3 was used in the M_s=800 e.m.u/cm^3 study. It is clear that only minor quantitative differences exist between the two curves, with the mechanism of domain wall motion being the dominant scheme of reversal.

3.4.4 Irradiated region width

Finally the calculations were repeated on samples with different irradiated region widths, X, equal to 0.5 μm, 1.0 μm and 2.0 μm. The calculations become increasingly costly in terms of computational time required, not only is the iteration time increased with system width but the total number of iterations required to move the domain walls along the wider samples is also greater, resulting in poor scaling with system size. For this reason the 4 μm wide system has not been considered, however the results obtained are sufficient to illustrate the physics involved. These hysteresis curves are displayed in figure 3.11. The main plot shows the averaged magnetisation over the entire sample. The negative saturation magnetisations is greater for the larger systems, but this is hardly surprising as the domain wall region has a smaller diluting effect on the averaged magnetisation in the larger sample. The domain walls remain stationary until a positive field is applied at which point the domain wall motion described in the previous section occurs in all three systems. Again the demagnetising field provides a barrier to complete saturation at lower fields. Shown in the inset of figure 3.11 is the total magnetic moment over the sample, as opposed to the averaged magnetic moment density in the main plot. From this it can be seen that the reversal mechanism is essentially identical in the three samples: the domain walls travel towards the centre of the sample and are halted by the demagnetising field overlap mechanism at exactly the same domain wall separation. The domain walls in the larger systems must travel further as seen in the inset figure, but we can say that in a system free of defects the reversal fields are identical for all system sizes tested here.

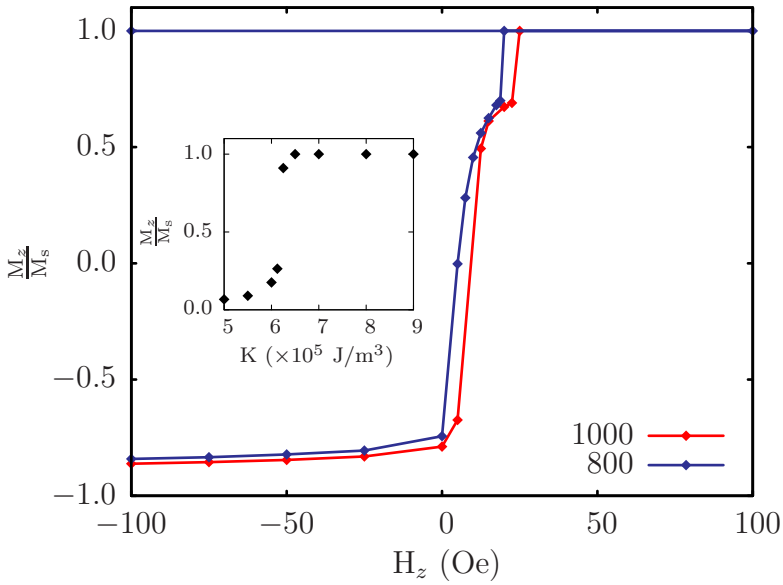

Figure 3.10: Hysteresis curve of 0.5 μm wide samples with different value of M_s indicated in the key in units of e.m.u/cm^3. The value of used K in the simulations was altered between the two systems: 6×10^5 J/m^3 (M_s=800 e.m.u/cm^3) and 8×10^5 J/m^3 (M_s=1000 e.m.u/cm^3). [*inset*] Saturation of sample as a function of the anisotropy strength parameter for a system with M_s=1000 e.m.u/cm^3. A field of +50 Oe was used as a biasing field from an initial random magnetic configuration. [A=1×10^{-11} J/m]

The hysteresis curves measured in the experiment display a rapid switching at a slightly higher field than in the simulations, and a smoother overall curve, albeit with discrete jumps along the profile. These differences can be attributed to Barkhausen jumps that are expected in the experiment. Defects in the sample result in the pinning of domain walls undergoing motion, potentially requiring a larger driving field to overcome these potential wells. These can be directly attributed to the jumps found on the curves, and also the slightly larger driving fields required, dominating over the demagnetising field governed mechanism found in the simulations. In the larger systems the domain walls must negotiate a greater number of potential pinning sites, thus increasing the probability of a pinning event resulting in the slight difference in saturation fields seen in figure 3.2.

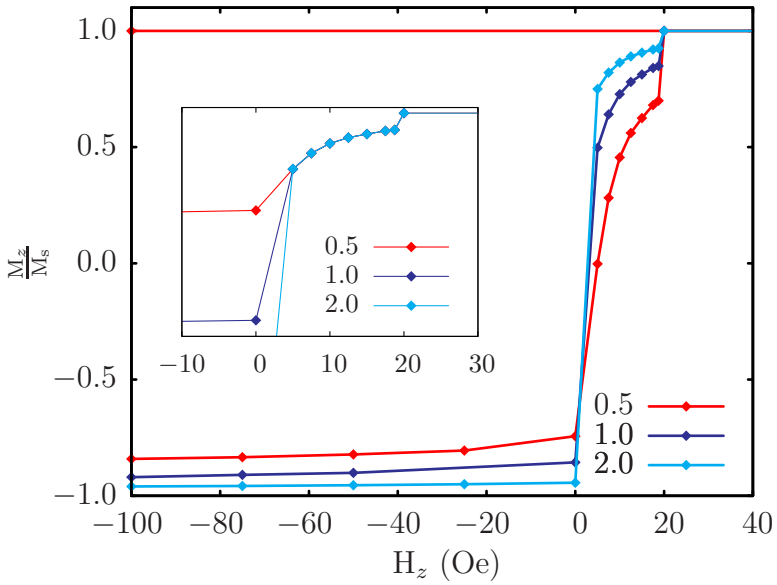

Figure 3.11: Hysteresis curve of 0.5 μm, 1.0 μm and 2.0 μm wide irradiated regions. [*inset*] Total z component of magnetic moment in the three systems demonstrating that the final stages of reversal are identical. The curves have been displaced vertically for illustration purposes. [M_s=800 e.m.u/cm^3, A=1×10^{-11} J/m, K=6×10^5 J/m^3]

3.5 Summary

In this chapter the reversal mechanisms of irradiated Co/Pt domain wall systems were studied by micromagnetic simulations. It was found that the likely scheme is domain wall nucleation, followed by rapid domain wall motion in the central region when switching from a fully saturated system to an antiferromagnetic configuration. The importance of defects was highlighted in controlling the exact value of the reversal field, by contrasting with defect free simulations.

On the reverse sweep a different mechanism was found to be responsible, that of domain wall motion involving two walls at the edges of the irradiated region. In the simulation the motion is controlled by the demagnetising field overlap of the two side domains, whilst in the experiment there is evidence of disorder related Barkhausen jumps, that account for the small differences observed in saturisation fields.

In addition to the above an alternative scheme of reversal was discovered in systems where K approaches the value of an out-of-plane to in-plane transition,

in which the moment rotation is more gradual as the weakened anisotropy can no longer hold the magnetisation out-of-plane.

Chapter 4

Ballistic transport in Pt/Co/Pt trilayers

Electron transport studies in metallic systems are commonly performed in one of two conventional frameworks. The first is the diffusive regime in which impurity scattering dominates, and the mean free path of an electron is smaller than the region under study. As will be demonstrated in the following Chapter this is the scheme expected in the experimental Cobalt Platinum trilayers upon which this work is based. On the other hand, in the limit where the electronic mean free path is greater than the transport region, electrons move coherently in the lattice, and the transport is ballistic. In this Chapter calculations of the domain wall conductance are described in this ballistic limit on Pt/Co/Pt trilayers, with the aim of studying systems analogous to those fabricated experimentally. Accepting that the fabricated systems are strictly outside the validity of this framework, the proposition still has merit. Ballistic transport calculations of domain wall resistance have previously been performed in the two band approximation [44, 28] and for more realistic bulk materials [27]. However we believe that this ballistic transport investigation of domain walls in multilayer sandwich systems is novel, and thus also of academic interest.

The method chosen to obtain the electronic structure of these multilayers is the semi-empirical tight binding method, with parameters derived from more accurate *ab initio* methods. A Green function formalism is used for transport calculations that allows the sandwiching of an active region representing the

domain wall between two reservoir leads. The conductances are obtained in the transmission probability framework of Landauer and Büttiker.

Initially, results are compared to bulk systems found in the literature. The conductance of single domain multilayers are then studied, before moving on to domain wall calculations. Conductances are presented for a range of systems as a function of the domain wall width, and the abrupt and realistic size domain wall limits are discussed separately. An attempt is made to connect the results to a simple model based on a resistance dilution effect by the Platinum layers, and it is shown that this model fails to sufficiently account for the trends found. The conductance is then studied as a function of energy to allow for the uncertainty in the Fermi energies of these systems, and the limitations of this model are discussed in greater detail.

4.1 Semi-empirical tight binding method

The semi-empirical tight binding method (TB method) reduces the problem of determining the band structure of real materials from one of a vastly complicated many body problem to one involving a minimal set of fitted parameters. A simple yet useful description of atomic states is provided, allowing access to systems that would be difficult to model efficiently using a full *ab initio* approach. Also referred to as the linear combination of atomic orbitals (LCAO) method, a set of atomic orbitals is used with Bloch summations to expand the wavefunctions of the valence states with wavevector $\mathbf{K}$ (we only consider periodic systems)

$$\psi_{\mathbf{K}\alpha l}(\mathbf{r}) = \sum_{\mathbf{R}} e^{i\mathbf{K}\cdot\mathbf{R}} \phi_\alpha \left(\mathbf{r} - \boldsymbol{\tau}_l - \mathbf{R}\right), \tag{4.1}$$

where $\mathbf{R}$ is an unit cell translation vector, $\boldsymbol{\tau}_l$ is the position of atom l within the primitive unit cell and ϕ_α are the atomic orbitals with α labelling the specific basis functions. This atomic basis is not orthogonal to those centred on neighbouring atoms, hence the wavefunction satisfies a Schrödinger equation of the form

$$\mathbf{H}(\mathbf{K})\psi_{\mathbf{K}} = E(\mathbf{K})\mathbf{S}(\mathbf{K})\psi_{\mathbf{K}}, \tag{4.2}$$

where $\mathbf{S}$ is the so-called overlap matrix that accounts for the non-orthogonality of the basis set. The wavefunction above is given by

$$\psi_{\mathbf{K}}(\mathbf{r}) = \sum_{\alpha l} C_{\alpha l}(\mathbf{K})\psi_{\mathbf{K}\alpha l}(\mathbf{r}), \tag{4.3}$$

where $C_{\alpha l}(\mathbf{K})$ are weighting coefficients. For convenience the composite indices $\{\alpha, l\} \rightarrow n$ and $\{\alpha', l'\} \rightarrow m$ are used, where n and m now label all the individual basis functions in a given unit cell. The matrix elements of the above Hamiltonian are determined by

$$H_{nm} = \sum_{\mathbf{R}} e^{i\mathbf{K}\cdot\mathbf{R}} \int \phi_n^*(\mathbf{r} - \boldsymbol{\tau}_n) H \phi_n(\mathbf{r} - \boldsymbol{\tau}_m - \mathbf{R}) dv \tag{4.4}$$

and the overlap matrix is

$$S_{nm} = \sum_{\mathbf{R}} e^{i\mathbf{K}\cdot\mathbf{R}} \int \phi_n^*(\mathbf{r} - \boldsymbol{\tau}_n) \phi_n(\mathbf{r} - \boldsymbol{\tau}_m - \mathbf{R}) dv, \tag{4.5}$$

with the summations running over the whole crystal lattice. Evaluating (4.4) gives rise to integrals that involve basis functions expanded about two atomic positions and the potential part of the Hamiltonian centred around a third, and, for this reason, are commonly referred to as three-centre integrals. Assuming these summations are known or can be approximated then the eigenvalue problem (4.2) can be solved via the vanishing determinant:

$$\mathbf{det}(\mathbf{H} - E\mathbf{S}) = 0, \tag{4.6}$$

thus yielding the band energies at any value of $\mathbf{K}$.

Although this approach using non-orthogonal orbitals has been successfully employed in many studies, Slater and Koster proposed a simplification of this procedure in their classic paper. The atomic basis set is substituted for so called Löwdin functions, whose key feature is that they remain orthogonal to the neighbouring basis functions. As a result the integrals for the overlap matrix are trivially zero unless $n = m$, and thus $\mathbf{S}$ is equal to the unit matrix. Importantly these new functions retain the same symmetries as the atomic functions from which they are derived.

Another key feature of the Slater Koster TB method is the use of two centre

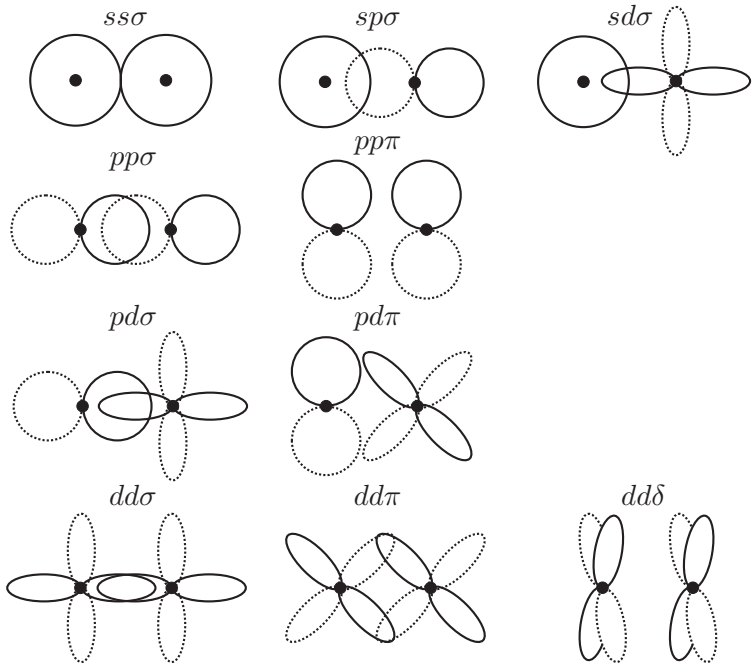

Figure 4.1: Schematic of orbital overlaps between the s,p and d states considered in this work. Positive and negative lobes are represented by solid and dashed lines.

integrals. The three centre integrals of equations 4.5 and 4.4 are simplified if one disregards potentials not situated on the atoms about which the basis sets are centred. In this case the system can be treated much in the same way as a diatomic molecule, where interactions are described in terms of an irreducible set of parameters that depend on the character of the orbitals and their orientation relative to the vector that connects them. The parameters are labelled by their angular momentum type and relative orientation defined by the angular momentum about their separating vector, with the notation $\sigma(m = 0)$, $\pi(m = 1)$ and $\delta(m = 2)$. The labelling scheme and orientations of these basic interactions are demonstrated in figure 4.1 for the 9 orbital s, p, d basis used in this work, with a total of 10 parameters required for a complete set. The matrix elements of any other orientation can be deduced from these base terms by angular dependencies that have been tabulated by many authors, but Podolskiy and Vogl [183] present compact expressions for these dependencies that are used here. The summations of equation 4.4 run over all atoms in the crystal, thus 10 unique parameters are required for each set of first, second, third, ... nearest neighbours. However, it is reasonable to expect the integrals to vanish rapidly as the spacing between orbitals is increased, thus only atoms in the immediate region will significantly impact the band structure of the system. In the code used in the work described

here third nearest neighbours are never considered, with second nearest neighbours only used when required. Integrals where $n = m$ are the so called onsite terms that are based on the energy levels of electrons in an isolated atomic state, with shifts incorporated due to the local environment.

In practice the energy parameters are fitted to the results of *ab initio* calculations or experiment to reproduce the electronic properties of known and representative systems as closely as possible and then assumed transferable in studies of new systems. The fittings used here are based on the work of Papaconstantopoulos [126] who performed a least-squares procedure on the results of *ab initio* augmented planewave (APW) calculations for Cobalt and Platinum in both the two and three centre approximation with orthogonal and non-orthogonal basis sets. The parameters used in this thesis are from the results of calculations using the 2 centre approximation with an orthogonal basis set.

4.1.1 Parameter fitting

The parameters deduced and tabulated by Papaconstantopoulos [126] are not sufficient for the purposes of this work for several reasons: the FCC Cobalt fit is not spin polarised — a crucial feature of this work; the tensile stress expected in the Cobalt layers after alloying will lead to deviations from the bulk Cobalt lattice; and a reasonable set of Cobalt-Platinum interaction parameters are required for the alloy interfaces. For this purpose APW calculations were performed on structures of interest to improve the elemental parameters and test a simple averaging procedure for the interspecies tight binding parameters. The scalar-relativistic full-potential APW calculations employed the LDA using a Perdew-Zunger exchange-correlation functional, a 666 Monkhorst-Pack [136] k-point sampling set, and angular momentum expansions up to ℓ=8. To account for variations in bond length in the systems modelled, we follow Harrison [184] who has deduced the dependencies of the interaction energy terms on the lattice spacing, finding

$$ss, sp, pp \propto \left(\frac{l}{l_{\text{orig}}}\right)^{-2}, \qquad sd, pd \propto \left(\frac{l}{l_{\text{orig}}}\right)^{-7/2}, \qquad dd \propto \left(\frac{l}{l_{\text{orig}}}\right)^{-5}, \quad (4.7)$$

where l is the new bond length and l_{orig} the original.

Bulk Cobalt

The first task is to change the paramagnetic FCC Cobalt parameters into two distinct sets representing spin up and spin down configurations, giving a total of 18 basis functions per atom. A well tested course of action is to vary the onsite energy terms of each channel to simply shift the band energies up and down as required. The bands were fitted by eye using both first and second nearest neighbours, and the best fit was found by altering not only the onsite energy terms but also the interaction parameters independently for both spin channels. It was found that good parameters can be obtained by altering the effective bond length of each channel independently, in a purely empirical fashion, to adjust the interactions strengths. However to simplify the parameter set an average was taken that still produces a good, although compromise band structure. In this case the interaction terms for both spin types are the same, a fact that becomes advantageous when considering the coupling between the two spin channels in the domain wall. The value of the effective spacing used is increased so that $l/l_{\text{orig}} = 1.01146$ and Papaconstantopoulos's original interaction terms, shown in table (4.1), are scaled via relationships (4.7). If it is assumed that the atom-atom distance in FCC Cobalt is 2.506Å then the effective original spacing, l_{orig}, is 2.477 Å, and this is the value used for all subsequent parameter fits. The paramagnetic onsite parameters of Papaconstantopoulos are shown in the first column of table (4.2), whilst the onsite energy shifts are shown in the next two columns. A fixed energy of 0.714 Ry is removed from the bands to align the Fermi energy with zero. The final TB band structures for majority and minority spin channels are compared to APW results in figures (4.2) and (4.3).

Tetragonal Cobalt

In the calculations it is assumed that the in-plane spacing of the Platinum substrate is dominant in determining the crystal structure, with the Cobalt contracting out-of-plane to compensate as detailed in Chapter 2. The Platinum atoms remain unaffected by the lattice change and thus Platinum-Platinum interactions are described well with the unaltered parameters of Papaconstantopoulos. So far parameters have been derived that are suitable for spin polarised bulk FCC Cobalt, and these parameters must be tested in a tetragonal environment

First NN	Energy integrals Ry	Second NN	Energy integrals Ry
$ss\sigma$	−0.09043	$ss\sigma$	−0.00337
$pp\sigma$	0.23748	$pp\sigma$	0.02849
$pp\pi$	0.00142	$pp\pi$	0.01099
$dd\sigma$	0.04213	$dd\sigma$	−0.00759
$dd\pi$	0.02976	$dd\pi$	0.00495
$dd\delta$	−0.00684	$dd\delta$	−0.00016
$sp\sigma$	0.13649	$sp\sigma$	0.00135
$sd\sigma$	−0.03806	$sd\sigma$	−0.01119
$pd\sigma$	−0.04069	$pd\sigma$	−0.01061
$pd\pi$	0.02797	$pd\pi$	0.01134

Table 4.1: Values of the interaction terms for both nearest neighbour and second nearest neighbour atoms in a paramagnetic FCC Cobalt system after Papaconstantopoulos [126]. Values used for calculations presented in this thesis have been altered as described in the main text.

Papaconstantopoulos Onsite energy Ry	Minority spin adjustment Ry	Majority spin adjustment Ry
1.12946	0.035	0.000
1.75262	−0.020	−0.030
0.60547	0.060	−0.055
0.60445	0.060	−0.055

Table 4.2: Onsite energy parameters for paramagnetic Cobalt as calculated by Papaconstantopoulos [126] (column 1), and spin-dependent shifts determined for ferromagnetic Cobalt (columns 2 and 3).

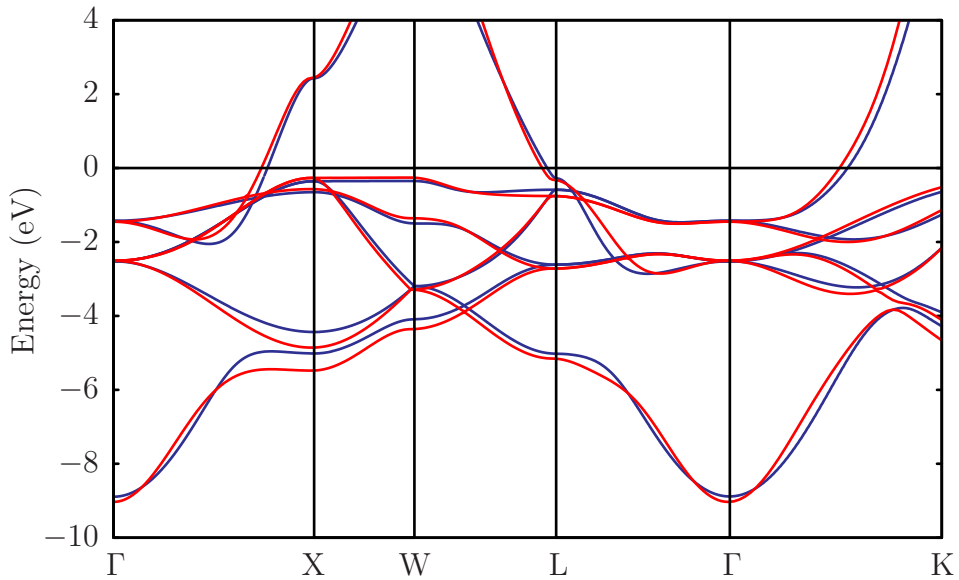

Figure 4.2: Band structure of bulk FCC Cobalt (**majority** spin). The blue line is the result obtained from APW calculations and the red is the TB fit.

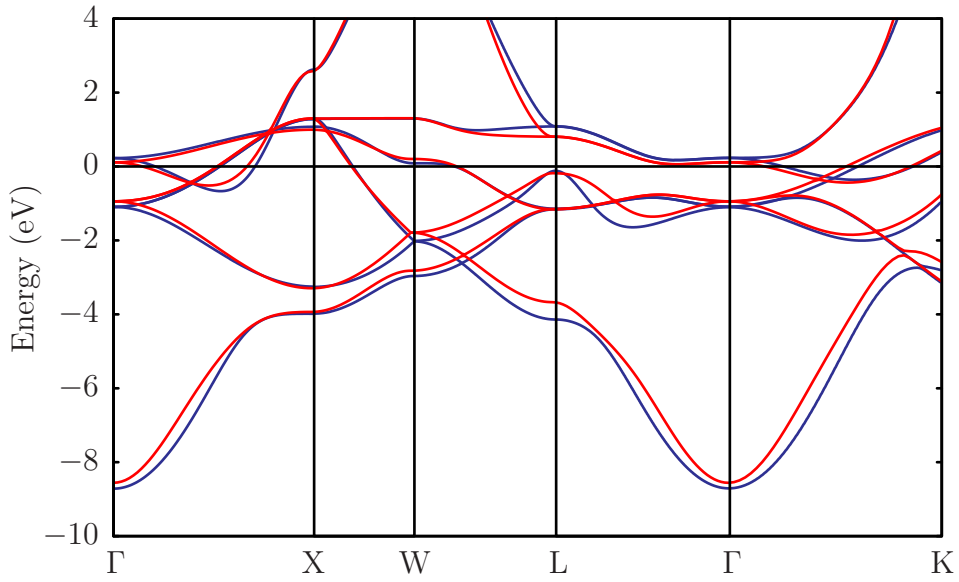

Figure 4.3: Band structure of bulk FCC Cobalt (**minority** spin). The blue line is the result obtained from APW calculations and the red is the TB fit.

to ensure their transferability to the problem at hand. Calculations of the energy bands were performed using the same onsite energies as in the bulk case, but with interactions scaled according to relationships (4.7), with a=2.775 Å, c=2.901 Å and l_{orig}=2.4766 Å. Because of these distortions the overlaps between the orbitals in the plane are reduced, making the second nearest neighbour interactions less significant. With this in mind these in-plane contributions are not included in the fit. In contrast, the out-of-plane second nearest neighbour terms become more significant and are included. This is convenient for the method presented in the following sections as the sample is divided up into slices that may only have nearest neighbour coupling with surrounding slices, whereas the intraslice Hamiltonian is arbitrary. These bands are compared to those obtained from APW calculations, and it is found that a Fermi energy shift from 0.714 Ry to 0.730 Ry is required to reproduce the alignment found in the *ab initio* calculations. The results are shown in figures 4.4 and 4.5.

Cobalt-Platinum interactions

Finally the interspecies Cobalt-Platinum interactions must be fitted, requiring a new set of parameters that describe the Cobalt-Platinum interactions in an alloyed system. A tetragonally distorted 1:1 ordered alloy was used, with lattice constants a=2.775 Å, c=3.407 Å stacked in a (100) style configuration.

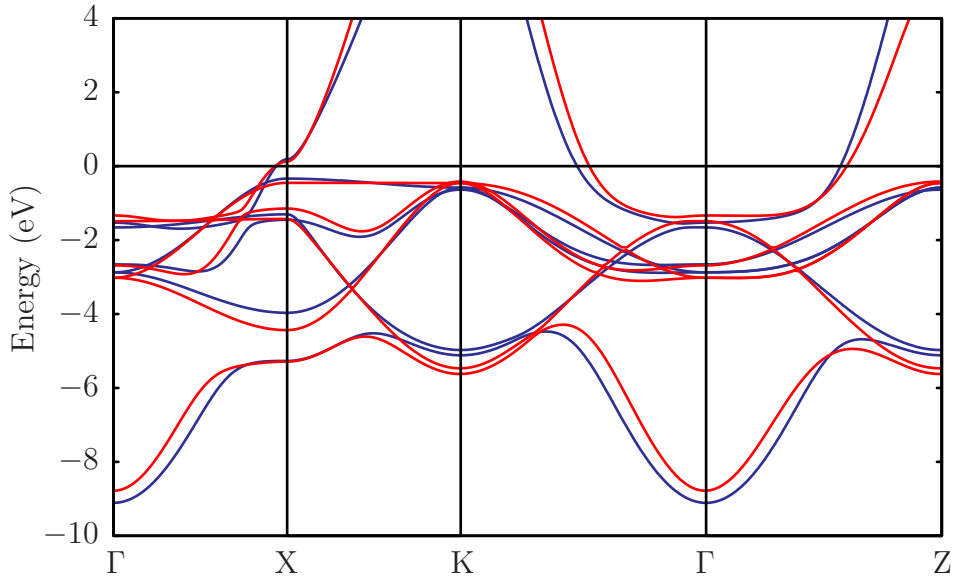

Figure 4.4: Band structure of tetragonal Cobalt (**majority** spin). The blue line is the result obtained from APW calculations and the red is the TB fit.

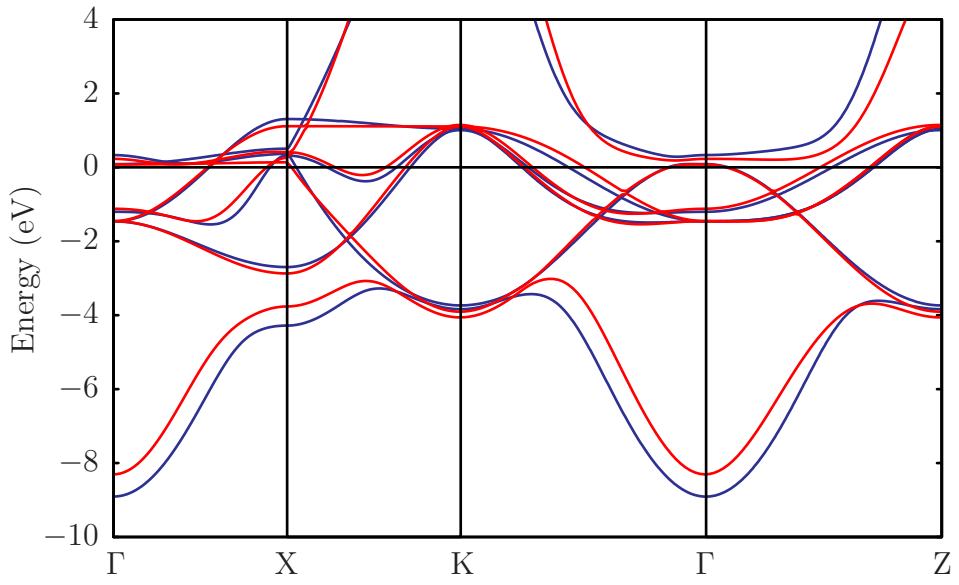

Figure 4.5: Band structure of tetragonal Cobalt (**minority** spin). The blue line is the result obtained from APW calculations and the red is the TB fit.

New interaction terms are obtained by taking the geometric mean of the existing scaled first nearest neighbour parameters, as used by other authors (e.g. reference [185]), whilst for simplicity the second nearest neighbours parameters are scaled as $2(p_{\mathrm{Co}}+p_{\mathrm{Pt}})/5$, where p is an interaction parameter, with this scaling determined empirically. The Fermi energy of Cobalt was 0.730 Ry, as used in the tetragonal system; and that of Platinum was 0.638 Ry, as determined by Papaconstantopoulos. Band structure diagrams are shown in figures 4.6 and 4.7. Although some deviation in bands exists from those of the APW method, particularly for bands with an out-of-plane component, it must be remembered that these interactions will play only a small part in the overall band structure of the trilayer systems, and the band structure in the direction of transport is generally much improved. Any further fine tuning results in a loss of generality of the parameters.

To recap, parameters have been derived for spin polarised Cobalt that apply to bulk, tetragonal and alloy situations, and have been shown to provide a suitable representation of the bands near the Fermi energy. These parameters will be used for transport calculations presented in the next sections.

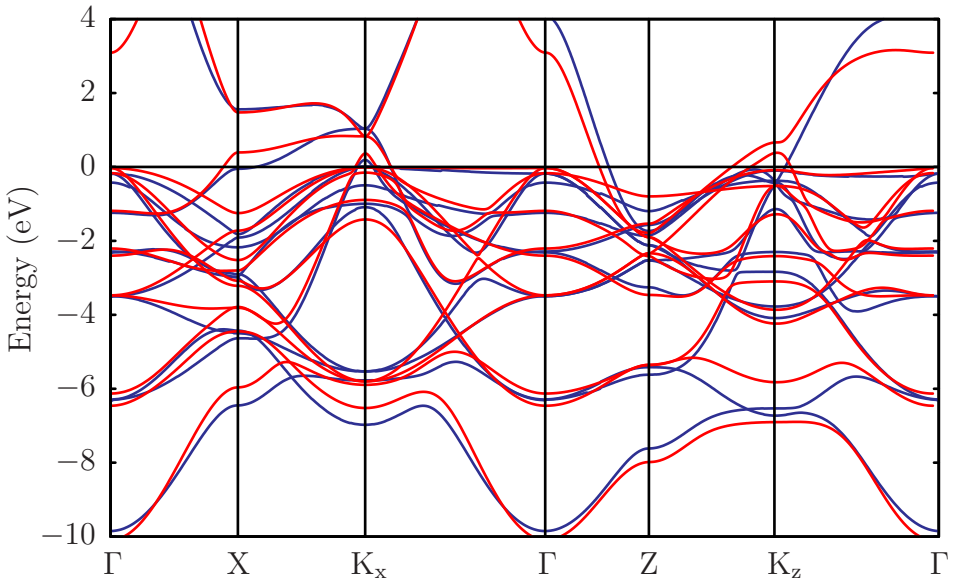

Figure 4.6: Band structure of tetragonal equiatomic Cobalt-Platinum alloy (**majority** spin). The blue line is the result obtained from APW calculations and the red is the TB fit.

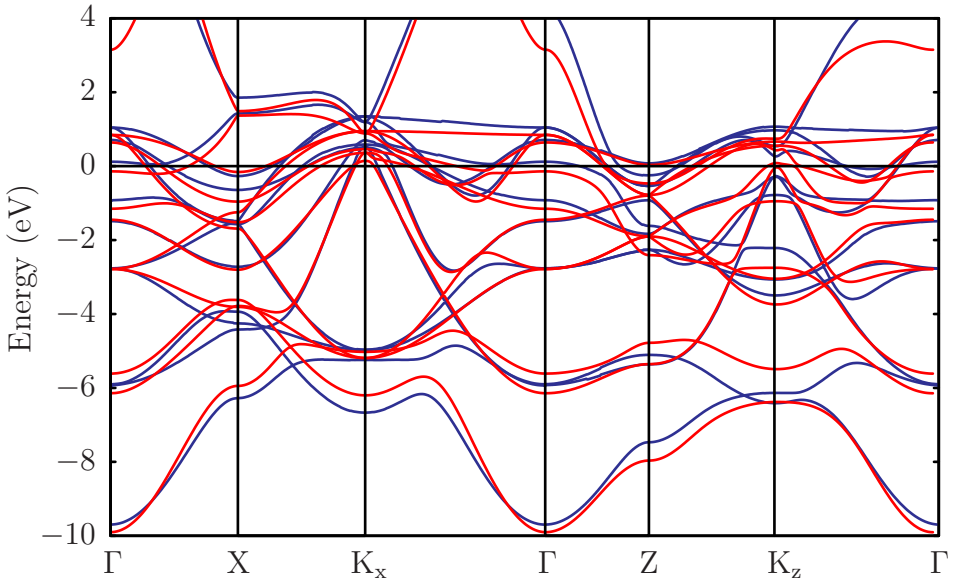

Figure 4.7: Band structure of tetragonal equiatomic Cobalt-Platinum alloy (**minority** spin). The blue line is the result obtained from APW calculations and the red is the TB fit.

4.2 Transport framework

In this section a framework for performing domain wall ballistic transport calculations is presented in which the band structure of the material is described in terms of the tight binding method outlined in the previous section. The work is based on the transmission matrix formalism of Landauer and Büttiker [186, 187, 188] that provides quantitative predictions of electron transport for realistic materials.

4.2.1 Landauer-Büttiker Theory

The theory of Landau and Büttiker has been used extensively in the field of ballistic transport calculations, e.g. [189, 190], and is used here to relate the Fermi energy eigenvectors of a crystalline solid to transport properties. This direct dependence on the crystalline environment makes the method ideal for studying the systematic changes in conductance that occur as the chemical composition of a system is altered. In this theory certain assumptions are made about the experimental setup: that of low voltage bias and low temperature. For illustration, a pseudo-1D example system is shown in figure 4.8 in which a single incoming electron $\mathfrak{I}$ has unit flux representing a single conductance channel in the left lead. The electron is transmitted ballistically through the scattering region (grey area) with probability T, and is accepted in the right hand lead, or is reflected back with probability R, thus account for all possibilities. The equation of Landauer and Büttiker that relates the current, I, to this transmission probability via a quantised conductance is

$$I = \frac{e^2}{h} T \Delta V, \tag{4.8}$$

where ΔV is the driving chemical potential difference. In a real system there are in general many scattering channels open in the leads and the above equation can be generalised. If open scattering channels are labelled i and j for the left and right channels respectively, then the transmission probability between the states is T_{ji}, with the possibility of scattering between channels that were independent in the leads. The conductance is $\Gamma = I/\Delta V$, and we define a transmission matrix t as $T_{ji} = |t_{ji}|^2$ that will be determined later in the work. By these definitions

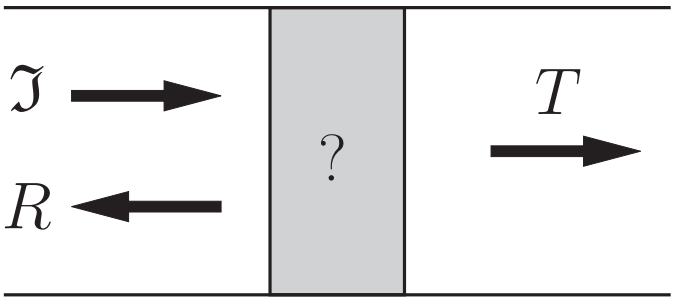

Figure 4.8: Two semi-infinite leads are separated by an unspecified scattering region shown in grey. The incoming electron $\mathfrak{I}$ is of unit flux and is transmitted through the scatterer with probability T, or reflected with probability $R = 1 - T$.

the total conductance of the system is given by

$$\Gamma = \frac{e^2}{h} \sum_{ij} T_{ij} = \frac{e^2}{h} \text{Tr } tt^\dagger. \tag{4.9}$$

These equations are useful for systems containing a finite number of scattering channels in the leads, such as narrow wires where the transverse modes can easily be evaluated. For larger systems such as bulk or multilayers a reciprocal space approach is usually employed, so that the transmission properties are averaged over the Brillouin zone. To maintain consistency with the previous section, in the following the current flows along the $\perp$ $\{x\}$ direction, whilst the coordinates of the cross-section perpendicular to the current is represented by the symbol $\parallel$ $\{y, z\}$. Assuming that the system is periodic in $\parallel$ so that $\mathbf{K}_\parallel$ is a good quantum number, the conductance becomes

$$\Gamma = \sum_{\mathbf{K}_\parallel} \Gamma(\mathbf{K}_\parallel) = \frac{e^2}{h} \sum_{\mathbf{K}_\parallel} \sum_{ij} T_{ij}(\mathbf{K}_\parallel). \tag{4.10}$$

In the work considered here the slab is of a finite thickness, but infinite width resulting in a 1D Brillouin zone summation. However this method can be used for both bulk materials (2D BZ) and finite cross-section wires via equation 4.9 where the Brillouin zone concept is not required.

Thus a scattering framework is required in terms of our tight binding method that enables the evaluation of the transmission matrix that enters the expressions for the conductance. One such framework outlined by Sanvito *et al.* [190] in terms of a Green function formalism is suitable for our purpose here. The first stage is to calculate the Green function of right and left semi-infinite leads that will be

used to sandwich the scattering region.

4.2.2 Green function of a semi-infinite lead

Sanvito *et al.* initially consider an infinitely long wire made up of identical slabs of finite cross-section, so that the direction of current flow, x (z in Sanvito [190]), is perpendicular to these slabs as shown in the top diagram of figure 4.9. Here each slice is described by a Hamiltonian matrix H_0 and coupled to its neighbours by inter-slice hopping matrices H_1 and H_{-1}. These Hamiltonian elements are quite general and the slices can refer to individual atoms, single or multiple layers, or even more complicated units. The infinite tridiagonal Hamiltonian that describes this system is thus of the form

$$H = \begin{pmatrix} \ldots & \ldots & \ldots & \ldots & \ldots & \ldots & \ldots & \ldots \\ \ldots & H_{-1} & H_0 & H_1 & 0 & 0 & 0 & \ldots \\ \ldots & 0 & H_{-1} & H_0 & H_1 & 0 & 0 & \ldots \\ \ldots & 0 & 0 & H_{-1} & H_0 & H_1 & 0 & \ldots \\ \ldots & 0 & 0 & 0 & H_{-1} & H_0 & H_1 & \ldots \\ \ldots & \ldots & \ldots & \ldots & \ldots & \ldots & \ldots & \ldots \end{pmatrix}. \tag{4.11}$$

The Schrödinger equation of this system is then

$$H_0\psi_x + H_1\psi_{x+1} + H_{-1}\psi_{x-1} = E\psi_x, \tag{4.12}$$

where ψ_x is a column vector and the indices $x+1$ and $x-1$ refer to the neighbours of slice x. These wave functions will be written in terms of our basis set of atomic-like orbitals, with a total of 18 basis functions per atom in a slice after accounting for spin, and this number is labelled M. A Bloch equation is introduced for the slices of the form

$$\psi_x = N_{K_\perp} e^{iK_\perp x} \phi_{K_\perp}, \tag{4.13}$$

where $\phi_{K_\perp}$ is an atomic basis vector of size M; $N_{K_\perp}$ is an arbitrary normalisation constant; and $K_\perp$ is the component of $\mathbf{K}$ perpendicular to the slices. This expression can be used in equation (4.12) to yield a secular equation of form 4.6. In conventional band structure calculations the objective is to calculate the allowed energy states at a given location in k-space, of which there are M such states.

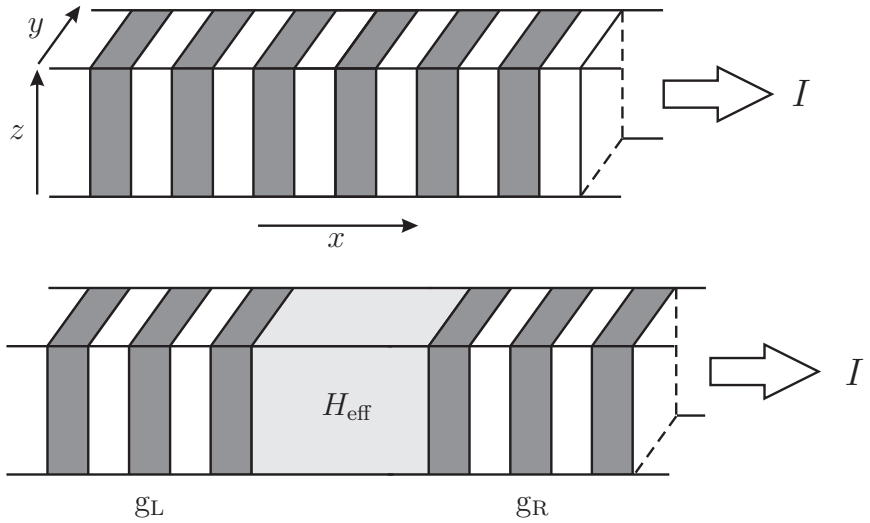

Figure 4.9: [*top*] Illustration of system considered by Sanvito *et al.*. The device has finite cross-section in the yz plane, and is divided up into slices orientated in this plane. The identical slices are stacked without termination in the x direction, which is also the direction of current flow. Interslice interactions are nearest neighbour only and described by hopping matrices H_1 and H_{-1}. The alternate shading is for illustration only. [*bottom*] Illustration of a full system consisting of two semi-infinite leads sandwiching an "active" region (light grey shading). Green functions are derived for the semi-infinite leads and are coupled to the effective Hamiltonian of the central region via a Dyson equation.

Here however we seek to calculate the transport properties at the Fermi energy, and as such require a method that allows us to fix the energy of the system and determine the eigenvectors and $K_\perp$ that correspond to open channels.

These $K_\perp$ values and the eigenvectors $\phi_{K_\perp}$ can be obtained by mapping the problem onto an equivalent eigenvalue problem of the form

$$\begin{pmatrix} -H_1^{-1}(H_0 - E) & -H_1^{-1}H_{-1} \\ I & 0 \end{pmatrix} \begin{pmatrix} \phi_{K_\perp} \\ e^{-iK_\perp}\phi_{K_\perp} \end{pmatrix} = e^{iK_\perp} \begin{pmatrix} \phi_{K_\perp} \\ e^{-iK_\perp}\phi_{K_\perp} \end{pmatrix}. \tag{4.14}$$

This equation yields 2M solutions with the M component column eigenvectors taken from the top half of the eigenvectors of this equation, whilst the equivalent values of $K_\perp$ are extracted from the eigenvalues. At first it may appear that we have twice as many solutions as required, but because of the reflection symmetry along the x axis, any mode travelling in the positive x direction with group velocity $v_{K_\perp}$ will have a partner wave travelling in the opposite direction with a negative group velocity. These two waves are denoted by the convention $K_\perp$ = K for $v_K > 0$ and $K_\perp = \bar{K}$ for $v_{\bar{K}} < 0$. These travelling solutions represent the so-called open channels of the system, in which the electron wave function propagates unperturbed through the lattice. However there exists another set of solutions for which $K_\perp$ has a large imaginary part, and thus represent a decaying or closed channel. Similarly to the open channels they can be paired into "right" and "left" solutions depending on the sign of this imaginary component — so called left and right decaying solutions. These two sets of solutions are thus labelled K_l consisting of right-travelling and right-decaying solutions and their counterparts $\bar{K}_l$ that consist of left-travelling and left-decaying solutions that make up the 2M solutions of equation (4.14). Practically, these solutions need to be sorted and for decaying wavefunctions this is done by trivially comparing the sign of the imaginary component, whereas for travelling waves the group velocity is required, and given by

$$v_K = \frac{1}{\hbar}\frac{\partial}{\partial K}\langle\psi_K|H|\psi_k\rangle = \frac{i}{\hbar}\phi_K^\dagger(H_1 e^{iK} - H_{-1}e^{-iK})\phi_k. \tag{4.15}$$

This procedure enables one to obtain the eigenfunctions and K states at an energy E. The next step is to calculate the Green function of this system. It can be

shown that the Green function of the infinite slab [190] is given by

$$g_{xx'} = \begin{cases} \sum_{l=1}^{M} \phi_{K_l} e^{iK_l(x-x')} \widetilde{\phi}^{\dagger}_{K_l} \mathcal{V}^{-1}, & x \geq x' \\ \sum_{l=1}^{M} \phi_{\bar{K}_l} e^{i\bar{K}_l(x-x')} \widetilde{\phi}^{\dagger}_{\bar{K}_l} \mathcal{V}^{-1}, & x \leq x'. \end{cases} \tag{4.16}$$

The vectors $\widetilde{\phi}^{\dagger}_{K_l}$ and $\widetilde{\phi}^{\dagger}_{\bar{K}_l}$ are the duals of the vectors ϕ_{K_l} and $\phi_{\bar{K}_l}$ respectively, with the definition

$$\widetilde{\phi}^{\dagger}_{K_l} \phi_{K_l} = \widetilde{\phi}^{\dagger}_{\bar{K}_l} \phi_{\bar{K}_l} = I, \tag{4.17}$$

and the matrix $\mathcal{V}$ is given by

$$\mathcal{V} = \sum_{l=1}^{M} H_{-1} \left[\phi_{K_l} e^{-iK_l} \widetilde{\phi}^{\dagger}_{K_l} - \phi_{\bar{K}_l} e^{-i\bar{K}_l} \widetilde{\phi}^{\dagger}_{\bar{K}_l} \right]. \tag{4.18}$$

With these definition the Green function of a system corresponding to the top panel of figure 4.9 can be obtained.

Using equation 4.14 the band structure along $0 \rightarrow$ X of a 3 Cobalt atom thick infinite slab is demonstrated in figure 4.10. Also plotted in the same figure is the equivalent density of states obtained in the usual way from the imaginary part of Green function 4.16.

The next step is to calculate the Green function of the two semi-infinite leads as seen in figure 4.9. The left lead is terminated at $x = x_0 - 1$ so that the first missing slice is at x_0. It is possible to determine a wavefunction from the condition that the Green function vanishes at x_0, resulting in the equations

$$g_L = \left[I - \sum_{l,h} \phi_{\bar{K}_h} e^{-i\bar{K}_h} \widetilde{\phi}^{\dagger}_{\bar{K}_h} \phi_{K_l} e^{iK_l} \widetilde{\phi}^{\dagger}_{K_l} \right] \mathcal{V}^{-1}, \tag{4.19}$$

for the left lead and

$$g_R = \left[I - \sum_{l,h} \phi_{K_h} e^{iK_h} \widetilde{\phi}^{\dagger}_{K_h} \phi_{\bar{K}_l} e^{-i\bar{K}_l} \widetilde{\phi}^{\dagger}_{\bar{K}_l} \right] \mathcal{V}^{-1} \tag{4.20}$$

for the right lead.

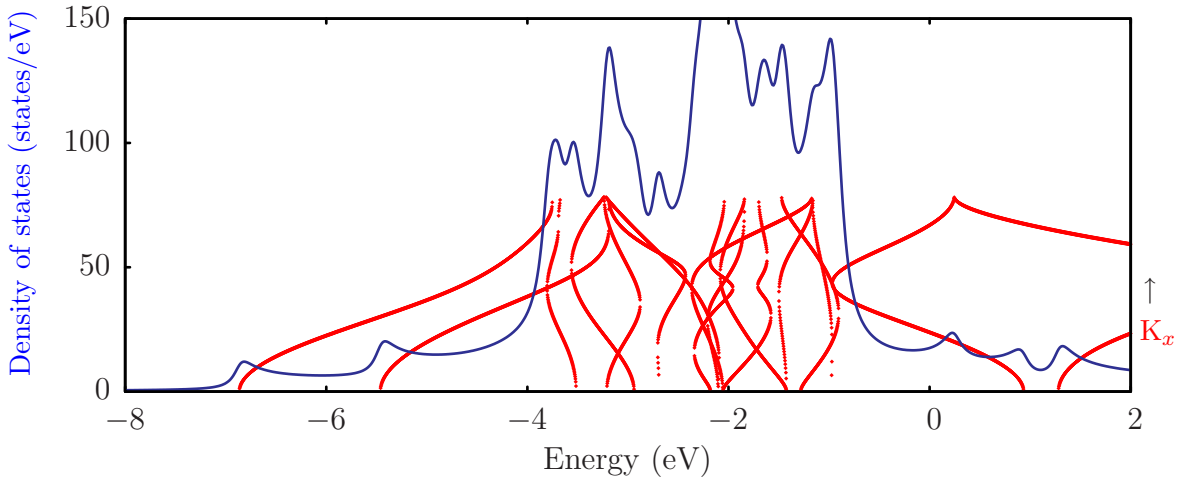

Figure 4.10: Band structure (red points) and corresponding density of states (blue line) of system consisting of 3 tetragonal Cobalt layers. The value of K_y was set to a fixed value of 0, and the allowed values of K_x are calculated as a function of energy. The density of states is thus not averaged over the reciprocal space, but serves to illustrate that the Green function of the lead is functioning as expected.

4.2.3 The active region and the recursive Green function method

Now that the Green function of both left and right semi-infinite leads have been obtained, the details of the scattering region must be specified. The active region is built up from perpendicular-to-the-current layers with nearest neighbour interactions, in a similar fashion to the leads. However there is no constraint that the slices must be identical. In this case the whole Hamiltonian must be considered, and the dimensions of the tridiagonal matrix grows with the number of slices in the active region. Given the tridiagonal nature of this matrix makes a Gaussian elimination method easy to implement, and the method is often referred to as the recursive Green function method.

This block-tridiagonal Hamiltonian contains N×N block elements with N−2 slices in the scattering region and the additional two elements describing couplings to the left and right leads. Elements are eliminated in the usual fashion, with the Hamiltonian after l operations given by:

$$H_{ij}^{(l)} = H_{ij}^{(l-1)} + \frac{H_{il}^{(l-1)} H_{lj}^{(l-1)}}{E - H_{ll}^{(l-1)}}. \tag{4.21}$$

After this procedure has been performed N−2 times an effective Hamiltonian is obtained:

$$H_{\text{eff}}(E) = \begin{pmatrix} H_L(E) & H_{LR}(E) \\ H_{RL}(E) & H_R(E) \end{pmatrix}. \tag{4.22}$$

This 2M×2M matrix encompasses the scattering properties of the central region and coupling to the leads, with superfluous degrees of freedom eliminated.

4.2.4 Coupling the system

All that remains is to bring together the calculated lead surface Green functions and the reduced Hamiltonian of the active region to produce a Green function for the system. This is accomplished via a Dyson equation of the form:

$$G(E) = \left[g(E)^{-1} - H_{\text{eff}}(E)\right]^{-1}, \tag{4.23}$$

where

$$g(E) = \begin{pmatrix} g_L(E) & 0 \\ 0 & g_R(E) \end{pmatrix}. \tag{4.24}$$

4.2.5 The t matrix

The final stage is to extract the required t matrix from the known Green function. This is achieved by using a projector operator to project out the wavefunction from the Green function; the projector

$$P_l(x') = \mathcal{V}\phi_{K_l}\frac{e^{ik_l x'}}{\sqrt{v_l}} \tag{4.25}$$

projects a Green function $g_{xx'}$ from the right, to yield the wave function ψ_x at position x for $x \geq x'$. An equivalent exists for $x \leq x'$. Thus for Green function G_{L0} the projector can be used to equate the extracted wavefunction to that

obtained via the transmission coefficient matrix, t, so that:

$$\sum_h \frac{t_{hl}}{\sqrt{v_h}} e^{ik_h L} \phi_{K_h} = G_{L0} P_l(0). \tag{4.26}$$

A simple rearrangement gives

$$t_{hl} = \widetilde{\phi}^{\dagger}_{K_h} G_{L0} \mathcal{V} \phi_{K_l} \sqrt{\frac{v_h}{v_l}} e^{-ik_h L}, \tag{4.27}$$

thus the derivation is complete and the conductance is obtained via equation (4.10). Further details of the method can be found in [190].

4.3 Transport calculations

The objective of this work is to evaluate the ballistic transport properties of ferromagnetic domain walls in Pt/Co/Pt trilayers. A framework suitable for such a study was outlined in the previous section. Before the results of such calculations are presented, attention is given to the single domain transport properties of a range of trilayer structures. Because the Fermi energies produced by the parameterisation may differ from the true values, the Fermi energies of these systems must be found initially. Unless otherwise stated, the structures used here correspond to the relaxed lattices that were described in Chapter 2, with the spacing of bulk Platinum used in the plane of a layer, while the interlayer spacing is relaxed to conserve the atomic volumes.

4.3.1 Fermi energy adjustments

The Fermi energies of the systems of interest must be determined for the purposes of the transport calculations presented later in this Chapter. Thus the condition

$$N = \int_{E_{\min}}^{E_f} \rho(E) \, \mathrm{d}E \tag{4.28}$$

must be satisfied, where N is the total number of electrons in an unit cell. For this integral a simple trapezoidal scheme was employed, starting below the deepest

valence band and progressing until the above self-consistency condition is met. Because of the low dispersion at band edges the density of states is troublesome to integrate owing to the discontinuities that arise at these points, thus a large number of energy points, N_e, are required to accurately perform this task. To overcome this numerical problem a small imaginary component was added to the energy to provide Gaussian smoothing of the density of states curve, and consequently facilitate the numerical integration. This must be balanced with inaccuracies introduced to the Fermi energy location by the Gaussian spreading. The imaginary energy used in these calculations was 2×10^{-4} Ry, which provided a good compromise between these factors. For the systems tested, 1024 energy points were found sufficient to converge the Fermi energy location with this imaginary energy value. The same degree of convergence was achieved for a system with an imaginary energy of 2×10^{-6} Ry with 16384 points — a considerable saving.

The density of states was averaged over the Brillouin zone, thus consideration must be given to the k-point set used. Systems were tested with $N_K = 2$, 4, 8, 16 and 32 points in the irreducible Brillouin zone and very little variation was found between the results. In finding the Fermi energy 8 k-points were used in the following work.

4.3.2 Single domain conductances

The conductance of bulk FCC Cobalt was approximated by a 30 layer slab of Cobalt with the bulk Cobalt spacings. Only first nearest neighbours interactions were used out-of-plane as the broken crystal symmetry is no longer present. The Fermi energy was set to that of bulk FCC Cobalt. The conductance per unit area $\Gamma/A_\perp$ was calculated using 64 k-points and found to be 1.45×10^{15} $\Omega^{-1}m^{-2}$. Sabirianov *et al.* [191] give the results of transport calculations in a fully *ab initio* LMTO framework and deduce the value 1.59×10^{15} $\Omega^{-1}m^{-2}$ for transport in the (100) plane. The agreement can be considered relatively good, with differences due to both edge effects and general limitations of the TB method, especially given that only a first nearest neighbour description is used here.

Transport in these layers are dominated by the *d*-bands that exhibit a large density of states at the Fermi energy. As an example, the system $Pt_3Co_3Pt_3$ has

a band-resolved Fermi energy density of states of s - 3.7%, p - 2.9%, and d - 93.6%. This dominating contribution from the d bands is common to all systems tested.

Figure 4.11 shows results of conductance calculations for a system consisting of 3 Cobalt layers sandwiched between two Platinum sheets each consisting of an equal number of layers, n. Also shown in the inset is the Fermi energy shift that satisfies charge neutrality as detailed previously. As the Platinum layers grow in thickness the Fermi energy change converges on a stable value, that is shown as $\Delta E_f = 0$ in the plot. This value lies -6.4×10^{-3} Ry below the Fermi energy determined by the TB parameters alone. For systems with n > 11 this converged value of the Fermi energy was used. Despite small deviations due to finite size effects a clear linear increase is found in the conductance as the number of Platinum atoms is increased, implying that a conductance value of $1.2{\times}10^{-4}$ Ω^{-1} can be directly attributed to each Platinum layer.

Shown in figure 4.12 is the conductance of a $Pt_5Co_nPt_5$ system as a function of n, and also the Fermi energy shifts used in each calculation. The Fermi energy adjustment required is fairly constant for all systems studied, thus for slabs with n>12 the value of this shift is equal to that of the n=12 system, shown as zero in this plot but lies -1.0×10^{-2} Ry below the parameterised Fermi energy. These fairly constant shifts are in contrast those documented above where the Platinum layer thickness is varied. The difference is explained by the relative dispersion of the bands that populate the Fermi energy region of both metals. The narrower d-bands of the Platinum are more susceptible to crossing the Fermi energy as the process of band narrowing occurs in the thinner films, thus altering the number of states that must be corrected by the energy shift. In terms of transport, above n=5 a linear relationship was found with increasing layer thickness, implying a conductance of $6.3{\times}10^{-5}$ Ω^{-1} per Cobalt layer. Below 5 layers, effects relating to the thinness of the Cobalt layer increase the conductance above that of the linear portion of the plot.

4.3.3 Transport across domain walls

The domain wall width is dependent on material parameters and typical domain walls are of the order of 10–100 nm wide. As has been mentioned in previous

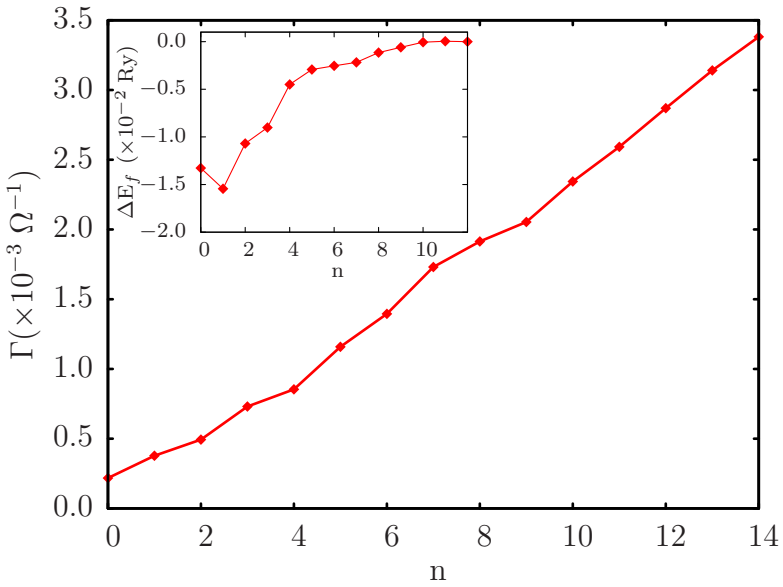

Figure 4.11: Conductance of a $Pt_nCo_3Pt_n$ system as a function of n. [*inset*] Fermi energy shift relative to the n$\rightarrow \infty$ limit required for charge neutrality versus n.

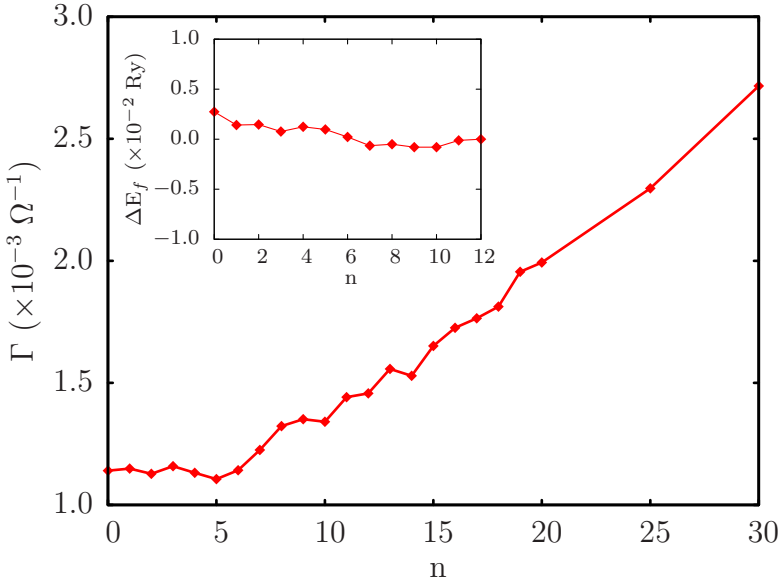

Figure 4.12: Conductance of a $Pt_5Co_nPt_5$ system as a function of n. [*inset*] Fermi energy shift relative to the n$\rightarrow \infty$ limit required for charge neutrality versus n.

chapters it is possible to artificially tailor the wall width by techniques such as placing geometric constrictions in the material, whereby domain walls of atomic width have been created. In the limit that the magnetisation change between two domains is abrupt, with no relaxation of spins, an electron must reverse its spin instantaneously when traversing the abrupt domain wall. It is reasonable to expect that this represents one extreme of transport behaviour, with the greatest number of reflection events producing the largest MR effect. The abrupt domain wall can be modelled simply by swapping the coupling of the spin channels appropriately, aided by the fact that the coupling Hamiltonians are identical for both spin up and down.

For comparison with work in the literature, van Hoof [192] performed such an abrupt domain wall calculation using an LAPW method on bulk Cobalt, with transport perpendicular to the FCC (111) plane. The total single domain conductance per unit area was found to be 1.53×10^{15} $\Omega^{-1}\mathrm{m}^{-1}$, whilst in the presence of an abrupt domain wall this was reduced to 0.51×10^{15} $\Omega^{-1}\mathrm{m}^{-2}$, or 33% of bulk. In the calculations here on the (100) plane the conductance per unit area was found to be 1.45×10^{15} $\Omega^{-1}\mathrm{m}^{-2}$ using a 30 Cobalt atom thick slab of material as an approximation to the bulk state. Introducing an abrupt domain wall was found to change the conductance per unit area to 0.44×10^{15} $\Omega^{-1}\mathrm{m}^{-2}$, or 31% of the bulk value.

4.3.4 Domain wall rotation

To model more realistic domain walls, it is assumed that the local spin degree of freedom in each slice was rotated by an amount θ about a vector $\mathbf{u}$. The spinor rotation matrix employed here is defined as

$$U(\theta,\mathbf{u}) = \begin{pmatrix} \cos\frac{\theta}{2} - iu_z\sin\frac{\theta}{2} & (-iu_x - u_y)\sin\frac{\theta}{2} \\ (-iu_x + u_y)\sin\frac{\theta}{2} & \cos\frac{\theta}{2} + iu_z\sin\frac{\theta}{2} \end{pmatrix}, \tag{4.29}$$

with the unrotated magnetisation lying along the z axis. If the Hamiltonian of this unrotated system is H then the new rotated Hamiltonian, H_θ is given by

$$H_\theta = U^\dagger(\theta,\mathbf{u})HU(\theta,\mathbf{u}) = U^\dagger(\theta,\mathbf{u}) \begin{pmatrix} H_u & 0 \\ 0 & H_d \end{pmatrix} U(\theta,\mathbf{u}). \tag{4.30}$$

Thus through rotating the spin direction independently in each slice of the active region and performing the decimation procedure, the effective Hamiltonian of a region containing a domain wall can be obtained.

4.3.5 Domain wall transport

In this section the results of ballistic transport calculations on Cobalt Platinum trilayers are documented. A linear domain wall profile given by $\theta = \pi x/d$ has been used in the initial calculations, where the domain wall width, and for this specific profile, the active region is d. Both Bloch and Néel type domain walls have been treated by altering the rotation vector $\mathbf{u}$, and it is found that the ballistic transport properties are identical. In figure 4.13 the conductivity as a percentage of the bulk value is shown for a 30 layer thick Cobalt system with bulk Cobalt spacing and Fermi energy as a function of the linear domain wall width. For narrower walls ($d < 5$ nm) the domain wall is found to produce an increasingly large impedance to current flow. As described previously, the abrupt domain wall reduces the conductivity to 31% of the single domain value, but this is found to rapidly diminish as the domain wall is lengthened. In bulk Cobalt the domain wall width is estimated to be 15 nm, and at this value the conductance is 99.4% of the bulk value implying that the domain wall is traversed nearly adiabatically in this system, consistent with other ballistic transport studies on bulk Cobalt, e.g. van Hoof [192] who found a conductance ratio of 99.5%. As expected similar calculations on homogeneous Platinum layers showed no domain wall resistance.

Now we present studies of mixed Cobalt Platinum trilayer systems. As a crude approximation one might expect the magnetic Cobalt to act as the source of domain wall resistance, whilst the usually spin-degenerate Platinum would present a diluting effect. However, the LKKR calculations show that this cannot strictly be that case as the interfacial Platinum atoms gain a moment from interactions with Cobalt. Indeed, any deviations from this source/dilution effect must arise as a result of interactions between the two species, and this will be commented upon with the subsequently presented results. Figure 4.14 shows the conductance of a domain wall versus the wall width for $Pt_nCo_3Pt_n$ systems as a percentage of the single domain conductance, for n = 0, 3, 5, 10. In the narrow/abrupt domain wall regime the same large conductance drop is found in these systems as in the bulk

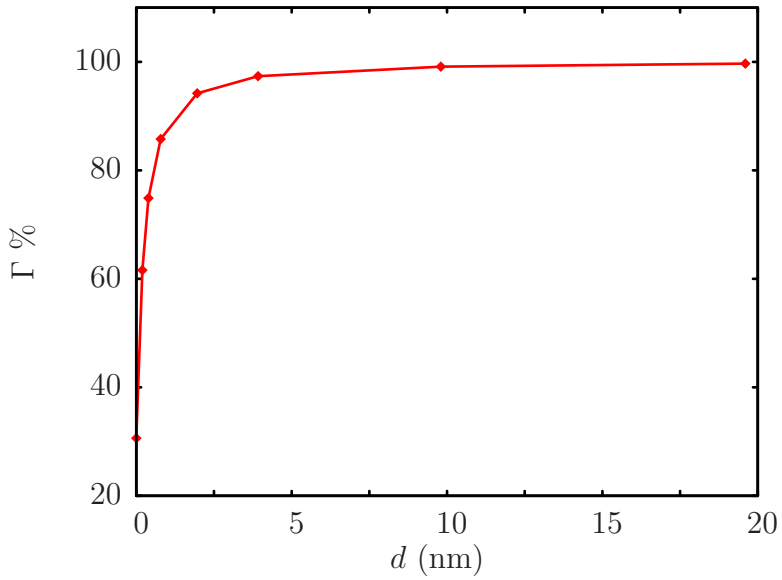

Figure 4.13: Conductance of a 30 layer Cobalt sheet with bulk FCC Cobalt spacing and Fermi energy as a function of the domain wall width d.

Cobalt, with a rapid decay occurring as the wall approaches the abrupt limit. However the diluting effect of the natively spin unpolarised Platinum atoms can be seen as the relative contribution from the domain wall is lessened with increasing n. To explore this phenomenon further the inset of figure 4.14 displays the relative conductivity of an abrupt wall for systems with different values of n. At n=0 the abrupt conductance is 19.8% of the background, and as n$\rightarrow \infty$ we assume that $\Gamma \rightarrow$100%. If the Cobalt layer acts as a constant source of resistance and the Platinum only dilutes this effect then one would expect the resistance behaviour to scale simply with respect to the number of Platinum layers. Assuming the 2:1 single domain conductivity ratio found previously, and the conductivity limits given above, this scaling function can be determined and is shown by the dashed line in the inset figure. Clear deviations between this curve and the calculations are found. These can be attributed to finite size effects, and also suggest that the Platinum layers contribute to the domain wall resistance, implying that a simple dilution model may be inappropriate for these interacting systems.

As the domain wall width d is increased the conductance is found to vary smoothly in these systems, with the exception of the Co_3 case where the decreased number of electrons in an unit cell results in the opening of only a small number of conduction channels at the Fermi energy. As a result the transport properties are particularly sensitive to the conductance of a single channel, and the possible closing of a channel by the domain wall. This is manifested in the results as

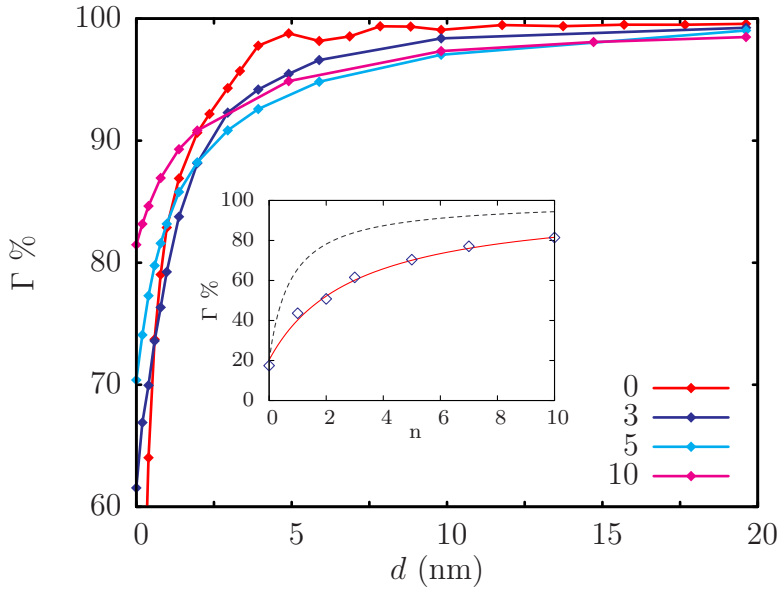

Figure 4.14: Conductance of a domain wall as a percentage of the bulk value. The data is presented as a function of the domain wall width, d, for $Pt_nCo_3Pt_n$ systems. The value of n is shown in the caption. [*inset*] Percentage conductance of an abrupt domain wall in these systems as a function of n.

weak conductance oscillations that are visible between $d \approx 3$ nm and $d \approx 12$ nm. It can be argued that these exact quantum effects are unlikely to be found experimentally as they are extremely sensitive to conditions at the Fermi energy.

Unusually, the ordering of the relative conductance by n observed for narrow domain walls does not persist in the results as d is increased to values approaching those of bulk Cobalt. To understand this behaviour a discussion of the limits of these calculations will be given with respect to the domain wall resistance. Based on intuitive reasoning one would expect the influence of a domain wall on the transport properties to bear some correlation with the degree of spin-polarisation in the material, so that strong ferromagnets experience a greater effect than materials with only small induced polarisations, such a Platinum in the presence of Cobalt. However in the ballistic model used here the conductivity is dependent on the coupling of states at the Fermi energy with particular values of transverse momentum. In this case it is not automatically the case that largely spin polarised bands will contribute any more to the resistance than bands with a small, but finite, splitting. The Cobalt slab acts as a spin-polarised source and as found in the LKKR calculations the induced polarisation decays away from the Cobalt Platinum interface. Nevertheless even at the furthermost Platinum atom there exists a small polarisation of spin that breaks the degeneracy of states. Thus in

these purely ballistic calculations a domain wall resistance contribution may also be expected from these atoms due to this sensitivity to the band structure.

Further to the above explanation of this change of ordering there is another aspect of these calculations that must be considered. The ordering is seen to change and at first appears to be in contrast to the expected behaviour. Given that there is some ambiguity in the precise location of the Fermi energy due to the tight binding method employed in this work, the energy dependence of the conductance is now investigated. Shown in figure 4.15 are the transport properties of a domain wall ($d = 20$ nm) in a Co_3 slab within an energy range of $5{\times}10^{-3}$ Ry of the determined Fermi energy, that is, within an interval of the order of the uncertainty in the parameterisation. In the main plot the change in fractional conductance from bulk due to the domain wall is shown, and it is clear that a large range of values exist within this modest energy window. At $E \approx -2 \times 10^{-3}$ Ry a large peak is found in the conductivity difference indicating that the domain wall is reflecting a significant number of states at this energy. Shown in the inset is the behaviour of the conductivity with respect to the domain wall width at this value of the energy. It can be seen that eventually, at long domain wall widths, an adiabatic traversing of the wall occurs, however at the 20 nm width a significant resistance exists. In the main plot a conductivity difference range spanning two orders of magnitude is found in the energy dependence, indicating that the transmission of electrons is highly dependent on the specifics of the available states in the leads. The same set of calculations were repeated for an abrupt domain wall, and the results are shown in figure 4.16. Here the conductance properties vary smoothly with respect to the electron energy, which is attributed to the averaging of the properties over the increased number of reflected states.

The realistic domain wall conductance variations detailed above are not as severe in larger systems, where the increased number of total conducting states smooths out transport properties, although significant variations are still found in $Pt_5Co_3Pt_5$ for the same domain wall width and energy range, shown in figure 4.17. The results clearly demonstrate that the transport properties of bulk length domain walls in the thin film systems are highly sensitive to the details of the bands at the Fermi energy. In contrast, for narrower domain walls where the resistance change is much greater, it was found that the value of the conductance is significantly more robust to changes in the Fermi energy, which explains the consistent trends found in these abrupt domain wall systems.

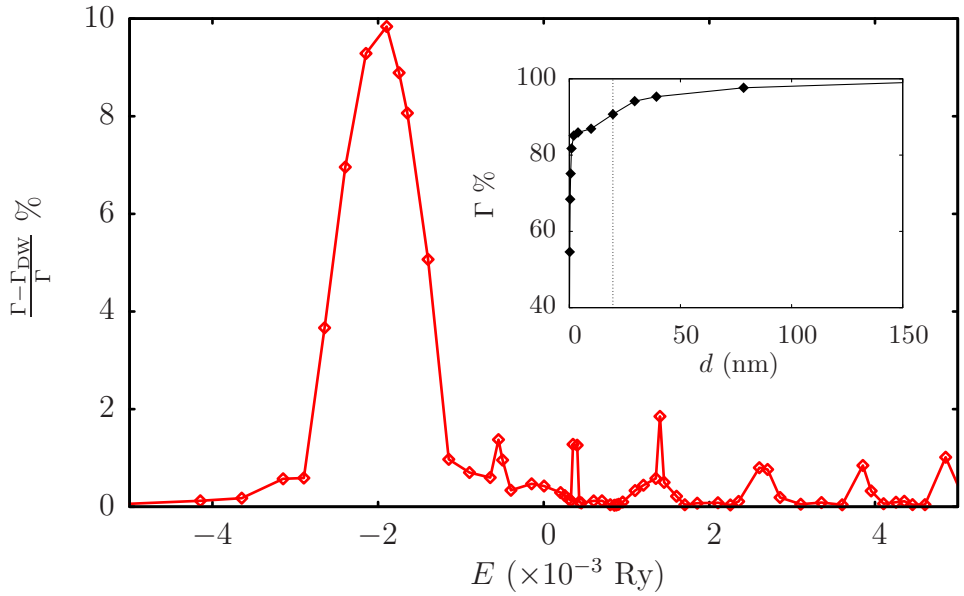

Figure 4.15: Energy dependence of domain wall transport in a Co_3 slab with a $d \approx 20$ nm wall. [*inset*] Percentage conductance as a function of the domain wall width in the slab for a system with energy corresponding to the large peak found in the conductance spectrum. The dashed grey line corresponds to the domain wall width used in the energy spectrum calculations.

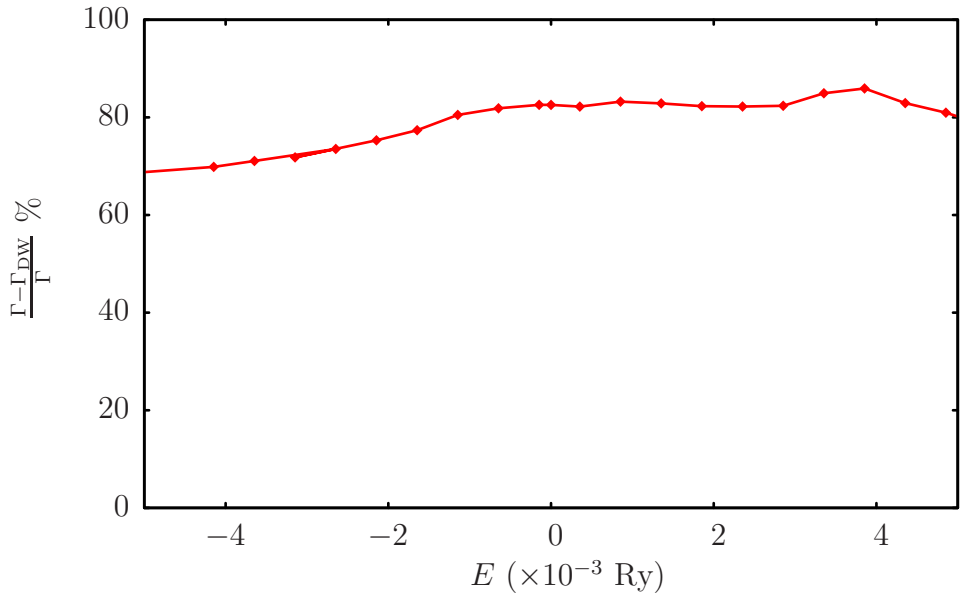

Figure 4.16: Energy dependence of domain wall transport in a Co_3 slab with an abrupt domain wall.

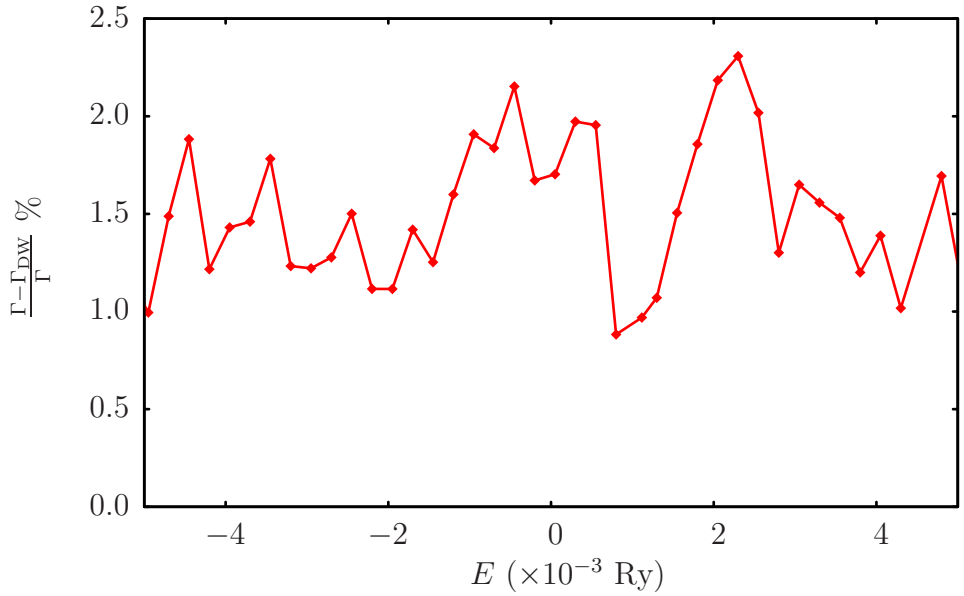

Figure 4.17: Energy dependence of domain wall transport in a $Pt_5Co_3Pt_5$ slab with a $d \approx 20$ nm wall.

So far, the domain wall has been approximated by a linear profile that is convenient for computational reasons, and used in many works by other authors (e.g. [192]). Moving beyond this, a more realistic domain wall profile of $\theta = \pi/2 + \arcsin\tanh(\pi x/d)$ has been considered for comparison, and the form of this function is plotted in figure 1.2b along with the new definition of the domain wall width, d. This function only aligns with the domains asymptotically, and as a result the active region was taken to extend from $x = -2d$ to $x = +2d$ to contain the tails of this profile sufficiently. A comparison of the conductance of these two types of wall in a $Pt_3Co_3Pt_3$ system is shown in figure 4.18. For realistic domain walls the profile is difficult to define when approaching the abrupt wall limit, thus results are not presented near this point. Firstly it is clear that for all value of d the linear wall exhibits *lower* conductivity than an equivalent realistic domain wall. As the linear wall rate $d\theta/dx$ is defined as the *steepest* part of a realistic domain wall, this result is no surprise. At small domain wall widths the realistic domain wall becomes linearised due to the small number of points used to defined the profile, and the relative difference between the two types is minimal. As the domain wall width is increased the difference between the two types of wall becomes more pronounced, and a significant fractional difference exists at higher values. For instance, for $d \approx 10$ nm the resistance of a realistic domain wall is $\approx 60\%$ that of an equivalent linear wall.

For completeness, we now model a system corresponding as closely as possible

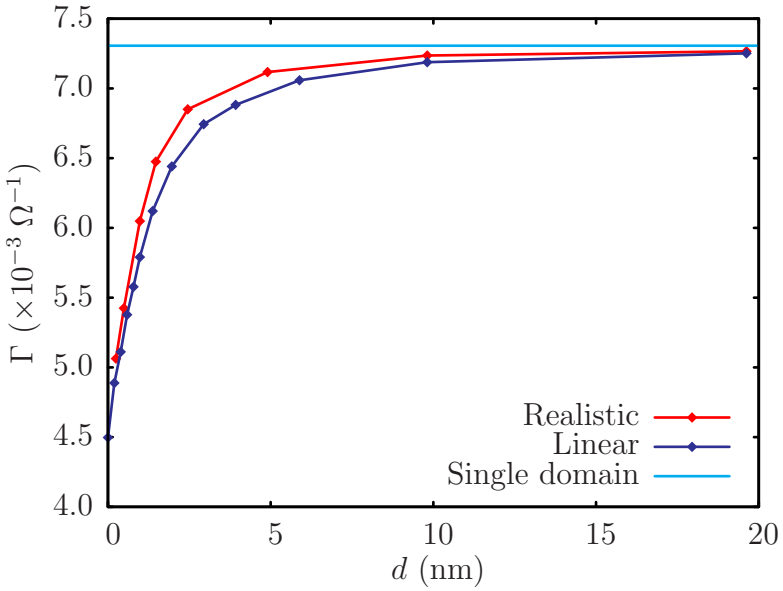

Figure 4.18: Conductance of a $Pt_3Co_3Pt_3$ trilayer containing a single domain wall of width d. Results for both realistic and linear domain wall profiles are shown.

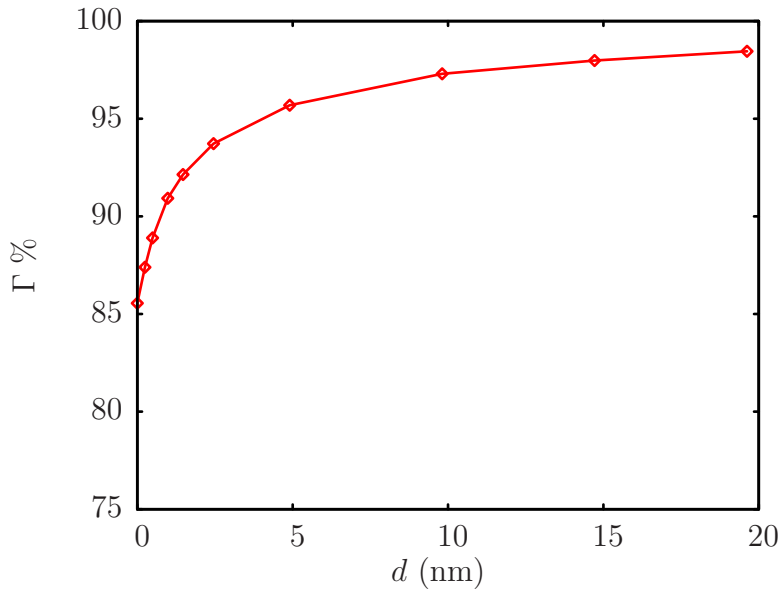

Figure 4.19: Relative conductance of a $Pt_{18}Co_3Pt_7$ trilayer system as a function of the realistic domain wall width d.

to the Pt/Co/Pt thin film sandwiches investigated experimentally. Although it will be shown in subsequent chapters that the transport in these system is in the diffusive regime, it still serves as an interesting exercise to explore the ballistic predictions of the domain wall conductance. The assumptions made about the perfect crystal lattice in this method are clearly different to the situation found experimentally. The sputtering process used to grow the samples in general does not grow perfect crystals, and it was shown in Chapter 3 that the presence of considerable defects can be inferred from the results of micromagnetic simulations. However, here we proceed by modelling the systems with a $Pt_{18}Co_3Pt_7$ trilayer, and the results of calculations using realistic domain wall profiles are shown in figure 4.19. It is found that the abrupt domain wall reduces the relative conductance to 86%, consistent with the diluting effect of the Platinum. At realistic values of the domain wall width ($d = 15$ nm) the conductance is 98 % of the single domain value, considerably greater than in bulk Cobalt, again showing the large influence of the Fermi energy band structure on the wide domain wall transport properties. To gain an insight into the contribution from the Cobalt layer, the conductance is analysed by a few simple arguments. If we assume a parallel conductance model for the transport in these trilayers then the single domain conductance, Γ_{tot}, is

$$\Gamma_{\mathrm{tot}} = 18\Gamma_{\mathrm{Pt}} + 3\Gamma_{\mathrm{Co}} + 7\Gamma_{\mathrm{Pt}}. \tag{4.31}$$

If one assumes that the domain wall is contained fully within the Co layers, and that the Platinum acts as a dilution factor then the resistance in the presence of a domain wall, Γ'_{tot}, is

$$\Gamma'_{\mathrm{tot}} = 18\Gamma_{\mathrm{Pt}} + 3\Gamma'_{\mathrm{Co}} + 7\Gamma_{\mathrm{Pt}}, \tag{4.32}$$

where Γ'_{Co} is the modified conductance of a Cobalt layer due to a domain wall. Given that $R = 1/\Gamma$, and using $\Gamma'_{\mathrm{tot}}/\Gamma_{\mathrm{tot}} = 0.98$ obtained from the calculations on a 15 nm domain wall yields a domain wall resistance of 54.8% – a value much larger than typical experimental measurements. Arguments were presented earlier in this Chapter that demonstrate that the independent resistor model used here does not describe the physics of these system sufficiently, an assertion further supported by this result. If it is assumed that the domain wall resistance is diffuse throughout the sample thickness then the domain wall resistance in this case is 2% of the background resistance. In the ballistic regime the electrons in these systems are coherent, thus the transport properties are sensitive to the

entire composition of the material. In this case a simple analysis is unable to explain the resistance phenomena found in these inherently quantum systems. The situation is expected to differ in the experiment where coherence will be disrupted by impurity scattering and the like. It is therefore clear that to proceed in modelling the experimental systems a more phenomenological approach is required to conductance in these trilayers.

4.4 Summary

In this Chapter the ballistic transport properties of Cobalt Platinum systems have been studied using realistic band structures, motivated by experiments on Pt/Co/Pt trilayers. A semi-empirical tight binding method was used to model the electrons in these materials, and parameters suitable for studying a range of systems were determined in the first part of the Chapter by fitting energy bands to the results of *ab initio* methods. A transport model based on a Green function formalism was used to calculate conductivities in both single domain systems and systems containing a domain wall, which was modelled by rotating the local spin degree of freedom in each atomic slice perpendicular to the direction of transport.

The conductances obtained for bulk Cobalt agreed well with previous *ab initio* calculations given the limits of the parameterisation used. This agreement continued for bulk Cobalt systems containing both abrupt and realistic length domain walls.

Cobalt Platinum trilayers were modelled assuming the relaxed crystalline lattices presented in Chapter 2. The Fermi energies of these systems were determined individually by integrating the densities of states obtained from the Green functions. Finite size effects were found in the conductance of thinner trilayers, but the systems were found to converge as the thickness increases, thus an effective conductivity per layer can be deduced. In this case it was found that the ratio of Cobalt to Platinum conductivity is 1:2.

The conductances of linear domain walls were explored in a set of trilayer systems with varying Platinum thicknesses. Abrupt domain walls were found to backscatter the electrons significantly, with conductances dropping to 20% of bulk values

in pure Cobalt layers. It was found in this short domain wall regime that the conductances were ordered by the Platinum layer size – the thicker the layer the greater the dilution effect. It was demonstrated, however, that this dilution differs from that expected from an independent resistor model, demonstrating that interlayer interactions are significant in these systems. The resistance was shown to be rapidly quenched as the domain wall width is increased, with realistic width domain walls exhibiting resistances of a few percent of the total layer resistance. The ordering found for abrupt domain walls vanished, and it was demonstrated that the conductance is extremely sensitive to the precise band structure at the Fermi energy, and within the Fermi energy uncertainty a large range of domain wall resistances were found. This sensitivity was shown to be greater in smaller systems where the number of quantised conduction channels is reduced.

A realistic domain wall profile was employed for further calculations and it was shown that the resistance of such a wall is less than that of an equivalent linear wall. This is consistent with the general rate of magnetic rotation in the two models of domain wall. Calculations of the conductivity profile in a system that mimics the situation found experimentally once again showed the limits of such a study. It was found that the coherence of the electrons in these quantum systems have a strong influence on transport properties, and that a simple independent resistor model fails to explain the results satisfactorily. This is compounded by the sensitivity of the conductance to the Fermi energy location, so that establishing meaningful trends in the studied systems is difficult in the realistic domain wall limit. To proceed, a more phenomenological model is more appropriate, one that can include the effects of defects and impurities and thus account for more realistic diffusive transport in these systems.

Chapter 5

Angular dependence of domain wall resistance

In this Chapter a model to study the angular dependence of domain wall resistivity in Pt/Co/Pt sandwich structures is presented. The domain wall is treated as an anisotropic perturbation to the background resistivity tensor, and the applicability of this model is discussed beforehand. After appropriate coordinate transforms, the equations are solved via a finite difference multigrid method, giving an effective but straightforwardly implemented scheme without the additional complexities of finite element methods. The results of calculations using this method are presented for single and multiple domain walls, and it is found that the angular dependence of domain wall resistivity in these systems can be successfully described by a simple analytic expression. Subsequently, the domain wall resistivity tensor elements are extracted from experimental data using this method. The results are then compared to DFT calculations of the spin density providing an important verification of the Levy-Zhang model [21].

5.1 Introduction

According to the theory of Levy and Zhang [21] a domain wall makes a positive contribution to the sample resistivity. This additional contribution is anisotropic, with a different resistivity experienced by currents flowing perpendicular and par-

allel to the surface of the wall. Several groups have used this interpretation of domain wall resistivity in the discussion of their experimental results. Ravelosona *et al.* [65] performed transport calculations on FePd systems and compared their data to the Levy-Zhang model. Although they use the concept of an anisotropic resistivity tensor in their calculations, the maze domain configuration of their samples prevents the extraction of this anisotropy explicitly from their data, although averaged properties agree well with the theory. Stronger evidence for the anisotropy model comes from the work of Viret *et al.* [66] who use an 'union jack' system to directly measure the resistivities, and they find excellent agreement with the predictions of the Levy-Zhang model. In this experiment the measurement angle was fixed, thus it was not possible to map out the angular dependence of the resistivity. Such a study is the aim of the work presented here.

In experiments performed by Aziz and Bending [193] the transport measurements were made on Pt(3.5 nm)/Co(0.6 nm)/Pt(1.6 nm) trilayer systems containing domains and domain walls created artificially by the ion beam irradiation procedure described in Chapters 1 and 3. An 8 nm capping layer of SiO_2 was used to shield the layers from excessive damage by the 30 KeV Ga ion beam used in the fabrication process at a dose of 0.009 pC/μm^2.

A Wheatstone bridge geometry was employed for transport measurements on parallel striped domain 'superlattices', resulting in reproducible multiple domain wall transport measurements. In Chapter 1 experimental results were shown that demonstrate the linear scaling of the domain wall resistance with respect to the number of domain walls. It can be implied from this that the resistance measured can be attributed to the domain walls themselves and not some other, extrinsic contribution, although this will be studied further by the model presented in this Chapter. Owing to the flexibility afforded by the irradiation procedure, domain walls can be fabricated at arbitrary angles with respect to the channel length, and consequently the current flow, thereby allowing the probing of the angular dependence of the domain wall resistivity. The width of the channel in these systems was 1 μm, whilst the widths of the irradiated artificial domains were 1 μm as shown in figure 5.1. This latter width is defined as the distance perpendicular to the inclined interfaces as seen in the figure, and not the distance parallel to the channel itself. The same is true of the domain walls shown as the thick lines at the interfaces; the domain wall width, d, is estimated to be 15 nm and always measured perpendicular to the domain wall interface. Owing to this

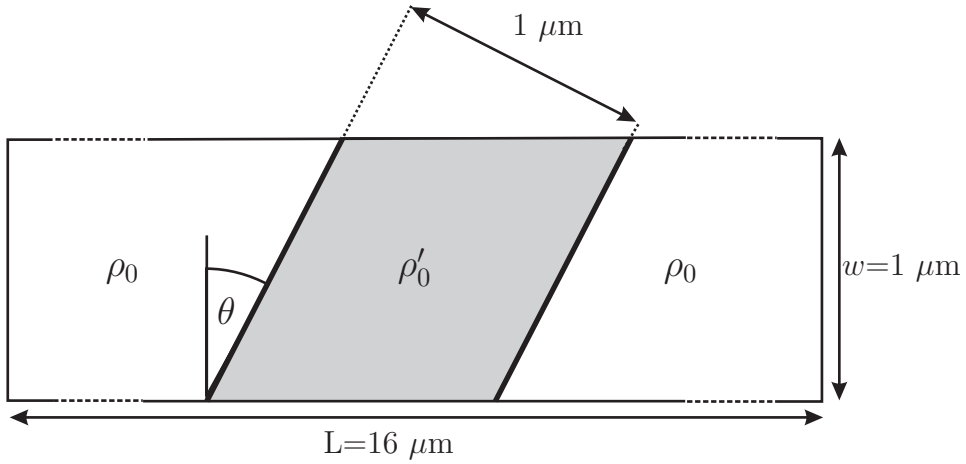

Figure 5.1: Schematic of experimental system showing a single irradiated region (shaded region). The figure is truncated along its length and therefore the other parallel irradiated regions are not shown. The two domain walls at the boundaries are indicated by the thick lines.

consideration the domain wall has a width component $d/\cos\theta$ along the direction of current flow, where θ is the interface angle. In terms of the theory presented in this Chapter the sample is assumed to lie parallel to the xy plane with the long edge parallel to the x axis having total length L, whilst the rectangular cross-section consists of width w and thickness t.

The domain superlattices were formed in 16 μm long wires, and this length placed a geometrical constraint on the number of domains that could be placed in each wire. For systems with domain wall angles $\theta = 0°$, $20°$ and $30°$ six irradiated stripes were patterned, whilst for $\theta = 40°$, $50°$ and $60°$ only three could be fitted on the wire. These correspond to twelve domain walls in the former sets and six in the latter.

The irradiation process is known to alter the local resistivity of the material. The resistivity in the irradiated region ρ_0' was found to be 2.5% greater than that of the unirradiated region, ρ_0. The value of ρ_0 measured in the samples studied here was 21 $\mu\Omega$ cm.

In one of the first theoretical works on domain wall resistivity Berger and co-workers [194, 195] considered a resistivity tensor for a thin film of Cobalt with off-diagonal terms owing to a Hall contribution that switches sign either side of the domain wall. Physically this situation is realised for an out-of-plane antipar-

allel magnetisation between the two domains. Assuming an uniform background current flows they deduce an additional contribution to the resistivity from induced currents that exist at the boundary. This new resistance is not related to the scattering from the rotating magnetic background at a domain wall but purely a Hall effect phenomena, and as such is an *extrinsic* contribution to the resistivity that should be removed before any measurement of the intrinsic contribution can be made.

In a sample containing a domain wall or irradiated area the local resistivity tensor $\hat{\rho}$ is a function of position, a situation that has parallels to the work of Berger — although this is not a Hall effect phenomena. This leads to the obvious questions about any extrinsic contributions that may arise as a result. In this Chapter we seek to evaluate the total longitudinal resistivity of these multi domain wall systems by assuming homogenous resistivity tensors in the domains and domain walls. The angular dependence of this resistivity will be determined and compared to the experimental results. Any additional extrinsic effects can be accounted for by this model, therefore enabling the extraction of the true intrinsic domain wall resistivity from the experimental data.

5.2 Formalism

This section contains the derivation of equations suitable for studying the behaviour of a domain wall system in which the wall acts as a perturbation to the otherwise homogenous background resistivity.

A basic assumption made is that the transport is diffusive. According to the Sommerfeld theory of metals [196] the mean free path of an electron in a metal, λ, is given by

$$\lambda = \frac{(r_s/a_0)^2}{\rho_\mu} \times 92 \text{ Å}, \tag{5.1}$$

where r_s is a measure of the electronic density, a_0 is the ground state Hydrogen atom radius, and ρ_μ is the background resistivity in $\mu\Omega$ cm. Assuming an r_s/a_0 of 2.5 [196] for Cobalt and using the measured background resistance of 21 $\mu\Omega$ cm gives $\lambda = 2.7$ nm. The domain wall width is estimated to be 15 nm, thus an

electron will typically undergo several scatterings whilst traversing the wall, and the transport can be treated as diffusive.

The electric current in the sample, **I**, is related to the current density **J** by the expression

$$\mathbf{J} = \frac{\mathbf{I}}{\mathrm{A}}, \tag{5.2}$$

where A is the cross-sectional area element through which **I** flows. The equations that must be satisfied to obtain **J** are

- The current continuity equation:

$$\nabla \cdot \mathbf{J} = 0. \tag{5.3}$$

- The steady state Maxwell equation for the electric field **E**:

$$\nabla \times \mathbf{E} = 0 \tag{5.4}$$

- Ohm's law, relating the above quantities via the resistivity:

$$\mathbf{E} = \hat{\rho}\mathbf{J} \tag{5.5}$$

These equations apply throughout the sample. Owing to the thickness of the film these equations need only be solved in 2D, with the sample thickness only entering expressions for evaluating the potentials and resistivities. This 2D model is an approximation given the roughness of the experimental systems.

Boundary conditions must also be stated for the system. At the edges of the sample the boundary conditions are obtained from the physical behaviour of the current at these locations. An uniform applied current flows in and out of the system at the ends of the sample yielding

$$\mathbf{J} = (J_0, 0) \qquad x = 0, L, \tag{5.6}$$

where the assumption is made that the sample is of sufficient length so that any eddy currents have decayed before reaching the ends. This can be verified

numerically once the current density has been determined. Boundary conditions at the sides of the sample are derived from the fact that the current must be confined within the sample width, corresponding to the condition

$$\mathbf{J}_y = 0 \qquad y = \pm w/2. \tag{5.7}$$

5.2.1 Resistivity tensors

In this section the representation of the resistivity tensor in the domain and domain wall regions will be discussed, including a mention of how these regions are labelled in the numerical approach used in this Chapter. The altered resistivity in the irradiated region is neglected in this section for convenience.

At any location in the sample the local resistivity can be defined in terms of a resistivity tensor in a 2D (xy) Cartesian coordinate system:

$$\hat{\rho}^{xy} = \begin{pmatrix} \rho_{xx} & \rho_{yx} \\ \rho_{xy} & \rho_{yy} \end{pmatrix}. \tag{5.8}$$

Terms entering the off-diagonal elements in samples of homogenous magnetisation typically account for phenomena such as the Hall effect, as was the case in the work of Berger. However, in the systems studied here the resistivity tensor of the domain regions, $\hat{\rho}_0^{xy}$, has a diagonal representation owing to the high background resistivity of the samples. This tensor is then given by

$$\hat{\rho}_0^{xy} = \begin{pmatrix} \rho_0 & 0 \\ 0 & \rho_0 \end{pmatrix}, \tag{5.9}$$

where ρ_0 is the value of the background resistivity. In the region occupied by a domain wall that is aligned perpendicularly to x (see figure 5.2a) the tensor has the form

$$\hat{\rho}_{\mathrm{dw}}^{xy} = \begin{pmatrix} \rho_0 + \rho'_\perp & 0 \\ 0 & \rho_0 + \rho'_\parallel \end{pmatrix}, \tag{5.10}$$

where $\rho'_\perp$ and $\rho'_\parallel$ are the values of the *additional* resistivity acting on a current flowing parallel and perpendicular to the wall respectively. This extra resistivity is due to an intrinsic domain wall contribution, which is generally not isotropic

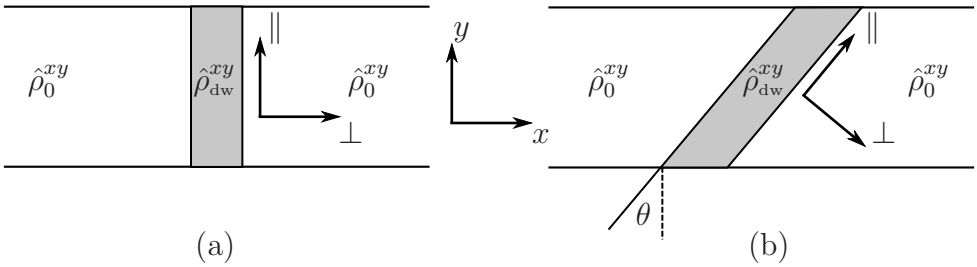

Figure 5.2: Diagram of a single domain wall system where the local resistivity tensor $\hat{\rho}$ is a function of position. The domain wall region is represented by the shaded area and has a tensor $\hat{\rho}_{dw}^{xy}$ in the xy reference system. Similarly, the domain regions have a tensor $\hat{\rho}_0^{xy}$. In (a) the domain wall is perpendicular to the sample edges and the coordinates $\perp$ and $\parallel$, defined relative to the domain wall orientation, are aligned with x and y. This is not the case in (b) where the domain wall is inclined at an angle θ with respect to the sample boundaries. In this situation the domain wall coordinates are not aligned with $x - y$ and a rotation operation must be performed to change between the two representations.

$(\rho'_\perp \neq \rho'_\parallel)$.

In the systems studied experimentally the domains are patterned such that the domain wall angle with respect to the system boundaries, θ, is varied between samples (see figure 5.2b). In this case the domain wall's internal coordinates $\perp$ and $\parallel$ are no longer aligned with x and y and expression (5.10) is not valid. To recover the xy representation of $\hat{\rho}$, the rotation matrix

$$R_\theta = \begin{pmatrix} \cos\theta & -\sin\theta \\ \sin\theta & \cos\theta \end{pmatrix} \tag{5.11}$$

is used. Defining $\rho_\perp$ and $\rho_\parallel$ as the diagonal values of a resistivity tensor in the domain wall coordinates, $\rho_{\rm dw}^{\perp\parallel}$, and applying the rotation matrix to this tensor gives

$$\hat{\rho}_{xy} = R_\theta^{-1}\rho_{\rm dw}^{\perp\parallel}R_\theta = R_\theta^{-1}\begin{pmatrix} \rho_\perp & 0 \\ 0 & \rho_\parallel \end{pmatrix}R_\theta \tag{5.12}$$

$$= \bar{\rho}\begin{pmatrix} 1-\frac{\beta}{2}\cos 2\theta & \frac{\beta}{2}\sin 2\theta \\ \frac{\beta}{2}\sin 2\theta & 1+\frac{\beta}{2}\cos 2\theta \end{pmatrix}, \tag{5.13}$$

where the average resistivity $\bar{\rho}$ and anisotropy factor β are given by

$$\bar{\rho} = \frac{\rho_\parallel + \rho_\perp}{2}, \qquad \beta = \frac{\rho_\parallel - \rho_\perp}{\bar{\rho}}. \tag{5.14}$$

Within each domain $\beta = 0$ and $\bar{\rho} = \rho_0$, reproducing equation (5.9) when placed in expression (5.13). For the domain wall region, where β is non-zero, off-diagonal terms are introduced to the tensor when $\theta \neq 0$. As a result, an applied current flowing along the channel will be scattered in a non-trivial way by this additional coupling when entering a region containing a domain wall. To successfully model the experimental systems requires quantifying this perturbed current via equations (5.3)–(5.5), a task made difficult by the fact that this off-diagonal term makes the transport equations non-separable, and that $\hat{\rho}$ is a function of the spatial coordinates. To tackle these issues a numerical approach has been adopted, details of which are given in the following section.

In terms of the numerical approach the sample is partitioned along its length into $l = 1, 2, \ldots M$ regions within which the resistivity is constant. Separating regions l and $l+1$ is an inclined interface with its centre at $(x_l, 0)$ making an angle θ with respect to the system boundaries. All interfaces are parallel in our subsequent calculations which simplifies aspects of the numerical simulation. However as is shown later, the scheme developed to obtain a solution to the equations can be used when this is not the case.

In addition to the physical boundary conditions outlined in the previous section, a new set of interface conditions exist between neighbouring regions. In this case the component of the current perpendicular to the interface must be conserved, and the parallel component of the electric field must be continuous.

5.2.2 The stream function

In the previous section we discussed the form of the local resistivity tensor, and gave an expression for this tensor valid in all regions. This tensor relates the local current density and the local electric field, which along with current continuity (5.3) and Maxwell's equation (5.4) may be used to determine the current throughout the sample. To do so it is convenient to develop a partial differential equation (PDE) in terms of a stream function, that must be satisfied in each region of homogenous resistivity.

The total current density $\mathbf{J}(x, y)$ is sought that satisfies equations (5.3)–(5.5). The problem of calculating this vector field can be simplified by the introduction

of a scalar stream function $\psi(x, y)$ defined by

$$\mathbf{J} = \left(\frac{\partial \psi}{\partial y}, -\frac{\partial \psi}{\partial x} \right). \tag{5.15}$$

along with the boundary conditions

$$\psi = J_0 y \qquad x = 0, L \tag{5.16}$$

and

$$\psi = \pm J_0 \frac{w}{2} \qquad y = \pm \frac{w}{2}, \tag{5.17}$$

that are equivalent to equations (5.6) and (5.7) in terms of the stream function.

As a result of definition (5.15) equation (5.3) is automatically satisfied, whilst (5.4) and (5.5) combined with the definition of the tensor (5.13) yield the following elliptic partial differential equation to be satisfied by the stream function:

$$a \frac{\partial^2 \psi}{\partial x^2} + b \frac{\partial^2 \psi}{\partial y^2} - c \frac{\partial^2 \psi}{\partial x \partial y} = 0, \tag{5.18}$$

where the prefactors

$$\begin{aligned} a &= \left(1 + \frac{\beta}{2} \cos 2\theta \right) \\ b &= \left(1 - \frac{\beta}{2} \cos 2\theta \right) \\ c &= \beta \sin 2\theta. \end{aligned} \tag{5.19}$$

are constant within each separate region (domain, domain wall).

The interface boundary conditions between the regions of differing resistivity must be evaluated. The $\perp$ component of the current in terms of the stream function is given by

$$J_\perp = \frac{\partial \psi}{\partial y} \cos\theta + \frac{\partial \psi}{\partial x} \sin\theta \tag{5.20}$$

and the component of the electric field parallel to the domain wall is

$$E_{\parallel} = \rho_{\parallel} J_{\parallel} = \rho_{\parallel} \left(\frac{\partial \psi}{\partial y} \sin\theta - \frac{\partial \psi}{\partial x} \cos\theta \right). \tag{5.21}$$

Both these must be matched at the interfaces between neighbouring regions.

5.2.3 Coordinate change

In this section we deal with the problem of the inclined interfaces and the difficulty they present in terms of representation on a grid that is useful for computation. It is convenient if grid points used in the numerical implementation fall exactly on the interface between two regions. To achieve this, the equations are reformulated in a non-orthogonal coordinate system:

$$\eta = y, \qquad \xi = x - y\tan\theta. \tag{5.22}$$

In this new coordinate system the interfaces separating regions correspond to lines of constant ξ, and this transform is illustrated in figure 5.3. In terms of the new coordinates, equation (5.18) becomes

$$a'_l \frac{\partial^2 \psi}{\partial \xi^2} + b'_l \frac{\partial^2 \psi}{\partial \eta^2} - c'_l \frac{\partial^2 \psi}{\partial \xi \partial \eta} = 0, \tag{5.23}$$

where the dependence of the prefactor on the region is shown explicitly. These prefactors are now

$$\begin{aligned} a'_l &= \frac{(1+\beta_l/2)}{\cos^2\theta} \\ b'_l &= 1 - \beta_l \cos 2\theta \\ c'_l &= \tan(1+\beta_l/2). \end{aligned} \tag{5.24}$$

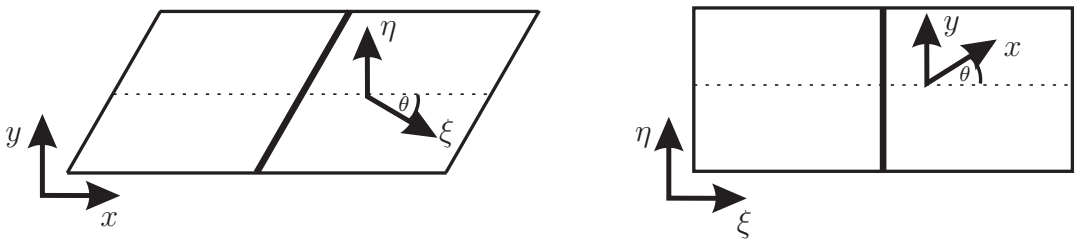

(x, y) (ξ, η)

Figure 5.3: Illustration of the coordinate transform used in the numerical implementation showing equivalent systems in both the (x, y) and (ξ, η) coordinates. A domain wall inclined at angle θ is shown by the thick line.

Equation (5.23) follows straightforwardly from (5.18) as a result of the change of variables (5.22) which yields

$$\begin{aligned}
\frac{\partial}{\partial x} &= \frac{\partial}{\partial \xi}, \\
\frac{\partial}{\partial y} &= -\tan\theta \frac{\partial}{\partial \xi} + \frac{\partial}{\partial \eta}, \\
\frac{\partial^2}{\partial x^2} &= \frac{\partial^2}{\partial \xi^2}, \\
\frac{\partial^2}{\partial y^2} &= \tan^2\theta \frac{\partial^2}{\partial \xi^2} + \frac{\partial^2}{\partial \eta^2} - 2\tan\theta \frac{\partial^2}{\partial \xi \partial \eta}, \\
\frac{\partial^2}{\partial x \partial y} &= -\tan\theta \frac{\partial^2}{\partial \xi^2} + \frac{\partial^2}{\partial \xi \partial \eta}.
\end{aligned} \tag{5.25}$$

Boundary conditions (5.6) and (5.7) must be converted to their equivalent in the new coordinates. When the equations are solved numerically a rectangular domain was used in (ξ,η) space, corresponding to a parallelogram with internal angles θ and ($180°-\theta$) in xy space, as demonstrated in figure 5.3. As a result boundary condition 5.6 is now defined along the ends of this parallelogram in the xy representation. Uniform current flow along the device channel at large distances from the domain wall therefore corresponds to the boundary condition

$$\psi = J_0 \eta \qquad\qquad \xi = 0, L. \tag{5.26}$$

Again it is assumed that the perturbed current has decayed fully before reaching these newly defined edges. No current flow through the sides of the device channel

corresponds to

$$\psi = \pm\frac{J_0 w}{2} \qquad\qquad \eta = \pm\frac{w}{2}. \tag{5.27}$$

Remaining boundary conditions relate the stream function on each side of an interface. These follow from the requirement that the current perpendicular to the interface and the electric field parallel to the interface be continuous. The component of the current perpendicular to the interface is

$$J_\perp = J_x \cos\theta - J_y \sin\theta = \frac{\partial\psi}{\partial\eta}\cos\theta, \tag{5.28}$$

giving rise to the boundary condition

$$\frac{\partial\psi^l}{\partial\eta} = \frac{\partial\psi^{l+1}}{\partial\eta} \qquad \xi = \xi_l. \tag{5.29}$$

The electric field parallel to the interface is

$$E_\parallel = \rho_\parallel J_\parallel = \rho_\parallel \left(\sin\theta\cos\theta\frac{\partial\psi}{\partial\eta} - \frac{\partial\psi}{\partial\xi}\right), \tag{5.30}$$

leading to the boundary condition

$$\sin\theta\cos\theta\left(\rho_\parallel^l\frac{\partial\psi^l}{\partial\eta} - \rho_\parallel^{l+1}\frac{\partial\psi^{l+1}}{\partial\eta}\right) = \rho_\parallel^l\frac{\partial\psi^l}{\partial\xi} - \rho_\parallel^{l+1}\frac{\partial\psi^{l+1}}{\partial\xi}. \tag{5.31}$$

It now remains to describe the solution of equation (5.23) along with boundary conditions (5.26), (5.27), (5.29) and (5.31), which yield the stream function ψ from which the current and associated resistivities are obtained.

5.3 Numerical solution

So far, equations appropriate for describing current flow in a 2D system of domains separated by inclined domain walls have been described. In this section a numerical scheme for solving the problem equations is documented.

5.3.1 Meshing and discretisation of solution

The non-separable nature of the PDE (5.23) precludes an analytical solution or a standard separation of variables approach. Instead, to obtain ψ the well proven finite difference method was employed to divide up the continuous solution into values at discrete points on a rectangular mesh. This choice of simple meshing is ideal for the rectangular solution domain that has been obtained by the coordinate transform $(x,y)\rightarrow(\xi,\eta)$. In particular, there are no issues regarding aliasing at curved surfaces or other geometric problems that require more sophisticated approaches such as the finite element method.

In the notation used in the subsequent presentation $\psi_{i,j} = \psi(\xi_i, \eta_j)$ where ξ_i is the value of ξ at grid point i. The grid spacing along η is $\Delta\eta$ with points ranging from 0 to N_η. This spacing is kept constant throughout the sample for ease of matching points at the interface. In contrast the spacing along ξ is chosen to vary between regions, allowing the possibility of increasing the grid density in the vicinity of the domain wall, for example by subdividing domains to increase the density where the solution exhibits greater variation. In region l, points are labelled from N_ξ^{l-1} to N_ξ^l. At interfaces the regions are coupled by overlapping points lying on the boundary. It it here that the coordinate transform pays dividend as grid points align exactly on the boundary, removing the need for messy interpolation methods.

In the finite difference method gradients are approximated by a nearest neighbour difference approach. At a point away from the edges the central difference approximation gives

$$\left.\frac{\partial\psi_{i,j}}{\partial\eta}\right|_{(\xi_i,\eta_j)} = \frac{\psi_{i,j+1} - \psi_{i,j-1}}{2\Delta\eta} \tag{5.32}$$

for the first derivative with respect to η, with associated error scaling as $O(\Delta\eta^2)$. Further expressions for derivatives, including those at boundaries/interfaces are given in Appendix B.

In the systems considered here all region interfaces are parallel, simplifying the numerical work significantly. However the formalism can be extended to include interfaces that are not aligned, requiring an alteration to the mesh used in the work presented here. Such an extension is documented in Appendix B.

Solution of the discretised equations is obtained through relaxation. A detailed account of relaxation methods can be found in the literature [197, 198], however the key concepts and methods will be reproduced here.

We consider an elliptic equation of the form

$$\mathcal{L}\psi = \sigma, \tag{5.33}$$

where $\mathcal{L}$ represents an elliptic operator and σ is a source term. In a relaxation method an initial solution, ψ^0, is specified as a starting point and is evolved until the true solution is approximated to a sufficient accuracy. This is achieved by rewriting the above as a diffusion equation of the form

$$\frac{\partial \psi}{\partial t} = \mathcal{L}\psi - \sigma. \tag{5.34}$$

Thus as $t \to \infty$ the time derivative vanishes restoring the original equation, and in this limit ψ is the exact solution to the problem. Here the solution is discretised and it can be shown that in 2D the scheme is stable for $\Delta t/\Delta^2 \leq \frac{1}{4}$ [198], where Δ is the spacing of the 2D grid. For efficiency this ratio is usually set to the largest allowed value of $\frac{1}{4}$. In PDE (5.23) the spacings of the two spatial coordinates can differ, but by using the same methodology and the derivatives given above the $n+1^{\text{th}}$ iteration at point (i,j) is satisfied by

$$\psi_{i,j}^{n+1} = \frac{1}{2[\Delta\eta^2 a_l' + \Delta\xi_l^2 b_l']}\Big(a_l'\Delta\eta^2(\psi_{i+1,j}^n + \psi_{i-1,j}^n) + b_l'\Delta\xi_l^2(\psi_{i,j+1}^n + \psi_{i,j-1}^n) - \frac{c_l'\Delta\xi_l\Delta\eta}{2}(\psi_{i+1,j+1}^n - \psi_{i+1,j-1}^n - \psi_{i-1,j+1}^n + \psi_{i-1,j-1}^n)\Big). \tag{5.35}$$

This iterative scheme, known as the Jacobi method [197], satisfies the equations away from the region boundaries. However, this nearest neighbour scheme is slow to converge, partly due to the low rate at which information passes through the system. After discussing the initial solution and boundary conditions in the next section, this problem of slow convergence is addressed and improvements implemented in the code are documented.

5.3.2 Initial solution and boundary conditions

Before proceeding an initial solution satisfying boundary conditions (5.26) and (5.27) must be placed in $\psi^0_{i,j}$. A natural choice for the initial guess is the uniform background current applied in the experiment,

$$\psi^0_{i,j} = J_0 \eta_j, \tag{5.36}$$

which conveniently satisfies the sample boundary conditions also. Note that to ensure satisfaction of these boundary conditions for subsequent iterations, nodes at the physical edges of the sample are never updated, remaining at these predefined values. At the internal interface between any two regions — either physical or computational — the coupling is made by overlapping points at the boundary. The point $\psi_{N^{l-1}_\eta,j}$ coincides with both the right hand boundary value of ψ in the $l-1$ region, and also the left hand side boundary in region l. This ensures that the current continuity boundary condition (5.29) is automatically satisfied.

Finally, boundary condition (5.31) originating in the continuity of the parallel component of the E field between interfaces l and $l+1$ gives:

$$\psi_{N^l_\xi,j} = M_l^{-1}\Bigg(\frac{\Delta\xi_l\Delta\xi_{l+1}}{2\Delta\eta}(\rho^l_\parallel - \rho^{l+1}_\parallel)(\psi_{N^l_\xi,j+1} - \psi_{N^l_\xi,j-1})\sin 2\theta \tag{5.37}$$

$$+\rho^l_\parallel\Delta\xi_{l+1}(4\psi_{N^l_\xi-1,j} - \psi_{N^l_\xi-2,j}) + \rho^{l+1}_\parallel\Delta\xi_l(4\psi_{N^l_\xi+1,j} - \psi_{N^l_\xi+2,j})\Bigg),$$

with the definition

$$M_l = 3(\rho^{l+1}_\parallel\Delta\xi_l + \rho^l_\parallel\Delta\xi_{l+1}). \tag{5.38}$$

In the Jacobi method equation (5.35) is scanned through the grid of ψ^n to calculate the updated solution ψ^{n+1} on a separate, identical grid. Finally, once all points away from the interface have been updated, the boundary conditions at iteration $n+1$ are calculated via equation (5.37).

5.3.3 Residuals

This iterative procedure is repeated until the residuals, the total difference in ψ between subsequent iterations, is below a predefined threshold:

$$\sum_{i=0}^{N_\xi^l} \sum_{j=0}^{N_\eta} |\psi_{i,j}^{n+1} - \psi_{i,j}^{n}| < \mathrm{T}, \tag{5.39}$$

where T is the predefined tolerance parameter. In practice the condition is checked at set intervals, with the summation performed by keeping a running total of the residuals, so it is unnecessary to store previous iterations in memory. In the calculation presented below the value of the parameter T was chosen to be 10^{-10}.

5.3.4 Accelerating convergence

As mentioned when describing the iterative scheme, the rate of convergence of a system can be made more efficient by several methods. An outline of each is now given.

Gauss-Seidl method

In the Gauss-Seidl method [197] each iteration scans the grid rows in lexicographical order and immediately overwrites the old solution with the new. The reason this improves convergence times is that part of the new solution is used immediately when calculating subsequent derivatives. The Gauss-Seidl method has been shown to give faster convergence that other schemes such as the Jacobi method which also requires the simultaneous storage of both the new and old solutions. In the numerical implementation used here the solution is updated starting from the top left of the sample in the left most domain, moving in the positive ξ direction, updating all the values within the domain before moving on the next row. When the grid point at the bottom right is reached the updating moves to the next region. Finally, all interface values are calculated and updated.

Successive over-relaxation method

The Gauss-Seidl method provides an improvement over the standard iterative method in terms of the convergence rate. However, considerable benefits can be made by employing the successive over-relaxation (SOR) method. The technique works by extrapolating the Gauss-Seidl method through weighting the current and previous iterations:

$$\psi_{\text{sor}}^{n+1} = \alpha\psi^{n+1} + (1-\alpha)\,\psi^{n}, \tag{5.40}$$

where α is the weighting parameter. Over-relaxation corresponds to $\alpha > 1$. It has been shown by Kahan [199] that the method converges if the condition $0 < \alpha < 2$ is met, whilst the optimal value of α depends on the grid spacing. Methods used for optimising α are beyond the scope of this thesis. Figure 5.4 displays the value of $\Delta\psi_{\text{int}}$, the change in ψ from the background value at an interface (at $y = 0$), between a domain and domain wall as a function of the iteration count. Results are plotted for different values of the parameter α. The simulation was stopped when the value of $\Delta\psi_{\text{int}}$ is converged to 6 significant figures. Considerable convergence benefits are found when α is increased from the starting value of 1.00. Initially, in the strongly overdriven examples ($\alpha \geq 1.90$) $\Delta\psi_{\text{int}}$ overshoots the converged value, but this is quickly corrected as the iteration process proceeds. For the modest grid used in these calculations (32 points/μm) the convergence shows a steady improvement with respect to α. However for larger grids this is not always the case, as the overshoot in the solutions become significant. When the value of α is 2 or greater the solution does not converge, which is consistent with the limits given by Kahan. In the calculations presented the value of α used was 1.95.

Multi-grid method

In the approach employed here information about the updated solution can travel by first nearest neighbour interactions only by virtue of the discretisation and derivative representations chosen. To increase the rate at which the changes in ψ spread out from a source a large grid spacing was employed for meshing the solution space, at the expense of accuracy in the overall solution. The finer features are absent in these coarse grid calculations, however they can be corrected

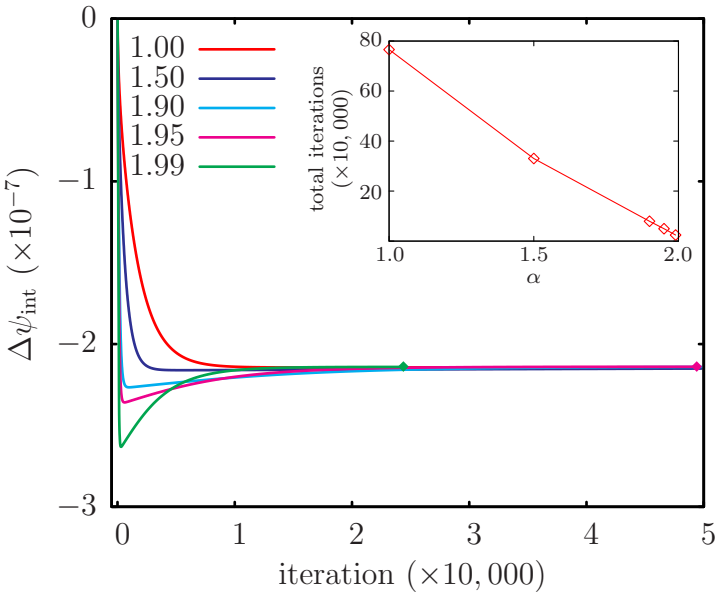

Figure 5.4: Convergence of the change in ψ from the background current at the interface of a domain wall. The inset plot shows the total number of iterations required to achieve convergence as defined by (5.39) as a function of the over-relaxation parameter, α.

by transferring the converged stream function to a finer mesh and reconverging.

In the implementation used in this work a multi-grid method was employed. Initially the equations are solved on a coarse grid and subsequently interpolated onto a mesh with twice the number of points in each dimension. This process is repeated until the desired mesh refinement is reached. The method is useful for rapidly converging low frequency components of the solution, however considerable effort must still be made by Gauss-Seidel iterations on the final mesh to converge the important higher frequency elements of the solution. In the results presented here a total of 3 meshes were used in the multi-grid procedure.

Figure (5.5) shows a chart illustrating the basic logic of the code implemented in this study.

5.3.5 Calculating physical quantities

In the calculations, the asymptotic background current density, J_0, was fixed at 1 A/μm^2. Therefore, we seek to calculate the potential required to drive this

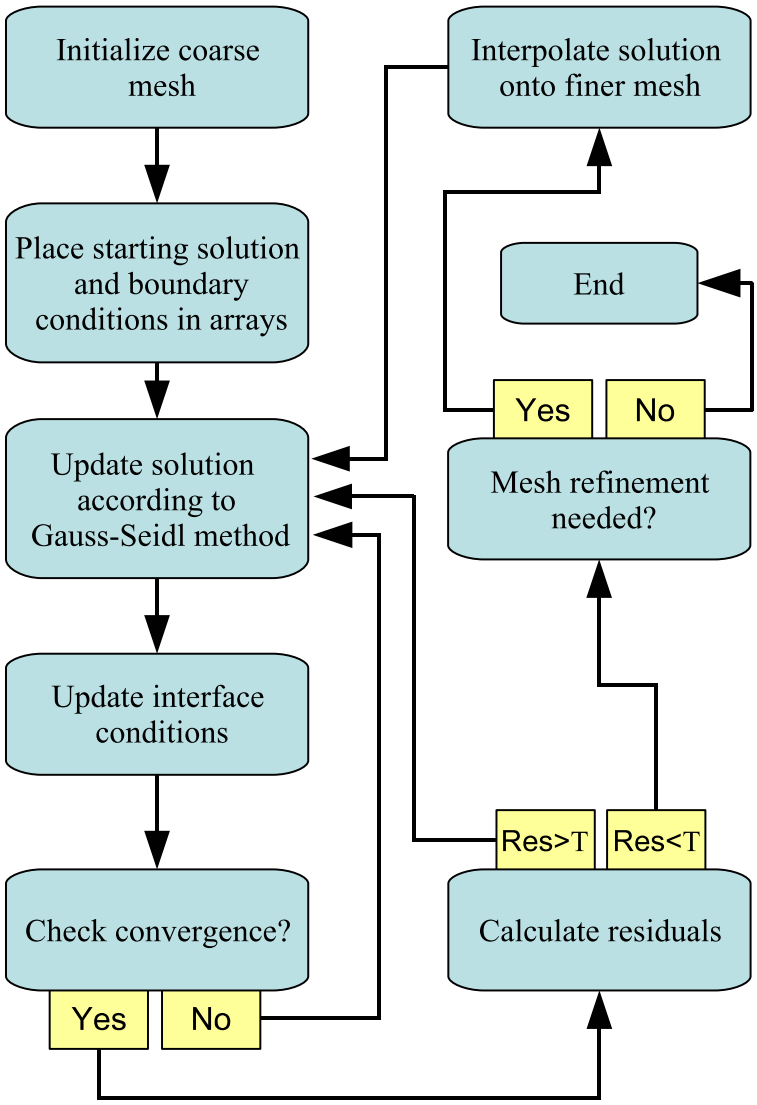

Figure 5.5: Illustration of computational scheme employed in solving for the stream function. T is the tolerance value for the sum of the residuals.

current, from which the resistivities can be determined. Specifically, the potential between ficticious probes located at either end of the sample is calculated. This longitudinal potential is obtained by firstly calculating the x component of the electric field:

$$E_x = \bar{\rho}\left[\left(1 - \frac{\beta}{2}\cos 2\theta\right)\frac{\partial\psi}{\partial\eta} - \left(1 + \frac{\beta}{2}\right)\tan\theta\frac{\partial\psi}{\partial\xi}\right]. \tag{5.41}$$

Similarly, when calculating the transverse potential, E_y is required:

$$E_y = \bar{\rho}\left[\frac{\beta}{2}\sin 2\theta\frac{\partial\psi}{\partial\eta} - \left(1 + \frac{\beta}{2}\right)\frac{\partial\psi}{\partial\eta}\right]. \tag{5.42}$$

The potential between two longitudinal probes located at A and B, and the potential between two transverse probes located at C and D (see inset of figure 5.6) are then calculated by performing the integrals

$$V_x = -\int_{\mathrm{A}}^{\mathrm{B}} E_x \, dx, \tag{5.43}$$

$$V_y = -\int_{\mathrm{C}}^{\mathrm{D}} E_y \, dy, \tag{5.44}$$

taking care regarding the direction of current flow in relation to the sign of the potentials. The domain wall resistivity is related to the potential difference by the relationship

$$\rho_{\mathrm{DW}} = \frac{(V_x - V_0) wt \cos\theta}{I_0 d}. \tag{5.45}$$

Here V_0 is the single domain "background" potential, and I_0 is the magnitude of the applied current. To convert to a resistivity the area perpendicular to the applied current, and the domain wall width component parallel to the current are used.

5.3.6 Grid convergence

In this study the primary quantity of interest is the longitudinal potential, from which the resistivities of a domain wall can be derived. Before presenting investigations on systems of interest the convergence of the potential must be demonstrated with respect to the mesh size. The test system contains a single domain wall of width 15 nm and inclined with $\theta = 10°$, centred between two 1 μm wide domains of length 8 μm. The resistivities used were $\rho_0 = 21$ $\mu\Omega$ cm, $\rho'_\perp = 23.1 \times 10^{-3}$ $\mu\Omega$ cm and $\rho'_\parallel = 3.5 \times 10^{-3}$ $\mu\Omega$ cm.

The total number of grid points can be varied independently in the ξ and η directions. However in the domain regions the numbers are chosen so that the point density is equal in both directions, thus reducing the number of parameters that must be monitored. In the narrow domain wall region a fixed number of ξ points (128) was used in all the calculations presented in this section, which proved sufficient to converge the stream function in this region.

Convergence data for this system is shown in figure 5.6. The main plot shows the profile of the perturbation to ψ along the interface between the domain wall and right hand domain. The stream function shows the greatest variation at the edges of the device, where the current density is high, and thus is the slowest feature of the system to converge with respect to the grid. In contrast, along the centre of the channel ψ is slowly varying. These differences are apparent in the inset plot showing the change in the longitudinal potential due to a domain wall as a function of the grid density along two different paths. It is clear that the longitudinal potential at the centre of the channel converges more rapidly than that measured along the bottom of the sample with respect to the grid point density. Because of the homogenous resistivity tensor in the domain regions, and consequent absence of any Hall like effect, away from the domain wall the longitudinal potential difference must be equal for longitudinal measurements made at any transverse position. Thus, in subsequent calculation a density of 1024 points/μm was used to calculate the potential along the centre of the channel ($y = 0$).

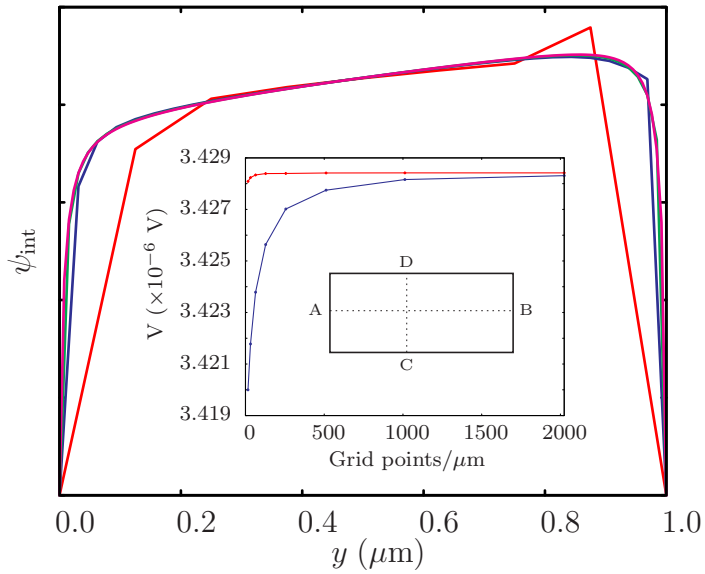

Figure 5.6: Plot of ψ along the domain-DW interface for a single domain wall system. The density of points used in the domain region is 8 (Red), 32 (Blue), 64 (Green), 128 (Magenta) points/μm. [*inset*] Magnitude of the change in the longitudinal potential due to a domain wall as a function of the grid density. The red line represent the potential measured down the centre of the channel ($y = 0$) and the blue line is measured at the bottom ($y = -w/2$). [d=15 nm, $\theta = 10°$, $\rho_0 = 21$ $\mu\Omega$ cm, $\rho'_\perp = 23.1 \times 10^{-3}$ $\mu\Omega$ cm and $\rho'_\parallel = 3.5 \times 10^{-3}$ $\mu\Omega$ cm]. Also shown inset is the probe configuration used for longitudinal and transverse potential measurements.

5.4 Calculations

In the previous sections a formalism to determine the perturbed currents in the vicinity of a domain wall was outlined and the numerical details regarding the meshing and the iterative procedure given. In this section the focus is on the results of calculations that aim to model the domain wall resistivity in Cobalt Platinum trilayer systems. After illustrating the form of ψ in some test systems, a study of a multiple domain wall system is presented. The aim of this latter investigation is to determine if any significant interactions are present between neighbouring walls, and the extent to which the resistivity of the domain wall superlattices used in the experiments can be considered a linear superposition of the individual domain wall contributions. Following this, the range of the eddy currents are discussed in more detail before the angular dependence of the domain wall resistivity is studied and the predictions are compared to experimental results. The individual contributions to the measured resistivities are then discussed, before finally the parameters extracted from experiment are compared to the Levy and Zhang theory of domain wall resistivity by use of LKKR calculations similar to those presented in Chapter 2.

The scalar function ψ is the key numerical quantity in the formalism outlined in the first half of this Chapter, therefore, before investigating the physical quantities in systems of interest, the form of this function is demonstrated for a test system. The parameters used to generate the stream functions shown here are $\rho_0 = 21$ $\mu\Omega$ cm, $\rho'_\perp = 23.1 \times 10^{-3}$ $\mu\Omega$ cm and $\rho'_\parallel = 3.5 \times 10^{-3}$ $\mu\Omega$ cm, and the sample is 1 μm wide, with a domain wall width of 15 nm in the single domain wall system. The values of θ used for illustration are 0°, 20° and 50°. In the first case the domain wall is perpendicular to the applied current, and it was found that no eddy currents were formed in the sample, with the initial trial solution of a steady background current satisfying the governing equations throughout the system. This was found to be in contrast to the systems containing inclined domain walls. After subtracting the background contributions due to the applied current, $\psi_0 = J_0\eta$, only the perturbed part of the stream function remains. This function is plotted in figures 5.7 and 5.8 for $\theta = 20°$ and $\theta = 50°$ respectively. In these calculations a reduced number of grid points were used for plotting purposes with N_ξ=1024 in two 4 μm long domains and 256 points along η. The functions are plotted in xy space, and the domain wall region has been expanded along x by a factor of 50 for illustration purposes. The value of the scalar function is

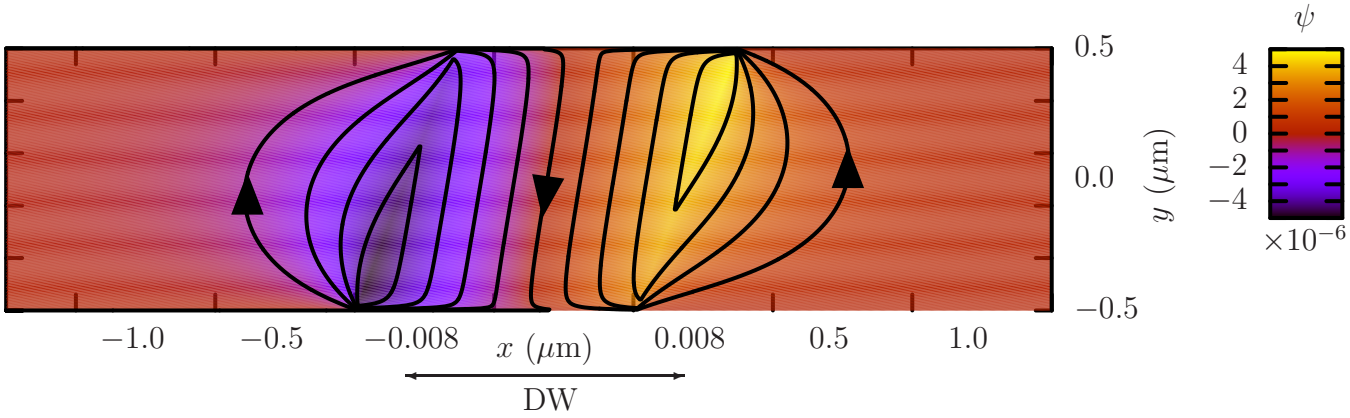

Figure 5.7: The perturbed stream function in a sample containing a 20° domain wall. The colour scheme indicates the magnitude of the function, with the key providing a numerical scale. The domain wall region has been expanded by a factor of 50 along the length of the channel for illustration. The domain wall is centred at $x = 0$.

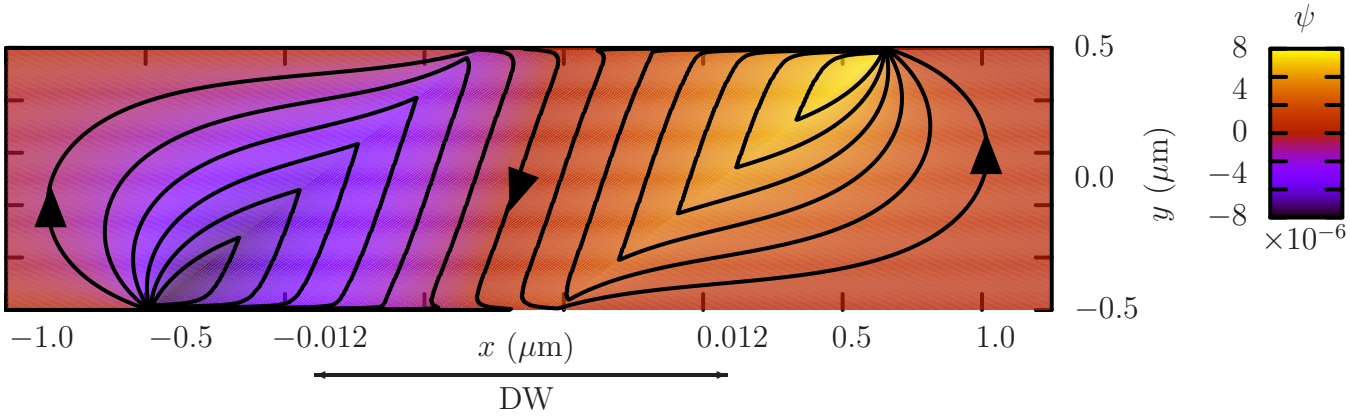

Figure 5.8: The perturbed stream function in a sample containing a 50° domain wall. The colour scheme indicates the magnitude of the function, with the key providing a numerical scale. The domain wall region has been expanded by a factor of 50 along the length of the channel for illustration. The domain wall is centred at $x = 0$.

indicated by the colour scheme, and in the same figures lines of constant ψ are indicated by the black lines. Owing to definition (5.15) these contour lines are also lines of current flow.

The variation in ψ is concentrated in the vicinity of the domain wall, where the change in the resistivity tensor is abrupt. On the left interface a dip is found in the function, with a minimum near the leading edge of the domain wall. This trough is partnered by a peak on the right hand side interface, which after a 180° rotation has an identical, albeit inverted, distribution. The resulting current perturbation has a double vortex structure with origins located at the leading and trailing edges of the domain wall. The two have opposite vorticity, with the current extending out into the domain regions while sharing a common current flow direction along the length of the domain wall. Whilst many features remain the same in both the 20° and 50° walls, it is found that the peak value of the stream function is greater for the latter, implying a more strongly perturbed current. The range of the current is also clearly greater for the 50° wall, with streamlines extending further away from the domain wall interface. If the ratio $\rho'_\perp/\rho'_\parallel$ is maintained it was found that the magnitude of the perturbed current scales linearly with respect to the domain wall tensor elements $\rho'_\perp$ and $\rho'_\parallel$.

It is useful for arguments presented later in this Chapter to expand the electric field in to its component contributions. Hence, we write the total current density in the system as a superposition of the background current $\mathbf{J}_0$, and the induced current $\delta\mathbf{J}$. Similarly the resistivity of the sample can be split into the background resistivity $\hat{\rho}_0$ and the contribution from the domain wall $\delta\hat{\rho}$. Then equation (5.5) becomes

$$\begin{aligned}\mathbf{E} &= (\hat{\rho}_0 + \delta\hat{\rho})(\mathbf{J}_0 + \delta\mathbf{J}) \\ &= \hat{\rho}_0\,\mathbf{J}_0 + \delta\hat{\rho}\,\mathbf{J}_0 + \hat{\rho}_0\,\delta\mathbf{J} + \delta\hat{\rho}\,\delta\mathbf{J}. \end{aligned} \tag{5.46}$$

The first term represents the field along a uniform sample, and provides the dominating 'background' potential that arises in both the presence and absence of a domain wall. The second term describes the electric field due to the uniform background current acting on the additional resistivity due to the domain wall. The third term represents the induced eddy currents acting on the background resistivity and finally the last term is the second order effect of the eddy current acting on the domain wall resistivity.

Figure 5.9 displays the longitudinal potential profile along the top, middle and bottom of a test system, with $\theta = 50°$. In this plot, as in all results presented in the subsequent sections, the background potential corresponding to the device in the absence of domains has been subtracted. The most striking feature is the rapid increase in the potential when traversing the domain wall, indeed the majority of the measured potential change is confined within the small domain wall region. The relative displacements of the jumps are due to domain wall's inclination such that $\Delta x = \pm\frac{w}{2}\tan\theta$. Either side of the domain wall we observe the effect of the circulating currents induced in the oppositely magnetised domains. Along the centre of the sample there is a gradual change in the potential that can be attributed to the decay of the current. Along the sample edges the potential undergoes a divergence near the domain wall due to the strong concentration of current crossing the interface. As expected in the absence of the Hall effect the potential change sufficiently far away from the domain wall is uniform along the width of the channel due to the decay of the currents. A further study of the eddy current range is presented in subsequent sections.

It was stated earlier that the eddy current strength is in direct proportion to the resistivity elements of the domain wall. With this result it is clear that terms 2 and 3 of equation (5.46) also share this relationship. Term 1 in this case can be disregarded as the background contribution. If both the resistivity elements are scaled by a factor ζ then the final term will scale as ζ^2. However, this term is of second order and for realistic values of domain wall resistivities expected in metals is insignificant in comparison to the other three terms. Therefore, disregarding this small correction, $V_x(x, y)/\zeta$ can be considered invariant in these systems.

5.4.1 Multiple domain walls

In the previous section only a single, isolated domain wall was considered when demonstrating ψ. Experimentally, to enhance the signal from the domain walls as well as to unambiguously demonstrate the domain wall origin of the resistance changes, a multiple domain wall system was employed in the experiments as described in the Chapter introduction. A natural question arises about any possible interaction between neighbouring walls owing to the spatial extent of the induced currents, and concequently whether a model involving a single domain wall is sufficient to adequately describe the physics in the experimental systems. The last

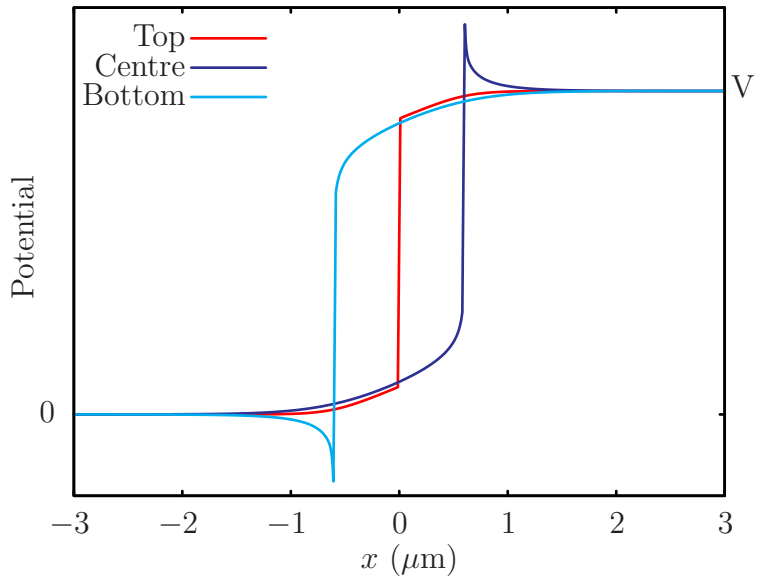

Figure 5.9: Variation of the longitudinal electric potential along the sample for a domain wall inclined at $\theta = 50°$, and with the domain wall centred at $x = 0$. Plotted are the potentials along the bottom ($y = -w/2$), centre ($y = 0$) and top ($y = w/2$) of the sample where $w = 1\mu$m.

term in equation (5.46) indicates that any current induced from a domain wall can in principle alter the potential if it extends as far as the neighbouring wall.

To explore the coupling between neighbouring domain walls we present a study of a two domain wall system with varying angles of wall inclination. The inset of figure 5.10 shows the geometry of the system in which the separation of the 15 nm wide domain walls was kept constant at 1 μm for all values of θ, and the width of the sample was 1 μm. The resistivity parameters used were $\rho_0 = 21$ $\mu\Omega$ cm, $\rho'_\perp = 23.1 \times 10^{-3}$ $\mu\Omega$ cm and $\rho'_\parallel = 3.5 \times 10^{-3}$ $\mu\Omega$ cm. Longitudinal potential profiles are given in the main panel of this figure for θ values of 20°, 30°, 40° and 60° in these two domain wall systems. The range of the induced current is found to be a function of the domain wall inclination; the larger the angle the greater the magnitude of the induced currents. However, due to the increase in the domain's projection along x with respect to θ the induced currents do not significantly overlap with neighbouring walls even for larger values of θ. The range of the potential change due to the eddy currents described here will be discussed more fully in subsequent sections. Even if the perturbed current reaches a neighbouring domain wall the change in the potential is of second order due to the small relative magnitude of the perturbation and the overlapping decayed current. Due to the scaling behaviour of the potential found in the previous section this conclusion

remains valid for other realistic value of the domain wall resistivity tensors as well.

The irradiation process has been shown to increase the resistivity locally by 2.5%. This additional resistivity was added to the central domain region in the two domain wall calculations. It was found that the resulting domain wall resistivity is increased by a negligible amount: in the case of a 20° system the additional contribution was 0.06% of the total domain wall resistivity.

5.4.2 Sample dimensions and eddy current range

In the previous section it was demonstrated that a single domain wall model is sufficient to adequately predict the individual domain wall potentials in a superlattice system. However, another issue that could affect the measurements is that the eddy currents may reach the ends of the device, and thus the probes used for measurements of the potentials. In an experimental situation such eddy currents reaching a probe may produce erroneous results. In this case the potential difference measured would be smaller than the true value as both probes would be inside the decaying tail of the potential. Another possible complicating factor is the perturbing effect of the probes on the current distribution, which can in principle also affect the measured values of the potential. In this work no attempt to quantify such changes is made. In terms of the computational work, an additional factor is the boundary conditions at the ends of the device that enforce an uniform current. Current perturbations reaching these locations would violate these requirements and invalidate the resulting potential measurements. In this section the factors influencing the eddy current range are studied, in particular the channel width and domain wall inclination.

Figure 5.11 displays the longitudinal potential profile for single domain wall systems with the resistivity parameters $\rho_0 = 21$ $\mu\Omega$ cm, $\rho'_\perp = 23.1 \times 10^{-3}$ $\mu\Omega$ cm and $\rho'_\parallel = 3.5 \times 10^{-3}$ $\mu\Omega$ cm and a domain wall angle of 50° for different values of the sample width, w. The potential is measured along the centre of the channel. The first conclusion of note is that the total potential drop is *independent* of the sample width, apart from the 4.0 μm case which is discussed separately. It follows that the domain wall resistivity is also independent of the sample width in these systems, a conclusion in agreement with the experimental results pre-

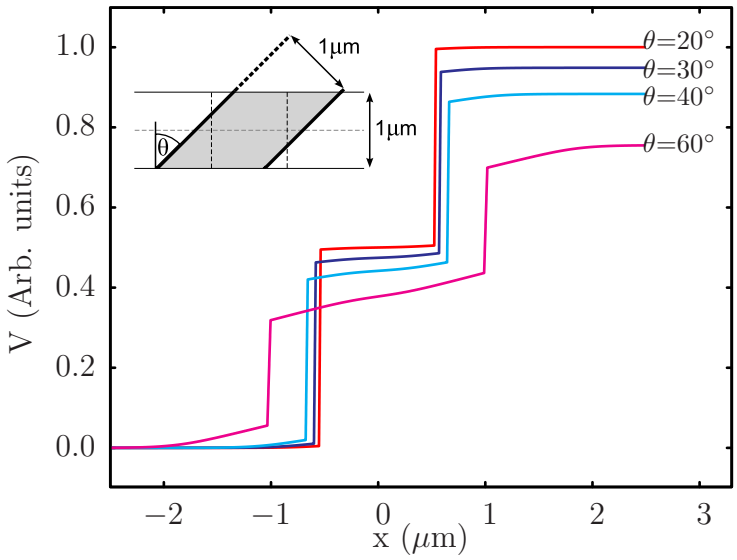

Figure 5.10: Plots of longitudinal potential profiles along the width of the sample at $w = 0$ in a two domain wall system. [*inset*] Geometry of system. Shaded region represents a single irradiated domain and the two thick lines are domain walls. The domain wall separation is kept constant at 1 μm.

sented in Chapter 1 and expected in measurements of the *intrinsic* domain wall resistivity. However, in contrast, the decay length of the current perturbations varies with w, and is found to be directly proportional to the sample widths. The domain lengths in the calculations were kept constant at 4.50 μm, which proves sufficient to contain the eddy currents for the samples of width 0.25–2.00 μm. For the largest sample width considered — 4 μm — the current perturbations are no longer adequately contained, as manifested by the slight increase in the measured potential. In the simulations the boundary conditions on the ends of the sample ensure an uniform current flow, thus this result is not directly comparable to the experimental situation owing to the unphysical nature of the constraint.

The previous results show the dependence of the eddy current range on the sample width for a fixed domain wall inclination. As was seen in the two domain wall systems discussed previously the potential change and eddy current tail is a function of this angle. The longitudinal potential profiles of the eddy currents decaying to the left of the domain wall are shown in figure 5.12, as measured along the centre of the channel. Shown are results for systems with different values of θ, and the domain wall is situated at $x = 0$. The profiles show that the range of the eddy current grows with increasing angle, although the exact scaling is not trivial. At the domain wall boundary the amplitude of the current is greater in

systems of larger inclination, and also the decay rate is slower in these systems, with both factors contributing to the observed relationship.

In the experiments modelled here the probes are sufficiently spaced to fully contain the decaying eddy current tails. As a guide to any future experiments that employ a similar setup to those examined here, the probes should be placed a minimum of $w/\cos\theta$ away from the domain wall locations at either end of the channel.

These studies show that in practice an experimental setup with a 1 μm domain separating neighbouring walls is sufficient to isolate the properties of a single domain wall, and that the measured resistance is a simple addition of the individual domain wall values. Thus, in terms of the simulations presented here we need only model a single domain wall for results that can be compared directly to experiment. Additionally, the 2.5% increase in the local resistivity in the irradiated region has a negligible effect on the measured domain wall resistivity.

5.5 Angular dependence of domain wall resistivity in isolated domain walls

We now consider in detail the resistivity of a device containing a single domain wall, inclined at various angles. Note this system does not correspond to any that were fabricated experimentally, where the formation of irradiated region domains results in two or more domain walls. However we have shown that the experimental configuration produces results that correspond to a linear superposition of individual domain wall effects, so study in detail on isolated domain walls is sufficient to understand the physics.

We consider three regions of uniform resistivity. Regions $l = 1$ and $l = 3$ have isotropic resistivity $\rho_0 = 21$ $\mu\Omega$ cm, and region $l = 2$, representing the domain wall, has resistivity elements $\rho_0 + \rho'_\perp$ perpendicular to the domain wall and $\rho_0 + \rho'_\parallel$ parallel to the domain wall. The width of the domain wall used is 15 nm. Previous studies on perpendicular domain walls in metals have shown that the intrinsic domain wall resistivity is typically 0.1–1% of the background resistivity. In these initial calculations presented here, the values $\rho'_\perp = 0.20$, 0.15, 0.10, 0.05 and

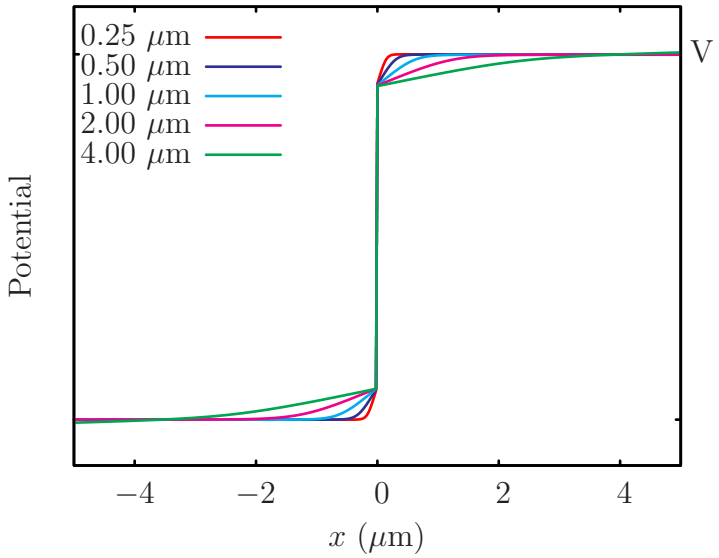

Figure 5.11: Calculated longitudinal voltage profile for systems with $\theta = 50°$ of different transverse widths w. The domain wall is located at x=0 and the length of the domains are set at 4.5 μm each. Sample widths are 0.25 μm, 0.5 μm, 1.0 μm, 2.0 μm and 4.0 μm. The potential of the 4.0 μm device has been offset for clarity where the current reaches the ends of the device.

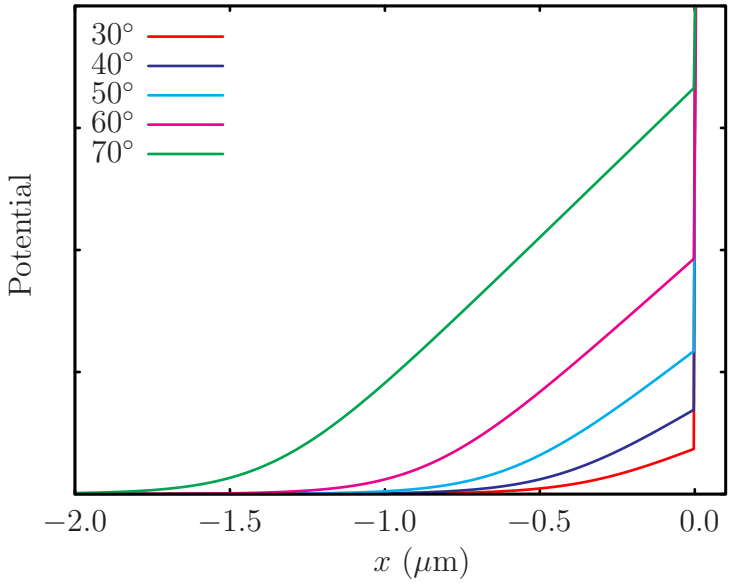

Figure 5.12: Longitudinal potential change along sample at $y = 0$. Results show the region to the left of the domain wall, with the domain wall located at $x = 0$. The value of θ is varied between 30–70°.

0.02 $\mu\Omega$ cm are used. The theory of Levy-Zhang predicts that $\rho'_\perp > \rho'_\parallel$ and a quantitative estimate for this difference in bulk Cobalt can be obtained, with $\rho'_\parallel \approx 0.15\rho'_\perp$. In these preliminary calculations the ratios $\rho'_\parallel/\rho'_\perp = 0.01$, 0.025, 0.05, 0.10 were used. The lengths of regions 1 and 3 are made sufficiently large so that the current perturbations are fully contained, which in these calculations was achieved with lengths of 4 μm.

Results showing the system resistivities obtained from potentials in these systems are plotted as a function of $\cos^2\theta$ in figures 5.13 and 5.14. From the linearity of the plots it is clear that the angular dependence of the resistivity in these system is proportional to $\cos^2\theta$. The start and end points of the plots are clearly related to the parallel and perpendicular resistivities of the domain wall. To understand the origin of this behaviour we consider the individual contributions to the domain wall resistivity in more detail.

5.5.1 Contributions to domain wall resistivity

Expression (5.46) gives the electric field in these systems in terms of a superposition of background and perturbed currents, $\mathbf{J}_0$ and $\delta\mathbf{J}_0$, with the resistivities decomposed in a similar fashion to the background and domain wall resistivities tensors, $\hat{\rho}_0$ and $\delta\hat{\rho}$.

The first term of the expansion, $\hat{\rho}_0\mathbf{J}_0$, represents the background contribution to the electric field which is also present in the absence of a domain wall. It does not enter the analysis of the domain wall resistivity.

The term $\rho_0\delta\mathbf{J}$ accounts for the perturbed current at a domain wall acting on the background resistivity. The effective resistivity due to this term can be divided into contributions from both inside and outside the domain wall. In figure 5.15 the angular dependence of these two contributions is plotted for a 1 μm wide system with the resistivity parameters $\rho_0 = 21$ $\mu\Omega$ cm, $\rho'_\perp = 23.1 \times 10^{-3}$ $\mu\Omega$ cm and $\rho'_\parallel = 3.5 \times 10^{-3}$ $\mu\Omega$ cm. A domain wall width of 15 nm is assumed. It is found that the magnitude of the individual contributions increase linearly with respect to $\cos^2\theta$, with more acute angles exhibiting a stronger effect, consistent with the observation that the eddy currents are stronger near a wall of greater inclination. Despite exhibiting the sought scaling behaviour, these are not responsible for

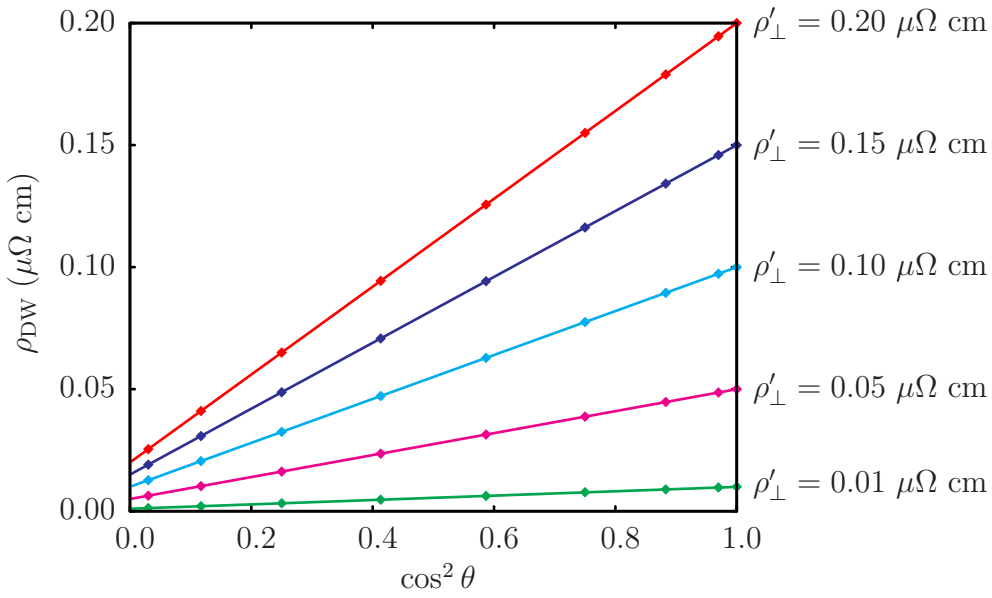

Figure 5.13: Calculated values of domain wall resistivity plotted against $\cos^2\theta$. The values of $\rho'_\perp$ range from 0.01–0.20 $\mu\Omega$ cm and $\rho'_\parallel = 0.1\rho'_\perp$.

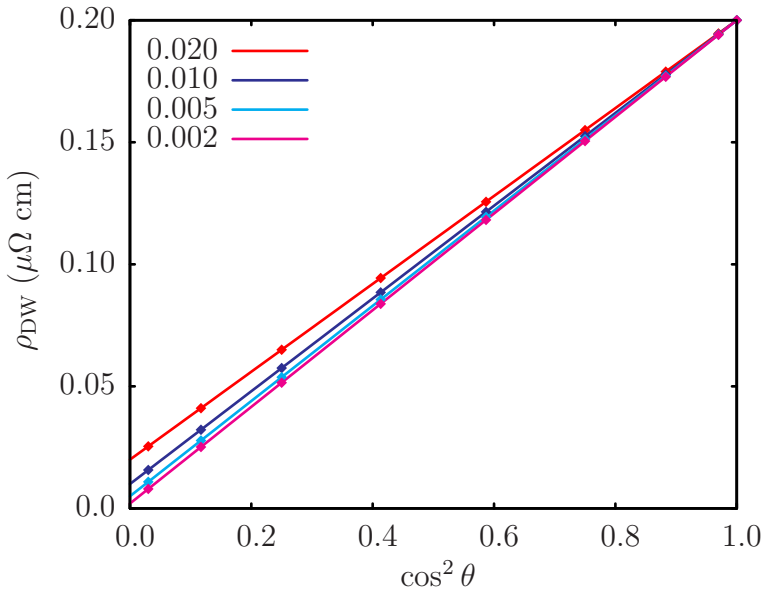

Figure 5.14: Calculated values of domain wall resistivity plotted against $\cos^2\theta$. The value of $\rho'_\perp$ is 0.20 $\mu\Omega$ cm and $\rho'_\parallel$ takes the values in the key in $\mu\Omega$ cm .

the measured resistivity. The contributions to this term from the outside and inside of the domain wall are equal and opposite, with exact cancellation when the potential is integrated along the length of the sample. If the eddy currents are fully contained within the probes they make no contribution to the measured resistivity through this term.

The second order term $\delta\hat{\rho}\delta\mathbf{J}$ is also plotted in figure 5.15. This contribution describes the electric field generated by the localised domain wall perturbation acting on the induced current in the domain wall area. As expected, this term is insignificant in magnitude compared to others, making a small negative contribution.

The remaining term in (5.46), $\delta\hat{\rho}\mathbf{J}_0$, must therefore be responsible for the resistivity behaviour observed in these systems. The corresponding contribution to the resistivity is plotted in figure 5.15, and exhibits the $\cos^2\theta$ dependence. To understand the origin of the angular variation we apply Ohm's law to this term. In this case equation 5.5 is written as

$$\begin{pmatrix} E_\perp \\ E_\parallel \end{pmatrix} = \begin{pmatrix} \rho'_\perp & 0 \\ 0 & \rho'_\parallel \end{pmatrix} \begin{pmatrix} J_{0\perp} \\ J_{0\parallel} \end{pmatrix}. \tag{5.47}$$

Using rotation matrix (5.11) to put the above in an xy representation gives

$$\begin{pmatrix} E_x \\ E_y \end{pmatrix} = R_\theta^{-1} \begin{pmatrix} \rho'_\perp & 0 \\ 0 & \rho'_\parallel \end{pmatrix} R_\theta \begin{pmatrix} J_{0x} \\ J_{0y} \end{pmatrix} \tag{5.48}$$

$$= \begin{pmatrix} \rho'_\parallel + (\rho'_\perp - \rho'_\parallel)\cos^2\theta & (\rho'_\parallel - \rho'_\perp)\cos\theta\sin\theta \\ (\rho'_\parallel - \rho'_\perp)\cos\theta\sin\theta & \rho'_\perp + (\rho'_\parallel - \rho'_\perp)\cos^2\theta \end{pmatrix} \begin{pmatrix} J_{0x} \\ J_{0y} \end{pmatrix}. \tag{5.49}$$

The background current flow is parallel to the sample channel, thus $\hat{y}\cdot J_0 = 0$, and the sought longitudinal resistivity element of the domain wall is given by the top left term in the above tensor:

$$\rho_{\mathrm{DW}} = \rho'_\parallel + (\rho'_\perp - \rho'_\parallel)\cos^2\theta. \tag{5.50}$$

This relationship also successfully reproduces the results plotted previously in figures 5.13 and 5.14.

By applying (5.50) to fit experimentally obtained resistances, values of $\rho'_\perp$ and

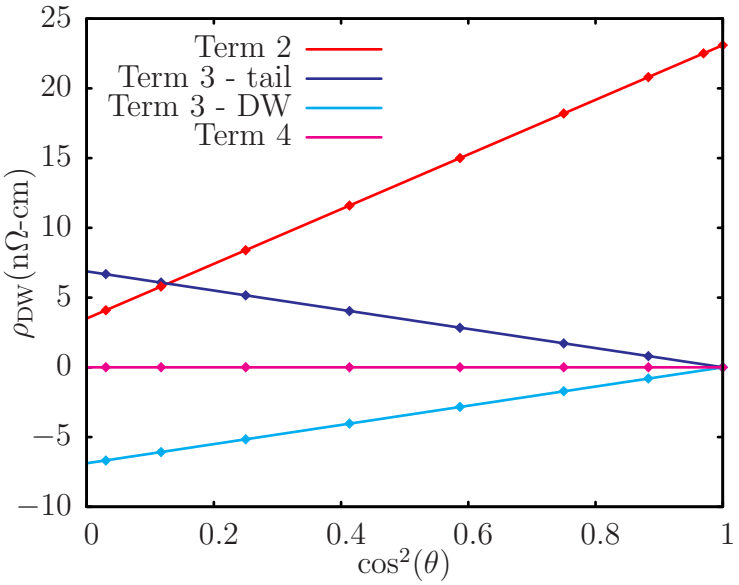

Figure 5.15: Plot of contributions to the measured domain wall resistivity in a single domain wall system with experimental parameters. The key refers to the terms of equation (5.46) that expands the electric field via background and perturbed elements of the current and resistivity.

$\rho'_{\parallel}$ can be extracted. Figure 5.16 shows such an analysis, in which the measured resistivities have been scaled by the number of domain walls in the superlattice to obtain the resistivity of a single domain wall. The resulting straight line fit yields $\rho'_{\perp} = 23.1 \pm 1.1 \times 10^{-3}$ $\mu\Omega$ cm and $\rho'_{\parallel} = 3.5 \pm 1.1 \times 10^{-3}$ $\mu\Omega$ cm, implying a domain wall resistivity that is 0.11% of the background resistivity and an anisotropy ratio of 6.6. A direct comparison can be made with the experimental work of Viret *et al.* [66] who extracted values of the perpendicular and parallel resistivity from domain walls in FePd. They obtained values of 8.2% and 1.3% of the background resistivity respectively, giving a ratio of 6.3, similar to that obtained here. The larger proportional value of the resistivities can be explained by the high quality of the films used in the experiment of Viret *et al.*. Molecular beam epitaxy was employed to deposit the material providing high quality crystalline growth, and subsequent low background resistivity.

5.6 Discussion

We have shown how the resistivity tensor elements perpendicular and parallel to a domain wall can be extracted from experimental data using a simple analytic

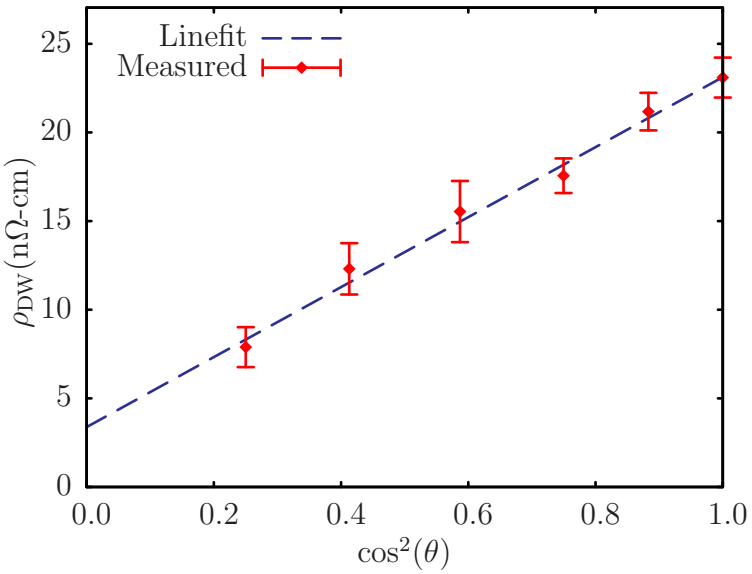

Figure 5.16: Plot of angular dependence of domain wall resistivity obtained from experiment. The dashed line represents a fit to the data points. The implied value of $\rho'_\perp$ is $23.1 \pm 1.1 \times 10^{-3}$ $\mu\Omega$ cm and $\rho'_\parallel = 3.5 \pm 1.1 \times 10^{-3}$ $\mu\Omega$ cm.

expression supported by extensive numerical analysis. We now discuss these results with respect to the domain wall resistivity theory of Levy and Zhang [21].

The theory of Levy and Zhang makes contact between the resistivities of the independent spin channels and the domain wall resistivity anisotropy in a ferromagnetic material. According to this theory the ratio of CPW to CIW resistivities (labelled $\rho'_\perp$ and $\rho'_\parallel$ here) is given by the expression:

$$\frac{\rho'_\perp}{\rho'_\parallel} = 3 + 10\frac{\sqrt{\rho_\downarrow/\rho_\uparrow}}{\rho_\downarrow/\rho_\uparrow + 1}, \tag{5.51}$$

where $\rho_\uparrow/\rho_\downarrow$ is the ratio of of minority to majority spin carrier resistivities. Using the resistivities deduced from the analysis in the previous section, $\rho'_\perp = 23.1$ $\mu\Omega$ cm and $\rho'_\parallel = 3.5$ $\mu\Omega$ cm, gives an anisotropy ratio of $\rho'_\perp/\rho'_\parallel \approx 6.6 \pm 1.2$, which implies a value ≈ 5.5 for the spin resistivity ratio.

The spin ratio can be obtained independently from the LKKR calculations described in Chapter 2 by relating the transport properties to the Fermi energy population. In this section the results of LKKR calculations are presented and compared to the analysis based upon applying the Levy-Zhang model to the experimental data.

Cobalt has two stable bulk structures and calculations were performed on both HCP and FCC configurations using the experimental lattice parameters. Self-consistent potentials in the HCP system were calculated with $\ell_{\max} = 3$, $N_E = 16$, $N_{\rm pw} = 19$ and $N_K = 45$. The FCC systems were built from layers stacked in the (100) plane, and were converged with $\ell_{\max} = 3$, $N_E = 16$, $N_{\rm pw} = 25$ and $N_K = 36$. To calculate the density of states the number of $\mathbf{K}_{\|}$-points was increased for presentation purposes to $N_K = 135$ (HCP) and $N_K = 136$ (FCC), with a resolution of 250 energy points in a window of 12.25 eV.

Two separate calculations were performed on a [Pt]/Pt_3/Co_3/Pt_7 surface in the FCC (100) configuration. As described in Chapter 2, to replicate surface effects the potentials of the semi-infinite Platinum region is fixed at that of bulk Platinum, with electronic relaxations allowed in the Cobalt Platinum trilayer placed on top. Following the arguments of Chapter 2 calculations were performed on both unrelaxed and relaxed structures. To recap, in the unrelaxed systems all atoms are fixed at the bulk Platinum spacing, whilst in the relaxed structures the z-component of the lattice spacings are allowed to relax to preserve the atomic volume.

Figure 5.17 shows the density of states plots for these systems and table 5.6 contains values of $\rho_\downarrow/\rho_\uparrow$ deduced from the data. It is clear that the presence of the Platinum and the altered spacing has a dramatic effect on the DOS of the Cobalt atom, and comparing the unrelaxed surface to the bulk we see a substantial increase in the spin ratio at the Fermi surface, table 5.6 . It is clear from figure 5.17c that narrowing of the d bands occurs in both spin channels, leading to a greater contribution to the number of states available in the minority spin channel at the Fermi energy. However the majority channel has sp like states crossing the Fermi energy which are not significantly altered by the environment and hence the large increase in the ratio. Relaxing the Cobalt in the z direction (d) reduces the degree of the band narrowing and hence the resistivity ratio, but there is still a significant increase over the bulk value. It is probable that

Bulk Cobalt		[Pt]/Pt_3/Co_3/Pt_7	
HCP	FCC	Unrelaxed	Relaxed
3.3	4.4	7.1	5.0

Table 5.1: Density of states spin ratios for HCP and FCC Cobalt, and the Cobalt atoms in [Pt]/Pt_3/Co_3/Pt_7 surface systems with both unrelaxed and relaxed structures.

in the experiment the system would be similar to the relaxed lattice with some lattice strain caused by dislocations/pin hole defects increasing the degree of band narrowing as seen in calculation (c). We therefore conclude that the ratio of spin dependent densities of states found in these self-consistent electronic structure calculations is consistent with the value that follows from applying the Levy-Zhang model to the domain wall resistivity anisotropy deduced from experiment. This provides evidence in support of Levy-Zhang theory for understanding the origins of domain wall resistivities.

5.7 Summary

This Chapter has described an analysis of domain wall resistivity in artificially irradiated Pt/Co/Pt sandwich structures. A model was outlined for obtaining the resistivities of an inclined domain wall described by an anisotropic resistivity tensor. A PDE and associated boundary conditions were developed for a system consisting of multiple regions of homogenous resistivity in terms of a stream function, and solved using an overdriven Gauss-Seidl relaxation method. It was found that eddy currents form in the vicinity of the domain wall that can alter the measured longitudinal potentials. Calculations on multiple domain wall systems were used to demonstrate that the superlattices used in experiments can be adequately described by a single domain wall model, and the small change in the resistivity of an irradiated region does not impact the results significantly.

The model showed that when the device channel is of sufficient length so that the eddy currents are fully contained, the measured resistivity should be independent of the system width. It was also shown that a simple analytic expression can describe the angular dependence of the domain wall resistivity, and can be used to obtain the parallel and perpendicular components of the domain wall resistivity from experimental measurements. The resulting values are consistent with the behaviour expected on the basis of the Levy-Zhang model of domain wall resistivity, and further support obtained from spin ratios calculated using the LKKR electronic structure technique.

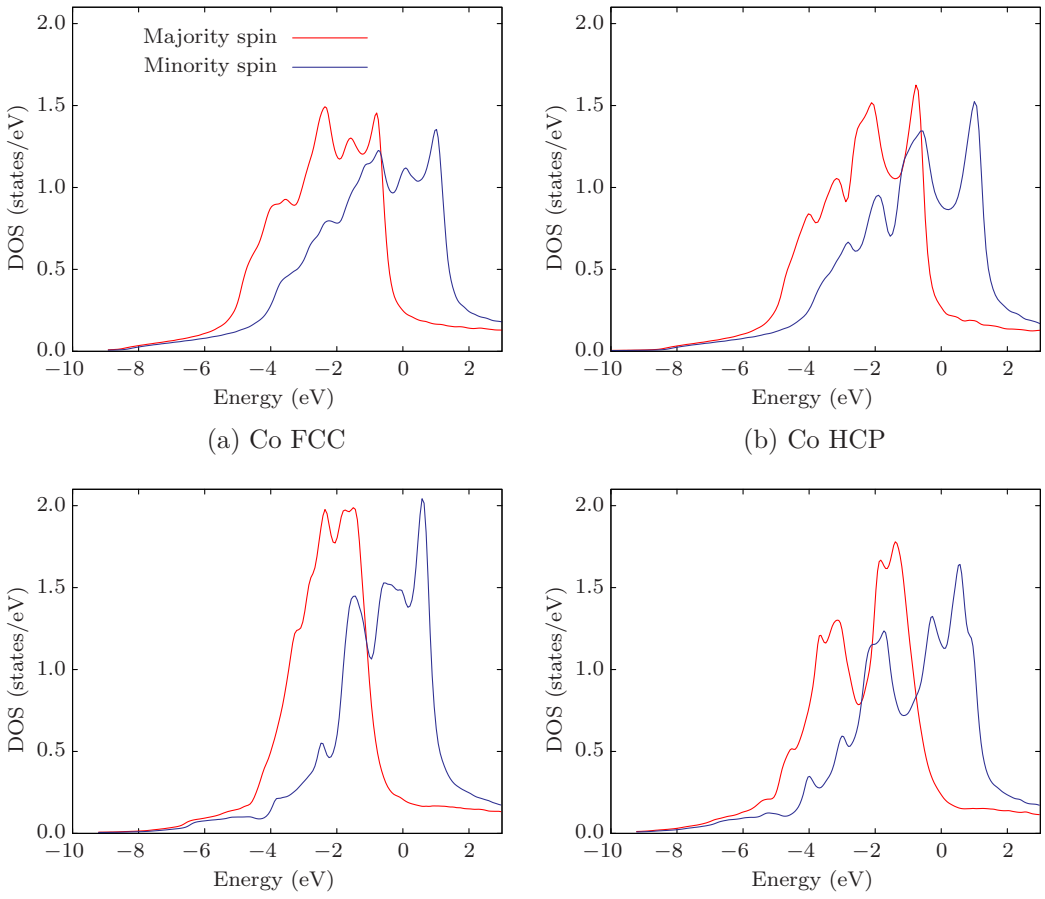

(a) Co FCC

(b) Co HCP

(c) [Pt]/Pt_3/Co_3/Pt_7 unrelaxed surface

(d) [Pt]/Pt_3/Co_3/Pt_7 relaxed surface

Figure 5.17: (a) and (b) Densities of states for bulk Cobalt in the FCC and HCP configuration respectively. (c) and (d) Density of states of the centre Cobalt atom in [Pt]/Pt_3/Co_3/Pt_7 surface systems in both an unrelaxed and relaxed lattice.

Chapter 6

Anisotropic magnetoresistance in (Ga,Mn)As

Recent experiments on transport across domain walls in in-plane magnetised (Ga,Mn)As epilayers have intriguingly been interpreted in terms of a negative domain wall resistivity. In this Chapter the model presented in Chapter 5 is extended to describe these experiments. Firstly, the applicability of the model is discussed with regards to the material parameters in terms of the mean free path determined from a simple parabolic band model. Extensions to the previously documented theory given in Chapter 5 are then presented, including the introduction of a new coordinate that corresponds to the direction of the local magnetisation in the dilute magnetic semiconductor. (Ga,Mn)As epilayers are then modelled using parameters taken from the literature, and a new extrinsic contribution to the domain wall resistance identified. An analytic expression is derived that provides a reasonable estimate of this resistance contribution for the case of domain walls aligned perpendicularly to the sample length, without the complexities of obtaining a full numerical solution. It is shown that this extrinsic contribution to the domain wall resistance can account for the experimental observations, without the need to invoke a negative domain wall resistivity.

6.1 Experimental studies of domain wall resistivity in (Ga,Mn)As epilayers

Dilute magnetic semiconductors present many new opportunities for study and applications in the field of spintronics. Magnetic impurities are added to a standard semiconductor during the growth process, and randomly distribute throughout the lattice via substitution of a native atom. It is found that these materials exhibit both magnetic and semiconducting properties, providing potential for novel hybrid devices.

Tang *et al.* [87] have performed resistance measurements on *in-plane* magnetised ($Ga_{0.948}$,$Mn_{0.052}$)As epilayers containing a single, mobile domain wall. In-plane magnetised (Ga,Mn)As exhibits anomalous magnetoresistance (AMR), in which the resistivity parallel ($\rho_{\parallel}$) to the local magnetisation vector differs from the resistivity perpendicular to it ($\rho_{\perp}$). In the systems studied here $\rho_{\parallel} < \rho_{\perp}$ [200], which has its origins in the spin-orbit interaction. In a sample containing two domains the resistivity tensors, in general, will be different in each due to this AMR effect. In this case, the interdomain boundary conditions cannot be met with an uniform current, and as a result eddy currents must be formed at the boundary. It should be noted that this is not the case in systems with 180° domain walls, such as those documented in [55], where the magnetisation vectors are parallel, and the resistivity tensors are identical in both domains. This induced current is distinct from that found in the previous Chapter, where an intrinsic domain wall resistivity is responsible.

The strong in-plane cubic anisotropy present in (Ga,Mn)As favours magnetic configurations in which the interdomain magnetisation angles are either 90° or 180°. In practise, modifications are made to these interdomain angles by the presence of a weak uniaxial anisotropy [87].

Figure 6.1a shows an image of a typical experimental device. In the fabrication process the channel length is aligned as closely to the (110) crystallographical direction as possible, and if perfect alignment is achieved the cubic anisotropy axes — aligned along (100) and (010) — make angles of ±45° with the device channel. Although efforts are made to minimise any misalignment, a small misalignment persists in all samples. Ignoring this misalignment, it is energetically favourable

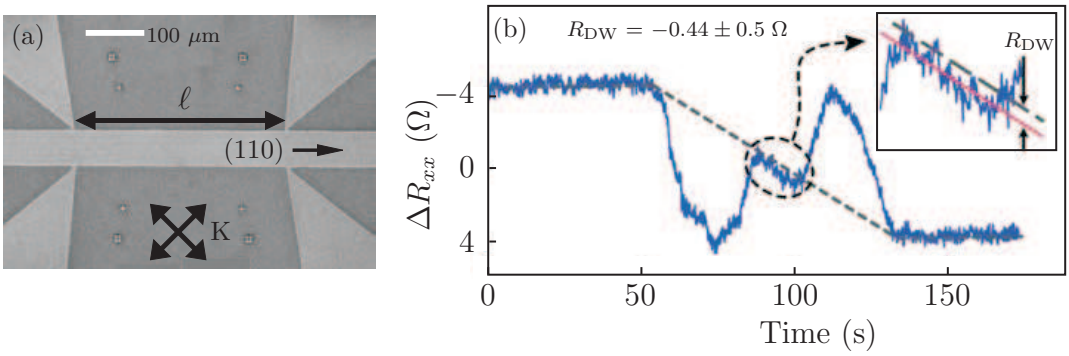

Figure 6.1: (a) From reference [87]. Magnified view of 60 μm-wide device, showing the region between between two transverse probes. The lighter region represents the device channel and probes. Also shown are the inter-probe spacing ℓ and the cubic anisotropy axes, K. (b) From reference [87]. Averaged resistance between probes for device 1 (w = 100 μm, ℓ/w=2). The offset in the central region (highlighted in inset) is attributed to a negative intrinsic domain wall resistance.

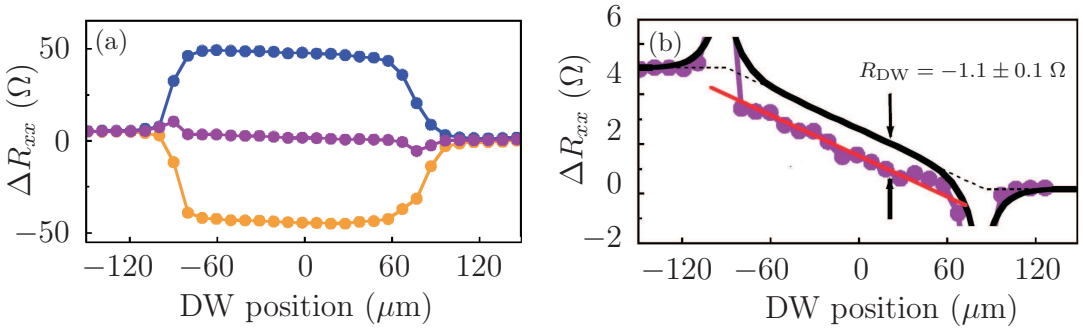

Figure 6.2: From reference [87]. (a) Measured longitudinal resistances between probes along the top and bottom of the sample (blue and orange) as the domain wall is swept from left to right. This system has a width $w = 30$ μm and aspect ratio $\ell/w = 6$. The purple line is the average of these two measurements, and a fixed background resistance has been removed for clarity. (b) Close up of averaged resistance. The purple line denotes experiment, whilst the thick black line is a theoretical prediction using the model of Tang and Roukes, and the dashed line is a simple linear interpolation. The offset is attributed to a negative intrinsic domain wall resistance.

for the atomic moments to make angles of $\pm 45^\circ$ with respect to the device channel as denoted by the easy axis vectors shown in figure 6.1a (additional small modifications must be made for the uniaxial anisotropy).

Measurements of the electric potentials are made by a four-probe system, also visible in figure 6.1a, and the rectangle defined by the probes has a length ℓ, width w and the thickness of the epilayer is t. The purpose of this probe setup is to cancel extrinsic contributions from the linearly varying planar Hall effect by averaging longitudinal measurements along the top and bottom of the sample. 90° walls are formed at the leftmost edge of the device by carefully controlling the magnetic reversal process. Upon nucleation, a fixed driving field results in domain growth via domain wall motion, and the wall travels from the left of the device to the right, passing through the region measured by the probes at a constant velocity [201]. Measurements are made of the inter-probe voltages and thus a profile of the averaged longitudinal resistance, $\langle R \rangle(x_0) = (R_{xx}^{\mathrm{up}}(x_0) + R_{xx}^{\mathrm{dn}}(x_0))/2$, as a function of domain wall position, x_0, is measured as the domain wall passes through the probe region. Here R_{xx}^{up} is the longitudinal resistance measured along the top of the device, and similarly R_{xx}^{dn} is measured along the bottom of the channel.

Tang *et al.* present results for 3 unique systems:

System 1 is an initial test device, with width $w = 100$ μm and length ℓ of 200 μm, (ℓ to w ratio of 2:1). The thickness of the (Ga,Mn)As layer is $t = 150$ nm. The averaged resistance profile $\Delta R_{xx} = \langle R \rangle - R_0$, where R_0 is the background resistance, is shown by the blue line in figure 6.1, for a domain wall swept from left to right in the sample. As will be demonstrated later, the uncertainties in the measurements made on this device are high due to the failure to isolate the induced eddy current from the probes due to the low aspect ratio.

Subsequently, devices were fabricated with larger aspect ratios of 6:1, with widths $w = 30$ μm (system 2) and $w = 60$ μm (system 3), whilst the thickness of all these devices is $t = 100$ nm. Many sets of these high aspect ratio devices were fabricated and tested to reduce the uncertainty in measurements of the longitudinal resistance. Figure 6.2a shows the signal from the individual, top and bottom, probe measurements before averaging in a 30 μm device; also shown is the averaged signal represented by the purple line. This average is magnified

in figure 6.2b.

The features of the obtained curves cannot be directly attributed to an intrinsic domain wall resistance as large resistance changes are expected from the induced eddy current at the domain wall boundary, and to obtain any intrinsic domain wall resistance values requires evaluating and subtracting these contributions from the acquired data.

6.1.1 Tang and Roukes model

To do this, Tang *et al.* [200] make use of results using a 2D model similar to that outlined in the previous Chapter, but in which the resistivity anisotropy is due to the anomalous magnetoresistance as opposed to the Levy-Zhang type intrinsic domain wall anisotropy. This theoretical treatment is documented in reference [202]. No intrinsic domain wall resistance was included in their calculations, and therefore the difference between theory and experiment should isolate any intrinsic resistance contribution.

Although they do not do so, the use of the transport model employed by Tang and Roukes similar to that described in Chapter 5 can be justified for (Ga,Mn)As due to the resistivity of the sample. The transport properties of (Ga,Mn)As are dominated by hole motion owing to the parabolic hole bands at the Fermi energy. These bands are split into so-called light and heavy holes, according to their dispersion at the Fermi surface. In terms of charge motion, the limit is set by the slower, low dispersion heavy hole bands, and it is these that must be considered to calculate the mean free path of the material.

In a purely free electron/hole picture the energy-wavevector relationship is

$$E = E_0 \pm \frac{\hbar k^2}{2m}, \tag{6.1}$$

where E_0 is the band edge and m is equal to the electron mass, m_e. In the semiconductor the bands can deviate significantly from the curvature given by this expression. A correction is made by the introduction of an effective mass, m^*, that alters the coefficient of the above expression, with $m = m^* m_e$.

The Drude model [196] provides a method of estimating the conductivity in a material by a free electron gas model, in which particles are subject to collisions with lifetime τ, and mean free path λ. The expression for the lifetime is

$$\tau = \frac{m}{\bar{\rho} n e^2}, \tag{6.2}$$

where n is the density of particles, $\bar{\rho}$ is the material resistivity and e the electronic charge. The mean free path is related to the lifetime through the Fermi velocity: $\lambda = v_f \tau$. Given that in the free electron gas picture the density of particles is $k_f^3/3\pi^2$ and the Fermi velocity is $\hbar k_f/m$, the following expression can be derived for the mean free path of the particles

$$\lambda = \frac{2\hbar\pi^2}{\bar{\rho} e^2 k_f^2}. \tag{6.3}$$

These equations can be applied to the hole dominated transport in the systems studied here. Estimates of the $(Ga_{1-x},Mn_x)As$ Fermi energy and effective mass can be found in the literature, including E_f =150 meV, m^*=0.5 [49] for samples doped with x=0.024, and E_f =130 meV, m^*=0.61 [203] in samples doped at x=0.02. In the (Ga,Mn)As epilayers used to measure the domain wall resistivity the background resistivity varies between samples, but a typical value is 4×10^{-4} Ω m. Combining with the Fermi energy and hole mass from the first study, the mean free path is deduced to be $\approx$1.6 Å — considerably smaller than the estimated domain wall size of 10 nm [87]. The use of a similar model to that outlined in the previous Chapter is therefore justified as no ballistic transport effects need be considered.

In modelling the experiments, Tang and Roukes initially consider two domains with magnetisation vectors separated by 90° and mirrored symmetrically about the device channel. A similar PDE (equation 12 in [202]) to the one derived in the previous Chapter is obtained in terms of transformed coordinates, that in this case have the definition $\xi = x - x_0 - y/k$ and $\eta = y$, where x_0 is the location of the domain wall and k is the domain wall slope. The PDE they obtained is

$$\left(1 + k^{-2} + \sin 2\phi k^{-1} - \frac{\beta}{2}\cos 2\phi\right)\frac{\partial^2\psi}{\partial\xi^2} + \left(1 + \frac{\beta}{2}\cos 2\phi\right)\frac{\partial^2\psi}{\partial\eta^2} - \left[2k^{-1}\left(1 + \frac{\beta}{2}\cos 2\phi\right) + \sin 2\phi\right]\frac{\partial^2\psi}{\partial\xi\partial\eta} = 0. \tag{6.4}$$

Here ϕ is the angle between the local magnetisation and the device channel, and

the quantity β is related to the degree of resistivity anisotropy in the system. Tang and Roukes proceeded by obtaining an analytic solution for the perturbed stream function $\psi^{(1)}$ in terms of the series expansion

$$\psi^{(1)} = \sum_{n=0}^{\infty} f_n(\xi) \cos \frac{\pi(2n+1)}{w} \eta, \tag{6.5}$$

where $f_n(\xi)$ is a function that describes the ξ dependence of this stream function. (The dependence on the width w of the device was omitted in their expression, but is corrected here.) Substituting equation (6.5) into (6.4) and adding the background current contribution, Tang and Roukes obtained the following stream function

$$\begin{aligned}\psi(x,y) = J_0 y + \frac{4\beta J_0 w}{F(\phi_1)^{-1/2} + F(\phi_2)^{-1/2}} \\ \times \sum_{n=0}^{\infty} \frac{(-1)^{n+1} \exp\left[-\alpha_n F(\phi(x,y))^{1/2} |x - x_0 - y/k|\right]}{\alpha_n^2} \cos\left(\frac{\pi(2n+1)y}{w}\right),\end{aligned} \tag{6.6}$$

where J_0 is the background current. For clarity the (x, y) dependence of ϕ has been added where necessary, and $F(\phi)$ is used here to compact their original expression, and given by:

$$F(\phi) = \frac{1 + \frac{\beta}{2}\cos 2\phi}{1 + k^{-2} + \sin 2\phi k^{-1} - \frac{\beta}{2}\cos 2\phi}. \tag{6.7}$$

Here ϕ_1 and ϕ_2 are the magnetisation angles in the left and right hand domain respectively. The factor α_n is not given explicitly in their work, but it can be inferred that $\alpha_n = \pi(2n+1)/w$. From this stream function the eddy currents are calculated and the resistance profiles of a domain wall at various locations along the device channel are produced.

The results of these calculations obtained by Tang and Roukes are reproduced in figure 6.3a. The resistance profiles at the top and bottom of the device are shown along with ΔR_{xx} for devices with domain wall inclination $\theta = 0°$ and $30°$ and no misalignment of the easy axis. The average resistance is found to be zero except in the regions near the probes where two peaks of opposite magnitude are found for $\theta \neq 0°$, consistent with the relative displacement of the top and bottom resistance curves. Figure 6.3b shows results obtained by Tang and Roukes in which the model has been extended to include misalignment in the device from

the (110) direction, leading to non-zero asymptotic values, and it is seen that when the domain wall is in the region between the probes (which are located at ± 3 in the figure), the resistance is simply given by a linear interpolation of the asymptotic values between these locations.

To deduce the value of the intrinsic domain wall resistance in the (Ga,Mn)As epilayers this model is applied to the various experimental configurations, and the deviation from the straight line interpolation that is predicted in the calculations is attributed to an intrinsic contribution. As seen in figure 6.1b and figure 6.2b, a negative contribution from the domain wall resistivity is inferred, as the linear portion of the experimental curves lie *below* the theoretical predictions. The resistances found from this method are $-0.44 \pm 0.5\ \Omega$ for the first small-aspect-ratio device, and averaged data of $-1.0 \pm 0.2\ \Omega$ for the 30 μm devices and $-0.3 \pm 0.2\ \Omega$ in the 60 μm wide devices. Assuming a domain wall width of 10 nm the resistivities of the domain walls can be determined. In the 30 μm wide epilayers Tang *et al.* deduce a resistivity as large as -100% of the background resistivity, a remarkable result, implying resistance-free current transport through the domain wall. Although some of the theories outlined in the introduction describe mechanisms that can lead to a negative domain wall resistance [22, 30], this result is many orders of magnitude greater than any negative domain wall resistivity previously reported in a metal.

Unfortunately, there is good reason to question the validity of these finding. In particular, considering the theoretical analysis of Tang and Roukes upon which the modelling of the experiment is based it is apparent that several errors were made. The first significant mistake is in the omission of a β factor in the cross-derivative term of the real space PDE (equation 9 in [202]). This error is carried forward after the coordinate change to obtain equation 12 in the manuscript, shown here in (6.4). In this expression both $\sin 2\phi$ terms are missing a factor β, that are never recovered in the subsequent derivation. In addition, when performing the coordinate change (9→12) a factor $(1 - \frac{\beta}{2}\cos 2\phi)$ is missing in the prefactors of the double ξ derivative, this also remains absent in the work that follows. The most severe ramifications in terms of the end result arise out of the series expansion used for solving PDE (6.4). This expansion (16 in [202]) shown here in (6.5) does not satisfy the original equation owing to the presence of the cross derivative term, which appears to have been neglected by Tang and Roukes in their analysis. As a result, the expansion enforces a $\eta \rightarrow -\eta$ symmetry

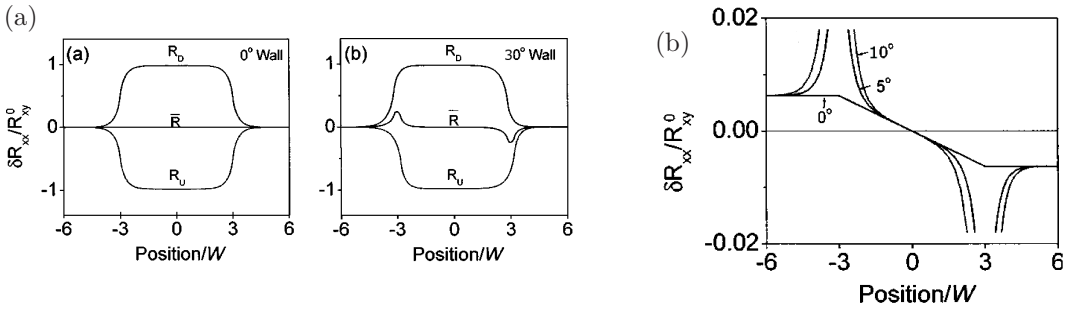

Figure 6.3: From reference [202]. (a) Prediction of Tang and Roukes' analytic method for the longitudinal resistances of moving domain walls with angles $\theta = 0°$ (left) and $\theta = 30°$ (right). Shown are the resistances along the top and bottom of the sample and the averaged resistance. (b) Theoretical predictions of the averaged resistance profiles in a set of systems with inclined domain walls. In these systems the offset of the asymptotic values is due to a misalignment of the device from the (110) direction. Between the probes there exists a linear region that is given by an interpolation of the asymptotic value between the probe locations ($x/w = \pm 3$ in this case). Shown are their predictions for 0°, 5° and 10° degree walls.

that is not intrinsic to the original equation. In addition to these errors, equation 25 in reference [202] describing the transverse resistance generated by a domain wall has typographical errors, and a missing factor of $1/w$ in the argument of the function Γ. Also equation 28 in reference [202] used to calculate the potentials is missing a factor $\bar{\rho}$ as well as containing a typographical error. This list of errata, whilst not complete, serves to cast doubt on the original analysis of Tang and Roukes that was used by Tang *et al.* to extract the domain wall resistance in their experiments.

In the remainder of this chapter the equations describing the current flow in (Ga,Mn)As microdevices are re-derived, and then solved numerically to obtain the channel resistance. Differences that arise between the results obtained and found previously by Tang and Roukes are discussed.

6.2 Current flow and resistance in (Ga,Mn)As microdevices

In this section 2D transport calculations are performed to obtain the current profiles near a domain wall in (Ga,Mn)As. This work is an extension of the formalism outlined in Chapter 5, and much of the same discussion applies here. The governing equations of the system are Maxwell's equation, the current continuity condition and Ohm's law, shown in (5.3)–(5.5). Also still valid in this systems are the physical boundary conditions of a steady current flow at the ends of the device, given in (5.6); and that no current can leave the sample through the top and bottom edges, equation (5.7).

In the Cobalt Platinum systems studied previously the coordinates ($\perp$,$\parallel$) relate to the domain wall resistivity anisotropy, and are defined by a vector perpendicular to the domain wall surface. When this is the case these coordinates are always parallel/perpendicular to the wall, and are trivially related to the domain wall inclination, θ. In contrast, the resistivity anisotropy we wish to study here is due to the anomalous magnetoresistance effect, and present *in the domains* of (Ga,Mn)As. This anisotropic resistivity is defined relative to the magnetisation vector of a domain and is therefore *independent* of the domain wall inclination, and governed primarily by the magnetocrystalline anisotropy. Clearly a new definition of the system coordinates is required, including an additional set that account for this new degree of freedom. Therefore in the modified formalism presented here ϕ represents the angle between the local magnetisation and the channel length, with the magnetic vector parallel to $\parallel$, and perpendicular to the $\perp$ coordinate, as shown in figure 6.4. The angle θ still denotes the inclination of the domain wall and is also shown in this figure. A new set of coordinates (p, q) are introduced for dealing with the interface conditions at domain boundaries, and are defined to be perpendicular/parallel to the domain wall surface, much in the same way as the ($\perp$,$\parallel$) coordinates in the previous study. They are also shown in figure 6.4. The definition of the device coordinates xy is retained, along with the sample length, width and thickness given by L, w and t respectively.

With these definitions, the resistivity tensor in the xy reference frame, $\hat{\rho}^{xy}$, is

now given by

$$\hat{\rho}^{xy} = \bar{\rho} \begin{pmatrix} 1 + \frac{\beta}{2}\cos 2\phi & \frac{\beta}{2}\sin 2\phi \\ \frac{\beta}{2}\sin 2\phi & 1 - \frac{\beta}{2}\cos 2\phi \end{pmatrix}. \tag{6.8}$$

The average resistivity $\bar{\rho} = (\rho_{\parallel} + \rho_{\perp})/2$ and anisotropy factor $\beta = (\rho_{\parallel} - \rho_{\perp})/\bar{\rho}$ first defined in the previous chapter are restated. This definition of the resistivity tensor holds throughout the entire sample, with neighbouring domain regions having differing values of ϕ in the (Ga,Mn)As epilayer.

The system is divided up along its length into M regions of homogenous resistivity tensor, separated by $M-1$ interfaces inclined at an angle θ as seen in figure 6.4. The individual regions are labelled l, so that region dependent quantities such as ϕ_l represent the value of ϕ in region l. In general, although not in the experiments presented here, $\bar{\rho}$ and β can also vary between regions.

6.2.1 The stream function

As previously, for the problem of obtaining the current density $\mathbf{J}(x, y)$ a scalar stream function is used, with the definition $\mathbf{J} = (\partial\psi/\partial y, -\partial\psi/\partial x)$, along with the physical boundary conditions in terms of this stream function

$$\psi = J_0 y \qquad x = 0, L \tag{6.9}$$

and

$$\psi = \pm J_0 \frac{w}{2} \qquad y = \pm \frac{w}{2}. \tag{6.10}$$

As a result of the above definition of the stream function the current continuity equation (5.3) is automatically satisfied, whilst Maxwell's equation (5.4) and Ohm's law (5.5) combine with the definition of the tensor (6.8) to yield the following elliptic partial differential equation to be satisfied by the stream function in each region l:

$$a_l \frac{\partial^2\psi}{\partial x^2} + b_l \frac{\partial^2\psi}{\partial y^2} - c_l \frac{\partial^2\psi}{\partial x \partial y} = 0. \tag{6.11}$$

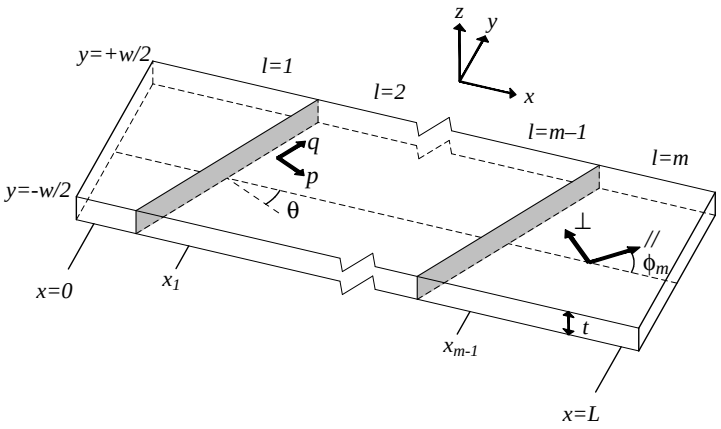

Figure 6.4: The physical system modelled has length L, width w and thickness t. The system is divided into M regions of homogenous resistivity labelled l. The $M-1$ interfaces are located at x_l. Defined in the image are the AMR vectors $(\parallel, \perp)$ and angle ϕ_l. The interfaces have an angle θ and parallel/perpendicular coordinated (p, q).

The prefactors are given by

$$\begin{aligned} a_l &= \left(1 - \frac{\beta}{2}\cos 2\phi_l\right) \\ b_l &= \left(1 + \frac{\beta}{2}\cos 2\phi_l\right) \\ c_l &= \beta \sin 2\phi_l. \end{aligned} \tag{6.12}$$

At the interface between regions the boundary conditions that must be satisfied are that the current perpendicular to the interface must be continuous, and that the electric field parallel to the interface must be continuous. The component of the current perpendicular to the interface is given by

$$J_p = \frac{\partial \psi}{\partial y}\cos\theta + \frac{\partial \psi}{\partial x}\sin\theta \tag{6.13}$$

in terms of the stream function. The component of the electric field parallel to the domain wall is

$$E_q = \rho_q J_q = \rho_q \left(\frac{\partial \psi}{\partial y}\sin\theta - \frac{\partial \psi}{\partial x}\cos\theta\right), \tag{6.14}$$

where the ρ_q is a function of both the angles θ and ϕ.

6.2.2 Coordinate change

Following the same methodology used in the previous Chapter, PDE (6.11) is rewritten in terms of a new coordinate system (ξ, η), defined by $\xi = x - y\tan\theta$ and $\eta = y$. This transform is performed to obtain a rectangular domain for meshing with the rectangular piecewise grid employed in the numerical work. In this new system equation (6.11) becomes

$$a'_l \frac{\partial^2 \psi}{\partial \xi^2} + b'_l \frac{\partial^2 \psi}{\partial \eta^2} - c'_l \frac{\partial^2 \psi}{\partial \xi \partial \eta} = 0, \tag{6.15}$$

and the prefactors are not so compact after the separation of θ and ϕ terms.

$$\begin{aligned} a'_l &= \bar{\rho}\left[1 + \frac{\beta}{2}\cos 2\phi_l(\tan 2\theta - 1) + \tan\theta(\tan\theta + \beta \sin 2\phi_l)\right] \\ b'_l &= \bar{\rho}\left[1 + \frac{\beta}{2}\cos 2\phi_l\right] \\ c'_l &= \bar{\rho}\left[2\tan\theta(1 + \frac{\beta}{2}\cos 2\phi_l) + \beta \sin 2\phi_l\right] \end{aligned} \tag{6.16}$$

The new derivatives used in (6.15) are defined in (5.25).

The physical boundary condition governing current flow in and out of the channel ends becomes

$$\psi = J_0 \eta \qquad\qquad \xi = 0, L. \tag{6.17}$$

No current flow through the sides of the device channel corresponds to

$$\psi = \pm\frac{J_0 w}{2} \qquad\qquad \eta = \pm\frac{w}{2}. \tag{6.18}$$

In terms of the inter-region boundary conditions the current component J_p given in equation (6.13) is conserved corresponding to the relationship

$$\frac{\partial \psi_l}{\partial \eta} = \frac{\partial \psi_{l+1}}{\partial \eta} \qquad \xi = \xi_l. \tag{6.19}$$

For the stream function, the electric field component parallel to the domain wall

is given by

$$E_q = -\bar{\rho}\left(\frac{\beta}{2}\cos 2(\phi-\theta)+1\right)\frac{\partial\psi}{\partial\xi} - \left(\frac{\beta}{2}\sin(2\phi-\theta)+\sin\theta\right)\frac{\partial\psi}{\partial\eta} \tag{6.20}$$

in terms of the new coordinates and must also be conserved at the interface.

6.2.3 Numerical solution

So far, equations have been presented for describing the current flow in a 2D system of domains with AMR, separated by inclined interfaces. The details of the numerical solution are similar to those outlined in Chapter 5, and much of the associated discussion remains relevant in this application.

Section 5.3.2 described the initial solution and the implementation of the boundary conditions in the numerical scheme employed to solve these equations. The same methods apply here, except for equations (5.37) and (5.38) describing the updated boundary condition, which are now

$$\begin{aligned}\psi_{N_\xi^l,j} = \frac{1}{M_l\Delta\xi_{l+1}+M_{l+1}\Delta\xi_l}\Bigg[&\Delta\xi_{l+1}M_l\left(4\psi_{N_\xi^l-1,j}-\psi^l_{N_\xi^l-2,j}\right)\\ &+\Delta\xi_l M_{l+1}\left(4\psi_{N_\xi^l+1,j}-\psi_{N_\xi^l+2,j}\right)+\frac{\Delta\xi_l\Delta\xi_{l+1}}{\Delta\eta}\left(N_{l+1}-N_l\right)\left(\psi_{N_\xi^l,j+1}-\psi_{N_\xi^l,j-1}\right)\Bigg],\end{aligned} \tag{6.21}$$

with

$$M_l = -\frac{\bar{\rho}_l\left(1+\frac{\beta}{2}\cos 2(\phi_l-\theta)\right)}{\cos\theta}, \tag{6.22}$$

$$N_l = \bar{\rho}_l\left[\frac{\beta}{2}\sin(2\phi_l-\theta)+\sin\theta\right]. \tag{6.23}$$

In section 5.3.1 a meshing scheme and iterative relaxation method were described for solving the governing PDE (5.23). This is identical to the scheme used here, including the final expression for obtaining the next iteration of ψ (5.35), using the new prefactors (6.16).

Sections 5.3.3 and 5.3.4 describe the terminating criterion and methods of accelerating the convergence of the iterative procedure. Both apply here.

Finally, in section 5.3.5 the method of calculating the potentials is given, and is identical to that used here except the electric fields are now given by

$$E_x = \bar{\rho}\left[-\left(\left(1+\frac{\beta}{2}\cos 2\phi\right)\tan\theta + \frac{\beta}{2}\sin 2\phi\right)\frac{\partial\psi}{\partial\xi} + \left(1+\frac{\beta}{2}\cos 2\phi\right)\frac{\partial\psi}{\partial\eta}\right] \tag{6.24}$$

$$E_y = \bar{\rho}\left[\left(\frac{\beta}{2}(\cos 2\phi - \sin 2\phi\tan\theta) - 1\right)\frac{\partial\psi}{\partial\xi} + \frac{\beta}{2}\sin 2\phi\frac{\partial\psi}{\partial\eta}\right]. \tag{6.25}$$

To calculate the potential profile of a moving domain wall, a total channel length of $L = 3\ell$ is used. The potential profile is calculated along the whole length of the sample, and the potential difference between a pair of probes, separated by distance ℓ, and centred at various positions along the sample is obtained, in order to replicate the experimental situation of a fixed probe position and a moving domain wall.

6.3 Numerical results

Numerical results for the current flow and associated resistances in the presence of a domain wall in (Ga,Mn)As are now presented, obtained using the above theory. Firstly, the grid size used for representing the stream function is described. Following this the effect of the domain wall inclination and device misalignment on the resistance profiles of domain walls at various locations in the device channel are investigated.

For numerical solution, the stream function ψ in the rotated coordinates was discretised onto a rectangular grid, allowing the point density to be varied along the length of the sample, an enabling a better representation of ψ in regions of greater variation. Such a scheme was employed in the calculations presented here, in which the density of ξ points is 30 points/μm except within a distance $\pm w$ of the interface where the density was increased to 70 points/μm. In the η direction a density of 20 points/μm was used. These are sufficient to converge the resistance profiles plotted in the subsequent sections. The key quantity presented in this

chapter is a resistance R_{AMR}, and a separate convergence study is presented later for this quantity.

6.3.1 Initial calculations

Before proceeding to document the results of calculations on test systems the coordinate x is redefined here for convenience. The origin, $x = 0$, is now located in the middle of the sample, halfway between the tranverse probe pairs.

As was mentioned in the introduction, a weak uniaxial anisotropy is present in the (Ga,Mn)As epilayers studied experimentally that alters the domain magnetisation angles from a true 90° separation. These changes are accounted for in later calculations presented in this work, whilst, for simplicity, early illustrative calculations and discussion assume perfect 90° domain walls. Figure 6.5 illustrates the change in the longitudinal resistance found between two sets of probes as a domain wall is driven between them in a 30 μm wide, $\ell/w = 6$ device [other parameters: $\beta = -0.02$, $\bar{\rho} = 3 \times 10^{-4}$ Ωm, $\phi_1 = -\phi_2 = -45°$, $\theta = 0°$]. The change in current induced by a domain wall within the region between the probes is found to increase the longitudinal potential difference along the bottom of the channel, and decrease it along the top. These changes are consistent with the single anti-clockwise current rotation that is found around the domain wall in the system; at $y = +w/2$ the current perturbation flows in the negative x direction giving a negative contribution to the resistance, and vice-versa at $y = -w/2$. The current vorticity was found to switch with the sign of β, or reversing of the domain order so that $\phi_1 = -\phi_2 = +45°$.

The regions of greatest variation are located at ± 90 μm — the positions of the probes — owing to the induced eddy currents passing the probes as the domain wall moves. A schematic showing the domain wall and induced current crossing the probes and midway between the probes is inset in figure 6.5. If the aspect ratio of the device is large enough, then these eddy currents originating from a domain wall located at the middle of the channel, $x = 0$, will have decayed fully before reaching the probes. In this case an useful expression may be derived for the difference between the resistances measured along the top and bottom of the sample by the probes, δR_{xx}, in terms of the anomalous Hall potential.

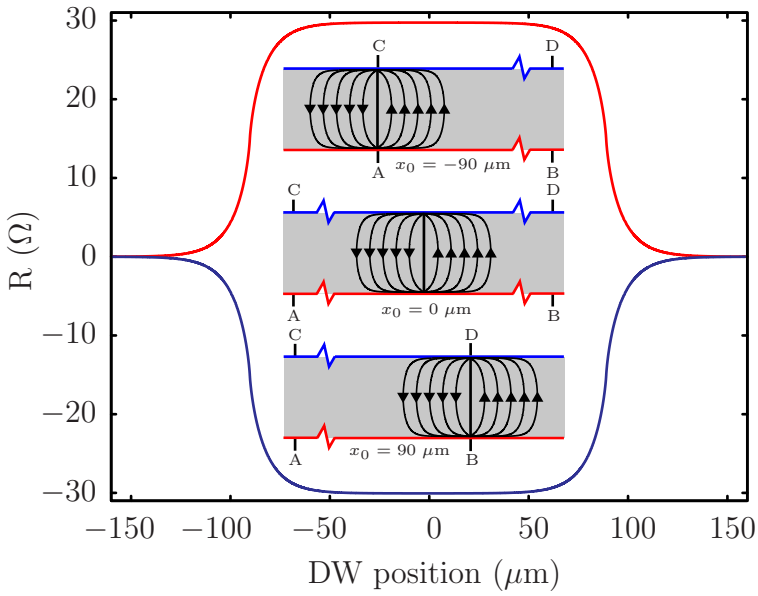

Figure 6.5: Resistance measured between probes at the top (DC) [Blue] and bottom (BA) [Red] of the sample. The probes are located at $x = \pm 90$ μm. [*inset*] From top to bottom: current profiles for a domain wall located at the left probe pair, centred between the probes, and at the right probe pair.

To see this, note that from the requirement that the potential around a closed loop is zero, the expression

$$V_{DC} + V_{CA} - V_{BA} - V_{DB} = 0 \tag{6.26}$$

is valid (see inset of figure 6.5 for probe configuration). Here the quantities V_{CA} and V_{DB} are the transverse voltages. If the perturbed current from the domain wall has decayed before reaching the probe location the current between probes C and A, and D and B, is $(J_0, 0)$, and so the y component of the electric field will be $E_y = (1/2)\bar{\rho}\beta J_0 \sin 2\phi$ from $\mathbf{E} = \hat{\rho}\mathbf{J}$. The potentials are obtained by integrating E_y between the probes, giving

$$V_{CA} = -\frac{\bar{\rho}\beta w J_0}{2} \sin 2\phi_1 \qquad V_{DB} = -\frac{\bar{\rho}\beta w J_0}{2} \sin 2\phi_2 \tag{6.27}$$

Hence, in the case where $\phi = -\phi_1 = \phi_2$ and using (6.26), the difference between the potential measured by the probes along the top and bottom of the sample is given by

$$V_{BA} - V_{DC} = \bar{\rho}\beta w J_0 \sin 2\phi, \tag{6.28}$$

and the corresponding difference in resistance ($\delta R_{xx} = (V_{BA} - V_{DC})/J_0 wt$) is

$$\delta R_{xx} = -\frac{\bar{\rho}\beta \sin 2\phi}{t}. \tag{6.29}$$

Using the parameters presented earlier gives a value for δR of 60 Ω, consistent with the value found in the numerical work shown in figure 6.5. This expression is used later in this Chapter to determine the anisotropy factor β for the (Ga,Mn)As samples studied experimentally by Tang *et al.* [87].

6.3.2 Domain wall angle

In this section the effect of the domain wall angle variation is considered. Experimentally, this variation is due to the imprecise nature of forming domain walls in the sample, thus the exact value of θ is not known for any particular measurement. The averaged inter-probe resistance along the top and bottom of the sample is used in the experiment to extract the intrinsic domain wall contribution. Figure 6.6 shows this calculated average resistance as a function of the domain wall position for systems in which θ is varied. The same parameters are used as in the previous section, with θ taking the values 0°, 10°, 20° and 40°.

The most striking features are the two peaks that occur when the domain wall passes the probes, a positive peak found when the domain wall passes the left probes which is then inverted as it approaches the right probes. The origin of these peaks can be explained in terms of the relative displacement of the resistance profiles at the top and bottom of the samples when the domain wall is inclined at angle θ. The curves in figure 6.5 are shifted by $\pm(1/2)w\tan\theta$ respectively due to the wall's orientation, and so systems with greater angles exhibit larger peaks owing to this displacement. In the case where $\theta = 0°$, some slight structure exists due to asymmetries in the perturbed current at the top and bottom of the sample.

A notable aspect of the calculated resistances is that in the region between the peaks, representing the situation where the domain wall induced eddy currents are fully contained between the probes, a small negative value is found. This is shown in the inset of figure 6.6. This negative offset is in sharp contrast to the behaviour found previously by Tang and Roukes, who found this part of the

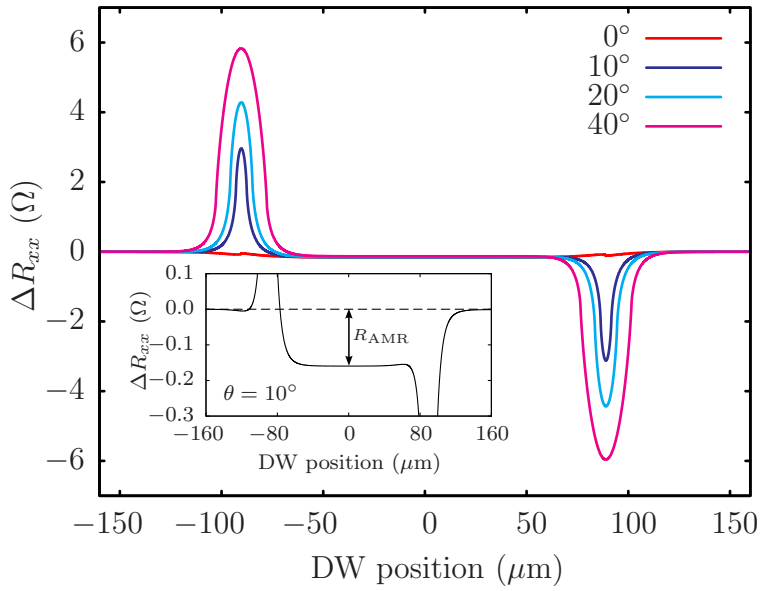

Figure 6.6: Averaged resistance measured between probes at the edges of the sample as a function of domain wall position. The numbers given in the key are values of the domain wall inclination θ. [*inset*] The curve corresponding to $\theta = 10°$ is rescaled to show the negative offset due to the circulating currents, R_{AMR}.

curve to show no resistance. For reasons made clear shortly, this new resistance is termed R_{AMR}. By repeating the calculations with different geometries, it is found that R_{AMR} is independent of the sample width, w.

In the following section the effect of the device alignment on the resistance profiles will be studied. However, before proceeding the convergence properties of R_{AMR} will be demonstrated with respect to the grid, demonstrating that this additional resistance is not due to an insufficient representation of the stream function.

Table 6.1 list values of R_{AMR} calculated with different grid densities. Owing to the linear variation of the transverse Hall voltage in the system, the averaged resistance contribution along the top and bottom of the sample should also equal the resistance found directly along the centre of the channel. Results are presented for both. The first three rows of this table show data for grids with an uniform ξ point density throughout the sample, whilst the last two employ a hybrid scheme where a larger number of points were employed within a distance $\pm w$ of the domain wall.

As found in the previous Chapter, convergence is slower at the sides of the sam-

η-point density Points/μm	ξ-point density Points/μm	R_{AMR} Average Ω	R_{AMR} Centre Ω
20	7.5	-0.149	-0.163
20	15	-0.159	-0.163
20	30	-0.162	-0.163
20	30,70*	-0.162	-0.163
40	30,70*	-0.162	-0.163

Table 6.1: Convergence of R_{AMR} with respect to the grid point density using both the averaging method employed by Tang and Roukes, and the potential obtained directly down the channel centre. $*$ denotes the density that is used within a distance $\pm w$ of the domain wall. [$\beta = -0.02$, $\bar{\rho} = 3 \times 10^{-4}$ Ωm, $w = 30$ μm, $\ell/w = 6$, $-\phi_1 = \phi_2 = 45°$, $\theta = 0°$].

ple, where the large current densities near the domain wall require an especially detailed representation of the gradient of ψ. In fact for the grid densities tabulated here the resistance along the centre of the channel remains well converged to 3 significant figures, whilst this is not the case for the averaged resistance. In subsequent calculations the better convergence properties of the channel centre R_{AMR} mean it is this value that is used.

6.3.3 Device misalignment

Experimentally, Tang *et al.* reported that the the device fabrication process resulted in a slight misalignment of the easy axis of magnetisation with respect to the sample boundaries. This misalignment is denoted by the angle δ, corresponding to the magnetisation angle in region 1 being $\phi_1 = -\phi + \delta$ and in region 2, $\phi_2 = \phi + \delta$.

Although experimentally steps were taken to minimise δ, it was not possible to prevent a small residual misalignment persisting. To study the effects of this misalignment on the device resistance, calculations have been performed for systems with $\theta = 10°$ in which the angle δ is 0.1°, 1°, 2° and $-1°$. The averaged probe resistance profiles are plotted in figure 6.7. It can be seen that the asymptotic resistance values are dependent on the degree of misalignment δ, whilst the resistance profile varies linearly when the domain wall is located between the probes. When the domain wall is located to the left of the probes, at sufficient distance so that none of the perturbed current is measured, then the longitudinal resistance

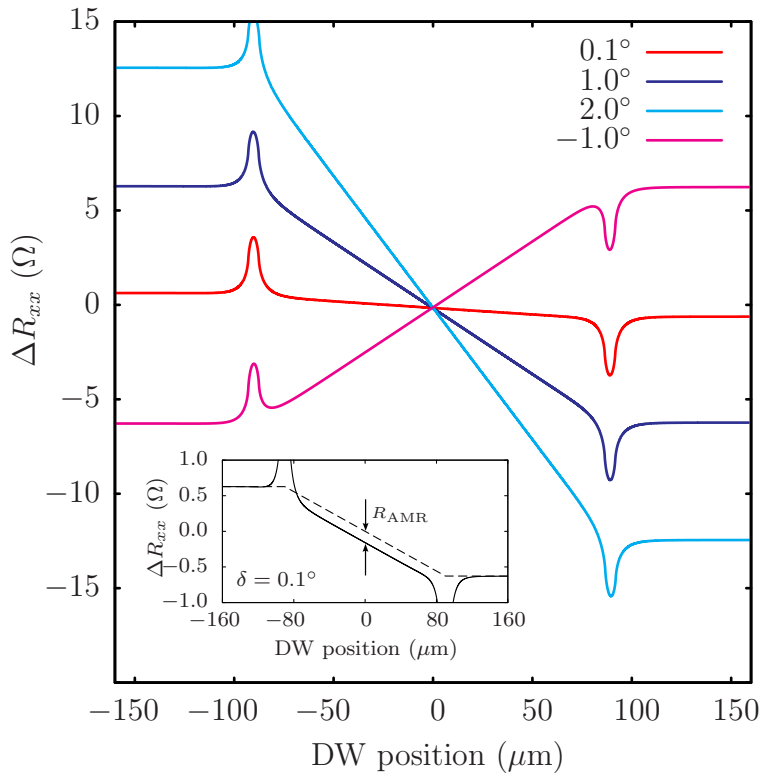

Figure 6.7: Averaged resistance measured between probes at the edges of the sample as a function of domain wall position. The value of θ is 10°, whilst the key displays values of the misalignment angle δ. [*inset*] Replot of the $\delta = 0.1°$ curve with a narrowed vertical range. The dashed line is the linear interpolation that describes the resistance variation in the absence of a perturbed current. A similar offset is found in the other three systems studied.

is that of a single region with magnetisation angle ϕ_2. Likewise, when the domain wall is sufficiently far to the right of the probes the longitudinal resistivity is that of a domain of magnetisation angle ϕ_1. Given the fact that for these domain wall locations the current density near and between the probes will be $(J_0, 0)$ then the resistance measured between both sets of probes will be

$$R_1 = \frac{\bar{\rho}(1 + \frac{\beta}{2}\cos 2\phi_1)\ell}{wt} \qquad \text{and} \qquad R_2 = \frac{\bar{\rho}(1 + \frac{\beta}{2}\cos 2\phi_2)\ell}{wt}. \tag{6.30}$$

Thus the difference in asymptotic values ($\Delta R = R_2 - R_1$) is

$$\Delta R = -\frac{\bar{\rho}\beta\ell}{wt}\sin 2\phi \sin 2\delta. \tag{6.31}$$

The numerical results are in perfect agreement with this value. If we choose to ignore the current perturbation, then as the domain wall moves between the probes the measured resistance is a proportional contribution from the background resistivity of each domain. Thus for probes located at x_A and x_B, where $x_\mathrm{A} < x_\mathrm{B}$, the longitudinal inter-probe resistance due to the background current will be

$$R^0_{xx}(x) = \begin{cases} R_1 & x \leq x_A \\ \frac{R_2 x_B - R_1 x_A + (R_1 - R_2)x}{x_B - x_A} & x_A < x < x_B \\ R_2 & x \geq x_B \end{cases} \tag{6.32}$$

However, the numerical results show that the actual profile lies *below* this interpolation, due to the contribution from the current perturbation. The inset in figure 6.7 shows the calculated average resistance curve for the system with misalignment angle $\delta = 0.1°$. With the adjusted vertical range a clear offset from the interpolation (dashed line) can be seen, labelled on the plot as R_AMR. This curve has obvious similarities to that obtained experimentally by Tang *et al.*, shown in figure 6.3b, where a similar offset is attributed to an intrinsic domain wall resistance.

6.4 Analytic model of $\mathbf{R_{AMR}}$

The broad features of the resistance that exists in (Ga,Mn)As epilayers containing moving domain walls, in particular the effects of the domain wall inclination and misalignment from the easy axis of magnetisation have so far been established.

It has also been shown that the domain wall resistance lies below a straight line interpolation between the two asymptotic channel resistivities of the two magnetisation states, which has been attributed to the currents induced at the domain wall boundary. The aim of this section is demonstrate the existence of this new resistance analytically, and to derive a simple expression that provides an estimate of this AMR induced resistance, R_{AMR}.

The starting point is to note that the averaged longitudinal resistance measured along opposite sides of the device, used to eliminate contributions from the planar Hall effect, can be expressed in terms of a difference in voltages at either end of the device channel:

$$\begin{aligned} -I\langle R\rangle &= (V_B - V_A)/2 + (V_D - V_C)/2 \\ &= (V_B + V_D)/2 - (V_A + V_C)/2. \end{aligned} \tag{6.33}$$

Assuming that the probe separation is large enough so that the eddy currents are fully contained within the area defined by the four probes, then the current between points A and C; and B and D is given by $(J_0, 0)$. The electric field is therefore constant and the potential varies linearly between probes C and A; and B and D. The voltage averages in equation 6.33 can be combined by the use of $V(-\ell/2, y) - V(0, y) = -\int_{-\ell/2}^{\ell/2} E_x(x, y)\, dx$ to give $\langle R\rangle$ in terms of an integral of the electric field over the area of the device defined by the probes:

$$I\langle R\rangle = \frac{1}{w}\int_{x=-\ell/2}^{\ell/2}\int_{y=-w/2}^{w/2} E_x(x, y)\, dx\, dy. \tag{6.34}$$

By integrating the continuity equation over regions $\Omega = \{(x', y) \in \mathbb{R}^2 | -\ell/2 \leq x' \leq x, -w/2 \leq y \leq w/2\}$ and $\Omega = \{(x, y') \in \mathbb{R}^2 | -\ell/2 \leq x \leq \ell/2, -w/2 \leq y' \leq y\}$ it can be shown (see Appendix C) that

$$\int_{-w/2}^{w/2} J_x(x, y)\, dy = J_0 w, \qquad \int_{-\ell/2}^{\ell/2} J_y(x, y)\, dx = 0. \tag{6.35}$$

By splitting equation (6.34) into contributions from both domains in which each of the resistivity contributions is constant, replacing E_x by $\rho_{xx}J_x + \rho_{xy}J_y$ and

using (6.35), one finds

$$\langle R\rangle = \frac{1}{wt}\left[\rho^1_{xx}\left(\frac{\ell}{2}+x_0\right)+\rho^2_{xx}\left(\frac{\ell}{2}-x_0\right)\right]+\frac{1}{J_0w^2t}(\rho^1_{xy} - \rho^2_{xy})\int_{x=-\ell/2}^{x_0}\int_{y=-w/2}^{w/2} J_y(x,y)\,dx\,dy, \tag{6.36}$$

where x_0 is the location of the domain wall. The first term in square brackets is the linear interpolation between the asymptotic values that was previously described. This interpolation was used by Tang *et al.* in interpreting their experimental results, and was assumed to represent the "extrinsic" resistance expected in the device channel. However, the final term in equation (6.36) is a contribution that does not appear in Tang and Roukes' solution, and which clearly deviates from the simple interpolation method they employed. The source of this term is the current loop that is formed as a result of the discontinuity of the resistivity tensor at the domain wall, and as seen in numerical results presented in the previous section it is found to give a negative contribution to the device resistance. To proceed in estimating the magnitude of this additional contribution, the case where $-\phi_1 = \phi_2 = \phi$ is considered, which applies when $\delta = 0$. The diagonal components of the resistivity tensor are continuous across the domain wall and the off-diagonal components change sign. If the magnitude of β is small then the J_x contribution will be dominated by the uniform background current J_0, except within a distance $\approx \beta w$ of the sides of the device near the domain wall where the edge current perturbation is concentrated. If this edge correction is neglected then it follows from matching equations (6.13) and (6.14) at the interface that immediately on either side of the domain wall,

$$J_y(x_0 \pm 0^+, y) \simeq \mp\frac{J_0\beta}{2}\sin 2\phi. \tag{6.37}$$

Ignoring anisotropy, the slowest decaying current perturbation will decay like $\exp(-\pi|x|/w)$ [204], and making the assumption that J_y decays with this profile, i.e.

$$J_y(x,y) \simeq \mp\frac{J_0\beta}{2}\sin 2\phi\ \exp(-\pi|x|/w), \tag{6.38}$$

it is possible to evaluate integral 6.36 to obtain the intrinsic AMR contribution

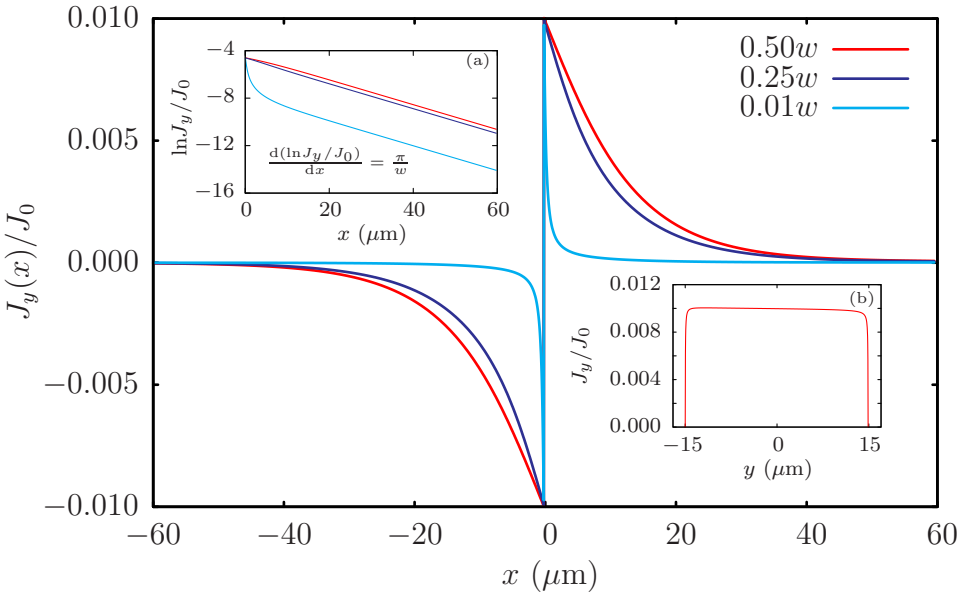

Figure 6.8: $J_y(x)$ profiles at different values of y for a domain wall located at $x = 0\mu$. The red line is taken down the centre of the channel, the dark blue line at $0.25w$ away from the top edge, and finally the cyan line is at a distance $0.01w$ away from the top edge. [*inset* (a)] Logarithmic representation of these currents, the linear regions have gradients π/w. [*inset* (b)] J_y at interface.

to the averaged longitudinal resistance,

$$R_{\mathrm{AMR}} = -R_{\square}\frac{\beta^2}{2\pi}\sin^2 2\phi, \tag{6.39}$$

where $R_{\square} = \bar{\rho}/t$ is the sheet resistance. This is the desired analytic expression for the new resistance contribution.

This result confirms that the resistance due to the circulating current is negative, as was previously found in the numerical calculations. It is also notable that this expression is independent of the width w of the device, also in agreement with the numerical findings. However, the approximations made regarding the values of J_y at the interface, and the decay rate of the current will result in differences between (6.39) and the true value of R_{AMR}, for which a full numerical treatment is required. Figure 6.8 shows the $J_y(x)$ current profile for a typical system, with $\beta = -0.02$, and giving an interface value of $\approx \mp 0.01 J_0$, as predicted by equation (6.37). The $J_y(x)$ cross section is shown at different value of y, and it can be seen that near the edges of the sample (blue line), the J_y component decays more rapidly than at the centre of the channel (red line). This deviation from the exponential decay assumed in our analytic model is highlighted in inset (a)

of figure 6.8, which shows the logarithm of $|J_y|$ versus x. Along the centre of the channel and at $0.25w$ from the edges the deviation is small from the π/w gradient expected from equation (6.38). However, at the edges of the device a significant difference is found, and consequently the actual magnitude of the negative resistance will be slightly *lower* than the value predicted by expression (6.39). Inset (b) shows the value of J_y along the domain wall, showing the interfacial value in (6.37) holds true apart from at the very edges of the sample.

Figure 6.9 displays a comparison between the analytic estimate (6.39) and the full numerical solutions for evaluating R_{AMR} for different values of β. It is found that the magnitude of the negative resistance predicted by the analytic expression is greater, consistent with overestimate of the current integral. The resistance magnitudes are of the order 15% lower in the numerical study, but the analytic expression still has some value in estimating this contribution. The β^2 relationship predicted by the analytic expression is seen to describe the numerical result, with the current loop reversing its rotation for positive value of β.

Finally, figure 6.10 shows the variation of the numerically calculated value of R_{AMR} with respect to the domain wall inclination θ and misalignment δ. The analytic expression defined above is not valid for these cases. It can be seen that R_{AMR} decreases for greater wall inclinations, θ, due to the decreasing negative contribution from the J_y current component as the wall is inclined. The inset of figure 6.10 shows that R_{AMR} is relatively insensitive to realistic values of the misalignment angle, δ.

6.5 R_{AMR} contribution to experiment

In this section, the results and calculations of the previous sections are applied to the (Ga,Mn)As epilayer devices studied experimentally.

To determine the anisotropy factor β of the sample, equation (6.29) describing the difference between the resistance measured along the top and bottom of a channel for a domain wall at $x = 0$ was used to interpret the experimental data reported in [87]. This yields a value of $\beta \approx -0.03$ which is used in the following calculations.

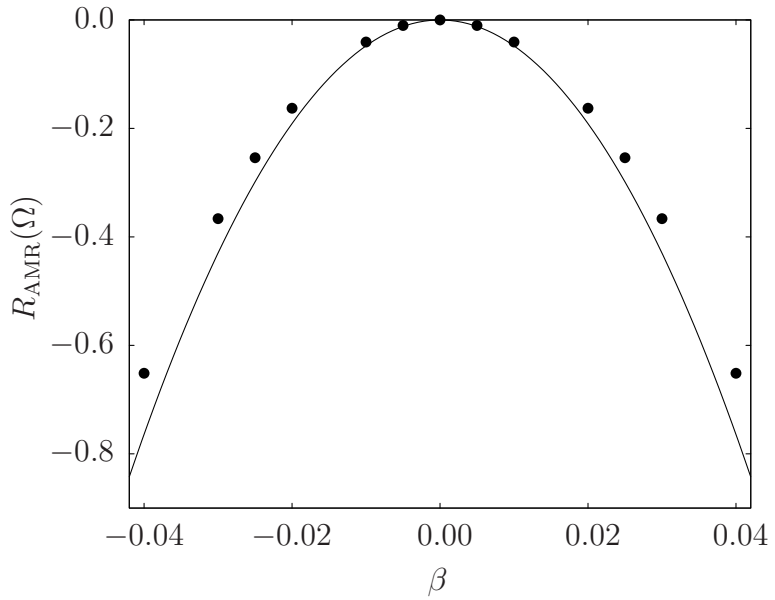

Figure 6.9: Calculated extrinsic AMR contribution to the resistance across a domain wall with respect to the value of β. Numerical results are denoted by symbols, whilst the solid line is equation (6.39). Parameters used are $\bar{\rho} = 3 \times 10^{-4}\ \Omega$ m, $\delta = 0°$ and $-\phi_1 = \phi_2 = 45°$, $\theta = 0°$, $w = 30\ \mu$m, $\ell/w = 6$ and $t = 100$ nm.

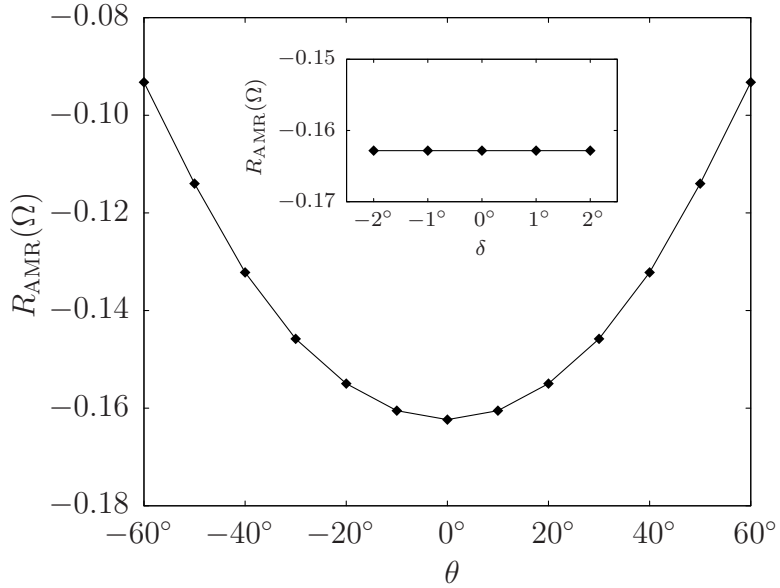

Figure 6.10: Calculated extrinsic AMR contribution to the resistance across a domain wall with respect to the domain wall inclination, θ. [*inset*] Dependence of R_{AMR} on the misalignment angle δ. Default parameters are $\beta = -0.02$, $\bar{\rho} = 3 \times 10^{-4}\Omega$ m, $\delta = 0°$ and $-\phi_1 = \phi_2 = 45°$, $\theta = 0°$, $w = 30\ \mu$m, $\ell/w = 6$ and $t = 100$ nm.

Firstly the 30 μm and 60 μm wide systems are modelled, corresponding to systems 2 and 3 in the Chapter introduction. For these epilayers the background resistivity is quoted as 3×10^{-4} Ω m, and the quoted thickness is $t = 100$ nm. The value $\phi = 45°$ has been used in the illustrative examples given in the previous section, however due to the presence of an uniaxial anisotropy in the experimental samples, a value $\phi = 37°$ is now used [200]. The difference in the asymptotic value visible in figure 6.3b is 5 Ω, giving a misalignment of $\delta = 0.28°$ via equation 6.31. Note that this is larger than the misalignment quoted by Tang *et al.*. The domain walls form with a small random orientation with a quoted dispersion of $\pm 20°$. For these two systems the value used in the simulations was $\theta = 20°$. Calculations were performed on samples with both values of the channel width. The results found are that the resistance is lowered by 0.33 Ω as a result of the eddy currents induced at the domain wall. The resistance profile $\Delta R_{xx}(x)$ for a system with $w = 30$ μm is shown in figure 6.11, for a domain inclined at $\theta = 20°$.

The initial test device is now considered, reported as system 1 in the Chapter introduction. From the documented work of Tang *et al.* the following parameters can be deduced: $\bar{\rho} = 4 \times 10^{-4}$ Ω m, $t = 150$ nm, $\beta = -0.03$ with channel width $w = 100$ μm and probe separation $\ell = 200$ μm. The angle ϕ is $-37°$ and $\delta = 1.5°$. The greater structure seen experimentally in ΔR_{xx} is due to the lower aspect ratio and larger domain wall inclination; using $\theta = 50°$ gives a reasonable reproduction of figure 6.1b. As a result, the linear regime is present only over a small range of domain wall positions, midway between the voltage probes. In this regime the large spacial extent of the eddy current relative to the probe spacing affects the slope of the resistance curve, which no longer coincides with a linear interpolation of the asymptotic resistances. The dashed line in figure 6.12 represents a line that is parallel to the linear section, to give an indication of the extent of R_{AMR}. The calculated resistance is lowered by 0.16 Ω due to these current, although if the aspect ratio were increased to fully contain the eddy currents, then this value would be 0.18 Ω.

6.6 Discussion

Before discussing the implications of the new resistance R_{AMR} to the interpretation of domain wall resistance measurements in (Ga,Mn)As, there remains an-

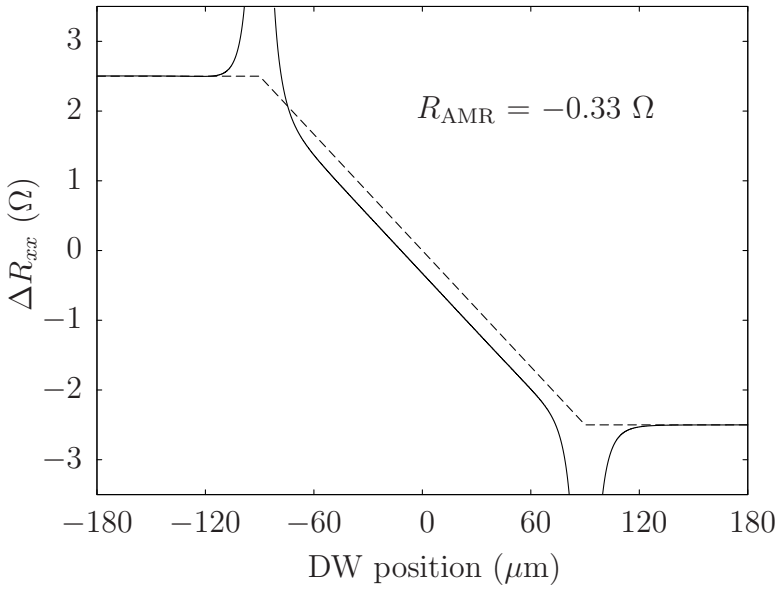

Figure 6.11: Average probe resistance profile along the sides of the channel. The dashed line represents the linear interpolation used by Tang and Roukes. [$\beta = -0.03$, $\bar{\rho} = 3 \times 10^{-4}\ \Omega$ m, $\phi = 37°$, $\theta = 20°$, $\delta = 0.28°$, $w = 60\ \mu$m and $t = 100$ nm]

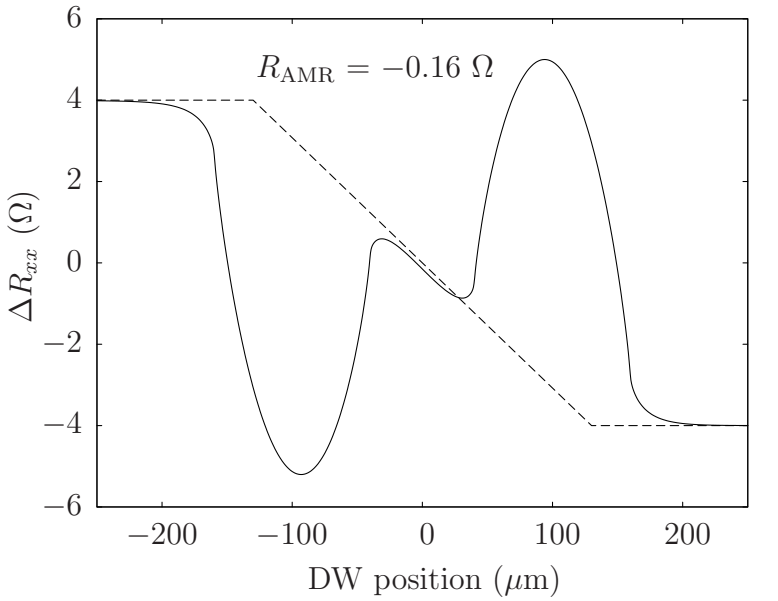

Figure 6.12: Averaged longitudinal resistance of a moving domain wall in a system with parameters $\beta = -0.03$, $\bar{\rho} = 4 \times 10^{-4}\ \Omega$, $\phi = -37°$, $\theta = 50°$, $\delta = 1.5°$, $w = 100\ \mu$m and $t = 150$ nm. For direct comparison with system 1 of Tang *et al.*.

other potentially significant contribution to the measured resistance that must be considered. The vectors of the resistivity anisotropy due to the AMR effect coincide with the direction of the local magnetisation, and at a domain wall a rapid rotation occurs in both. As a result a domain wall can alter the longitudinal potential via this mechanism with modifications to the electric field given by equation (6.24). Other authors have studied this phenomena, including Kläui *et al.* [205], who found a negative contribution to the resistivity both theoretically and experimentally in notched Py rings containing domain walls.

A realistic profile for a Néel-like wall separating two domains with magnetisation $\phi_1 = \pm 45^\circ$ and $\phi_2 = \mp 45^\circ$ is given in radians by the expression [206]

$$\phi(x) = \mp \frac{1}{2} \arctan \left[\sinh \frac{\pi x}{d} \right], \tag{6.40}$$

where d is the domain wall width. For a system with $\theta = 0^\circ$ the potential change along a domain wall placed symmetrically between the probes so that $x_0 = 0$ μm is given by

$$V = - \int_{\ell/2}^{-\ell/2} \bar{\rho} \left(1 + \frac{\beta}{2} \cos 2\phi(x) \right) J_x \, dx, \tag{6.41}$$

where it is assumed that the perturbed current, $\delta \mathbf{J}$, is small compared to the uniform background current. The first term in this integral, $\bar{\rho} J_x$, is the contribution from the background resistivity and is thus removed in experimental results. Integrating the remaining term and using the profile defined in (6.40) gives the expression

$$R_{\mathrm{AMR}}^{\mathrm{dw}} = \frac{\bar{\rho} \beta d}{2wt} \tag{6.42}$$

for the domain wall rotational AMR contribution to the resistance. Using parameters taken from experiment for a 30 μm wide sample [$\beta = -0.03$, $\bar{\rho} = 3 \times 10^{-4}$ Ωm, $t = 100$ nm, $d = 10$ nm], $R_{\mathrm{AMR}}^{\mathrm{dw}}$ is found to be -0.015 Ω. The measured resistance offset of the 30 μm wide devices in the experiment is -1.0 Ω — roughly two order of magnitude greater. Since expression (6.42) is inversely proportional to the width of the channel the 60 μm wide has $R_{\mathrm{AMR}}^{\mathrm{dw}} = -0.0075$ Ω. The domain wall rotational AMR effect can therefore not account for a significant proportion of the measured signal. The same conclusions were reached when the domain wall profile is changed from that given in (6.40) to a linear variation.

In thin films with in-plane magnetisation a Néel wall has a lower energy than a Bloch-type wall due to the existence of energetically unfavourable free poles at the film surface in the latter case. Even in the case where a Bloch type wall is considered, any out of plane component of the magnetisation only reduces the contribution from the second term in integral (6.41), thus reducing the magnitude of this extrinsic contribution.

Thus we can safely ignore the influence of the magnetisation reversal within the wall itself as a contribution to the measured resistance change.

Table 6.2 compares the calculated value of R_{AMR} for the three systems studied experimentally, and the equivalent value of the offset that was measured. It is clear that the AMR which has been identified in this Chapter term makes a large contribution to, and can largely explain, the negative values observed in the experiment, with the exception of one set of devices where a true negative intrinsic domain wall resistance may indeed have been observed. In previous studies [55] on 180° domain walls in (Ga,Mn)As a positive domain wall resistance was found after accounting for sizable contributions from the extraordinary Hall effect. Clearly, further studies are required before any quantitative conclusions can be drawn about the intrinsic contribution to the resistance of a domain wall with any degree of confidence. On the basis of the results obtained here, it is possible to identify the desirable characteristics of any subsequent experimental studies. In such devices it will be preferable to have a large probe separation to width ratio to enlarge the linear region of ΔR_{xx} between the probes, and for the same reason, keeping the domain wall perpendicular to the channel is also desirable.

System	Width μm	Experiment Ω	R_{AMR} Ω
1	100	-0.44 ± 0.5	-0.16
2	30	-1.0 ± 0.2	-0.33
3	60	-0.3 ± 0.2	-0.33

Table 6.2: Comparison of resistance offsets determined from experiment, and values of R_{AMR} found from the numerical model for the 3 unique classes of systems.

6.7 Summary

In this Chapter the domain wall resistance has been studied in devices based on the dilute magnetic semiconductor (Ga,Mn)As. The motivation for the work comes from experiments of Tang *et al.* [87], who performed measurements on epilayers containing mobile domain walls. Resistance profiles of these moving walls were obtained by averaging measurements of the longitudinal potential between sets of probes situated along the top and bottom of the sample. A model was presented and solved by Tang and Roukes [202] to obtain the current induced near a domain wall based on the homogenous resistivity tensor in a ferromagnetic domain. Comparing the resistance profiles predicted with those found experimentally, the differences were attributed to an intrinsic domain wall resistance. However, it has been shown in this Chapter that errors were made in their theoretical analysis, and that the analytical expression from which the currents were obtained does not satisfy the governing equations.

The model used in Chapter 5 was extended to these systems and solved numerically by an overdriven Gauss-Seidl method. The influence of the domain wall inclination and device misalignment on the resistance profiles have been studied, and useful equations obtained for the values of the differences relevant to the experiment. A new contribution has been identified to the longitudinal resistance measured when the domain wall is situated between the probes, that survives the averaging procedure used by Tang *et al.*. This contribution is absent in the analysis of Tang and Roukes. The sign of this resistance is found to be negative — independent of the magnetisation angles and domain wall inclination. An expression that provide an estimate of this resistance has been derived for domain walls aligned perpendicularly to the channel, this may be useful for further experimental work in this field. To obtain more accurate results, or to model inclined domain walls, a numerical procedure as outline in this Chapter has been found to be necessary.

On the basis of calculations that simulate the systems measured experimentally to date, it is found that this new resistance can account for the resistance attributed to an intrinsic domain wall contribution in two sets of devices. A third set cannot be fully accounted for by this AMR induced resistance, so it is possible that a true negative intrinsic domain wall resistance was measured in these samples. To fully understand the situation, further experimental measurements are desirable.

Chapter 7

Conclusions

This thesis has documented investigations of the physics in systems containing ferromagnetic domain walls. These regions of rotating magnetisation have, until recent years, been largely neglected in terms of both experimental and theoretical efforts. However the growth in the field of spintronics, fuelled by ever increasing data storage and processing demands, has seen the physics of domain walls being pursued with increased vigour. The transport properties of domain walls have been the subject of much contention in the literature, with little consensus on the sign let alone the magnitude of the domain wall resistance. The object of this thesis has been to further understanding of this matter by applying theoretical methods to examine systems investigated in experimental studies.

The primary experimental motivation for this work was experiments on Cobalt-Platinum trilayers in which the precise magnetic properties are controlled with remarkable spatial resolution using focused Ga ion beam irradiation. In these systems, an ultra-thin layer of Cobalt is deposited between a Platinum substrate and capping layer by a sputtering technique, and the strong out-of-plane uniaxial magnetocrystalline anisotropy reduced locally by the irradiation procedure through an increase in interfacial roughness at the Cobalt-Platinum boundary. This was exploited in the experiments to form reproducible 'artificial' domains that allow the pinning of domain walls for study. The magnetisation properties of irradiated samples were probed experimentally by hysteresis curves obtained from Hall effect measurements, before transport experiments were conducted on the artificially induced domain walls. Several different theoretical techniques

were required to illuminate the magnetism and transport properties of these systems, and the opportunity arose to extend the study to domain wall transport in (Ga,Mn)As devices. We will now briefly review each chapter and revisit the primary conclusions of each.

The magnetic properties of Cobalt Platinum systems were studied theoretically in Chapter 2 by the LKKR technique, a method designed specifically to deal with layered materials. The *ab initio* scattering framework is based on density functional theory, and was used here to obtain self-consistent potentials for systems that can usefully be compared to experiment. Initially bulk Cobalt systems were studied, and it was demonstrated that the electronic density of states around the Fermi energy is sensitive to the atomic volume, with clear band narrowing of the dominant *d*-bands observed as the inter-atomic spacing is decreased. Multilayers of mixed Cobalt and Platinum were subsequently studied in both the (111) and (100) layered geometries for systems that were constrained to adopt a rigid Platinum structure. Attempts were made to improve on this structural approximation by considering more realistic lattices. The tool employed for such a lattice relaxation task was the planewave DFT code CASTEP. It was however found that the pseudopotentials tested in the code cannot fully reproduce the results of full or spherically averaged potential calculations from the literature. In light of this, a volume conserving relaxation scheme was used and the results of the previous multilayer studies reconverged with these new structures. It was found that in both relaxed and unrelaxed cases that the Cobalt atomic moment is increased slightly (0.1–0.4 μ_b) in the systems tested, whilst Platinum atoms near the interface break their spin degeneracy to obtain a small polarisation (0.1–0.3 μ_b) that decays rapidly away from the Cobalt interface. To better match the situation found experimentally, these calculation were extended to surface systems. Here the trilayer is built upon a semi-infinite frozen potential bulk halfspace, with self-consistent relaxation of potentials allowed for the atoms placed on the surface. It was found that the increased magnetic polarisations found in the multilayer systems persists in these surface systems, for both relaxed and unrelaxed structures. Finally, to perform a study of disordered alloying effects in these systems the coherent potential approximation was employed, that, when coupled with the LKKR, allows the placement of an effective medium representing an alloy in the above systems on a layer by layer basis. Initially a study was performed on bulk alloy using a rigid structure, followed by concentration dependent relaxed lattices that used structural information gathered from the literature. It

was found that the concentration dependence of the magnetic moment in bulk alloys could also give a reasonable quantitative indication of the moments of an interfacial alloyed layer in surface calculations. Regarding the systems fabricated experimentally, it can be deduced from these calculations that the magnetic properties vary smoothly with respect to chemical composition, and no anomalous behaviour was found with respect to the magnetism in these systems. It can also be inferred that, although the material may not be chemically homogenous, the induced magnetisation on the Platinum atoms results in a material that is magnetically continuous, a fact that is useful for creating effective devices based on this material.

To extend the electronic structure work it would be interesting to perform these calculations in a fully relativistic picture allowing access to information about the spin-orbit effect in this material, that is expected to enhance the measured magnetic moment. In addition, the rigid lattice and volume conserving structures used in the above calculations could yet be improved upon by lattice relaxation calculations, either with improved CASTEP pseudopotentials or with other high accuracy methods.

The next study, documented in Chapter 3, made use of a micromagnetics framework to analyse the results of hysteresis measurements performed on Cobalt-Platinum trilayers undergoing a magnetic reversal due to an applied field. The irradiation procedure was used to define a region of lowered anisotropy of area $3\times X$ μm^2 , where X=0.5, 1, 2 and 4, that is favourable to the formation of a domain. The OOMMF code that has become a standard in micromagnetic calculations was used as the principle investigative tool in this work. Owing to the uncertainty in the relevant material parameters of the Cobalt Platinum systems modelled, calculations were performed in which the parameters were varied. It was found that an abrupt transition occurs between a largely in-plane and fully out-of-plane magnetisation regime, that was shown to depend on the balance between the magnetostatic and anisotropy energies.

Comparing the predicted hysteresis behaviour to that measured experimentally it was found that the systems breaks down rapidly from a fully saturated state to a three domain state in both cases, however the breakdown fields were unfeasibly high in the simulations. This was explained by contrasting the homogenous material modelled in the theory with the experimental systems that contain many

defects due to alloying and structural deviations. In the latter case these imperfections provide nucleation sites for the domain breakdown mechanism that lower the reversal fields considerably.

In the reverse sweep a different reversal process was found when going back from the three to single domain state. In the simulation the domain walls were found to travel from the artifical domain boundaries to meet in the centre and are eventually destroyed once the opposing demagnetising field is overcome. This interpretation was found to be consistent with experimental results, although in the experiment Barkhausen jumps are clearly observed, in which the domain wall motion is retarded by the pinning effects of impurities.

In terms of future work it would be interesting to study the effects of impurities in more detail. To do this a finite element code would provide greater flexibility in terms of defining the material properties on a point by point basis.

Transport calculations are usually performed in one of two frameworks: ballistic and diffusive. The former, when applied to domain wall systems, assumes that the mean free path of an electron is greater than the width of the domain wall, so that a tunnelling problem is present. Although the domain wall transport here is expected to be diffusive, a ballistic conductance framework was used initially to explore this limit in multilayer systems. To obtain realistic band structures the tight binding approximation was employed, and parameters obtained by fitting to APW calculations to account for alloying and structural effects. A formalism was presented to construct a systems from slices that are perpendicular to the direction of current flow, and allowing the Green function of a system comprising of an active region embedded between two semi-infinite leads to be determined. Transport properties were deduced in the Landauer-Büttiker framework.

It was found that the results agree reasonably well with more accurate *ab initio* calculations on conductance and domain wall resistances in bulk Cobalt systems. The calculations were extended to trilayer structures for which a well defined conductance could be determined for individual layers of Cobalt and Platinum in larger systems. Introducing abrupt domain walls was found to reduce the conductance of these multilayers significantly, with a diluting effect provided by the Platinum layers, although this phenomenon did not match the predictions of a simple independent resistor model. As the domain wall width is increased

the wall resistance is rapidly suppressed, with realistic domain walls exhibiting resistances of a few percent. The dilution effect found in the abrupt wall limit does not persist and it was found that in this low reflection regime that the resistance is sensitive to the details of the bands at the Fermi energy, and a large range of values were found within the uncertainty in the Fermi energy position. It was concluded that the coherence in these systems means that they are not suitable for studying transport in the experimentally fabricated trilayers, where impurity scattering leads to a diffusive transport regime, for which a more phenomenological approach is required.

The key experimental study analysed in this thesis is of the angular dependence of domain wall resistivity in Cobalt-Platinum trilayers. Taking advantage of the precise nature of the irradiation procedure it has been found possible to form domain walls at arbitrary angles to the current, thus allowing the exploration of angle dependent properties. In the experiment a 'superlattice' system was employed containing multiple domain walls with a separation of 1 μm. It was shown that the domain wall resistance scales linearly with the number of domain walls providing supporting evidence that the intrinsic domain wall resistance was measured.

To study these systems theoretically, a model was developed in the diffusive limit in terms of homogenous, anisotropic resistivity tensors that can be defined in separate regions along the channel. In the model, described in Chapter 5, a domain consists of an isotropic background resistivity, and a domain wall, which should exhibit anisotropic resistivity according to the theory of Levy and Zhang, defined by tensor elements parallel and perpendicular to the domain wall surface. The sought-after current distribution was obtained via a suitable PDE and boundary conditions in terms of a scalar stream function, with appropriate coordinate transforms that facilitate the use of the finite difference method. The solution was converged using an overdriven Gauss-Seidl method, and, once converged, physical quantities were obtained from the stream function via given equations.

It was found that for inclined walls currents are induced near the domain wall boundary that may provide a contribution to the mentioned resistance. In addition to this single wall effect an overlap with neighbouring walls can in principle also contribute to the resistance but it was shown that in the experimental systems the domain wall separation is sufficient to exclude any such interference,

thus the properties of a single domain wall are isolated in these studies. Evidence was also found that the length of the device channel used was sufficient to fully contain the current perturbations, confirming that the effects observed experimentally represents the full domain wall induced contributions. The calculations also demonstrated that the increase in local resistivity from the irradiation procedure has a negligible effect on the domain wall resistance.

Using test parameters for the system resistivities it was found that a potential shift exists across a domain wall that is a function the domain wall angle, θ. By analysing the contributions from the electric field expanded in terms of perturbed and background contributions from the resistivities and currents, the term responsible for the calculated potential difference was identified. From this a simple analytic expression was developed which is found to account for the angular dependence of domain wall resistivity in these systems, with a $\cos^2\theta$ dependence found, where θ is the domain wall angle. This model was used to extract the resistivity elements of a domain wall from experimental data, and it was found that for a domain wall in the Cobalt-Platinum trilayers that $\rho_\perp = (23.1 \pm 1.1) \times 10^{-3}$ $\mu\Omega$ cm and $\rho_\parallel = (3.5 \pm 0.7) \times 10^{-3}$ $\mu\Omega$ cm. The perpendicular domain wall resistivity in these systems was therefore deduced to be 0.11% of the background value. These resistivities were compared to LKKR calculations of the spin ratio via the theory of Levy and Zhang, and were found to be consistent, thereby providing an important verification of the Levy-Zhang model.

In the final theoretical study presented in this thesis, the formalism used to study the Pt/Co/Pt trilayers was extended to analyse domain walls in the dilute magnetic semiconductor (Ga,Mn)As, motivated by the recent experiments of Tang *et al.* [87]. In their work, the longitudinal resistance profile of a moving domain wall was measured along the top and bottom of a channel by a set of fixed probes, with the averaged profile used to cancel out the transverse Hall effect phenomena that arises as a result of the anomalous magnetoresistance that is present in this material. To extract the intrinsic domain wall resistance from these profiles Tang *et al.* used an analytic model in which contributions to the profile resistance from induced circulating currents were analysed. The difference between theory and experiment was attributed to an intrinsic domain wall contribution, that was found to be negative in value, and in a particular set of systems analysed experimentally implied resistance free transport through the domain wall. A different conclusion was arrived at on the basis of the analysis made in Chapter 6, which

are attributed to a number of errors identified in the derivation and analysis of the model used by Tang *et al.*. In Chapter 6 equations describing transport across the domain wall and suitable for numerical solution have been developed. The resistance profiles obtained from this new analysis have been documented with respect to the domain wall angle and device misalignment angle, and a new, negative, contribution to the resistance identified, termed R_{AMR}.

The origin of this term was highlighted via an analytic analysis, and an useful expression was derived for its magnitude in the case of a perpendicular domain wall, although numerical results are required in more general cases. Applying the analysis to the (Ga,Mn)As domain wall systems studied by Tang *et al.*, it was shown that the negative resistance they measured can largely be explained by this R_{AMR} term in two systems, while a genuine negative intrinsic domain wall resistance may have been measured in a third.

In terms of future work, further experimental study is invited to clarify the issues raised in this chapter, with the hope of deducing the true intrinsic domain wall resistances in these (Ga,Mn)As systems.

In this thesis the properties of domain wall containing systems have been investigated, and advances made in the understanding and characterisation of these systems, and the theoretical techniques used to analyse them. Undoubtedly, ferromagnetic domain walls are an area of research that has a promising future in terms of both academic study and potential applications.

Appendix A

Supplementary LKKR results

This appendix contains data that may be useful to readers studying Cobalt Platinum systems.

Figure A.1 shows a fit of data acquired from the literature on the lattice spacing of bulk Cobalt-Platinum alloy as a function of the elemental concentration. These spacings are used in the LKKR calculations presented in Chapter 2.

Tables A.1a and A.1b contain data used to generate figures 2.7a and 2.7b showing the layer resolved magnetic moments of (111) [Pt]/Pt_3/Co_n/Pt_7 surface systems in both unrelaxed and relaxed lattices. Tables A.2a and A.2b contain the equivalent for the (100) surfaces plotted in figures 2.8a and 2.8b.

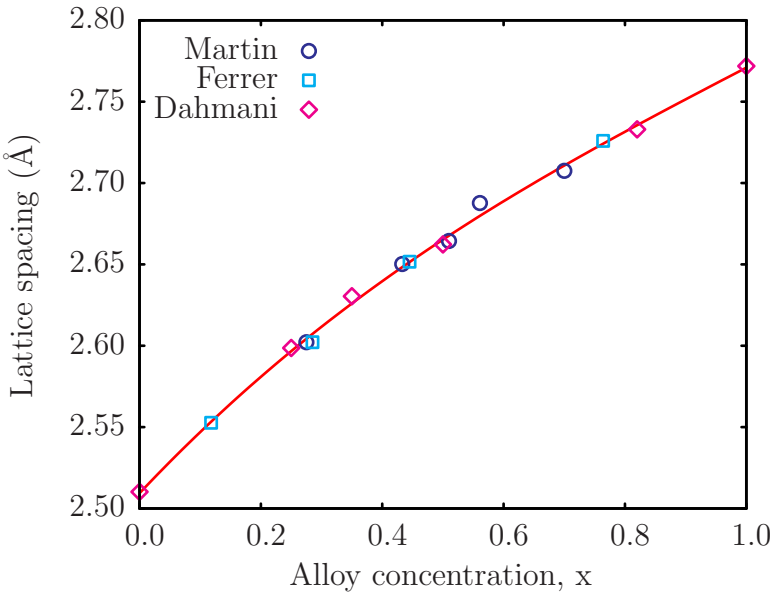

Figure A.1: Polynomial curve fit of experimental data on the lattice spacing of Co_xPt_{1-x} disordered alloy. Values are taken from the works of Martin [207], Ferrer [134] and Dahmani [208].

15	-	-	-	-	0.00
14	-	-	-	0.00	0.01
13	-	-	0.00	0.01	0.01
12	-	0.01	0.01	0.01	0.02
11	0.00	0.01	0.01	0.02	0.03
10	0.01	0.02	0.02	0.03	0.08
9	0.01	0.02	0.03	0.08	0.20
8	0.01	0.04	0.09	0.20	1.88
7	0.03	0.08	0.20	1.87	1.77
6	0.09	0.21	1.88	1.76	1.76
5	0.24	1.88	1.78	1.76	1.76
4	1.99	1.89	1.88	1.87	1.87
3	0.23	0.20	0.20	0.20	0.20
2	0.08	0.07	0.08	0.07	0.07
1	0.02	0.02	0.02	0.02	0.02
0	0.00	0.00	0.00	0.00	0.00

(a)

15	-	-	-	-	0.00
14	-	-	-	0.01	0.01
13	-	-	0.01	0.01	0.01
12	-	0.01	0.02	0.01	0.01
11	0.01	0.02	0.02	0.01	0.02
10	0.04	0.03	0.02	0.02	0.07
9	0.04	0.03	0.02	0.06	0.23
8	0.04	0.03	0.07	0.22	1.84
7	0.03	0.07	0.24	1.84	1.85
6	0.07	0.23	1.84	1.86	1.85
5	0.25	1.83	1.87	1.86	1.85
4	1.82	1.83	1.84	1.84	1.84
3	0.24	0.22	0.23	0.22	0.23
2	0.04	0.06	0.06	0.05	0.06
1	−0.01	0.01	0.00	0.00	0.01
0	0.00	0.00	0.00	0.00	0.00

(b)

Table A.1: Tabulated results of layer resolved moments in Co_nPt_7 (111) surface systems for (a) unrelaxed and (b) relaxed systems.

15	-	-	-	-	0.03
14	-	-	-	0.03	0.02
13	-	-	0.03	0.02	0.02
12	-	0.03	0.02	0.02	0.01
11	0.03	0.02	0.02	0.01	0.04
10	0.02	0.02	0.01	0.04	0.10
9	0.01	0.01	0.03	0.10	0.24
8	0.01	0.03	0.09	0.24	1.91
7	0.04	0.10	0.24	1.91	1.78
6	0.10	0.24	1.91	1.78	1.77
5	0.28	1.92	1.79	1.78	1.78
4	2.05	1.91	1.91	1.90	1.91
3	0.27	0.23	0.23	0.23	0.23
2	0.09	0.09	0.08	0.09	0.09
1	0.03	0.02	0.02	0.02	0.02
0	0.00	0.00	0.00	0.00	0.00

(a)

15	-	-	-	-	0.03
14	-	-	-	0.02	0.02
13	-	-	0.03	0.02	0.02
12	-	0.02	0.03	0.01	0.01
11	0.02	0.02	0.02	0.01	0.04
10	0.02	0.01	0.01	0.03	0.10
9	0.01	0.01	0.04	0.09	0.27
8	0.00	0.03	0.10	0.26	1.84
7	0.02	0.09	0.28	1.84	1.75
6	0.07	0.25	1.85	1.75	1.76
5	0.29	1.82	1.76	1.75	1.75
4	1.92	1.82	1.85	1.84	1.83
3	0.28	0.24	0.27	0.25	0.26
2	0.06	0.07	0.09	0.08	0.08
1	0.01	0.02	0.02	0.02	0.02
0	0.00	0.00	0.00	0.00	0.00

(b)

Table A.2: Tabulated results of layer resolved moments in Co_nPt_7 (100) surface systems for (a) unrelaxed and (b) relaxed systems.

Appendix B

Additional notes on meshing

B.1 Discretised derivatives

Here additional derivatives are presented in terms of the mesh and coordinate system used in Chapter 5 in solving for the stream function, ψ. Away from the boundaries in region l the derivative with respect to ξ is

$$\left.\frac{\partial \psi_{i,j}}{\partial \xi}\right|_{(\xi_i,\eta_j)} = \frac{\psi_{i+1,j} - \psi_{i-1,j}}{2\Delta\xi_l}. \tag{B.1}$$

At the interfaces between regions only points belonging to a specific region are used for calculating the derivatives, thus ξ^+ refers to the derivative to the right of the interface and ξ^- to the derivative on the left. For the same $O(\Delta\xi^2)$ scaling as above we have

$$\left.\frac{\partial \psi_{N_l,j}}{\partial \xi}\right|_{(\xi^{\pm}_{N_l},\eta_j)} = \frac{4\psi_{N_l\pm1,j} - \psi_{N_l\pm2,j} - 3\psi_{N_l,j}}{\pm 2\Delta\xi_l}. \tag{B.2}$$

The second derivative of η and ξ away from the boundaries are given by

$$\left.\frac{\partial^2 \psi_{i,j}}{\partial \eta^2}\right|_{(\xi_i,\eta_j)} = \frac{\psi_{i,j+1} + \psi_{i,j-1} - \psi_{i,j}}{\Delta\eta^2} \tag{B.3}$$

and

$$\left.\frac{\partial^2 \psi_{i,j}}{\partial \xi^2}\right|_{(\xi_i,\eta_j)} = \frac{\psi_{i+1,j} + \psi_{i-1,j} - \psi_{i,j}}{\Delta\xi_l^2}. \tag{B.4}$$

Finally the cross-derivative term is

$$\left.\frac{\partial^2 \psi_{i,j}}{\partial \xi \partial \eta}\right|_{(\xi_i,\eta_j)} = \frac{\psi_{i+1,j+1} - \psi_{i+1,j-1} - \psi_{i-1,j+1} + \psi_{i-1,j-1}}{4\Delta\xi_l\Delta\eta}. \tag{B.5}$$

B.2 Extension to non-parallel interfaces

In the work presented in Chapter 5 all domain interfaces were assumed to be parallel in alignment, having a common value of θ. However, it is possible that future modelling may require the study of systems with domain walls inclined at varying angles with respect to the current direction. The equations remain valid in this case as the prefactors are calculated in each domain separately. Figure B.1 shows a simple extension to the meshing, where a separating region is added to link two domains of differing geometry, while preserving the y and consequently η spacing of the system. In the example used here an arbitrary number of η points may be used, but along ξ the number of points is a function of η and must conform to

$$N_\xi(\eta_j) = \frac{N_\eta \eta_j}{w}, \tag{B.6}$$

where η_j is the value of η at the j^{th} point.

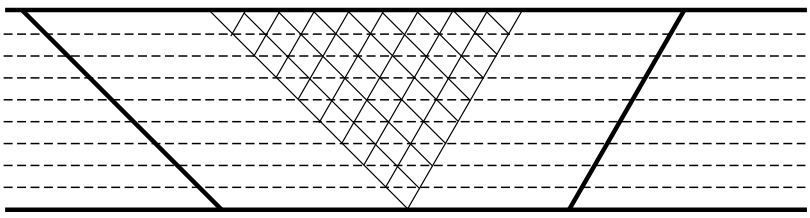

Figure B.1: Possible extension to the meshing scheme for a system with interfaces with differing values of θ. Domain walls are represented by thick black lines, while the central region show a mesh that couples the solution in the central domain while maintaining the spacing along the y axis (dashed lines).

Appendix C

Current integrals

Here proofs of the integrals (6.35) that were used in obtaining an analytic expression for the quantity R_{AMR} are presented. For the first integral, figure C.1 shows a device with the rectangular integral domain marked by the sides of the device and the dashed lines. The region shown here is to the left of the domain wall, with the left hand side boundary located between probes A and B. It is assumed that any current from the domain wall has decayed fully before reaching these probes, thus the current at this location is $(J_0, 0)$. Also, along the sides of the device no current can flow in or out, thus $J_y = 0$ at these locations. The right hand side boundary is located at an arbitrary longitudinal position, x, that may be to the left or right of the domain wall and may bisect a region containing a perturbed current.

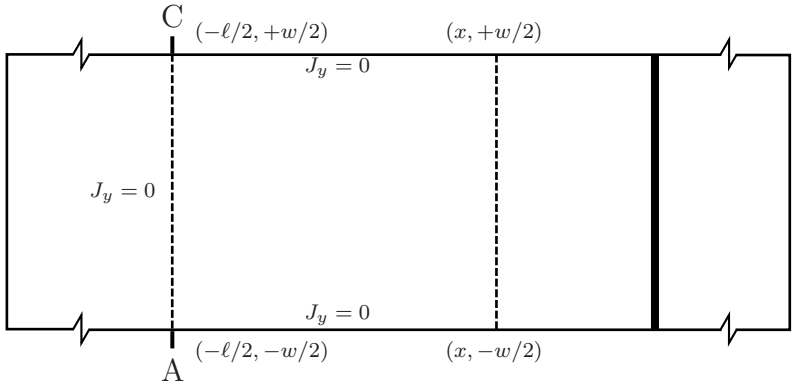

Figure C.1: System used for current integral. The domain wall is indicated by the thick line. A and C indicate the location of transverse probes, positioned at a distance $-\ell/2$ from the domain wall.

Integrating the current continuity condition $\nabla \cdot \mathbf{J} = 0$ over the rectangular region with coordinates (x', y) gives

$$\int_{-w/2}^{+w/2} \int_{-\ell/2}^{x} \frac{\partial J_x}{\partial x'} \, dx' \, dy = - \int_{-\ell/2}^{x} \int_{-w/2}^{+w/2} \frac{\partial J_y}{\partial y} \, dy \, dx'. \tag{C.1}$$

From the boundary condition that $J_y = 0$ at the top and bottom of the device the inner integral in the right hand side of this equation vanishes at at all locations along the device. Using this results and performing the inner integral of the left hand side of the above equation yields

$$\int_{-w/2}^{+w/2} (J_x(x, y) - J_x(-\ell/2, y)) \; dy = 0. \tag{C.2}$$

At $x' = -\ell/2$ the induced current has decayed fully and therefore $J_x = J_0$. Using this result and separating the above yields

$$\int_{-w/2}^{+w/2} J_x(x, y) \; dy = J_0 w. \tag{C.3}$$

The integral

$$\int_{-\ell/2}^{\ell/2} J_y(x, y) \; dx = 0 \tag{C.4}$$

is obtained in a similar fahsion.

References

[1] C. Kittel, *Introduction to solid state physics*, volume 7, Wiley, New York, 1996.

[2] J. Kondo, Progr. Theor. Phys. **27**, 772 (1962).

[3] B. A. Lilley, Philos. Mag. **41**, 792 (1950).

[4] L. Berger, J. Appl. Phys. **49**, 2156 (1978).

[5] L. Berger, J. Appl. Phys. **55**, 1954 (1984).

[6] L. Berger, J. Appl. Phys. **71**, 2721 (1992).

[7] C. H. Marrows, Adv. Phys. **54**, 585 (2005).

[8] E. Y. Tsymbal and D. G. Pettifor, *Perspectives of giant magnetoresistance, Solid State Physics*, volume 56, Academic Press, San Diego, 2001.

[9] W. Gerlach, Ann. Phys. **12**, 849 (1932).

[10] D. Steinberg and F. Miroschnischenko, Phys. Zeits. d. Sow. **3**, 602 (1933).

[11] C. W. Heaps, Phys. Rev. **45**, 320 (1934).

[12] A. Işin and R. V. Coleman, Phys. Rev. **142**, 372 (1966).

[13] G. R. Taylor, A. Isin, and R. V. Coleman, Phys. Rev. **165**, 621 (1968).

[14] P. W. Shumate, R. V. Coleman, and R. C. Fivaz, Phys. Rev. B **1**, 394 (1970).

[15] K. Okamoto, T. Shirakawa, S. Matsushita, and Y. Sakurai, A.I.P Conf. Proc. **24**, 113 (1974).

[16] K. Okamoto, M. Tanaka, S. Matsushita, Y. Sakurai, S. Honda, and T. Kusuda, A.I.P Conf. Proc. **34**, 55 (1976).

[17] M. Masuda, S. Yoshino, H. Tomita, and S. Uchiyama, A.I.P Conf. Proc. **34**, 58 (1976).

[18] G. G. Cabrera and L. M. Falicov, Phys. Stat. Sol. (b) **61**, 539 (1974).

[19] G. G. Cabrera and L. Falicov, Phys. Stat. Sol. (b) **62**, 217 (1974).

[20] M. Viret, D. Vignoles, D. Cole, J. M. D. Coey, W. Allen, D. S. Daniel, and J. F. Gregg, Phys. Rev. B **53**, 8464 (1996).

[21] P. M. Levy and S. Zhang, Phys. Rev. Lett. **79**, 5110 (1997).

[22] G. Tatara and H. Fukuyama, Phys. Rev. Lett. **78**, 3773 (1997).

[23] M. Brands, A. Carl, and G. Dumpich, Europhys. Letters **68**, 268 (2004).

[24] M. Brands, A. Carl, and G. Dumpich, Ann. Phys. **14**, 745 (2005).

[25] M. Brands, C. Hassel, A. Carl, and G. Dumpich, Phys. Rev. B **74**, 033406 (2006).

[26] P. A. E. Jonkers, S. J. Pickering, H. De Raedt, and G. Tatara, Phys. Rev. B **60**, 15970 (1999).

[27] J. B. A. N. van Hoof, K. M. Schep, A. Brataas, G. E. W. Bauer, and P. J. Kelly, Phys. Rev. B **59**, 138 (1999).

[28] A. Brataas, G. Tatara, and G. E. W. Bauer, Phys. Rev. B **60**, 3406 (1999).

[29] A. Braatas, G. Tatara, and G. Bauer, Phil. Mag. B **78**, 586 (1998).

[30] R. P. van Gorkom, A. Brataas, and G. E. W. Bauer, Phys. Rev. Lett. **83**, 4401 (1999).

[31] V. K. Dugaev, J. Barnas, A. Lusakowski, and L. A. Turski, Phys. Rev. B **65**, 224419 (2002).

[32] V. K. Dugaev, J. Barnas, A. Lusakowski, and L. A. Turski, Phys. Stat. Sol. (a) **196**, 177 (2003).

[33] V. K. Dugaev, J. Barnas, A. Lusakowski, and L. A. Turski, J. Supercon. **16**, 15 (2003).

[34] M. Dzero, L. P. Gor'kov, A. K. Zvezdin, and K. A. Zvezdin, Phys. Rev. B **67**, 100402 (2003).

[35] U. Ebels, A. Radulescu, Y. Henry, L. Piraux, and K. Ounadjela, Phys. Rev. Lett. **84**, 983 (2000).

[36] E. Šimánek, Phys. Rev. B **63**, 224412 (2001).

[37] S. Gallego, P. Weinberger, L. Szunyogh, P. M. Levy, and C. Sommers, Phys. Rev. B **68**, 054406 (2003).

[38] F. S. Bergeret, A. F. Volkov, and K. B. Efetov, Phys. Rev. B **66**, 184403 (2002).

[39] B. Y. Yavorsky, I. Mertig, A. Y. Perlov, A. N. Yaresko, and V. N. Antonov, Phys. Rev. B **66**, 174422 (2002).

[40] J. Kudrnovský, V. Drchal, I. Turek, P. Streda, and P. Bruno, Surf. Sci. **482**, 1107 (2001).

[41] R. G. Pereira and E. Miranda, Phys. Rev. B **69**, 140402 (2004).

[42] J. Inoue, H. Itoh, S. Mitani, and K. Takanashi, Phys. Rev. B **68**, 094418 (2003).

[43] Z. Zhang and S. Xiong, Phys. Rev. B **67**, 094412 (2003).

[44] V. A. Gopar, D. Weinmann, R. A. Jalabert, and R. L. Stamps, Phys. Rev. B **69**, 014426 (2004).

[45] P. E. Falloon, R. A. Jalabert, D. Weinmann, and R. L. Stamps, Phys. Rev. B **70**, 174424 (2004).

[46] T. Koma and M. Yamanaka, Phys. Rev. B **65**, 094404 (2002).

[47] A. Nakamura and S. Nonoyama, Phys. Lett. A **324**, 51 (2004).

[48] Y. Ohno, D. K. Young, B. Beschoten, F. Matsukura, H. Ohno, and D. D. Awschalom, Nature **402**, 790 (1999).

[49] C. Rüster *et al.*, Phys. Rev. Lett. **91**, 216602 (2003).

[50] T. Wojtowicz *et al.*, Appl. Phys. Lett. **83**, 4220 (2003).

[51] A. M. Nazmul, S. Sugahara, and M. Tanaka, Phys. Rev. B **67**, 241308 (2003).

[52] G. Vignale and M. E. Flatté, Phys. Rev. Lett. **89**, 098302 (2002).

[53] A. K. Nguyen, R. V. Shchelushkin, and A. Brataas, Physical Review Letters **97**, 136603 (2006).

[54] R. Oszwaldowski, J. A. Majewski, and T. Dietl, Physical Review B (Condensed Matter and Materials Physics) **74**, 153310 (2006).

[55] D. Chiba, M. Yamanouchi, F. Matsukura, T. Dietl, and H. Ohno, Phys. Rev. Lett. **96**, 096602 (2006).

[56] A. Konstandin, J. Kopu, and M. Eschrig, Phys. Rev. B **72**, 140501 (2005).

[57] I. S. Burmistrov and N. M. Chtchelkatchev, Phys. Rev. B **72**, 144520 (2005).

[58] J. F. Gregg, W. Allen, K. Ounadjela, M. Viret, M. Hehn, S. M. Thompson, and J. M. D. Coey, Phys. Rev. Lett. **77**, 1580 (1996).

[59] U. Ebels, P. E. Wigen, and K. Ounadjela, Europhys. Letters **46**, 94 (1999).

[60] U. Rüdiger, J. Yu, L. Thomas, S. S. P. Parkin, and A. D. Kent, Phys. Rev. B **59**, 11914 (1999).

[61] L. Klein, Y. Kats, A. F. Marshall, J. W. Reiner, T. H. Geballe, M. R. Beasley, and A. Kapitulnik, Phys. Rev. Lett. **84**, 6090 (2000).

[62] A. F. Marshall *et al.*, J. Appl. Phys. **85**, 4131 (1999).

[63] Q. Li, Y. F. Hu, and H. S. Wang, J. Appl. Phys. **89**, 6952 (2001).

[64] M. T. Rahman, X. Liu, M. Matsumoto, A. Morisako, S. Meguro, and K. Akahane, J. Appl. Phys. **97**, 10C515 (2005).

[65] D. Ravelosona, A. Cebollada, F. Briones, C. Diaz-Paniagua, M. A. Hidalgo, and F. Batallan, Phys. Rev. B **59**, 4322 (1999).

[66] M. Viret, Y. Samson, P. Warin, A. Marty, F. Ott, E. Søndergård, O. Klein, and C. Fermon, Phys. Rev. Lett. **85**, 3962 (2000).

[67] R. Danneau *et al.*, Phys. Rev. Lett. **88**, 157201 (2002).

[68] H. Tanigawa, A. Yamaguchi, S. Kasai, T. Ono, T. Seki, T. Shima, and K. Takanashi, J. Appl. Phys. **99**, 08G520 (2006).

[69] K. Mibu, T. Nagahama, T. Shinjo, and T. Ono, Phys. Rev. B **58**, 6442 (1998).

[70] N. D. Mathur *et al.*, J. Appl. Phys. **86**, 6287 (1999).

[71] J. Wolfman, A. M. Haghiri-Gosnet, B. Raveau, C. Vieu, E. Cambril, A. Cornette, and H. Launois, J. Appl. Phys. **89**, 6955 (2001).

[72] Y. B. Xu *et al.*, Phys. Rev. B **61**, R14901 (2000).

[73] J. L. Prieto, M. G. Blamire, and J. E. Evetts, Phys. Rev. Lett. **90**, 027201 (2003).

[74] S. Lepadatu and Y. B. Xu, Phys. Rev. Lett. **92**, 127201 (2004).

[75] B. Leven, U. Nowak, and G. Dumpich, Europhys. Letters **70**, 803 (2005).

[76] D. Buntinx, S. Brems, A. Volodin, K. Temst, and C. V. Haesendonck, Phys. Rev. Lett. **94**, 017204 (2005).

[77] W. Lee, F. Q. Zhu, and C. L. Chien, Appl. Phys. Lett. **88**, 122503 (2006).

[78] K. Hong and N. Giordano, J. Phys.: Condens. Matter **10**, L401 (1998).

[79] B. Çetin and N. Giordano, Mater. Sci. Eng. B **84**, 133 (2001).

[80] B. Çetin and N. Giordano, Phys. Stat. Sol. (b) **241**, 2410 (2004).

[81] Y. Otani, G. K. Seung, K. Fukamichi, O. Kitakami, and Y. Shimada, IEEE Trans. Magn. **34**, 1096 (1998).

[82] T. Taniyama, I. Nakatani, T. Namikawa, and Y. Yamazaki, Phys. Rev. Lett. **82**, 2780 (1999).

[83] A. D. Kent, J. Yu, U. Rüdiger, and S. S. P. Parkin, J. Phys.: Condens. Matter **13**, R461 (2001).

[84] T. Nagahama, K. Mibu, and T. Shinjo, J. Appl. Phys. **87**, 5648 (2000).

[85] B. Hausmanns, T. P. Krome, G. Dumpich, E. F. Wassermann, D. Hinzke, U. Nowak, and K. D. Usadel, J. Magn. Magn. Mater. **240**, 297 (2002).

[86] D. Buntinx, S. Veldeman, A. Volodin, and C. Van Haesendonck, J. Magn. Magn. Mater. **242-245**, 1257 (2002).

[87] H. X. Tang, S. Masmanidis, R. K. Kawakami, D. D. Awschalom, and M. L. Roukes, Nature **431**, 52 (2004).

[88] T. Wosiński *et al.*, Phys. Stat. Sol. (a) **204**, 472 (2007).

[89] N. García, M. Muñoz, and Y. Zhao, Phys. Rev. Lett. **82**, 2923 (1999).

[90] P. Bruno, Phys. Rev. Lett. **83**, 2425 (1999).

[91] N. García, H. Rohrer, I. G. Saveliev, and Y. Zhao, Phys. Rev. Lett. **85**, 3053 (2000).

[92] H. D. Chopra and S. Z. Hua, Phys. Rev. B **66**, 020403 (2002).

[93] S. Z. Hua and H. D. Chopra, Phys. Rev. B **67**, 060401 (2003).

[94] H. Imamura, N. Kobayashi, S. Takahashi, and S. Maekawa, Phys. Rev. Lett. **84**, 1003 (2000).

[95] K. Nakanishi and Y. O. Nakamura, Phys. Rev. B **61**, 11278 (2000).

[96] S. H. Kim *et al.*, Phys. Stat. Sol. (b) **241**, 1654 (2004).

[97] M. J. Bonder, N. D. Telling, P. J. Grundy, C. A. Faunce, T. Shen, and V. M. Vishnyakov, J. Appl. Phys. **93**, 7226 (2003).

[98] D. Weller *et al.*, J. Appl. Phys. **87**, 5768 (2000).

[99] C. Vieu *et al.*, J. Appl. Phys. **91**, 3103 (2002).

[100] R. Hyndman *et al.*, J. Magn. Magn. Mater. **240**, 34 (2002).

[101] A. Aziz, S. J. Bending, H. Roberts, S. Crampin, P. J. Heard, and C. H. Marrows, J. Appl. Phys. **98**, 124102 (2005).

[102] A. Aziz, S. J. Bending, H. Roberts, S. Crampin, P. J. Heard, and C. H. Marrows, J. Appl. Phys. **99**, 08C504 (2006).

[103] P. Weiss, J. Phys. **6**, 661 (1907).

[104] V. Fock, Z. Phys. **61**, 126 (1930).

[105] P. Hohenberg and W. Kohn, Phys. Rev. **136**, B864 (1964).

[106] W. Kohn and L. J. Sham, Phys. Rev. **140**, A1133 (1965).

[107] A. D. Becke, Phys. Rev. A **38**, 3098 (1988).

[108] J. P. Perdew, K. Burke, and M. Ernzerhof, Phys. Rev. Lett. **80**, 891 (1998).

[109] J. P. Perdew and Y. Wang, Phys. Rev. B **45**, 13244 (1992).

[110] J. M. MacLaren, S. Crampin, D. D. Vvedensky, and J. B. Pendry, Phys. Rev. B **40**, 12164 (1989).

[111] J. M. MacLaren, S. Crampin, D. D. Vvedensky, R. C. Albers, and J. B. Pendry, Comp. Phys. Commun. **60**, 365 (1990).

[112] S. Crampin, K. Hampel, D. D. Vvedensky, and J. M. MacLaren, J. Mater. Res. **5**, 2107 (1990).

[113] J. Korringa, Physica **13**, 392 (1947).

[114] W. Kohn and N. Rostoker, Phys. Rev. **94**, 1111 (1954).

[115] O. K. Andersen, Phys. Rev. B **12**, 3060 (1975).

[116] R. Zeller, M. Asato, T. Hoshino, J. Zabloudil, P. Weinberger, and P. H. Dederichs, Philos. Mag. B **78**, 417 (1998).

[117] J. B. Pendry, *Low Energy Electron Diffraction*, Academic Press, New York, 1974.

[118] C. G. Broyden, Math. Comput. **19**, 577 (1965).

[119] H. Zhou, H. Tamura, S. Takami, M. Kubo, N. Zhanpeisov, and A. Miyamoto, Jpn. J. Appl. Phys. **39**, 4275 (2000).

[120] M. S. Mizielsinski, *A theory of electron-hole pair excitation in the adsorption of simple atoms on metal surfaces*, PhD thesis, University of Bath, 2007.

[121] E. Vazquez, J. Taguena-Martinez, L. E. Sansores, and C. Wang, J. Appl. Phys. **91**, 3085 (2002).

[122] M. C. Payne, M. P. Teter, D. C. Allan, T. A. Arias, and J. D. Joannopoulos, Rev. Mod. Phys. **64**, 1045 (1992).

[123] M. D. Segall, P. J. D. Lindan, M. J. Probert, C. J. Pickard, P. J. Hasnip, S. J. Clark, and M. C. Payne, J Phys.: Condens. Matter **14**, 2717 (2002).

[124] R. T. Johnson and R. D. Bragsdorf, J. Appl. Phys. **38**, 618 (1967).

[125] W. B. Pearson, *Handbook of lattice spacings and structures of metals*, Pergamon press, Oxford, 1967.

[126] D. A. Papaconstantopoulos, *Handbook of the band structure of elemental solids*, Plenum, New York, 1986.

[127] D. D. Koelling and B. N. Harmon, J. Phys. C: Solid State Phys. **10**, 3107 (1977).

[128] D. J. Langridge, *Multiple scattering theory for supported nanoscale metal chains*, PhD thesis, University of Bath, 2002.

[129] S. L. Cunningham, Phys. Rev. B **10**, 4988 (1974).

[130] U. Pustogowa, J. Zabloudil, C. Uiberacker, C. Blaas, P. Weinberger, L. Szunyogh, and C. Sommers, Phys. Rev. B **60**, 414 (1999).

[131] G. Steinle-Neumann, L. Stixrude, and R. E. Cohen, Phys. Rev. B **60**, 791 (1999).

[132] E. C. Stoner, Proc. Roy. Soc. **165**, 372 (1938).

[133] E. C. Stoner, Proc. Roy. Soc. **169**, 339 (1939).

[134] S. Ferrer, J. Alvarez, E. Lundgren, X. Torrelles, P. Fajardo, and F. Boscherini, Phys. Rev. B **56**, 9848 (1997).

[135] G. P. Francis and M. C. Payne, J. Phys.: Condens. Matter **2**, 4395 (1990).

[136] H. J. Monkhorst and J. D. Pack, Phys. Rev. B **13**, 5188 (1976).

[137] R. W. Newman and J. J. Hren, Surf. Sci. **8**, 373 (1967).

[138] H. Berg and J. H. Cohen, Metall. Trans. **3**, 1797 (1972).

[139] A. Kootte, C. Haas, and R. A. de Groot, J. Phys.: Condens. Matter **3**, 1133 (1991).

[140] L. Uba, S. Uba, V. N. Antonov, A. N. Yaresko, and R. Gontarz, Phys. Rev. B **64**, 125105 (2001).

[141] R. J. Lange, S. J. Lee, D. W. Lynch, P. C. Canfield, B. N. Harmon, and S. Zollner, Phys. Rev. B **58**, 351 (1998).

[142] E. T. Kulatov, Y. A. Uspenskii, and S. V. Halilov, J. Magn. Magn. Mater. **163**, 331 (1996).

[143] I. Galanakis, M. Alouani, and H. Dreyssé, Phys. Rev. B **62**, 6475 (2000).

[144] D. Paudyal, T. Saha-Dasgupta, and A. Mookerjee, J. Phys.: Condens. Matter **16**, 2317 (2004).

[145] F. Menzinger and A. Paoletti, Phys. Rev. **143**, 365 (1966).

[146] B. van Laar, J. d. Physique **25**, 600 (1964).

[147] A. Kashyap, K. B. Garg, A. K. Solanki, T. Nautiyal, and S. Auluck, Phys. Rev. B **60**, 2262 (1999).

[148] T. Bryk, D. M. Bylander, and L. Kleinman, Phys. Rev. B **61**, R3780 (2000).

[149] I. Turek, S. Blügel, and J. Kudrnovský, Phys. Rev. B **57**, R11065 (1998).

[150] R. L. Fink, C. A. Ballentine, J. L. Erskine, and J. A. Araya-Pochet, Phys. Rev. B **41**, 10175 (1990).

[151] I. G. Batyrev, J. Cho, and L. Kleinman, Phys. Rev. B **63**, 172420 (2001).

[152] G. Kresse, W. Bergermayer, and R. Podloucky, Phys. Rev. B **66**, 146401 (2002).

[153] V. Cocula and E. A. Carter, Phys. Rev. B **69**, 052404 (2004).

[154] L. Szunyogh, P. Weinberger, and C. Sommers, Phys. Rev. B **60**, 11910 (1999).

[155] H. L. Skriver and N. M. Rosengaard, Phys. Rev. B **43**, 9538 (1991).

[156] J. S. Faulkner, Prog. Mater. Sci. **27**, 1 (1982).

[157] D. D. Johnson, F. J. Pinski, and G. M. Stocks, J. Appl. Phys. **57**, 3018 (1985).

[158] D. D. Johnson, F. J. Pinski, and J. B. Staunton, J. Appl. Phys. **61**, 3715 (1987).

[159] S. Crampin, R. Monnier, T. Schulthess, G. H. Schadler, and D. D. Vvedensky, Phys. Rev. B **45**, 464 (1992).

[160] I. Turek, M. Freyss, P. Weinberger, D. Stoeffler, and H. Dreyssé, Phys. Rev. B **63**, 024413 (2000).

[161] R. H. Parmenter, Phys. Rev. B **97**, 587 (1955).

[162] L. Nordheim, Ann. Phys. **9**, 607 (1931).

[163] P. M. Oppeneer and A. Lodder, J. Phys. F: Met. Phys. **15**, L115 (1985).

[164] G. M. Stocks, W. M. Temmerman, and B. L. Gyorffy, Phys. Rev. Lett. **41**, 339 (1978).

[165] J. H. Kaiser, P. J. Durham, R. J. Blake, and L. T. Wille, J. Phys. C: Solid State Phys. **21**, 1159 (1988).

[166] B. Ginatempo and J. B. Staunton, J. Phys. F: Met. Phys. **18**, 1827 (1988).

[167] H. Ebert, B. Drittler, and H. Akai, J. Magn. Magn. Mater. **104-107**, 733 (1992).

[168] K. Koepernik, B. Velický, R. Hayn, and H. Eschrig, Phys. Rev. B **55**, 5717 (1997).

[169] K. Refson, Rutherford Appleton Laboratory, UK, Private communication, 2008.

[170] M. Donahue and D. Porter, *OOMMF User's Guide - Version 1.0*, National Institute of Standards and Technology, Gaithersburg, MD, interagency report nistir 6376 edition, 1999.

[171] C. L. Canedy, X. W. Li, and G. Xiao, The 41st annual conference on magnetism and magnetic materials **81**, 5367 (1997).

[172] W. Brown, *Micromagnetics*, Wiley, New York, 1963.

[173] W. Heisenberg, Z. Phys. **49**, 619 (1928).

[174] D. Jiles, *Introduction to magnetism and magnetic materials*, Chapman & Hall, 1998.

[175]

[176] D. R. Fredkin and T. R. Koehler, IEEE Trans. Magn. **26**, 415 (1990).

[177] A. J. Newell, W. Williams, and D. J. Dunlop, J. Geophys. Res. **98**, 9551 (1993).

[178] L. D. Landau and E. M. Lifshitz, Phys. Z. Sowjetunion **8**, 153 (1935).

[179] T. Gilbert, Phys. Rev. **100**, 1243 (1955).

[180] Z. Wang, L. He, D. Mapps, Y. Nakamura, W. Clegg, and D. Wilton, IEEE Trans. Magn. **33**, 3304 (1997).

[181] F. Cayssol, D. Ravelosona, C. Chappert, J. Ferre, and J. P. Jamet, Phys. Rev. Lett. **92**, 107202 (2004).

[182] M. Donahue and R. McMichael, Physica B **233**, 272 (1997).

[183] A. V. Podolskiy and P. Vogl, Phys. Rev. B **69**, 233101 (2004).

[184] W. Harrison, *Electronic structure and the properties of solids*, W.H Freeman and company, 1980.

[185] D. J. Chadi, J. Vac. Sci. Technol. A **5**, 834 (1987).

[186] R. Landauer, Philos. Mag. **21**, 863 (1970).

[187] M. Bütiker, Y. Imry, R. Landauer, and S. Pinhas, Phys. Rev. B **31**, 6207 (1985).

[188] M. Bütiker, IBM J. Res. Dev. **32**, 317 (1988).

[189] K. M. Schep, P. J. Kelly, and G. E. W. Bauer, Phys. Rev. B **57**, 8907 (1998).

[190] S. Sanvito, C. J. Lambert, J. H. Jefferson, and A. M. Bratkovsky, Phys. Rev. B **59**, 11936 (1999).

[191] R. F. Sabirianov, A. K. Solanki, J. D. Burton, S. S. Jaswal, and E. Y. Tsymbal, Physical Review B (Condensed Matter and Materials Physics) **72**, 054443 (2005).

[192] J. van Hoof, *How to handle locally broken symmetries*, PhD thesis, University of Nijmegen, 1996.

[193] A. Aziz, S. J. Bending, H. G. Roberts, S. Crampin, P. J. Heard, and C. H. Marrows, Phys. Rev. Lett. **97**, 206602 (2006).

[194] D. Partin, M. Karnezos, L. deMenezes, and L. Berger, J. Appl. Phys. **45**, 1852 (1974).

[195] L. Berger and A. R. De Vroomen, J. Appl. Phys. **36**, 2777 (1965).

[196] N. W. Ashcroft and N. D. Mermin, *Solid state physics*, Harcourt Brace college publishers, 1976.

[197] J. M. Thijssen, *Computational Physics*, Cambridge university press, Cambridge, 1999.

[198] W. H. Press, W. T. Teukolsky, W. T. Vetterling, and F. B. P, *Numerical Recipes*, Cambridge university press, 1992.

[199] W. Kahan, PhD thesis, University of Toronto, 1959.

[200] H. X. Tang, R. K. Kawakami, D. D. Awschalom, and M. L. Roukes, Phys. Rev. Lett. **90**, 107201 (2003).

[201] H. X. Tang, R. K. Kawakami, D. D. Awschalom, and M. L. Roukes, Phys. Rev. B **74**, 041310 (2006).

[202] H. Tang and M. L. Roukes, Phys. Rev. B **70**, 205213 (2004).

[203] K. Wagner, D. Neumaier, M. Reinwald, W. Wegscheider, and D. Weiss, Phys. Rev. Lett. **97**, 056803 (2006).

[204] R. T. Bate, J. C. Bell, and A. C. Beer, J. Appl. Phys. **32**, 806 (1961).

[205] M. Kläui, C. A. F. Vaz, J. Rothman, J. A. C. Bland, W. Wernsdorfer, G. Faini, and E. Cambril, Phys. Rev. Lett. **90**, 097202 (2003).

[206] S. Chikazumi, *Physics of Ferromagnetism*, Oxford university press, 1997.

[207] D. L. Martin, Trans Met Soc AIME **212**, 478 (1958).

[208] C. E. Dahmani, PhD thesis, Universite Louis Pasteur, Strasbourg, 1985.